SINGLE MOLECULE FLUORESCENCE STUDIES OF PRIONS AND PRION-LIKE PROTEINS

by

Chieh Sang

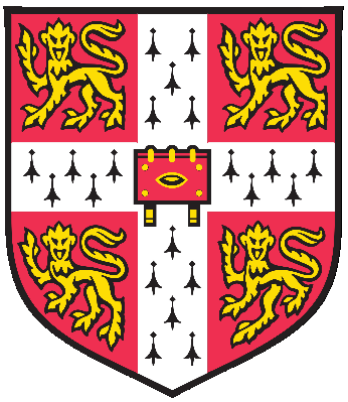

Department of Chemistry

Hughes Hall

August 2018

A dissertation submitted to the University of Cambridge
for the degree of Doctor of Philosophy

Title: Single Molecule Fluorescence Studies of Prions and Prion-like Proteins

Author: Chieh Sang

Research summary: Prions are infectious agents that cause fatal neurodegenerative diseases in brain. The widely accepted protein-only hypothesis states that the misfolded form of prion protein is the sole constituent of prions, and that its propagation and replication play a central role in prion pathogenesis. Prions propagate when disease-related prion protein enters a cell and replicates, leading to an exponential increase in aggregate numbers with time. A similar replication mechanism has also been suggested in other notorious neurodegenerative disorders, such as Alzheimer's disease and Parkinson's disease.

In this thesis, the aggregation mechanisms of prion protein and α-Synuclein were studied using single-molecule fluorescence methods. From fluorescence imaging of individual aggregates on a glass surface, elongation and fragmentation of prion protein were observed, which directly confirmed the existence of key mechanisms in prion biology. An increase in proteinase K resistance suggested that structural conversion to a disease-related conformation takes place during aggregation. Next, this process was quantified by kinetic modelling with a series of solution-seeded aggregation reactions in a test tube over a broad range of seed and monomer concentrations. The fitted kinetic rate constants for elongation and fragmentation thus provide a simple approach to estimate prion propagation in vivo.

The same method was applied to measurement of α-Synuclein (αS) aggregation, which has been suggested to be prion-like and is a key player in Parkinson's disease. αS was demonstrated to elongate and fragment significantly more slowly than prion protein in bulk solution, leading to a much slower replication rate. To extend the study to cellular environments, I applied super-resolution imaging to study the transcellular spread of αS seeds. Initial results showed seeded amplification in the number of aggregates with time.

The molecular details of prion protein aggregation were further characterised with various biophysical approaches. I explored the early events in aggregation and identified five oligomers with distinct structural and kinetic characteristics, co-existing during aggregation. Membrane disruption assay also indicated a higher membrane permeability for smaller-sized PK-sensitive oligomeric species.

Overall, my studies on neurodegenerative proteins identify fibril elongation with fragmentation as an important mechanism of replication and provide a new quantitative approach to describe prion-like properties. This work also provides a simple framework to explain differences in disease spreading among neurodegenerative diseases from a kinetic perspective that can be studied with other proteins.

This thesis is dedicated to my parents and all my family,

for without whom, I could never have gone this far.

Especially to my grandmother, who is a strong person with dementia.

Declaration

This dissertation summarises research carried out in the laboratory of Professor David Klenerman at the Department of Chemistry, University of Cambridge between October 2014 and August 2018.

This dissertation is the result of my own work and includes nothing which is the outcome of work done in collaboration except as specified in the text.

It is not substantially the same as any that I have submitted, or, is being concurrently submitted for a degree or diploma or other qualification at the University of Cambridge or any other University or similar institution. I further state that no substantial part of my dissertation has already been submitted, or, is being concurrently submitted for any such degree, diploma or other qualification at the University of Cambridge or any other University or similar institution.

It does not exceed the prescribed word limit for the Degree Committee for the Faculty of Physics & Chemistry.

Chieh Sang

August 2018

Acknowledgements

Once a well-renowned Cambridge alumnus in the 17th century said: If I have seen further it is by standing on the shoulders of Giants.' The last four years in Cambridge have been productive and enjoyable life to me. Closing to the end of my quest to pursue PhD, despite still being unsure if I have seen further, one thing is certain - this journey has not been alone and I can only complete it with help and advice from many people.

I would like to express my deep gratitude to my supervisor, *Professor David Klenerman*, for his positive attitude, inspiring guidance, and insightful feedback throughout my PhD life. The work I have done in this thesis are achieved through close collaboration with: *Dr Raymond Bujdoso* and *Dr Alana Thackray* at the Department of Veterinary Medicine, Cambridge; *Professor Tuomas Knowles*, *Dr Liu Hong*, *Dr Georg Meisl*, and *Alexander Dear* at the Department of Chemistry, Cambridge; *Dr Joel Watts* at the Tanz Centre for Research in Neurodegenerative Diseases, University of Toronto; *Professor Maria Spillantini* at the Department of Clinical Neurosciences, Cambridge; and *Dr Linda Julian* at Cancer Research UK, Cambridge. Many valuable ideas and insights have been generated through discussion with my collaborators, and I truly thank them for extending my knowledge, as well as kind supports from various fields during my PhD research.

The Klenerman and the Lee groups have been a supportive family. I am grateful to *Dr Marija Iljina*, *Dr Aleks Ponjavic*, *Dr Ji-Eun Lee*, *Dr Yu Ye*, *Rachel Cliffe*, *Dr Suman De, Dr Franziska Kundel*, *Dr Christopher Taylor*, and *Yukun Zuo*, who have been supportive colleagues and collaborators throughout my projects with enthusiasm. I also thank *Dr Steven Lee*, *Dr Mathew Horrocks*, *Dr Rohan Ranasinghe*, *Dr Nadia Shivji*, *Dr Laura Tosatto*, *Dr Anna Drews*, *Dr Yu Zhang*, *Dr Juan Varela*, *Dr Margarida Rodrigues*, *Dr Lisa-Maria Needham*, *Dimitri Sideris*, and all past and present group members for honest and practical academic and non-academic advices from time to time. I also thank *Dr Wei-Hsin Chen* for listening and cheering me up when in times of frustration. I thank *Dr Jeremy Skepper* in CAIC for the assistance in TEM imaging.

I am grateful to the *Cambridge Trust* and the *Ministry of Education, Republic of China (Taiwan)* for the funding and offering me an opportunity to explore science in Cambridge.

As an old Chinese saying describes 'one always needs friends' supports in a foreign land', I am grateful for the physical and emotional support from my friends in England and other countries, especially: *Shu-Wei*, *Eddy*, *Shawn*, *Henry*, *Wade*, *Iris*, *Emma*, for their constant presence whenever I need them; *Chi-Kai* and *Yvonne*, *Ian* and *Ting-Yin*, *Sandy* and *Thomas*, *Chia-Chi* and *Jinco*, for genuine hospitality with surprisingly high-quality food and snacks;

Chi-Kai, Hung-Chang, and *Tien-Li* for their alcoholic support and non-alcoholic advices with my highest regard. I am with all my heart thank *Yu-Chen* for her genuine support in the past nine years.

Dr Rita P.-Y. Chen, my master's supervisor and mentor, must be thanked for being the sole motivation for me pursuing PhD in Cambridge, for the continuous encouragement, and for opening a window for me in protein chemistry and neurodegeneration research. I also thank *Dr Hsin-Liang Chen*, *Paul*, *Tsung-Ho*, *Meng-Hueng*, *Lee, Rih-Teng Wu*, and *Che Yang* for their presence and supports from Taiwan and other countries. *Yung-Kang Peng* has been my life-long comrade friend since we served in the army, and he is still a loyal friend during our PhD in England. My special thank-you is given to a true old friend *Chia-Ju Pan* for inspiring me as a PhD in the first place, and now I have carried our dream and kept my promise from childhood.

My final gratitude is reserved for my beloved family. My parents and grandparents have raised and supported me unconditionally at any circumstances; my grandmother-in-law, aunt, and uncle have cared me. My little brother and cousin have been my best playmates and are enthusiastic when I come home. I am more than grateful for their disproportionate love to me.

Table of Contents

Index of Figures and Tables

Abbreviations

Aβ	Amyloid beta
AD	Alzheimer's disease
AFM	Atomic force microscopy
αS	α-Synuclein
BSA	Bovine serum albumin
BSE	Bovine spongiform encephalopathy
CD	Circular dichroism
CJD	Creutzfeldt-Jakob disease
CSF	Cerebral spinal fluid
CWD	Chronic wasting disease
DLB	Dementia with Lewy bodies
DMEM	Dulbecco's modified Eagle's medium
DMSO	Dimethyl sulfoxide
DTT	Dithiothreitol
EM	Electron microscopy
EMCCD	Electron multiplying charge coupled device
FBS	Fetal bovine serum
fCJD	Familial Creutzfeldt-Jakob disease
FFI	Fatal familial insomnia
FSE	Feline spongiform encephalopathy
GdnHCl	Guanidium hydrochloride
GOC scavenger system	Glucose oxidase in combination with catalase
GPI	Glycosylphosphatidylinositol
GSS	Gerstmann-Sträussler-Scheinker syndrome
iCJD	Iatrogenic Creutzfeldt-Jakob disease
iPSC	Induced pluripotent stem cells
LDH	Lactate dehydrogenase
MJFR-14-6-4-2	A conformation-specific antibody developed with support from the Michael J. Fox Foundation for Parkinson's Research
MSA	Multiple system atrophy
MTT	3-(4,5-Dimethylthiazol-2-yl)-2,5-diphenyltetrazolium bromide
NA	Numerical aperture
NMR	Nuclear magnetic resonance
NR	Nile red

PAGE	Polyacrylamide gel electrophoresis
PAINT	Points accumulation for imaging in nanoscale topography
PBS	Phosphate buffered saline
PD	Parkinson's disease
pFTAA	Pentameric formyl thiophene acetic acid
PIRIBS architecture	Parallel in-register intermolecular beta-sheet
PK	Proteinase K
PK-sen	PK-sensitive
PK-res	PK-resistant
PLL	Poly L-lysine
Prion	Proteinaceous infectious particle
PrP	Prion protein
PrP^{C}	Cellular PrP isoform
PrP^{Sc}	Scrapie PrP isoform
PSF	Point spread function
RA	Refraction index
RP	Regulatory particle of the proteasome
SBR	Signal-to-background ratio
sCJD	Sporadic Creutzfeldt-Jakob disease
SDS	Sodium dodecyl sulfate
sFI	Sporadic fatal insomnia
SMLM	Single-molecule localisation microscopy
SNR	Signal-to-noise ratio
SOD1	Superoxide dismutase-1
TCEP	Tris(2-carboxyethyl)phosphine
TIRF	Total internal reflection fluorescence
ThT	Thioflavin T
TEM	Transmission electron microscopy
TME	Transmissible mink encephalopathy
TSE	Transmissible spongiform encephalopathy
UA	Uranyl acetate
vCJD	variant Creutzfeldt-Jakob disease
WT	Wild type

Associated publications from this thesis

(1) Sang, J. C.; Meisl, G.; Thackray, A. M.; Hong, L.; Ponjavic, A.; Knowles, T. P. J.; Bujdoso, R.; Klenerman, D. Direct Observation of Murine Prion Protein Replication in Vitro. J. Am. Chem. Soc. 2018, 140 (44), 14789–14798.

(2) Lee, J.-E.; Sang, J. C.; Rodrigues, M.; Carr, A. R.; Horrocks, M. H.; De, S.; Bongiovanni, M. N.; Flagmeier, P.; Dobson, C. M.; Wales, D. J.; Lee, S. F.; Klenerman, D. Mapping Surface Hydrophobicity of α-Synuclein Oligomers at the Nanoscale. Nano Lett. 2018. Epub ahead of print.

Abstract

Prions are infectious agents that cause fatal neurodegenerative diseases in the brain. The wide-accepted protein-only hypothesis states that the misfolded form of prion protein (PrP) is the sole constituent of prions, and the self-propagating process of PrP is considered to play a central role in prion pathogenesis. Prions are believed to propagate when a PrP assembly enters a cell and replicates to produce two or more fibrils, leading to an exponential increase in PrP aggregate number with time. However, the molecular basis of this process has not yet been established in detail. This prion-like replication is also suggested to be the mechanism in the development of other notorious neurodegenerative disorders, such as Alzheimer's and Parkinson's disease.

In this thesis, I use single-aggregate imaging to study fibril fragmentation and elongation of individual murine PrP aggregates from seeded aggregation *in vitro*. From fluorescence imaging of individual PrP aggregates on the coverslip surface, elongation and fragmentation of the PrP assemblies have been directly observed. PrP elongation occurs *via* a structural conversion from a proteinase K (PK)-sensitive to PK-resistant conformer. Fibril fragmentation was found to be length-dependent and resulted in the formation of PK-sensitive fragments. To gain more insights into the mechanism of the spread of PrP, the quantified kinetic profiles allows the determination of the rate constants for these processes through the use of kinetic modelling. This enables the estimation of a simple framework for aggregate propagation through the brain, assuming that doubling of the aggregate number is rate-limiting.

In contrast, the same method was applied to measurement for α-Synuclein (αS) aggregation, which has been suggested to be prion-like and is associated with Parkinson's disease. While αS aggregated by the same mechanism, it showed significantly slower elongation and fragmentation rate constants than PrP, leading to much slower replication rate. Furthermore, the measurements in αS aggregation has been extended to the cellular environment, I use super-resolution imaging to study the amplification of endogenous αS aggregation in cells and the transcellular spread of αS. Endogenous αS showed a clear amplification in number of aggregates with time after seed transduction, and the newly-formed αS aggregates are likely to spread through cell-to-cell transmission. The proteasome was demonstrated to possess a novel disaggregase function for αS fibrils and thus produce more seeds for further replication. It partially explains that αS aggregation in cells was found to replicate at a substantially faster rate than that *in vitro*.

Determining the nature of the oligomers formed during aggregation has been experimentally difficult due to the lack of suitable methods capable of detecting and

characterising the low level of oligomers. To address this problem, I have studied the early formation of PrP oligomers formed during aggregation *in vitro* using various single-molecule methods. The early aggregation of PrP is observed to form a thioflavin T (ThT)-inactive and two ThT-active species of oligomers, which differ in size and temporal evolution. The ThT-active oligomers undergo a structural conversion from a PK-sensitive to PK-resistant conformer, while a fraction of which grow into mature fibrils. These results also enable the establishment of a kinetic framework for elucidating temporal evolution of PrP aggregation and the relationship between oligomers and fibrils.

Overall, my research identifies fibril elongation with fragmentation are the key molecular processes leading to PrP and αS aggregate replication, an important concept in prion biology, and provides a simple framework to estimate the rate of prion and prion-like spreading in animals. The results also show that a diverse range of oligomers is formed and co-exist during PrP aggregation which differ both in their structure and properties and provides mechanistic insights into a prion aggregation. The work provides a new quantitative approach to describe the prion-like property in neurodegenerative diseases from a kinetic perspective that can be verified in extending studies in other proteins or in cells.

Chapter 1 | Introduction

1.1 The molecular basis of protein aggregation I: an overview

Proteins are macromolecules that are responsible for implementing multiple essential functions within living organisms. Their expression patterns reflect the different requirements of cells at particular time points and locations. The importance of proteins can be attributed to their various roles in cellular maintenance, such as catalysing chemical reactions, transporting molecules, responding to external stimuli, and maintaining normal physiological conditions. To fulfil normal biological functions, the majority of proteins have to fold into precise three-dimensional structures *in vivo*. This behaviour has also been demonstrated *in vitro* for numerous proteins, confirming Anfinsen's hypothesis that the linear sequence of a polypeptide chain contains all information required for the folding into its correct three-dimensional conformation[1,2].

The discovery of misfolded states, or amyloid states, has challenged this central dogma and our understanding of the nature of proteins[3–6], leaving many fundamental questions unanswered. In particular, structural conversion of proteins from functional and soluble conformation into aberrant misfolded conformation is the origin of a broad range of human disorders[6,7]. Among these, neurodegenerative diseases are the largest subgroup responsible for many fatal diseases. To understand the origin of neurodegenerative diseases, the folding and misfolding mechanism of proteins is reviewed in the following section.

1.1.1 Protein folding and misfolding

Protein folding is described as a diffusional search process of an polypeptide sequence on a funnel surface of free energy, driven by various non-covalent interactions including hydrogen bonding, electrostatic interactions, van der Waals forces (or London dispersion force), and the hydrophobic effect involving solvent molecules interactions[8]. These relatively weak interactions among hundreds of amino acids have to direct the amino acid chain to one specific endpoint in the free energy funnel, such that a protein can acquire its own 3D structures to exert its normal functions. The nature of folding is a striking and complicated phenomenon for researchers, as an organism has 4000 (*Escherichia coli*) to 20000 (humans) proteins with distinct structures, many of them containing relatively long sequences of >100 amino acids[9]. The folding reaction is so complex that even today

correct protein structure cannot be precisely predicted.

We can use a thermodynamic approach to understand the folding process. The rugged energy landscape theory describes how a naïve and linear polypeptide chain is forced to search for a more stable energy state in order to reduce the entropy of the system; consequently, the free energy of the system decreases by excluding solvent molecules and then collapsing into a more compact state[8]. The ultimate state of the protein structure is achieved when a single energy minimum is reached, analogous to reaching the bottom of a funnel. This model provides a connection between the folding reaction, the driving forces involved, and free energy. However, several faults of the theory have been proposed, and one of the major issues is the incompatibility with the latter discovered misfolded products.

A modified version of the energy landscape theory retains the central idea of the funnel, while it can better illustrate the phenomenon by considering the whole folding reaction as a process on a rugged energy surface (Figure 1.1a). As the reaction direction is multiple and reversible, the protein dynamics might generate several routes and local minima of the energy state for a single final energy minimum, or global minimum[10–12]. Each potential route of folding is created by the interactions within the polypeptide chain and between the polypeptide chain and the environment. During folding, protein molecules travel downhill on the free energy surface. Partially folded intermediates and folded intermediates, occupy certain local minima (Figure 1.1a, green) and represent the energy traps *en route* towards the thermodynamically favourable native state[9].

The form of protein folding can be roughly divided into two categories based on molecular size. Smaller proteins ($<$100 amino acids) tend to fold in only one step, mainly achieved by a hydrophobic core collapsing process; in contrast, larger proteins with $>$100 amino acids are more likely to form folding intermediates before they collapse rapidly into a compact native structure[2,13]. As the cellular environment is a highly crowded environment (300-400 g of total protein per litre in the cytosol[14]), the correct folding of large proteins often requires molecular chaperones[2,8,9,15]. Molecular chaperones assist protein folding by lowering free energy barriers and preventing aberrant intermolecular interactions (Figure 1.1a, red; and Figure 1.1b), which can lead to various misfolded states of protein aggregates (amorphous, oligomeric, fibrillar) that will be discussed in the next section.

1.1.2 Protein misfolding leads to aggregation

The newly-synthesised proteins, either post-translated or co-translated from mRNA, fold *en route* through structural intermediates to their final native conformation, which

represents the global minimum of energy. However, the folding process is error-prone due to several reasons: 1) there are $>10^{30}$ possible conformations that can be adopted for a 100 a.a. protein chain; 2) correct folding has to rely on various pairs of weak non-covalent interactions among amino acids to overcome substantial kinetic energy barriers and a range of folding intermediates; 3) the phenomenon of molecular crowding in cells enhances the tendency to form folding intermediates and misfolded states *in vivo*[9].

Proteins in their partially folded or misfolded states tend to self-assemble into larger-sized aggregates. However, protein self-assembly with native conformations is not uncommon *in vivo*, of which their functional states are intrinsically insoluble in aqueous solutions and form into fibrillar assemblies. For example, both the cytoskeleton and silk are only functional as their monomers assemble into ordered fibrils in order to maintain the physical strength. In contrast, protein self-assembly with non-functional misfolded conformations leads to serious consequences and a broad range of human diseases.

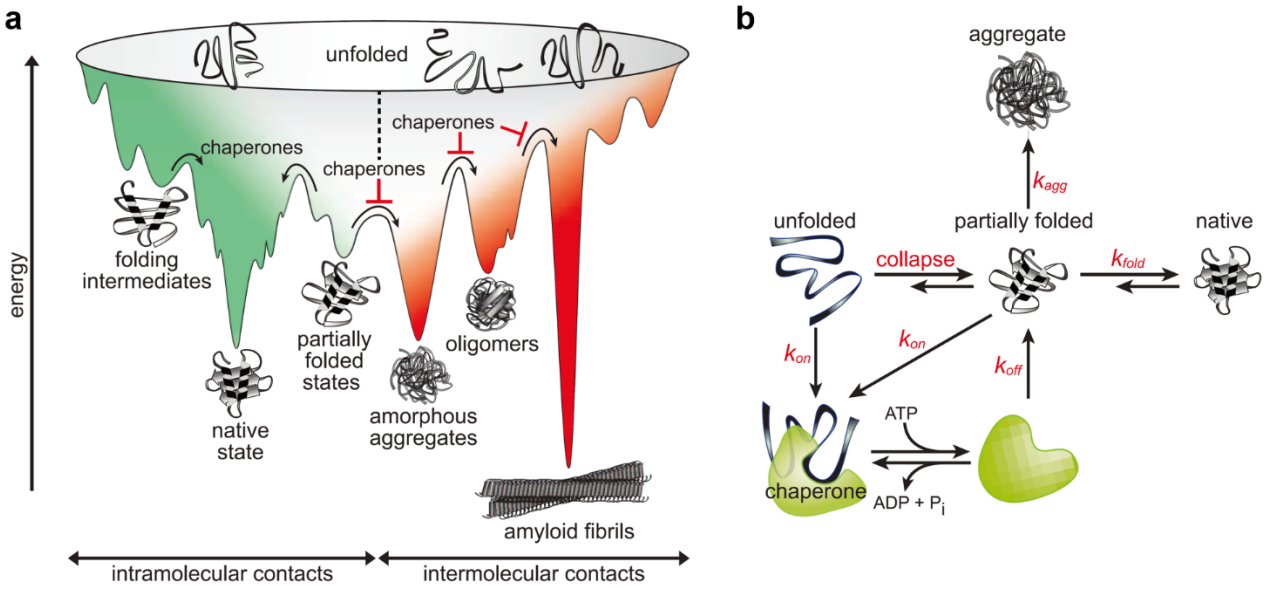

Figure 1.1 | Schematic diagram for protein folding and misfolding. (**a**) A schematic energy landscape for protein folding. During folding, protein molecules form a range of partially-folded intermediates with different conformations on the route travelling downhill on a free energy surface toward the native state (green). Chaperones assist folding by lowing energy barriers and preventing aberrant intermolecular interactions that form various misfolded conformations (red). (**b**) A kinetic scheme for protein folding. The spontaneous folding process can be assisted by chaperones binding to partially-folded intermediates that expose hydrophobic residues, thereby blocking the pathway to aggregation. Figure modified from ref. 9.

Protein misfolding involves substantial structural conversion from a native, soluble conformation to an insoluble conformation[7]. Misfolded proteins expose their hydrophobic amino acid residues to the solvent, thus are extremely unstable and reasonably could be considered as off-pathway products which are trapped in the valleys of the energy landscape (i.e. local minima)[13,16]. The resulting protein aggregation is a thermodynamically spontaneous reaction as the consequence of the unstable misfolded state. This intermolecular assembly process with misfolded conformations leads to a series of kinetically stable conformations[9]. Many aggregated states of proteins are structurally amorphous on a super-tertiary level, consisting of more or less disordered assemblies of interacting chains of the same or different sequences. In contrast, others might self-assemble as highly-ordered amyloid fibrils with "cross-β" structure due to their own structures and properties[6,17]. Amyloid fibrils are more thermodynamically stable than normal folding state and associated with many neurodegenerative diseases. This term 'amyloid' was first introduced in 1854. As the tissues and organs of patients who died from systemic amyloidosis were observed to contain deposits that stained with iodine, which is used for starch detection, the pathogenic agent was mistakenly regarded as starch-like materials, and hence the name 'amyloid' has been inherited until today[18,19].

1.2 Neurodegenerative diseases

The failure of correct protein folding and subsequent aggregation *in vivo* leads to protein deposits in tissues and a broad range of fatal human diseases. Major examples are provided by the amyloid β peptide (Aβ) of Alzheimer's disease, α-Synuclein (αS) of Parkinson's disease, and prion protein (PrP) of the different variants of spongiform encephalopathies (i.e. prion diseases). These diseases are collectively called neurodegenerative diseases, as these conditions lead to progressive degeneration in the central or peripheral nervous system[7]. With the global phenomenon of the increasingly ageing population, neurodegenerative diseases have arguably become the most dreaded maladies for elderly citizens, especially in the developed regions of the world[20]. This thesis covers the study of the aggregation mechanism of PrP and αS. Their pathology and structural biology are discussed in this section.

1.2.1 Prion diseases, prion protein, and the emergence of the prion concept

Prion diseases are an important model for neurodegenerative conditions in general. Since the term 'prion' was proposed thirty years ago[21], tremendous advances have been made in understanding the problem of protein misfolding based on the prion hypothesis. Prion diseases, or more officially termed *transmissible spongiform encephalopathies* (TSEs), are a class of fatal neurodegenerative disorders which has been identified in many mammalian species. A list of discovered TSEs is provided in Table 1.1 that includes several well-known variants such as bovine spongiform encephalopathy (BSE, or commonly named mad cow disease) in cattle, and Creutzfeldt-Jakob disease (CJD) and Kuru disease in humans[22]. Clinical features of prion diseases often display prolonged incubation periods, usually followed by progressive motor dysfunction, cerebral ataxia, and dementia prior to death[23]. Histological analysis of the brains from human sufferers reveals symptoms of characteristic spongiform degeneration (i.e. neuronal death), astrogliosis, and pathological amyloid plaques containing misfolded prion protein (Figure 1.2)[23–29]. The accumulation of abnormal PrP usually co-localise with TSE neuropathology[30].

The history of prion diseases was first documented in the 18th century. German literature in 1759 describes some sheep suffering from scrapie by the facts that "affected animals lie down, rub their backs against posts, fail to thrive, stop feeding and finally die"[31]. It also

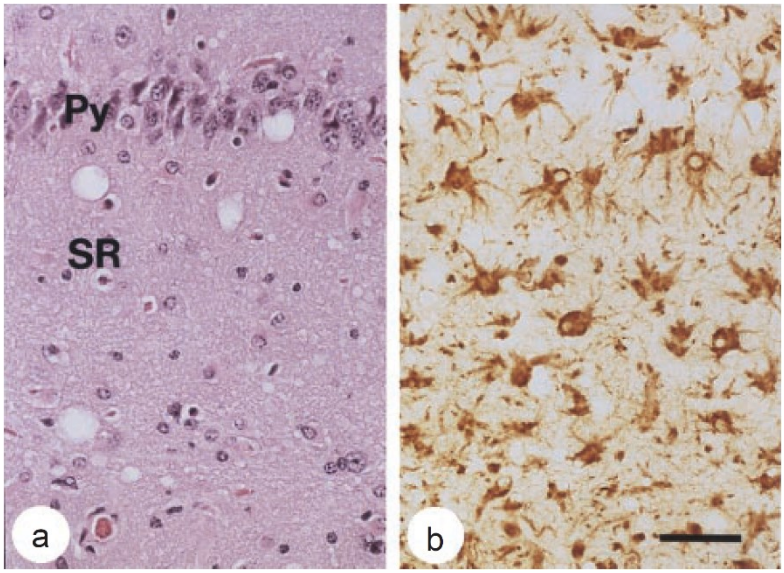

Figure 1.2 | Neuropathological changes of the brain in CD-1 Swiss mice induced by prions of RML strain. (**a**) Pyramidal cell layer (Py) and stratum radiatum (SR) regions in the hippocampus of mice after inoculation of RML prions shows spongiform degeneration with vacuoles ranging 20-30 μm using hematoxylin and eosin staining. (**b**) Astrocytic gliosis (i.e. non-specific reactive change in response to damage to the central nervous system) in the hippocampus is shown after Glial fibrillary acidic protein (GFAP) immunohistochemistry. The scale bar represents 30 μm for both images. Figure modified from ref. 24.

commented that the shepherds had to isolate the affected sheep from healthy stock immediately because it was infectious and could cause serious harm to the flock[31]. In the 19th century, European veterinarians initiated scientific research into this scrapie disease (i.e. the origin of the modern term for misfolded PrP, or PrP^{Sc}), and notably, Besnoit *et al.* in 1899 recognised neuronal vacuolation as a characteristic feature[31,32]. In 1936, another major finding was achieved by Cuillè and Chelle, who confirmed the transmissibility of scrapie disease by inoculating brain and spinal cord tissue from an affected animal to healthy sheep[31,32]. In 1961, transmission studies were extended to mice[33], confirming that the scrapie agent was able to transmit. It was a milestone for researchers previously obliged to work exclusively with sheep and goats.

TSEs had not been reported to be linked to humans until 1959. An American veterinarian Hadlow described that a newly discovered disease, Kuru disease, which was found in Papua New Guinea and reported by Gajdusek and Zigas two years earlier, was analogous

to scrapie and transmitted by the ritual of endocannibalism[34,35]. This is direct evidence that TSEs is infectious through interorganismal transmission. Later, based on the exhaustive study on 12 brains from Kuru patients, Klatzo in 1968 commented that Kuru resembled another human disease - Creutzfeldt-Jakob disease (CJD), first described in 1920s. Further comparisons between related human diseases such as FFI and GSS, which are now confirmed to result from genetic mutation of PrP nowadays, led to the classification of these neurodegenerative disorders as a subtype of TSEs[31,32] (Table 1.1). In 1996, a novel human TSE, variant CJD (vCJD), was emerging in the United Kingdom[36,37]. The vCJD can be distinguished from classical CJDs by distinct neuropathological features and electroencephalogram changes[32]. Since the neuropathological patterns of mice were very similar after infected BSE or vCJD, it was believed to be the human form of bovine spongiform encephalopathy (BSE, or mad cow disease in common term), and it was likely to spread from cattle to humans through consumption of BSE-contaminated meat product. Up until 2009, there have been 211 cases of vCJD reported worldwide, and 167 of them were UK residents[32,38]. This was the first time that TSE agents were shown to be capable of cross-species transmission.

The nature of TSE agents had been extensively debated for many decades. Early studies from scrapie disease in sheep in 1950 indicated the existence of a 'filterable virus'[39]. Later in 1967, Griffith in the Bedford College, London suggested a revolutionary idea that the

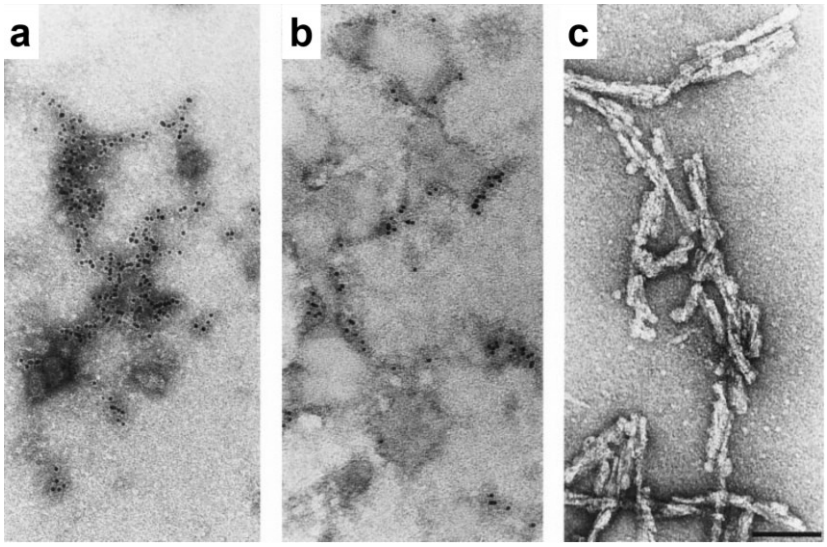

Figure 1.3 | TEM images of hamster PrP^{C} and PrP^{Sc} aggregates. (**a**) PrP^{C} and (**b**) PrP^{Sc} do not show distinguishable structure after negative staining with immunogold-labelled PrP. (**c**) PrP27-30 is derived from PrP^{Sc} after proteinase K (PK) treatment, showing rod-like structure. The scale bar represents 100 nm. Figure modified from ref. 24 and 29.

pathogen could be protein which folds itself into an abnormal form, thus acting as an infectious agent[40]. Inspired by this idea, in 1982 Stanley B. Prusiner at the University of California, San Francisco proposed that the transmissible pathogen was naturally proteinaceous, based on the results that the pathogen was resistant against radiation and nuclease treatment. The term 'prion' (for *pr*oteinaceous *i*nfectious particle) was coined by him to describe such TSE agents, thereby distinguishing them from viruses and viroids[21,23,41]. It is now generally accepted that the structural conversion of PrP from the normal cellular prion protein (PrP^{C}) to the misfolded scrapie form (PrP^{Sc}) is the trigger leading to prion diseases (Figure 1.3). Over the past two decades, a wealth of evidence has been supporting the protein-only hypothesis for prion transmission. These include the generation of PrP transgenic mice that develop neurodegenerative disease that is transmissible[42–44] and the *in vitro* generation of infectious prions[45–49]. With growing knowledge in neurodegeneration research, other associated diseases are shown to possess the features of prions and prion-like properties that will be discussed in Chapter 1.3. There has been a call for a unifying definition of prions in the last few years, that the prion should include all prion-like proteins based on their common propagation mechanism[50–52].

Disease	Natural host species	Route of transmission or disease-induction mechanism
Sporadic CJD (sCJD)	Humans	Unknown
Iatrogenic CJD (iCJD)	Humans	Accidental medical exposure to CJD-contaminated tissues, hormones or blood derivatives
Familial CJD (fCJD)	Humans	Genetic (germline *PRNP* mutations)[‡]
Variant CJD (vCJD)	Humans	Ingestion of BSE-contaminated food
Kuru	Humans	Ritualistic cannibalism
Fatal familial insomnia (FFI)	Humans	Genetic (germline *PRNP* mutations)
Sporadic fatal insomnia (sFI)	Humans	Unknown
Gerstmann-Sträussler-Scheinker syndrome (GSS)	Humans	Genetic (germline *PRNP* mutations)
Scrapie	Sheep, goat, and mouflon	Horizontal and possibly vertical
Atypical scrapie	Sheep and goat	Unknown
Chronic wasting disease (CWD)	Mule deer, white-tailed deer, Rocky Mountain elk, and moose	Horizontal and possibly vertical
BSE	Cattle	Ingestion of BSE-contaminated food
Atypical BSE	Cattle	Unknown
Feline spongiform encephalopathy (FSE)	Zoological and domestic felids	Ingestion of BSE-contaminated food
Transmissible mink encephalopathy (TME)	Farmed mink	Ingestion of BSE-contaminated food
Spongiform encephalopathy of zoo animals	Zoological ungulates and bovids	Ingestion of BSE-contaminated food

Table 1.1 | TSEs in human and mammals. Adapted from ref. 22.

1.2.2 Prion protein structures and functions

The cellular form of PrP (PrP^C) is a ~33-35 kDa glycoprotein (23 kDa for the recombinant protein) attached to the outer cell membrane by a glycosylphosphatidylinositol (GPI) anchor[41]. Lower PrP^C expression is also found in various cellular components of the immune system, bone marrow, blood, and peripheral tissues. Maturation events of the nascent peptide chain result in a final protein composed of 208 residues. Through a succession of post-translational modifications, a signal peptide at the N-terminus (a.a. 1-22) is removed, a GPI anchor is attached to the C-terminus, and the second and the third helix are linked with a disulfide bond[53]. The two helices also contain two N-glycosylation sites, which may be present as di-, mono-, or un-glycosylated forms with a large diversity of glycan molecules[41]. Structural studies of recombinant mouse PrP have identified it as a two-domain protein[54]: a predominantly disordered N-terminus (~100 residues) and a mainly α-helical C-terminus consisting of three α-helices and two short anti-parallel β-strands. The NMR structure of the globular C-terminus of mouse PrP^C is shown in Figure 1.4.

N-terminus of PrP^C

The structurally less-defined N-terminal region of PrP^C consists of residues 23-134, which accounts for approximately half of the whole sequence (Figure 1.4e). It contains a stretch of several octapeptide repeats (OR), flanked by two positively charged clusters (CC, a.a. 23-27 and 95-110). These domains are followed by a hydrophobic cluster of amino acids (HC, a.a. 111–134). Cooperative binding of four Cu^{2+} to the octarepeats is a unique and confirmed feature for PrP ligand, although its physiological role is still unclear[38]. *In vitro*, the octarepeats appear to strictly prefer Cu^{2+} over Cu^{+} and other metal ions. Binding of Cu^{2+} to PrP^C was reportedly the most effective at neutral pH, with a reduced affinity at lower pH[55]. It is worth noting that many human prion diseases, including inherited, iatrogenic, and sporadic CJD, are influenced by an amino acid polymorphism resulting in M to V substitution within the hydrophobic region at codon 129 of PrP [56]. The analysis in the *PRNP* gene in those patients with Kuru disease showed that most of them were heterozygous at codon 129 (i.e. MV genotype), a genotype associated with extended incubation periods and resistance to prion diseases[57].

C-terminus of PrP^C

The structure of the globular C-terminus is highly conserved among mammals[58]. The NMR structure in Figure 1.4 shows that the helices H2 and H3 are linked by a disulfide bond between C179 and C214. The folding of PrP has been demonstrated to be intrinsically disordered and stabilised by the disulfide bond[59], and structural conversion to a misfolded conformer is likely to take place from the unfolding of H2[60–62]. A rather large

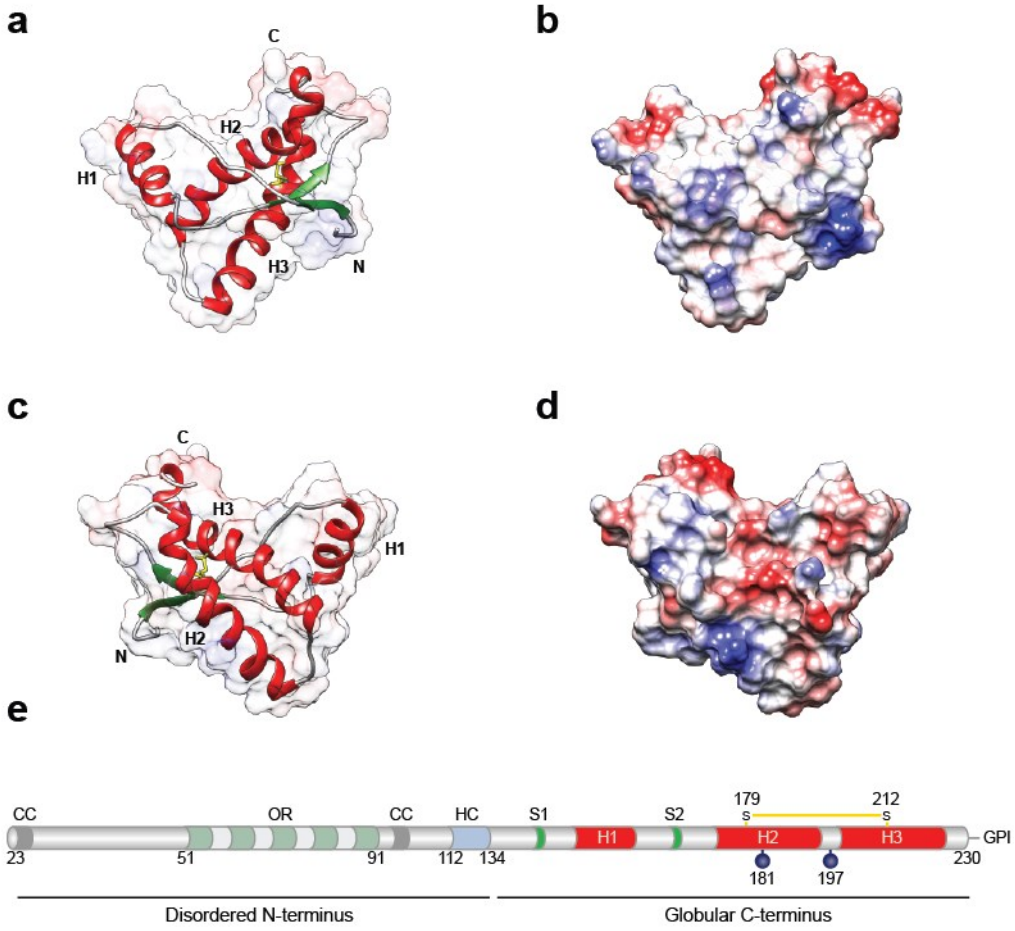

Figure 1.4 | NMR structure of mouse PrP (121-231). (**a**) Ribbon diagram of mouse PrP (121-231) shows the globular fold of native PrP. The 3D structure reveals three α-helices (red) and two anti-parallel β-sheets (green). The disulfide bond between C179 and C214 (yellow) is shown. The N-terminal segment of residues 23-120 is unstructured and not displayed. (**b**) The surface view reveals the electrostatic potential of PrP, with blue indicating positive charges and red indicating negative charges. The presentation in (**c**) and (**d**) relates to the one in (**a**) and (**b**) through a 180° rotation around a vertical axis. (**e**) Structural features of PrP polypeptide sequence. Disulfide bond (yellow), glycosylation sites (blue), and GPI anchor in S231 are displayed. CC: charged cluster; OR: octarepeat; HC: hydrophobic cluster. (PDB: 1AG2)

variety of N-glycans are found to attach to PrP^C at N181 and N197[63,64]. While di-glycosylated PrP^C is the dominant glycoform in the adult human brain, the ratio of di-, mono-, and unglycosylated PrP^C glycoforms is observed to vary in different brain regions[65]. The ratio is also found to increase with the course of neuronal differentiation, as well as with the increasing density of cells cultured *in vitro*[38,66,67]. Recent studies in sialylation of the N-linked glycans have shown the glycan composition plays a key role in regulating prion propagation rate and infectivity[68]. The propagation rate in hyper-sialylated PrP^{Sc}, which accounts for 35% of the total population in prions of the RML strain, is estimated to decrease by 500 folds[68–70].

PrP^C tissue expression and functions

PrP^C is predominantly expressed at high levels in the nervous system, but it is also found in several types of the immune system (e.g. lymphocytes and lymphoid cell lines, monocytes, T cells, NK cells, B cells), bone marrow, blood, and peripheral tissues[38]. The physiological function of PrP^C is still unclear, and whether the normal function contributes to the toxicity in prion diseases remains unknown[41]. Early studies in mice indicated that the ablation of the *Prnp* gene, which is located on the short arm of human chromosome 20 and responsible for prion protein expression, does not alter the gross phenotype[71]. In recent years, PrP^C has been shown to contribute to myelin maintenance[72], as well as to the development and interaction of T-cells, macrophages, dendritic cells, and stem cells[22]. However, conflicting results have often been reported[22].

Proposed models for PrP^{Sc} structure

PrP^C to PrP^{Sc} conversion is associated with structural refolding from a predominantly α-helical conformer into a β-sheet rich conformer[24]. However, progress in elucidating the molecular details of this transition has been relatively slow, largely due to experimental inaccessibility of the aggregated species. Information from low-resolution spectroscopies such as circular dichroism (CD), Fourier-transform infrared (FTIR) spectroscopy, and X-ray diffraction have revealed that amyloid fibrils exhibit a distinctive characteristic cross-β structure and consist of multiple twisted protofilaments[17]. Interestingly, it has become increasingly clear that the cross-β structure seems to be a common feature shared by a range of different proteins, indicating that the amyloid state could be a more common structural phenomenon than initially thought[6,7,73–75]. From biochemical assays based on limited proteolysis, it is known that PrP^{Sc} contains a proteinase K (PK)-resistant core at the C-terminus (termed PrP 27-30, as the molecular weight is between 27-30 kDa),

indicating the existence of a highly stable inter-molecular interaction within a single aggregate[28]. Several detailed structural models for PrP^{Sc} have been proposed based on different approaches[76–83]. Among them, two contradictory models received more attention from the PrP research community.

A PrP fibril model of the parallel in-register intermolecular beta-sheet (PIRIBS) architecture was proposed based on biochemical studies in recombinant PrP[79,84], where PrP monomers stack along the fibril axis and form stretches of parallel β-sheet with their entire C-terminal region, eliminating all native α-helices, has been supported by abundant experimental observations for a decade[82,84–89]. Although the results are encouraging, the *in vitro*-produced recombinant PrP fibrils and PrP^{Sc} appear to have substantially different cross-β architectures based on studies using X-ray fibre diffraction, hydrogen exchange and atomic force microscopy (AFM)[90–92].

In contrast, a recent cryo-electron microscopy (cryo-EM) study from purified infectious GPI-anchorless PrP^{Sc} provides evidence of a separate model, described by a 4-rung β-solenoid architecture within a protofilament while two protofilaments twisting about each other[83]. Despite the relatively low resolution, the average height of each PrP^{Sc} was determined to be ~17.7 Å along the fibril axis, while the four-rung β-solenoid fold was shown to have a height of 19.2 Å along the fibril axis. This extremely compact structure is in good agreement with several biophysical and biochemical data[77,90,93–96] and shares a similar cryo-EM structure with HET-s[97] and pectate lyase C[98] fibrils with high resolutions. As both models are supported by contradictory evidence, a newly proposed explanation is that both structures are correct since the architecture of infectious PrP^{Sc} may be one of the total PrP^{Sc} conformations. This also explains Collinge and Clarke's general model of diverse prion strains and their pathogenicity[99]. However, it cannot be ruled out that this difficulty may result from the different experimental methods used to produce misfolded PrP.

1.2.3 Parkinson's disease and α-Synuclein

Parkinson's disease (PD) is a long-term degenerative disorder in humans. The typical physical symptoms include resting tremor in limbs, bradykinesia (slowness of movement), muscular rigidity, postural instability, and festination, combined with mental disturbances of mood, speech, memory, and cognition[100]. PD is the second most common neurodegenerative disease after Alzheimer's disease[101]. The prevalence of the disease in industrialised countries is generally accepted to be around 0.3% of the general population and about 1% of the population older than 60 years[102–105]. Furthermore, the onset of PD

is highly correlated with the age, where the prevalence is rare before age of 50 years and reaches 4% for the highest age groups of 85-89 years in a study based in Europe[106,107]. It is noted that 90% of PD cases are sporadic and have no identifiable genetic cause[108].

PD was first described in *An Essay on the Shaking Palsy* in 1817 by an English surgeon James Parkinson[109,110]. The hallmark pathology of PD was identified by Frederic Lewy in 1912, which includes progressive loss in dopaminergic neurons in the substantia nigra and other regions in brain and presence of Lewy bodies (LBs) and Lewy neurites (LNs) inclusions in the remaining neurons[111–113]. In 1997, Spillantini *et al.* identified that the aggregated form of the protein, α-Synuclein (αS), is the main component of Lewy bodies in PD brains with an immunohistological approach[114], while in the same year,

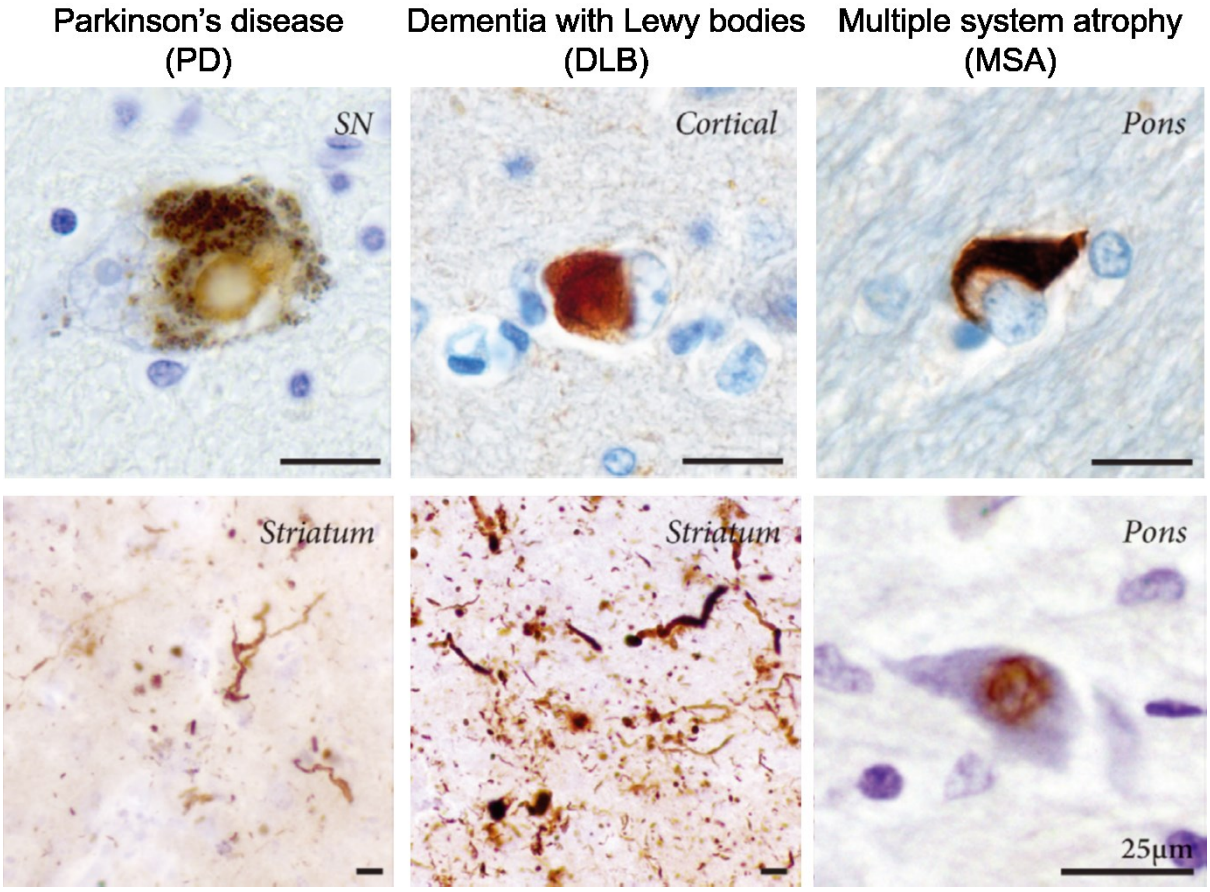

Figure 1.5 | Neuropathological changes of three main synucleinopathies in humans. Parkinson's disease (PD), dementia with Lewy bodies (DLB), and multiple system atrophy (MSA) are shown. Both PD and DLB have neuronal cytoplasmic and neuritic αS inclusions. MSA involves dysfunction of the autonomic nervous system in addition to Parkinsonism and cerebellar symptoms, characterized by glial cytoplasmic inclusions (GCIs) and neuronal nuclear inclusions (NNIs) formed by αS aggregates. SN: substantia nigra. All the scale bars represent 25 μm. Figure modified from ref. [411].

Polymeropoulos *et al.* showed that a mutation on the αS gene caused PD[115]. It is worth noting that αS aggregation is also the predominant neuropathological feature of two other neurodegenerative disorders: dementia with Lewy bodies (DLB) and multiple system atrophy (MSA)[116]. Together with PD, these αS-induced diseases are collectively termed synucleinopathies (Figure 1.5).

1.2.4 α-Synuclein structures

α-Synuclein (αS) is a 14.5 kDa protein expressed in the neuronal cytosol in vertebrates, containing 140 a.a. without post-translational modifications[117]. The name 'synuclein' derives from its localisation in cells when it was first discovered in the nuclear envelope and pre-synaptic axon terminals from the electric fish[118]. The protein belongs to a larger family that includes α-, β-, and γ-Synuclein, and their sequences share a highly-conserved

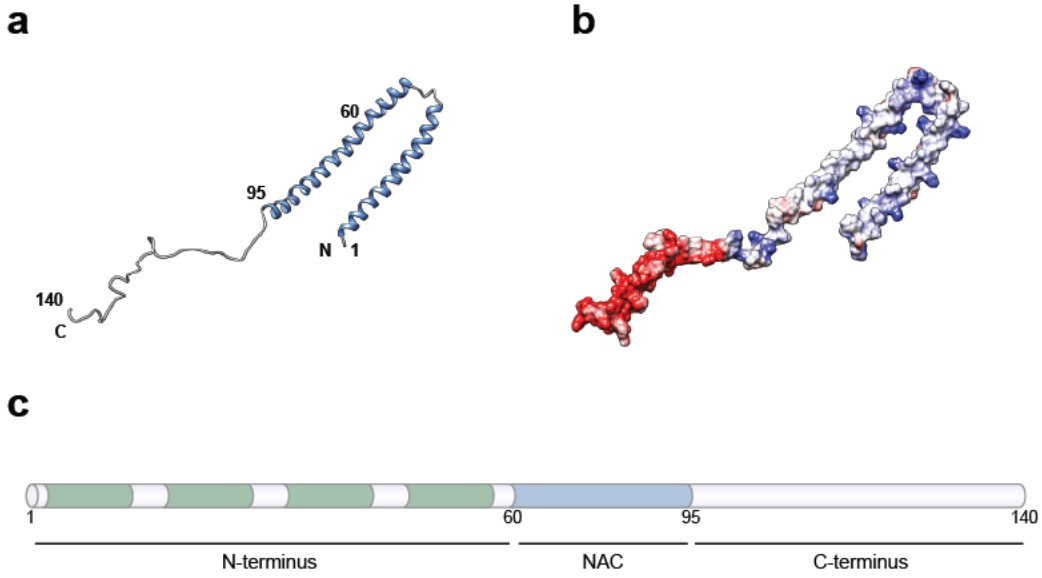

Figure 1.6 | NMR structure of lipid-bound α-Synuclein (1-140). (**a**) Ribbon diagram of the global fold of full-length human αS bound to lipid micelles. The structure reveals the N-terminus and the NAC region forms two α-helices (blue) while the C-terminus remains unstructured. αS in the lipid-free state is unstructured and not displayed. (**b**) The surface view reveals the electrostatic potential, with blue indicating positive charges and red indicating negative charges. (**c**) Structural features of αS polypeptide sequence show three major segments: N-terminus, non-amyloid component (NAC), and C-terminus. (PDB: 1XQ8)

N-terminus[119]. The primary sequence of human αS consists of three regions: a positively-charged N-terminus (1-60 a.a.), a central region of non-amyloid component (NAC, 61-95 a.a.), and a negatively-charged C-terminus (96-140 a.a.; Figure 1.6c) [120]. The protein is highly unstructured in lipid-free environment.

N-terminus of αS

The positively-charged N-terminus of αS contains seven 11-residue repeats that resembles the α-helical lipid-binding domain[121]. It has been demonstrated that αS binds with high affinity to lipid membranes with negative charge and high curvature, and that part of the N-terminus undergoes conformational changes to an α-helical structure[122–128] (Figure 1.6a and b). Interestingly, and all known pathogenic mutations (A30P[129], E46K[130], A53E[131,132], A53T[115], H50Q[133,134], and G51D[135,136]) are found in this region, suggesting an important role of the N-terminus in the structural flexibility and function of αS[137]. It is noted that the KTKEGV sequence is characteristic for the amphipathic lipid-binding α-helical domains of apolipoproteins, suggesting that the N-terminus of αS may be capable of reversibly binding to the surface of lipid membranes[123,138]. Truncation of the N-terminal segment was shown to promote αS fibrillisation; in contrast, the addition of an extra 11-residue repeat suppresses it[139]. It is still controversial whether lipid binding to the N-terminus impedes or enhances αS aggregation from various experimental approaches[138–140], a mechanism has been proposed for lipid-induced αS aggregation. In the model, extended- or broken-helix membrane-bound states of αS can partially release the lipid-binding region, thus converting to a partially helical intermediate on the lipid membrane for subsequent self-assembly[138,141]. Hence, the interaction between the N-terminus and lipid membrane is likely to be a key component in the initial misfolding of αS.

NAC region of αS

The hydrophobic non-amyloid component, NAC, is shown to be important in αS aggregation and the origin of toxicity[142]. The cryo-EM structure of the αS fibril made from recombinant proteins reveals that NAC, together with part of the N-terminus, contributes to the core of protofilaments[143], which is consistent with other structural studies[144–148]. Either partial deletions[149,150] or amino acid substitutions[140] in the NAC segment strongly inhibits αS fibrillisation, suggesting that this region is also critical during fibril formation.

C-terminus of αS

Although the negatively-charged C-terminus is not part of the cross-beta structure in the αS fibril[143], it has been shown to be responsible for protein stability both in its native conformation[151] and the fibrillar state[152]. The stabilisation is likely to result from shielding of the hydrophobic NAC region from solvents, suggesting that the interactions between the C-terminus and N-terminus or NAC region of αS are important in maintaining its natively-unfolded structure and thus prevent conformational change[153]. This is consistent with the fact that deletion of this region enhances fibril formation[154,155].

αS tissue expression and functions

αS is highly expressed in the brain, where it is specifically concentrated in pre-synaptic nerve terminals in close proximity to synaptic vesicles[156]. It has also been reported to localise at the nuclear envelope[118] and mitochondria[157]. However, the physiological function of αS is still unclear. Multiple functions have been proposed, including 1) storage, transmission, and biosynthesis of dopamine[158], 2) trafficking[159,160] and stabilisation[161] of synaptic vesicles, acting as a cellular ferrireductase[162], 4) participating in mitochondria function[157], and 5) neuronal protection from low levels of oxidative stress[163]. Mice lacking αS have been reported to show a deficit in dopamine secretion[164] and altered pattern of neurotransmission[164,165]. Furthermore, triple-knockout mice lacking synucleins are developed age-dependent neurological impairments and die prematurely[160]. As αS physically interacts with at least 30 proteins[166], the real function of αS is difficult to determine, while the studies above all suggest a critical role for αS in cell signalling in neurons.

αS fibril structure

Previous studies have determined some structural details of αS fibrils using micro-electron diffraction[167] and solid-state NMR (ssNMR)[168], and these were further validated by X-ray diffraction[169,170] and ssNMR at the secondary structure level[171,172], forming a parallel in-register cross-β structure. The data are consistent with a recent observation from cryo-EM with high resolution, which reveals two fibril polymorphs of recombinant αS with distinct protofilament interfaces[173]. Produced under different buffer conditions, the rod and twister polymorphs are composed of two protofilaments with a highly conserved kernel structure assembled around different steric zipper interfaces (a.a. 46-57 of the N-terminus and a.a. 68-78 of the NAC region for the rod and the twister

polymorph, respectively). The subunits of the twister polymorph have an ordered bent β-arch motif, while those of the rod polymorph have a bent β-arch with an additional Greek-key-like fold. It is worth noted that another recently released cryo-EM structure of a truncated αS (a.a. 1–121) fibril[143] shows a similar structure with the rod polymorph of the full-length protein.

Considering the fibril structures acquired from PrP^{Sc}, αS, and other aggregation-prone proteins, they can be classified as two main classes: β-solenoid structure and parallel in-register β-sheet structure, where both structures are governed by the same types of interactions and share many molecular details[96]. A detailed understanding of the molecular arrangement for fibrillar structures would bring more insights in terms of the difference of protein strains and their aggregation mechanisms.

1.3 The molecular basis of protein aggregation II: the prion paradigm

The prion paradigm has emerged as a unifying theory to explain the development of many neurodegenerative diseases[50]. The theory postulates the fundamental origin of these disorders is protein self-assembly and the subsequent spreading through a nucleation-dependent pathway. In this section, the propagation mechanism and the origin of toxicity of PrP and other associated aggregation-prone proteins are discussed.

1.3.1 Prion propagation at the molecular level

Prions are the pathogenic agent causing prion diseases and traditionally considered unique among the agents of neurodegenerative diseases due to their infectious behaviour. According to the widely-accepted protein-only hypothesis, the prion agent comprises principally aberrant PrP molecules; these aggregates in their misfolded state induce the structural conversion of the native PrP molecules to the same misfolded state, hence replicating and eventually forming amyloid deposits *in vivo*[21,24,25,41]. From macroscopic measurements, the overall aggregation reaction shows a characteristic sigmoidal shape including an initial nucleation phase, followed by a rapid growth phase, and finally an equilibrium phase due to the depletion of monomers[174] (Figure 1.7b).

Protein aggregation at the molecular level is described by a nucleation-dependent polymerisation reaction[175,176] (Figure 1.7a). In the initial nucleation phase, a series of meta-stable oligomeric intermediates are formed as a result of the stabilisation of misfolded proteins[175,177]. The nucleation process, or primary nucleation, is kinetically slow. It is the origin of the observed lag phase from macroscopic measurements (Figure 1.7b). At least in some cases, these oligomers undergo structural conversion from relatively disorganised species to more compact structures with a rudimentary cross-β structure[176,178–182]. These meta-stable nuclei thus function as a template and are capable of growing into highly-organised mature amyloid fibrils through further monomer recruitment[6,176]. The growing fibril can eventually break, either spontaneously or actively through cellular processes, and this may depend on the increasing length and conformational stability of the amyloid structure[174,175,183]. Pre-formed aggregates can act as a seed and thus shorten the lag phase for the overall reaction in proportion to the dose of seeds applied[6,184] (Figure 1.7b).

In contrast to conventional nucleation-dependent polymerisation that was found in actin and other functional fibrils, amyloid formation is distinct due to the occurrence of secondary pathways[185]. Multiple secondary events, such as secondary nucleation and fibril fragmentation, have been found to account for aggregation kinetics observed experimentally[186], which is insufficiently described by a simple nucleation process (Figure 1.7c). Secondary nucleation allows the formation of new aggregates from existing template seeds with concomitant amplification of the total number of protein assemblies. On the other hand, fibril fragmentation increases the number of protein assemblies by generating multiple fragments and thus providing new ends for monomer addition. In

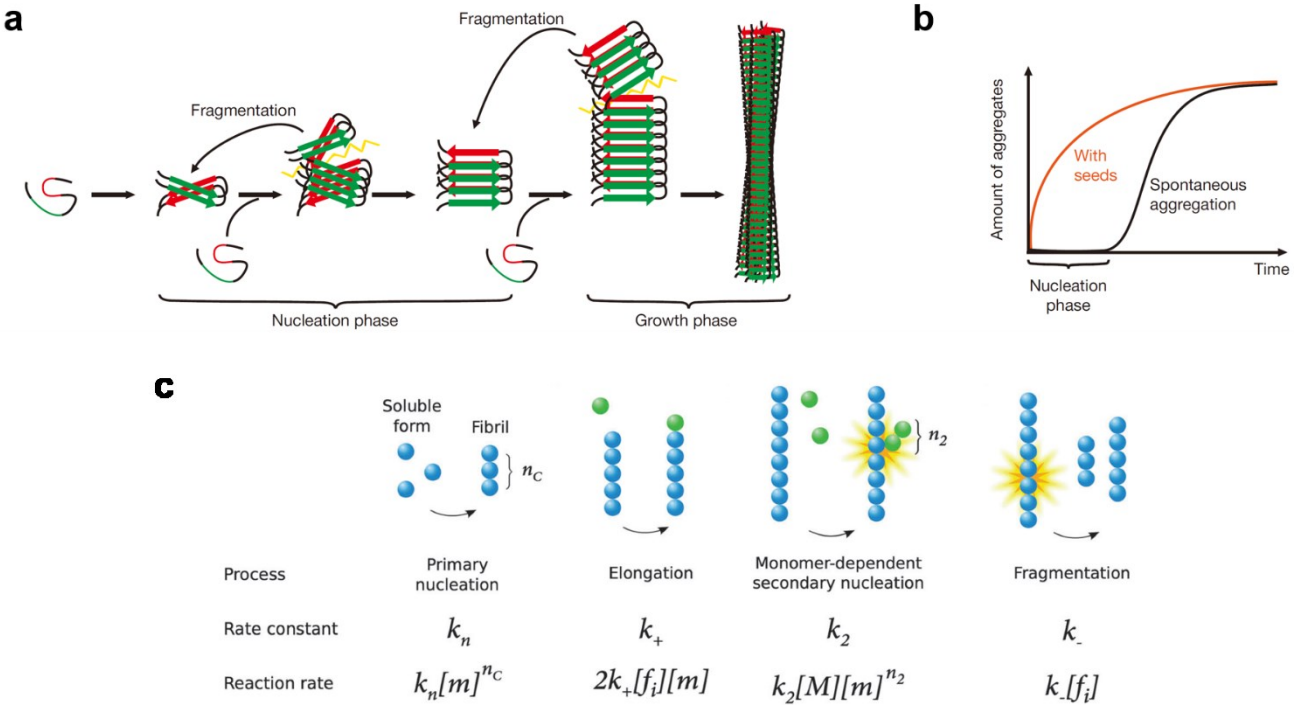

Figure 1.7 | The molecular mechanism of amyloid fibril formation. (**a**) Amyloid fibril formation begins with slow primary nucleation that involves a range of structurally diverse intermediates, followed by rapid growth of fibrils. The fibrils can break into smaller fragments and act as new templates for further growth. (**b**) The kinetic profiles of protein aggregation show a characteristic sigmoidal curve from macroscopic measurements. The lag time observed can be shortened by the addition of pre-formed seeds. (**c**) Multiple molecular events are involved in the self-replication process. Through the use of kinetic models such as the nucleation-elongation-fragmentation model (described in Section 1.3.1), the kinetics can be rationalised based on observed reactions, and hence their kinetic rates are acquired. Figure modified from ref. 174 and 412.

particular, fibril fragmentation has been shown to be a major secondary pathway for the amplification of amyloid fibrils both *in vitro* and *in vivo*[184,186–192].

Conventionally, aggregation kinetics is studied with empirical approaches by fitting kinetic profiles to generic sigmoidal equations. Instead, through the use of more complex kinetic models, a rationalised approach can provide mechanistic insights into the process of fibril formation and changes in the elementary rate constants. An example is provided by the nucleation-elongation-fragmentation model. This kinetic model treats the amyloid self-assembly process as a nucleation-dependent polymerisation with fragmentation as a secondary process[186,190,193]. Based upon substantial empirical evidence, this model allows for the calculation of elementary kinetic parameters including nucleus size (n_c), primary nucleation rate constant (k_n), fragmentation rate constant (k_-), and elongation rate constant (k_+) (Figure 1.7c). The theoretical framework has proved particularly useful for understanding the molecular mechanisms, provided by studies in wild-type (WT) αS[180,191], Aβ42[194], tau and its mutants[192,195], and yeast prion Ure2[178].

1.3.2 Prion neurotoxicity and infectivity: uncoupled features in protein propagation *in vivo*

Pre-fibrillar, oligomeric species of protein aggregates, rather than mature amyloid fibrils, have long been suggested to be the primary toxic agents in neurodegenerative diseases and generically damaging to cells[6,7,30,181,196–200]. This is supported by accumulating evidence from a range of *in vitro* and *in vivo* studies on prion diseases[200–204], Alzheimer's disease[30,194,205–208], Parkinson's disease[180,209], and non-pathological protein aggregates[196,198]. In contrast, several studies have shown that the fibrillar species of aggregates are toxic to neurons[200,202,210], but now it is thought more likely to act as a protective mechanism in cells in order to remove oligomeric aggregates[211–214].

It is still unclear how these protein aggregates cause neurotoxicity, and numerous toxicity mechanism has been proposed. Protein aggregates have been suggested to induce cell death through apoptosis[200,215,216], hyper-activity of the excitatory amino acid transmitters (e.g. glutamate)[217–220], ER stress[221–223], and autophagy[224–229]. Furthermore, neurotoxicity induced by protein aggregates may also come from the physical interaction between the aggregates and cell membranes. Hydrophobic chemical groups of misfolded protein aggregates are normally accessible to solvents within the cellular environment[181,230,231]. These exposed hydrophobic side chains have been shown to cause non-specific membrane disruption from biophysical studies and computer simulations in several aggregated proteins[6,181,231–236]. Interestingly, a report has observed that oligomeric

aggregates are able to form ion channels on lipid bilayers[237]. This aberrant interaction with the lipid membrane has been demonstrated to induce partial permeabilisation of the membrane, eventually resulting in disruption of cellular homeostasis[6,180,181,205,234,235,238]. In this context, the toxicity originating from oligomers may be attributed to their higher surface-to-volume ratio that leads to a greater extent of exposed hydrophobic side chains[182,231].

Prion infectivity is a unique feature among neurodegenerative diseases. It is defined that *bona fide* prions are transmissible from an affected individual to another recipient and induce pathogenesis[174]. The small-sized PrP aggregates have been found to account for a substantial proportion of the total infectivity in brain homogenate[239–241]. According to the light scattering data[242], the infectious species of PrP, purified and PK-treated from scrapie-infected (263K strain) hamster brain, appears to be around 300-600 kDa in size. In recent years, the proteins associated with other neurodegenerative diseases have been recognised to spread by cell-to-cell transmission of protein aggregates, although the infectivity of these aggregates is unclear[52]. From animal studies and the development of cell-based prion bioassays, the increase in infectivity during prion pathogenesis is likely to be uncoupled from the production of toxic species[99,243]. Prion propagation in the mouse brain has been suggested to proceed in two distinct mechanistic phases[99,244,245]. Phase 1 is a clinically silent exponential phase in which prion titre rapidly grows to its maximum. After plateauing of the prion titre, it is followed by Phase 2 that is characterised by a linear increase in the toxic species, which continues until the onset of clinical signs. In the same study, it is observed that the PK-resistant PrP^{Sc} may account for a small and variable minority of the total disease-related PrP species[244,246], indicating that a large amount of misfolded PrP *in vivo* may be sensitive to PK digestion. This is also supported by another hamster experiment[247]. The relative contribution of PrP^{Sc} to both infectivity and toxicity is still unclear[244]. At present, some of the disease-related species of PrP aggregates are thought to be PK-sensitive, which significantly contribute to the infectivity in some prion strains[244,246] and in sCJD patients[248].

1.3.3 Prion-like spread in other neurodegenerative diseases

The classical definition of the prion underlines self-replication of the misfolded protein as well as infectivity that enables the transmission of prion agents from one individual to another. With recent advances in the study of aggregation mechanisms, it is increasingly recognised that prion replication involves nucleation-dependent elongation with fragmentation, and this paradigm can be expanded to other aggregation-prone proteins that share the common 'prion-like' feature of structural refolding and self-

assembly[7,8,50,52,116,249–251]. Following this molecular perspective, many aggregation-prone proteins have been demonstrated to be able to induce pathogenic patterns *in vivo* with exogenous seed application through prion-like propagation in the host. These include yeast prions Sup 35[252] and Ure2[178], Aβ[253] and tau protein[254,255] in Alzheimer's disease, αS[256–261] in Parkinson's disease, and interestingly, p53[262–264] involved in malignant cancers. Despite the lack of evidence for individual-to-individual transmission, many aspects of the above diseases can be explained by prion-like spreading, and the prion paradigm could be a more general phenomenon among aggregation-prone proteins[41].

1.4 Single-molecule techniques

In structural studies of biomolecules such as proteins, the majority of experiments are carried out using various biochemical or biophysical approaches, and in many cases, these are effective at elucidating biological phenomena. A typical measurement in a bulk solution involves the simultaneous detection of billions of molecules and the observation of changes from an equilibrium state to another newly-equilibrated state. However, the results from the bulk measurements are the ensemble averages of the behaviour of individual molecules, and hence the transition undergone by any individual species within this ensemble is usually undetectable.

In the field of protein aggregation, current research aims to understand very complicated biological systems that involve kinetically-metastable, transiently formed, and heterogeneous species of aggregates. Single-molecule techniques offer us a new approach to resolve the individual behaviour of these species and are therefore highly advantageous over ensemble techniques[265]. Individual molecules can be identified and characterised through basic physical properties such as fluorescence intensity and the shape of objects. The distribution of subpopulations can be therefore classified and analysed statistically, allowing us to acquire new insights into the intricate process of protein aggregation.

1.4.1 Fluorescence and total internal reflection fluorescence microscopy (TIRFM)

Fluorescence is the emission of light from an electronically excited molecule with a wavelength equal to or longer than that of the absorbed light[266]. It was first described by Sir George G Stokes in 1852[267]. An electron of the molecule can be excited by absorption of a photon. When this electron reaches a certain excited electronic state, it relaxes to the lowest vibrational energy level in the same excited state *via* radiationless decay. Fluorescence occurs as the electron transfers back to its electronic ground state through photon emission. The emitted photon hence exhibits lower energy than the original excited photon, leading to a red shift of the emission spectrum from the absorption spectrum of this molecule, a phenomenon called 'Stokes shift'. Fluorescence measurements can be considerably more sensitive than absorbance measurements due to higher signal-to-noise ratios (SNR), such that lower sample concentrations are needed[266]. Furthermore, fluorescence is often extremely sensitive to the environment and can hence be employed to probe complex local environments[266]. Therefore, fluorescence measurements have been extensively adopted to study biological processes.

In single-molecule fluorescence imaging, signals from individual fluorophores cannot be increased with larger sample volume due to the presence of various sources of background noise, for instance from fluorescent impurities or Raman scattering[268]. Therefore, a key determinant for the resolution of images is acquiring a high SNR in a small volume. To achieve this goal, the most common method is to restrict the illumination volume from which the light is collected[265]. Total internal reflection fluorescence (TIRF) microscopy is one of the principal techniques applied to single-molecule experiments as the illumination volume is restricted to ~100 nm in thickness[269].

Total internal reflection (TIR) requires plane polarised light travelling through a higher-refraction index (RA) medium to a lower-RA medium (Figure 1.8). RA is a dimensionless number n that describes the amount of light refracted through that medium:

$$n = \frac{c}{v} \qquad \text{(Eq. 1.1)}$$

where c is the speed of light in a vacuum and v is that in a medium. The different RA between two substances regulates the refraction and reflection of an incident light at the interface as a function of incident angle. By increasing the laser incident angle over the specific critical angle (θ_c), the light beam obeys Snell's Law and is totally reflected from the media interface instead of refracting:

$$\theta_c = \sin^{-1}\left(\frac{n_2}{n_1}\right) \qquad \text{(Eq. 2.2)}$$

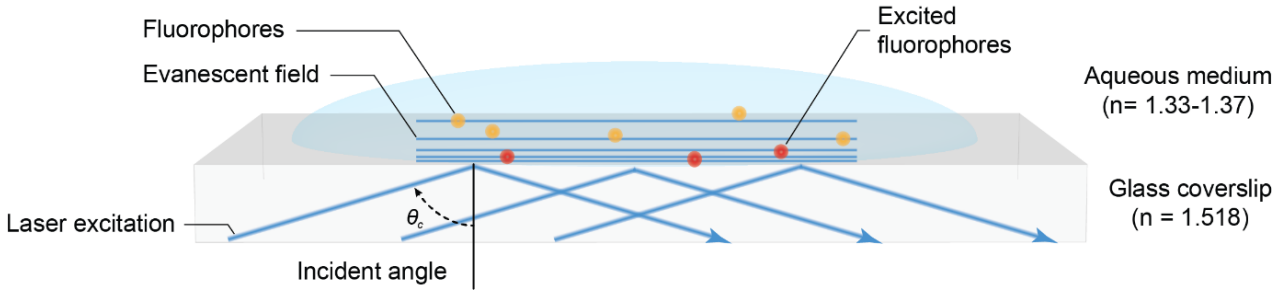

Figure 1.8 | TIRF illumination. As a laser source passes through the glass ($n = 1.518$) and is reflected from the glass-water interface ($n = 1.33$-1.37 for aqueous solutions) at a critical angle, θ_c, an evanescent wave is established that penetrates ~100 nm into the sample. This creates a confined illumination region in which fluorophores in an aqueous medium close to the surface of a glass slide are selectively excited (red) and subsequently emit fluorescence, whilst those farther away from the interface remain non-excited (yellow).

where n_1 is the RA of the first medium and n_2 is that of the second medium.

The TIR generates a very thin electromagnetic field termed the evanescent wave. This wave, which has an identical frequency to that of the incident light, undergoes exponential intensity decay with increasing distance, d, from the interface into the second medium:

$$I(z) = I_0 \exp\left(-\frac{z}{d}\right) \quad \text{(Eq. 2.3)}$$

where I_0 is the intensity of the evanescent wave at the interface. The penetration depth of the wave is given by:

$$d = \frac{\lambda_0}{4\pi}\left(n_1^2 \sin^2\theta - n_2^2\right)^{\frac{1}{2}} \quad \text{(Eq. 2.4)}$$

for $\theta > \theta_c$ and light of wavelength λ_0 in a vacuum[269]. Typical n values for microscope coverslips (for borosilicate glass, $n_{glass} = 1.518$) and for buffered samples (for water, $n_{water} = 1.33$) result in TIR angles higher than 61.2°. The phenomenon leads to a short penetration depth of only several hundred nanometres (in this case ~100 nm), which means a restricted volume of illumination is created in very close proximity to the glass-water interface. Since only those fluorophores within this region are able to be excited by the evanescent wave, the background noise can be decreased effectively, and thus single molecules are resolved. In a typical TIRF set-up (Figure 1.9a), a laser source excites a buffered sample in TIRF mode. The fluorescence emitted by the fluorophores in this sample is collected through a microscope objective and is separated from the incident light with a dichroic mirror, eventually collected by a sensitive electron multiplying charge coupled device (EMCCD) camera.

1.4.2 Thioflavin T dye and single-aggregate imaging

Thioflavin T (ThT, figure 1.9b) is a benzothiazole dye which has been extensively used in biochemical assays to determine the presence of amyloid fibrils both *in vitro* and in *vivo*. Although its fluorescence quantum yield is very low in water (φ<0.0001 at room temperature)[270], upon binding to cross-β structure of fibrils the quantum yield is substantially increased by several orders of magnitude with a dramatic Stokes shift[271], leading to fluorescence emission at peak around 480 nm[272,273]. As a representative amyloid dye, ThT is generally considered to be specific towards amyloid structures, and

the characteristic fluorescence emission does not generally occur upon binding to precursor proteins or amorphous protein aggregates[273], though in some cases it has been reported to bind to non-β sheet cavities on protein surfaces[274]. However, the mode and stoichiometry of ThT binding remain unclear and controversial. Formation of ThT micelles of ~3 nm in diameter was observed along the length of amyloid fibrils[275], while another excimer model suggested that the fluorescence is induced due to ThT binding in both monomeric and dimeric forms, ducking in channels along the long axis of fibrils[273,274].

'Single-aggregate' fluorescence imaging (Figure 1.10) is a newly-developed method aimed to directly detect the fluorescence emission of individual protein aggregates by taking advantage of sensitive TIRFM instrumentation and the specificity of ThT for amyloid structures[276]. In the present research, TIRFM coupled with single-aggregate imaging is applied to visualise the evolution of single ThT-active aggregates on the aggregation pathway at a sub-micromolar level of protein concentration. The morphology

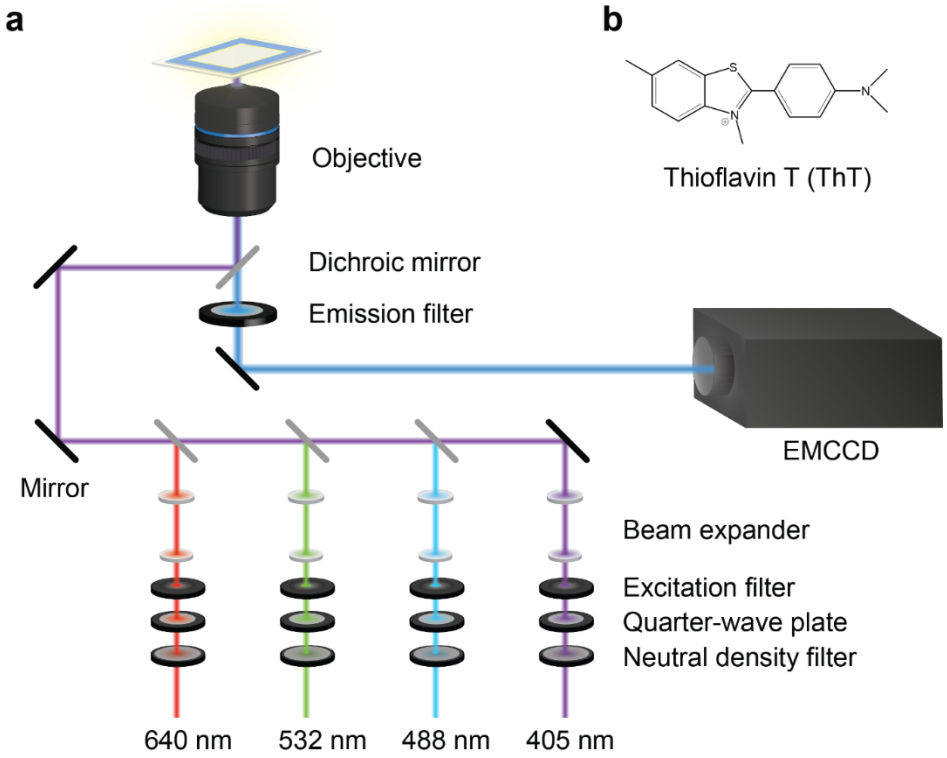

Figure 1.9 | Schematic representation of the TIRFM setup used in this thesis. (**a**) The sample in the presence of Thioflavin T (ThT) is excited by a one-colour laser source. Fluorescence is collected by a high numerical aperture objective lens and recorded by an EMCCD camera. (**b**) ThT structure. ThT is non-fluorescent in polar solvents, while selectively bound to cross-beta structure, the quantum yield is substantially enhanced.

of individual protein aggregates and their physical properties (e.g. fluorescence intensity, length) can be visualised using the imaging system and then extracted after image analysis. This advantage allows the characterisation and temporal tracking of sub-populations during aggregation kinetics that is likely to be averaged in conventional ThT assays. In addition, the non-covalent binding of ThT eliminates common concerns of covalent dye-labelling, such as interference with protein structure and kinetic behaviour. This method can be modified for multiple purposes such as dual-channel imaging, or sPaint and AD Paint for super-resolution imaging with protein aggregates, as will be discussed in the next sections.

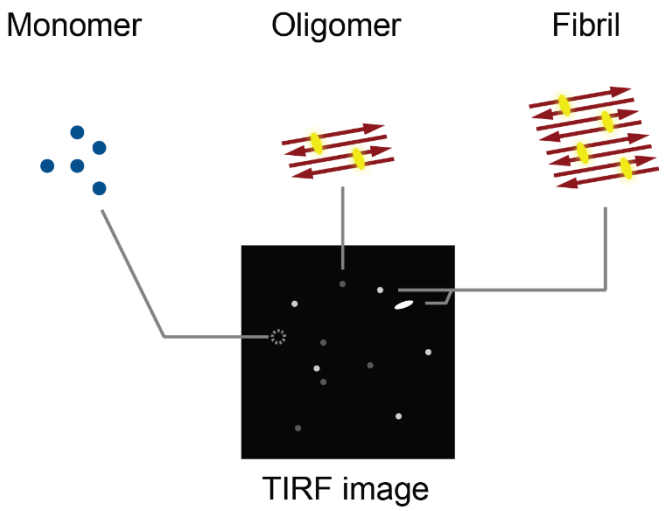

Figure 1.10 | Single-aggregate imaging using TIRFM. Thioflavin T (ThT) dye is used to visualise misfolded protein aggregates containing cross-beta sheet structure (red arrows) on a coverslip surface with TIRF illumination. ThT is normally non-fluorescent (white circles) in solution and non-reactive with protein monomers (blue dots). Upon binding to the cross-beta sheet folds, ThT becomes highly fluorescent (yellow circles), and the intensity emitted from individual aggregates in the resulting TIRF image is linearly dependent on the size of the aggregated assemblies. As the photobleached ThT molecules bound on the protein surface can exchange quickly with the large pool of unbound ThT molecules in solution, the ThT fluorescence remains constant intensity over time.

1.4.3 Super-resolution imaging: spectral Paint (sPaint)

In conventional light microscopy, there is a fundamental maximum to the resolution which is due to the diffraction of visible light. The theoretical resolution of a given optical system is dependent on the Abbe diffraction limit. Considering light travelling in a medium, it converges to a spot with certain diameter *d*, which can be described by:

$$d = \frac{\lambda}{2n\sin\theta} = \frac{\lambda}{2NA} \qquad \text{(Eq. 2.4)}$$

where λ is the wavelength of light, n is the refraction index of the medium, and θ is the maximal half-angle of the cone of light that can enter or exit the lens. NA (numerical aperture) $= n \sin\theta$, which is normally 1.4-1.6 in modern optical instruments. If we consider a single fluorophore is activated and emits purple light with a wavelength of 550 nm, travelling to an oil-immersed objective with NA=1.49, the Abbe limit is about 180 nm. Despite the advantages of fluorescence microscopy, the scale of the diffraction limit inevitably leads to obscure fluorescence images that can only be resolved as a point spread function (see below for description)[277], thus restricting observation of small biological agents such as proteins (1-10 nm).

Super-resolution microscopy is an advanced optical technique aimed to resolve structures beyond the diffraction-limited resolution of conventional light microscopy while retaining the advantages of conventional imaging. One of the stochastic functional approaches, single-molecule localisation microscopy (SMLM), achieves super-resolution by serially detecting individual fluorophores, isolating them, and fitting their images with the point spread function (PSF). PSF is the fixed size of the spread of a single point of light that is diffracted through a microscope, which is also a measure of the minimum-size point source or object that can be resolved by a microscope[277]. By fitting the spread of intensity of individual fluorophores from the image, the locations of their centres can be determined with high precision, and it is only limited by its own intensity, thus acquiring a high-resolution map of the fluorophores. Recent developments in SMLM techniques have enabled nanoscopic cellular components to be imaged with a precision of tens of nanometres[278–280], as well as simultaneous spectral and spatial imaging[281–283].

Spectrally-resolved Paint (points accumulation for imaging in nanoscale topography), or sPaint, is a recent application in SMLM that simultaneously records the spatial position and emission spectrum of single dye molecules to super-resolve an image[284] (Figure 1.11a). Developed in our group, this technique provides a stochastic imaging method that uses diffusing fluorophores at a very low nanomolar level to transiently interact with the

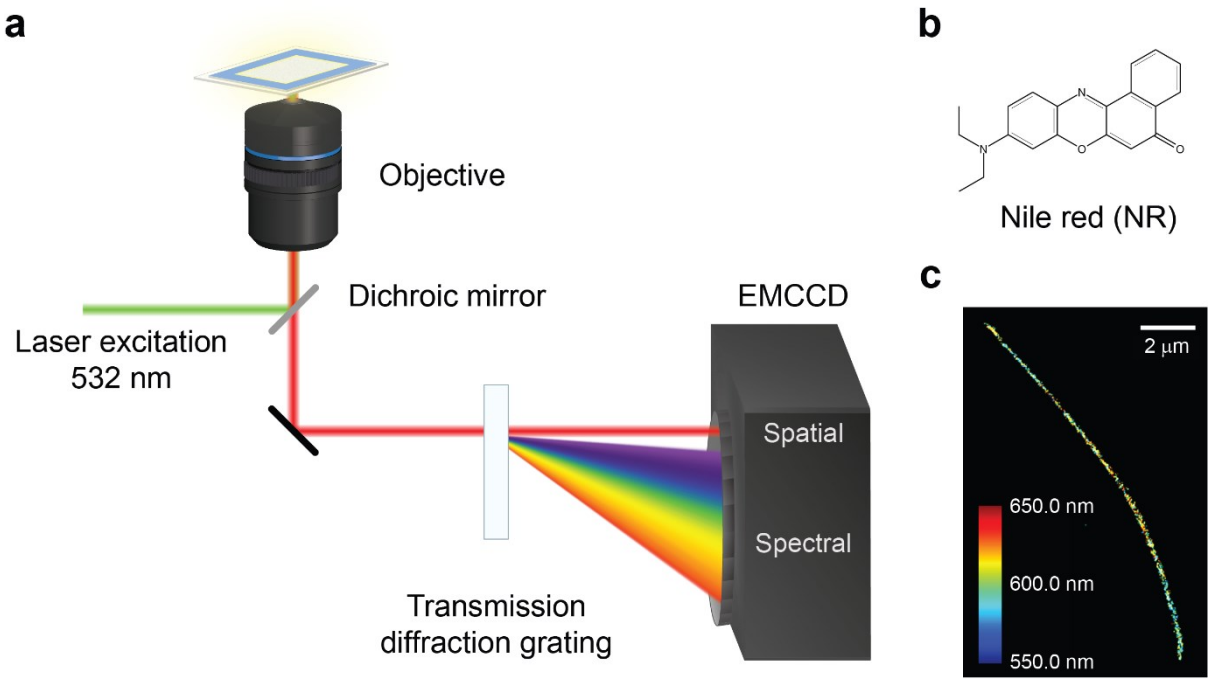

Figure 1.11 | Schematic representation of sPaint setup. After sample excitation, fluorescence is collected by a high numerical aperture objective lens and passed through a blazed transmission diffraction grating. The fluorescence emission is divided into the spatial region (0th diffraction order) and the spectral region (1st diffraction order) in the image plane and recorded by an EMCCD camera. 405 nm and 532 nm lasers are used to sequentially excite the dyes ThT and Nile red (NR), respectively. (**b**) NR structure. NR is a typical lipophilic stain that is non-fluorescent in polar solvents, while in nonpolar environments, the quantum yield is substantially enhanced. (**c**) Representative sPaint image detected with the NR channel shows the hydrophobicity landscape (i.e. density plot) of a single PrP fibril. To quantify the hydrophobicity of individual aggregates, the fluorescence wavelength of each localisation event (coloured dots with indicated wavelengths shown in the inlet) is recorded. The median wavelength ($\overline{x}$) of all localisation signals from a single aggregate is used to represent the hydrophobic level of the given aggregated assembly.

sample, so that the pattern of the sample can be clearly 'painted' in a sufficient time scale. The uniqueness of sPaint imaging is the ability to measure environment-specific properties of the fluorophore bound to protein aggregates. A spectrally-responsive dye fluorophore, Nile red (NR, figure 1.11b), has been shown to be an effective probe in hydrophobic surface of protein molecules in biochemical studies[285–287]. Through the use of NR, sPaint can generate information-enriched super-resolved images by measuring the variation of the emission wavelength of single NR molecules depending on the local environment. Hence, NR becomes a sensitive probe for structural conversion of proteins through the change in surface hydrophobicity while providing super-resolution images with a resolution of ~40 nm. A typical sPaint image is shown in Figure 1.11c, revealing the heterogeneity of surface hydrophobicity from a PrP filament. More importantly, combined with dual channel-imaging with ThT, sPaint can detect ThT-inactive protein aggregates that can only be imaged in the NR channel.

1.4.4 Super-resolution imaging: AD Paint

Prion and prion-like propagation in cells take place either in the cytosol or on the plasma membrane, and they normally involve the formation of small oligomers as well as large amyloid deposits with a distinct pattern for the spatio-temporal distribution. The need to characterise the cellular spatio-temporal distribution of proteins with high resolution has driven several advances in recent years[288–291]. One of the developments achieves super-resolution with the same stochastic principle as sPaint through the use of two complementary sequences of oligonucleotides labelled with fluorophores[290,291]. However, it is difficult to find a suitable ligand candidate to specifically recognise misfolded protein aggregates.

AD Paint (Antibody-DNA Paint, previously called Aptamer-DNA Paint) has been developed in our group for the purpose of visualising individual protein aggregates in fixed cells (Figure 1.12a). This method combines super-resolution microscopy with immunostaining of misfolded proteins using a fibrillar structure-specific antibody. To achieve stochastic imaging as in sPaint, the antibody is conjugated to a short single-stranded DNA sequence (docking strand), which is designed to be complementary with another single-stranded DNA sequence (imaging strand) labelled with a fluorophore Cy3b (Figure 1.12b). The transient binding between the docking strand and the imaging strand can thus provide super-resolution images for specific misfolded protein targets in cells with a resolution of ~30 nm. The representative image in Figure 1.12c shows the localisation of individual signals for endogenous αS aggregates in cells, and the aggregated clusters are found unevenly distributed in the cytosol. This technique not only

enables quantitative analysis for the accumulation of protein aggregates in cells, but also allows the detection of aggregates in cell media and other biofluids on a coverslip.

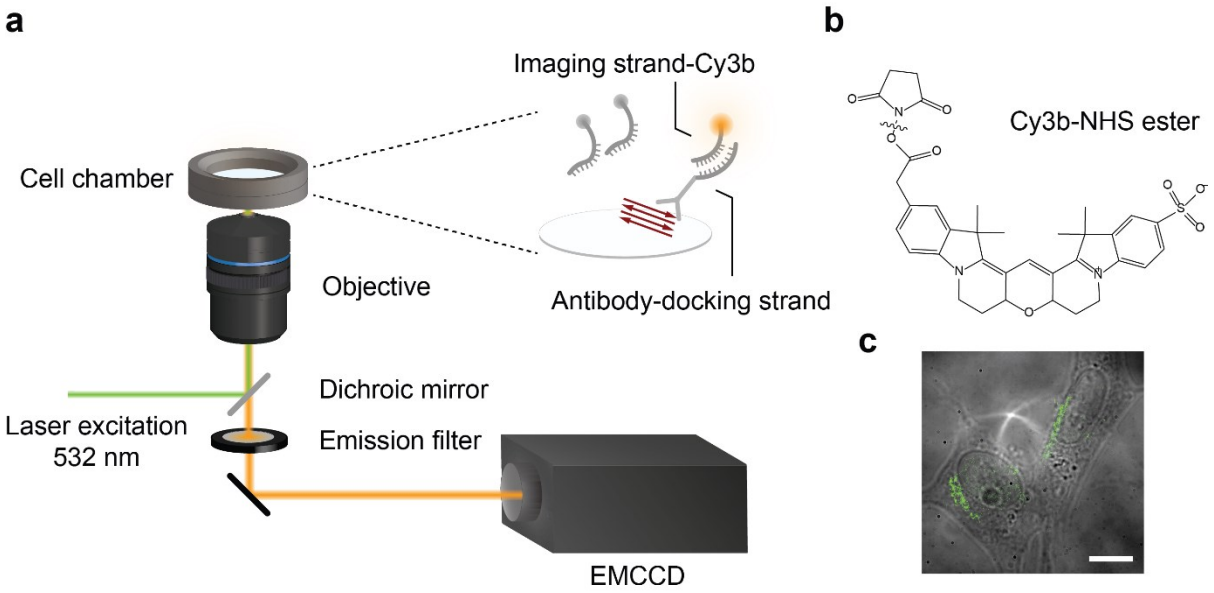

Figure 1.12 | Schematic representation of AD Paint setup. (**a**) The fixed cells that are recognised by an antibody conjugated to the docking strand are imaged in the presence of the imaging strand-Cy3b. Fluorescence is collected by a high numerical aperture objective lens and recorded by an EMCCD camera. (**b**) Cy3b-NHS structure. The NHS ester group acts as a leaving group and is released after the dye molecule is conjugated to an amine group of the imaging strand. (**c**) Representative AD Paint image combining the use of a fibrillar αS-specific antibody, MJFR-14-6-4-2. The localisations of individual endogenous αS aggregates (green) in SH-SY5Y cells are shown after 2 days post-transduction.

1.5 Aims of the thesis

Protein misfolding and associated diseases have been important research subjects over the past years. A central issue to be addressed in the field is how native proteins transform into misfolded amyloid aggregates, and how these molecules interact with other amyloidogenic proteins and the quality-control system in cells. To understand the explicit mechanism of the protein self-assembly process, the different misfolded states involved in amyloid fibril formation have to be identified. Although extensive information about fibril formation has been acquired from previous studies, the oligomeric intermediates remain largely unknown owing to their metastable, transient, and heterogeneous nature.

Prion diseases are an important model for protein misfolding neurodegenerative conditions in general since several of these diseases, including Alzheimer's disease (AD) and Parkinson's disease (PD), show features of prion-like transmission in experimental settings. From a structural perspective, PrP is distinct among the agents of neurodegenerative diseases by its larger molecular weight and natively-folded monomeric state, which could contribute to its complicated aggregation pathway. However, the aggregation kinetics of PrP are majorly studied using macroscopic approaches, and little is known about the molecular details, despite the prion-like phenomenon being increasingly invoked to explain the aggregation of other proteins. In the present research, there are four main objectives:

1. To explore seeded PrP aggregation under native conditions *in vitro* and dissect the molecular mechanism. PrP aggregation *in vitro* is known to be inefficient and hence conventionally requires physical approaches or chemical denaturants to facilitate the aggregation reaction. However, for measuring the kinetic parameters for this process, it is ideal to carry this out under native conditions. Using single-aggregate imaging, I am able to study PrP fibril formation starting from a single seed and the molecular details of the mechanisms involved. Furthermore, the aggregation mechanism can be quantitatively described using the nucleation-elongation-fragmentation kinetic model. With the kinetic parameters acquired, it enables the establishment of a simple spreading model and thus estimating the time scale about how misfolded PrP might replicate and spread in the brain during disease development. This approach will ultimately help us understand if the observed aggregation mechanism is likely due to fibril fragmentation and to what extent other external factors are likely to contribute to the spreading of PrP *in vivo*.

2. To study the early events of PrP aggregation and identify the formation of oligomeric species as a function of time. As the oligomeric aggregates have been suggested to play

a key role in neurodegenerative diseases, it is fundamentally important to acquire detailed information on the formation, structure, and toxicity of these oligomers. To characterise the low amount of oligomeric species with high heterogeneity in solution, a set of biophysical methods are exploited, including single-aggregate imaging, sPaint imaging, and a single-vesicle permeability assay for probing the disruption of the lipid membrane induced by aggregates. Despite the observation that early-formed PrP oligomers require semi-denaturing conditions, a kinetic scheme can be developed to explicitly describe the behaviours of the various oligomeric species during the lag phase in aggregation.

3. To measure the kinetic parameters for αS aggregation. To examine if misfolded αS aggregates through a prion-like mechanism and to what extent it is similar or different from PrP aggregation, the same quantitative approach is applied to study the WT αS and its A53T mutant. With the kinetic parameter measured, it also allows me to test the spreading model established.

4. To extend the quantitative study of protein aggregation to the cellular environment. This study aims to observe αS replication and spreading in cells at physiological protein levels using non-transfected cells. To achieve this, an advanced super-resolution microscopy developed for cell imaging, AD Paint, is exploited to follow the spatio-temporal change of endogenous αS amplification in cells. This study will help to understand the molecular basis of protein aggregation in cells and compare with the observations *in vitro*.

In summary, the aims of this thesis will endeavour to be a groundwork to dissect the kinetic scheme of PrP aggregation, enabling us to quantitatively describe the molecular basis of prion and prion-like aggregation, and establish a simple framework to start to determine the main factors that control the rate of prion and prion-like spreading in animals.

Chapter 2 | Methods

2.1 PrP aggregation and production of seeds

Amyloid fibril formation was carried out by aggregation under a semi-denaturing condition[292]. Recombinant WT mouse PrP (amino acid residues 23-231, with a methionine and serine residue at the N-terminus for optimum bacterial expression[293]), was kindly provided by Dr Raymond Bujdoso and Dr Alana Thackray at the Department of Veterinary Medicine, Cambridge and generated as previously described[294]. PrP solution (1.9 mg/mL) was added to a 1.5 mL centrifuge tube containing the reaction buffer (50 mM sodium phosphate, pH 7.0) and 2 M guanidine hydrochloride (GdnHCl, ≥ 99%, Sigma-Aldrich) to a final concentration of 27.5 μM and a volume of 150 μL. The reaction was carried out at 37 °C with 200 rpm shaking in an orbital incubator (ES-20 environmental shaker-incubator, Grant-Bio). To isolate large fibrils in solution, protein aggregates formed after 48 hr, when the number of aggregates reached equilibrium, were centrifuged at 16,000 ×g for 30 min. The soluble species from the supernatant were used as seeds, while the fibril pellet was re-suspended in the reaction buffer, sonicated for 1 min using Sonorex Super RK-52 (Bandelin) with effective power of 60 W, and then used as insoluble seeds in the following seeding reactions.

To probe the size of PrP aggregates, the soluble species from the above supernatant was first separated by 300k MWCO centrifugal filters (Vivaspin 500, Sartorius). The flow-through was then separated using 100k MWCO centrifugal filters (Amicon Ultra 0.5mL, Merck Millipore). The distinct oligomeric species, which contains 12 molecules, was generated based on previously reported protocols by Trevitt *et al* [295]. Briefly, fresh PrP solution no more than 1 mg/mL was denatured by 6 M GdnHCl in the presence of 100 mM DTT (Sigma-Aldrich) for at least 30 min. Subsequently, it was refolded by gently replacing the buffer with 10 mM sodium acetate (pH 4.0) and then enriched using 100k MWCO centrifugal filters (Amicon Ultra 0.5mL, Merck Millipore).

2.2 PrP seeding reactions

For surface-seeded fibril formation, typically, 300 nM soluble or insoluble seeds were transferred to a slide and incubated for ~10 min, until the initial particle count reached 100-200 per field of view. After the residual solution was washed out, 300 nM monomers in the reaction buffer were loaded to give a final volume of 25 μL, in the presence of 25 μM ThT, and then sealed with a coverslip in order to minimise evaporation. The aggregation was performed on a microscope stage at 37 °C, controlled by a custom-made chamber enclosure with a heat controller (AirTherm SMT, World Precision Instrument) around the objective and stage. For solution-seeded experiments under native conditions, soluble seeds at various concentrations were mixed with fresh monomers to a final volume of 100 μL in the reaction buffer. All aggregation reactions were carried out at 37 °C with 200 rpm shaking in an orbital incubator (ES-20 environmental shaker-incubator, Grant-Bio). At each given time point, a protein aliquot was diluted with the reaction buffer in the presence of ThT, bringing the final concentration to 300 nM and 25 μM, respectively, and loaded on a slide. All the solutions used in the continual measurements were vacuum-degassed.

2.3 WT and A53T α-Synuclein aggregation

WT αS was expressed and purified according to a previously established protocol[296]. A53T αS mutant was kindly provided by Dr Joel Watts and Angus Lau at the Tanz Centre for Research in Neurodegenerative Diseases, University of Toronto. A53T was expressed and purified according to a previously established protocol[297]. The two strains of A53T fibrils (S and NS) were generated by aggregation in 20 mM Tris-HCl (pH 7.4) with or without 100 mM NaCl.

αS aggregation was carried out in a 1.5 mL centrifuge tube containing PBS with 0.01% (v/v) NaN_3 at a starting concentration of 70 μM and a volume of 300 μL. The reaction was carried out in the dark at 37 °C with 200 rpm shaking in an orbital incubator (New Brunswick Scientific Innova 43), and aliquots were withdrawn for TIRF imaging as previously described. The αS seeds were generated by collecting the pellet after centrifugation at 16,000 ×g for 30 min, re-suspending in the reaction buffer, and then sonicating for 5 min using Sonorex Super RK-52 (Bandelin) with the effective power of 60 W.

2.4 ThT, Nile red solution and slide preparation

Thioflavin T (ThT) was purchased as a chloride salt (Sigma-Aldrich). The stock solution was prepared by fully dissolving the dye in pure dimethyl sulfoxide (DMSO, ≥ 99.9%, Sigma-Aldrich) to a concentration of 10-30 M with vigorous vortexing. The working solution was prepared at a concentration of 50 μM by diluting in the reaction buffer. Nile Red (NR, ThermoFisher scientific) stock solutions were prepared by dissolving NR into dimethyl sulfoxide (Sigma-Aldrich) to a concentration of 1 mM. The stock solution was divided into 10 μL aliquots, flash frozen in liquid N_2, and stored at -80 °C until use. For the working solution, the aliquot was diluted into filtered PBS buffer to a final concentration of 50 nM. All solutions, except for NR, in this study were filtrated by a 0.02 μm syringe filter (Anotop 10 inorganic membrane filter, Whatman) prior to use. The ThT solution used in the continual measurements was vacuum-degassed before use.

Borosilicate glass coverslips (Marienfeld, VWR International, 20×20 mm) were cleaned by argon plasma (PDC-002, Harrick Plasma) for 1 hr, and then attached to Frame-Seal slide chambers (Bio-Rad, 9×9 mm), with the surface coated with poly-L-lysine (PLL, MW = 150,000 - 300,000, 0.01%, Sigma-Aldrich).

2.5 TIRF imaging

Imaging was performed using a home-built total internal reflection fluorescence microscopy (TIRFM) setup. A 35 mW diode laser (Oxxius, LBX-LD) with a wavelength of 405 nm was used, passed through a single-band bandpass filter (Semrock, FF01-417/60-25), and directed into a 60× magnification oil-immersion TIRF objective (ApoN TIRF, Olympus, NA = 1.49) mounted on an inverted microscope (Eclipse Ti-S, Nikon). The TIRF mode was achieved by adjusting the position of the aligned laser beam before it entered the objective, illuminating samples mixed with ThT molecules. The emitted fluorescence was collected by the same objective, separated from the returning TIR beam by a dichroic mirror (Semrock, Di02-R442-25×36), and passed through an emission filter (BLP01-488R-25). The fluorescence signal was recorded by an Evolve Delta 512 EMCCD camera (Photometrics). Each recorded area contains a 3×3 grid (i.e. 9 images were recorded sequentially at adjacent positions) with a gap distance of 150 μm, in which the

dimensions of a single image were 512×512 pixels (i.e. 110×110 μm^2).

For each time point in kinetic measurements, three random areas (i.e. 27 images) were recorded. Each image sequence was acquired as a 100-framed stack at 30 frames s^{-1}. The image stacks were averaged for further analysis. For the continual measurements of surface-seeded fibril formation, one area was recorded at each time point (i.e. 9 images) with a time gap of 5 min. Each image stack contains 100 frames at 30 frames s^{-1}. Since the fields of view were fixed to the same positions throughout a measurement, single particles could be traced over time simply by averaging images at every time point and combining them as a video file. All the solutions used in the continual measurements were vacuum-degassed for four 1-minute cycles in order to prevent photooxegenation of the protein samples.

2.6 Single-molecule proteinase K digestion assay

Recombinant proteinase K (Fungal, Invitrogen) was prepared at a concentration of 50 μM in the reaction buffer. To determine the PK sensitivity, 300 nM PrP aggregates at defined time points were mixed with PK solution to a final enzyme concentration of 2 μM. For αS samples, 100 nM aggregates were mixed with PK solution to a final enzyme concentration of 0.1 μM. The sealed slides were loaded on a microscope stage and incubated at 37 °C in a custom-made chamber enclosure as described above. The images were continually acquired at fixed areas for 60 min with a time gap of 2.5 min. Each image contains 100 frames at 30 frames s^{-1}. All the solutions used in the continual measurements were vacuum-degassed for four 1-minute cycles.

2.7 TIRF image analysis

Individual image data were averaged over all the frames by ImageJ (National Institutes of Health, USA) and then subjected to image analysis. For single-particle tracing in the continual imaging experiments, the averaged images at the fixed fields of view were combined and aligned using the GDSC ImageJ Plugins (University of Sussex). Images were analysed with a custom-written MATLAB script (R2016a, MathWorks). For particle identification, images were bandpass-filtered to remove the modulated background and camera noise and then blurred using a 2D Gaussian filter. Particle boundaries were

identified by fine-tuning size and intensity thresholds, while their positions were located by calculating centroid positions. The length of particles was measured using built-in algorithms by thinning individual boundaries of particles and then calculated with the image pixel size of 207 nm. To eliminate the background effect in the intensity calculation, the signal-to-background ratio (SBR) was introduced to correct the intensity of pixels, where the SBR is defined as:

$$SBR = \frac{Intensity\ above\ the\ background}{Background} \qquad \text{(Eq. 2.1)}$$

For a given particle, its corrected intensity is the sum of SBR of each pixel within the boundary.

2.8 Kinetic analysis

The kinetic analyses for PrP and αS aggregation *in vitro* were performed by Prof Tuomas Knowles, Dr Lu Hong, and Dr Georg Meisl at the Department of Chemistry, Cambridge.

2.8.1 Calculating the fragmentation rate constants of PrP by directly observing events in surface-seeded aggregation

For the PrP aggregation carried out on a coverslip surface, the fragmentation rate constant was estimated from direct TIRF observation of the number of fragmentation events on the surface. This could be an under-estimate of the true value, because a part of aggregates, especially the very small-sized species, might be ThT-inactive. In addition, the fragmentation rate can be slower on the surface due to the steric hindrance. The fragmentation rate constant is given by:

$$k_f = \frac{Fragmentation\ events}{Number\ of\ fibrils \times Average\ fibril\ length \times Time} \qquad \text{(Eq. 2.2)}$$

where the average fibril length should be given in terms of the number of monomers in

the fibril to obtain the fragmentation rate in the usual units. Here, it was assumed that there is approximately one monomer per nm of a fibril[90]. In addition, since only one tenth of the glass coverslip was observed at any time during the measurement (i.e. one tenth of the fragmentation events was detected during the total measurement time), the number of events is multiplied by 10 to estimate the expected total number of events.

For soluble seed experiments, there are 500 fragmentation events in total and on average 6600 detectable fibrils on the glass coverslip at any time with an average length of 660 nm, giving a fragmentation rate constant of $k_f = 5\times10^{-9}$ s^{-1}. For insoluble seed experiments, there are 1200 fragmentation events in total and on average 6500 detectable fibrils on the glass coverslip at any time with an average length of 530 nm, giving a fragmentation rate constant of $k_f = 1.6\times10^{-8}$ s^{-1}.

2.8.2 Calculating the fragmentation rate constant of αS from decrease on average lengths in bulk solution-seeded aggregation

For the bulk seeded and non-seeded data of αS aggregation, the fragmentation rate constant was estimated from the decrease of the average fibril length after the aggregation reaction had plateaued.

At the plateau of the growth on average length of aggregates, the monomer concentration is depleted and the fibril mass concentration, *M(t)*, no longer changes. However, the average length decreases when the existing fibrils fragment. The moment equations for mass concentration, *M(t)*, and number concentration, *P(t)* are given by:

$$\frac{dM}{dt} = 0, \ \frac{dP}{dt} = k_f M_0 \qquad \text{(Eq. 2.3)}$$

where M_0 is the equilibrium fibril mass concentration. By solving these differential equations and defining the average length as $\mu(t) = M(t)/P(t)$, one obtained:

$$\mu(t) = \frac{M_0}{P_0 + k_f M_0 t} \qquad \text{(Eq. 2.4)}$$

where P_0 is the number concentration of fibrils at the plateau of the aggregation reaction.

The equilibrium fibril mass concentration, M_0, was obtained from the initial monomer concentration assuming all monomer had aggregated. The above equation was then fitted to the average fibril length data, with k_f and P_0 as free fitting parameters. The best fit was achieved for $k_f = 2\times10^{-10}$ nm^{-1}s^{-1} and an average length of 2300 nm at the plateau of the aggregation reaction. With the assumption that there is approximately one monomer per nanometre, the derived $k_f = 2\times10^{-10}$ s^{-1}.

2.8.3 Calculating the elongation rate constants of PrP and αS from initial average length growth for bulk solution-seeded aggregation reactions

The moment equations for mass concentration, $M(t)$, and number concentration, $P(t)$, at initial times (i.e. no monomer depletion) are given by:

$$\frac{dM}{dt} = 2k_e m_0 P, \qquad \frac{dP}{dt} = k_f M \tag{Eq. 2.5}$$

Correspondingly, the differential equation for the mean length reads:

$$\frac{d\mu}{dt} = 2k_e m_0 - k_f \mu^2 \tag{Eq. 2.6}$$

which can be solved to yield:

$$\mu_{early}(t) = \sqrt{\frac{2k_e m_0}{k_f}}\,\mathrm{Tanh}\left[\sqrt{2k_f k_e m_0}\,t + \mathrm{ArcTanh}\left(\sqrt{\frac{k_f}{2k_e m_0}}\,\mu_0\right)\right] \tag{Eq. 2.7}$$

where μ_0 is the initial fibril length in nm. This expression was then Taylor-expanded for small t about $t=0$ to obtain:

$$\mu_{early}(t) \approx \mu_0 + \left(2k_e m_0 - k_f {\mu_0}^2\right)t + o(t)^2 \tag{Eq. 2.8}$$

Experimentally, the data were fitted with a straight line to obtain the slope s, which is then used to obtain the elongation rate constant as:

$$k_e = \frac{s + k_f {\mu_0}^2}{2m_0} \tag{Eq. 2.9}$$

where μ_0 is the intercept of the fit. From the fit of the experimental data, one obtained:

αS: $s = 0.006$ nm/s; $\mu_0 \approx 0$ nm. The results are not sensitive to μ_0 due to the very low fragmentation rate.

PrP (insoluble seeds): $s = 0.0065$ nm/s; $\mu_0 = 460$ nm

PrP (soluble seeds): $s = 0.019$ nm/s; $\mu_0 = 450$ nm

2.8.4 Estimation of the PrP^C level and the doubling time in a mouse brain

For the calculation of the spreading time in a mouse brain, the PrP^C concentration on average was estimated. Previous studies suggest that the abnormal PrP^{Sc} accumulates in intracellular endosomal compartments and trafficks to the plasma membrane[298], while more recent research suggests that the plasma membrane is a more likely site for PrP^C-PrP^{Sc} conversion[299,300]. The amount of PrP^{Sc} accumulated in the brain of a wild-type $Prnp^{+/+}$ mouse at the terminal stage of prion diseases was reported to be around 13 ± 7 μg per g of tissue[301–303]. Hence, the PrP^{Sc} concentration in the brain was estimated to be 0.9 ± 0.50 μM on average, given the weight (0.4 g) and volume (~450 mm^3) of a typical mouse brain. Given that the *Prnp* gene expression level does not change[304,305] and the PrP^C concentration does not rise[306] during mouse prion disease pathogenesis, and that the initial PrP^C level is about 8-fold lower than the total PrP level in a mouse brain at the terminal stage[244], the cellular PrP^C concentration was estimated to be $\sim 0.12 \pm 0.06$ μM on average at a normal expression level in a mouse brain. Based on cryo-immunogold EM studies, ~56% and ~15% of PrP^C is located at the plasma membrane and in the endosomal compartments, respectively[298]. Therefore, cellular PrP^C concentration was estimated to be 60 nM and that in the endosomal compartments was ~15 nM. It is noted that for simplicity of the calculation, the variation of the PrP^C level in different cell types was not considered, and the mean value was used for estimation.

2.8.5 Comparing the doubling time for different prion strains

Two types of prion strains, fast (F) and slow (S), were considered with doubling times t_2 and $\alpha \cdot t_2$, respectively, where $\alpha > 1$ (i.e. the S strain with longer doubling time $\alpha \cdot t_2$). Their number increases as $P_0 \cdot \exp(t \cdot \ln 2 / t_2)$, where P_0 is the initial number of aggregates. Assuming that at $t=0$ they are present in equal proportions, their ratio of amount at any time t is given by:

$$\frac{P_F}{P_S} = \exp\left[\left(\frac{\ln 2}{t_2} - \frac{\ln 2}{\alpha t_2}\right)t\right] = \exp\left[\frac{\ln 2}{t_2}\left(\frac{\alpha - 1}{\alpha}\right)t\right] \quad \text{(Eq. 2.10)}$$

The time at which F strain is more abundant than S strain by a factor x is therefore given by:

$$t_x = t_2 \frac{\ln(x)}{\ln 2}\left(\frac{\alpha}{\alpha - 1}\right) \quad \text{(Eq. 2.11)}$$

which corresponds to $(ln(x)/ln2)(\alpha/(\alpha-1))$ rounds of doubling for F strain.

2.8.6 Kinetic analysis of the early stage of PrP aggregation under a semi-denaturing condition

The TIRF data at the early stage of PrP aggregation (≤ 8 hr) was fitted to the kinetic model described as follows. Since no fibrils were detected, depletion of monomers could be negligible, and the monomer concentration was approximated to be constant during the modelling process. The number of PK-sen species (S_L and S_H) remained unchanged over the measurement period (Figure 4.1b). Hence, the two species were modelled as being at equilibrium with monomers over this time period of the measurements. It has to be noted that the constant number of S_L and S_H was very unlikely due to the steady state of the aggregation kinetics, as there was insufficient production of PK-res species or fibrils at the early stage of the aggregation. Therefore, the number of the PK-sen species was approximated as:

$$S_L = K_L m^{n_L} \quad \text{(Eq. 2.12)}$$

$$S_H = K_H m^{n_H} \quad \text{(Eq. 2.13)}$$

where K_L and K_H are the equilibrium constants between monomers and PK-sen species for S_L and S_H, respectively. m is the monomer concentration. n_L and n_H are the equilibrium reaction orders for PK-sen species formation (i.e. they must be ≥ 1). Dissociation of PK-sen species to monomers was assumed to be well-described by a single process with a reaction order of 0.

At the early stage of PrP aggregation, the aggregate length did not show obvious increase compared to that of fibrils at 48 hr (Figure 4.2), and little increase in ThT intensity was seen during this time period (Figure 4.1a). Furthermore, the molecular size of the H species has been previously shown to be > 300 kDa (i.e. >12 PrP molecules), while the L species was < 300 kDa[307]. Therefore, all of the four ThT-active species: S_L, S_H, R_L, and R_H were highly unlikely to be fibrils.

Because R_L and R_H formed more slowly than S_L and S_H formation (Figure 4.1d), R_L and R_H could either convert from S_L and S_H, or be nucleated directly from monomers. From the observations, R_L shares a similar ThT intensity profile with S_L (and likewise, in the R_H and S_H pair) (Figure 4.1c), and the increase of the fraction of the PK-res species was at the same rate as that of the decrease of the PK-sen species (Figure 4.5d). Therefore, it is highly likely to be the case of a direct PK-sen → PK-res structural conversion (Figure 4.8a). We therefore described these relations as:

$$\frac{dR_L}{dt} = k_{cL} m^{n_{cL}} S_L - k_{dL} R_L \qquad \text{(Eq. 2.14)}$$

$$\frac{dR_H}{dt} = k_{cH} m^{n_{cH}} S_H - k_{dH} R_H \qquad \text{(Eq. 2.15)}$$

where k_{cL} and k_{cH} are the rate constants of structural conversion of S_L to R_L and of S_H to R_H, respectively. n_{cL} and n_{cH} are the monomer-dependent reaction orders of the conversion reaction. k_{dL} and k_{dH} are the rate constants of depletion of R_L and R_H. Solving the equations, the number of the PK-res species is obtained:

$$R_L = \alpha_L \left(1 - e^{-k_{dL} t}\right) \qquad \text{(Eq. 2.16)}$$

$$R_H = \alpha_H \left(1 - e^{-k_{dH} t}\right) \qquad \text{(Eq. 2.17)}$$

where $\alpha_L = k_{cL} K_L m^{n_{cL}+n_L} / k_{dL}$, and $\alpha_H = k_{cH} K_H m^{(n_{cH}+n_H)} k_{dH}$

To determine the kinetic parameters in this nucleation-dissociation-conversion model, the quantitative TIRF data obtained from 3 different starting monomer concentrations (Figure 4.1b) were fitted to these equations individually, and then the fitted parameters

in Table 1 was obtained. It has to be noted that the fitted results are only proportional to the monomer concentrations. However, the fitted equilibrium constant K may contain unknown proportionality coefficients and thus cannot be compared with other aggregation systems.

From Table 4.1, S_L and S_H share similar kinetic parameters, as do R_L and R_H. This suggests that the L and H species are likely to interconvert rapidly on the time scale of the measurements. Therefore for convenience, the scheme can be simplified to that shown in Figure 4.8b, where S_L and S_H are treated as a single species, as are R_L and R_H. This simplified model is given by:

$$S = Km^n \quad \text{(Eq. 2.18)}$$

$$R = \alpha\left(1 - e^{-k_d t}\right) \quad \text{(Eq. 2.19)}$$

where $S = S_L + S_H$, $R = R_L + R_H$, and $\alpha = k_c m^{n_c+n} / k_d$

Fitting the number of S and R to this simplified model, good fits were obtained (Figure 4.8c) with the fitted parameters given in Table 4.2. It is clear that an equally good fit can be obtained from the two models, which share the same functional form, based on the same TIRF data, as the reaction orders and rate constants are very close or identical between the two models. It is noted that the fitted reaction order of nucleation n=1 implies that this rate-determining step involves only 1 monomer for nucleation, which suggested that this process may involve surface interaction e.g. microcentrifugal tube surface.

2.9 TEM imaging

To prepare TEM samples, protein solutions were applied and fixed on a carbon-coated 400-mesh copper grid for 3 min, and then excess solution was removed from the surface by washing twice with distilled water. Negative staining was carried out using 2% (v/v) uranyl acetate for 1 min. After drying, the samples were transferred to the Cambridge Advanced Imaging Centre (CAIC) for imaging. Image acquisition was carried out by a Tecnai G2 microscope operated at 200 kV.

2.10 Gel electrophoresis

Aliquots of αS aggregates at defined time points, incubated as described above, were taken and mixed with 1x NuPAGE LDS sample buffer (Thermo, Invitrogen) supplemented with 5 mM β-mercaptoethanol, and boiled at 95°C for 10 min. The samples were then separated by NuPAGE 4-12% Bis-Tris Gel (Thermo, Invitrogen) at 200 V.

2.11 sPaint imaging with PrP aggregates

PrP aggregated in partially denaturing condition was described in Chapter 2.1. At defined time points, an aliquot was removed and diluted to 50 nM (oligomeric species) or 100 nM (fibrillar species) with 0.22 μm-filtered PBS buffer containing 5 μM ThT, 2 nM NR and 10% (v/v) fiducial markers. The sample mix was added to the coverslip and incubated for 10 minutes allowing aggregates to adhere to the surface of glass coverslips. The coverslip was then immediately loaded onto the microscope stage for imaging.

The sPaint imaging was performed in collaboration with Dr Ji-Eun Lee at the Department of Chemistry, Cambridge. Fluorescence imaging was performed using a separate home-built TIRF setup based on an inverted optical microscope (IX73, Olympus) and coupled to an EMCCD (Evolve II 512, Photometrics). Lasers operating at 405 nm continuous wave (CW) diode laser (Cobolt, MLD 0405-06-01-0100-100) for ThT imaging, and 532 nm CW diode-pumped solid-state laser (LASOS Lasertechnik GmbH) for NR imaging were used as excitation sources. Images were acquired at a frame rate of 20 ms and 200 frames for ThT channel and 2000 frames for NR channel.

The lasers were circularly polarised light by a quarter wave plate and directed off dichroic mirrors for 532 nm and 405 nm illumination (Di02-R532-25x36 and Di02-R405-25x36, Semrock) towards a high numerical aperture, oil-immersion objective lens (Plan Apochromat 60× NA 1.49, Olympus APON 60XOTIRF) to the sample coverslip. Total internal reflection was achieved by focusing the laser at the back focal plane of the objective, off axis, such that the emergent beam at the sample interface was near-collimated and incident at an angle greater than the critical angle θ_c (~67° for a glass/water interface). This generated a ~50 μm diameter excitation footprint with power densities in the range ~0.5 kW-cm^{-2} at the coverslip. The emitted fluorescence was subsequently collected through the same objective and further filtered using a long-pass filter BLP01-532R-25 (Semrock), a bandpass filter FF01-650/200-25 (Semrock), and a

short-pass filter FF01-715/SP-25 (Semrock) for 532 nm illumination (NR channel) or a long-pass filter FF02-409/LP-25 (Semrock) for 405 nm illumination (ThT channel) before being expanded by a 2.5× relay lens (Olympus PE 2.5X 125). Finally, a mechanical slit (VA100/M, Thorlabs) and a transmission diffraction grating (600 Grooves/mm 22.0° Blaze Angle - GTU13-06, Thorlabs) with a homebuilt grating holder were mounted on the camera port path prior to the detector. The camera-to-grating distance was optimized using TetraSpeck beads (0.1 μm, T7297, Invitrogen) such that undiffracted (0th) and first order (1st) diffraction was visible on the same image. The fluorescence image was finally projected onto the EMCCD running in frame transfer mode with at 20 Hz, with an electron multiplication gain of 250, operating at -70 °C with a pixel size of 16 μm and automated using the open source microscopy platform Micromanager.

The sPaint images were calibrated as described previously[284]. The distance between 0th and 1st order diffraction patterns are determined by imaging four colour fluorescence beads (0.1 μm, T7297, Invitrogen) in order to determine the relation to the emission wavelength. Based on the clustered localisations and the final result file, the spectral information of individual proteins was extracted and plotted using custom-written MATLAB software (R2014b, Mathworks). A localisation threshold of 20 was used to identify single aggregates. The achievable spatial localisation precision of the instrument was measured by imaging diffraction-limited TetraSpeck beads (0.1 mm, T7279, Invitrogen) using a 532 nm excitation laser. 500 frames at 20 ms per frame were collected at a range of excitation powers and localised using the PeakFit plugin for ImageJ from the GDSC SMLM package. TetraSpeck 'orange' peak centres, at 581.5 nm, were fitted and used to determine the spectral localisation precision.

2.12 Membrane permeability assay using TIRFM

The membrane permeability assay was performed in collaboration with Dr Suman De at the Department of Chemistry, Cambridge. The assay was implemented from a previously described method[308]. Briefly, vesicles were prepared by mixing phospholipids 16:0-18:1 PC (catalogue no 850457, Avanti Polar Lipids) and biotinylated lipids 18:1-12:0 biotin-PC (catalogue no 860563, Avanti Polar Lipids) at 100:1 ratio in HEPES buffer (pH 6.5). The mean diameter of the vesicles was ~200 nm. They were filled with 100 μM Cal-520 dye (Stratech Scientific Ltd) using five freeze-and-thaw cycles. Non-incorporated Cal-520 dye molecules were separated from the vesicles by size-exclusion chromatography. Then the vesicles were tethered to the glass coverslips using biotin-neutravidin linkage and

incubated with of HEPES buffer of pH 6.5. Just before the imaging, HEPES buffer was replaced with 50 µL Ca^{2+} containing buffer solution L-15 and a different position of the coverslips was imaged (F_{blank}). Then, the 27.5 µM PrP aggregation solution was diluted and added to the coverslips so that the final protein concentration in the coverslip is 250 nM. The same area of the coverslips was imaged to evaluate the protein aggregate-induced membrane permeabilisation by measuring the resulting Ca^{2+} influx ($F_{aggregate}$). Then, 10 µL of 1 mg/mL of ionomycin (Cambridge Bioscience Ltd, Cambridge, UK) was added to the same coverslips and the same fields of views were imaged ($F_{ionomycin}$). As ionomycin induces a high degree of membrane permeation, each vesicle is saturated with bath Ca^{2+} and maximum fluorescence is observed. Therefore, the fluorescence originating from ionomycin-induced Ca^{2+} influx is used for normalization, which enables quantification of the aggregate-induced Ca^{2+} influx. All the images were taken using a homebuilt TIRF set-up based on an inverted Olympus IX-71 microscope, which was equipped with 60×, 1.49 NA oil immersion objective lens (APON60XO TIRF, Olympus) and an EMCCD camera (Evolve II 512, Photometrics). A 488 nm laser (Toptica, iBeam smart) was used to excite the sample. All the imaging experiments were performed at ambient temperature (295 K) with a 488 nm laser (~10 W-cm^{-2}) for 0 frames with a scan speed of 20 Hz. The acquired images were analysed using ImageJ to calculate the localised fluorescence intensity of each vesicle under the three different experimental conditions, namely in presence of L15 buffer (F_{blank}), in the presence of the aggregation mixture collected at different time points ($F_{aggregate}$), and after the addition of ionomycin ($F_{ionomycin}$). The influx of Ca^{2+} into an individual vesicle was calculated as:

$$\mathrm{Ca^{2+}influx} = \frac{F_{aggregate} - F_{blank}}{F_{ionomycin} - F_{blank}} \qquad \text{(Eq. 2.20)}$$

The Ca^{2+} influx from individual experiments was then normalised with the number of aggregates observed from TIRF images. The relative influx level at the earliest time point of aggregation (in this thesis, 0.5 hr of PrP aggregation at an initial concentration of 27.5 µM) is set as 1.

2.13 Proteasome assay with αS aggregates using TIRFM

The proteasome assay was performed in collaboration with Dr Yu Ye and Rachel Cliffe at the Department of Chemistry, Cambridge. Purification of mammalian proteasome holoenzymes or the free regulatory particle (RP) was carried out by Dr Yu Ye in Prof Daniel Finley's laboratory at Harvard Medical School with a published protocol[309]. αS aggregation was carried out as described in Chapter 2.3. Aliquots were removed from aggregation reactions after 24 hrs and incubated with the proteasome. The final reactions contained 8 µL of 200 nM proteasome, 8 µL of the aggregated αS substrate, 5 µL of 10 × degradation buffer (50mM Tris [pH7.5], 5 mM ATP, 5 mM $MgCl_2$), 2.5 µL of a 20 × ATP regeneration system (2 M creatine phosphate and 100 µM creatine kinase) and ddH_2O to make up 50 µL final reaction volume. The reactions were performed at 25 °C to avoid further aggregation. After 0 and 20 hr of incubation, 1 µL aliquot was removed from each reaction and serially diluted 50-fold in PBS buffer containing 30 nM pFTAA (kindly provided by Dr Michel Goedert at MRC Laboratory of Molecular Biology) for TIRF imaging. Prior to the proteasome treatment, aggregated samples were centrifuged on a benchtop centrifuge at maximum velocity for 30 min. The supernatant was subsequently removed and resuspended with an equal volume of proteasome buffer before incubation with the proteasome. Addition of the proteasome was omitted in control reactions and replaced with an equal volume of the proteasome buffer.

2.14 Cell culture and fibril transduction to cells

SH-SY5Y cells were cultured on round borosilicate coverslips (Marienfeld, VWR International, Ø =20 mm) in 6-well tissue culture plates (Greiner CELLSTAR, Sigma) and allowed to reach 60–70% confluence for transduction experiments. Before seed transduction, cells were washed with PBS and transferred to serum-free OptiMEM (Thermo) for 1 hr. For each well, one reaction of the cationic-liposomal transduction reagent (BioPORTER, Sigma) was resuspended with PBS and then gently mixed with 2.5 µM sonicated αS fibrillar seeds generated as described in Chapter 2.3. Protein-reagent complexes were allowed to form at room temperature for 5 min. After that, the mixture was diluted in OptiMEM and added to cells. Cells were then further incubated for 4 hr, washed three times. Transduced cells were maintained in Dulbecco's modified Eagle's medium (DMEM, Thermo) containing 10% fetal bovine serum (FBS, US sourced HyClone characterised, GE) and 1% penicillin-streptomycin (Thermo) unless otherwise indicated.

2.15 Immunostaining of endogenous αS filaments and AD Paint imaging

The AD Paint imaging was performed in collaboration with Yukun Zuo at the Department of Chemistry, Cambridge. To prepare samples for imaging, the coverslips cultured with cells were transferred to a separate dish at defined time points, washed with cold PBS three times, and fixed with paraformaldehyde 4% (w/v) for 10 min at room temperature. The cells were then rinsed three times with phosphate buffered saline (PBS) before being membrane-permeabilised by 0.5% Triton X-100 in PBS containing 3% bovine serum albumin (BSA) for 20 min at room temperature. After rinsing three times with PBS, samples were blocked with 3% BSA/10% salmon sperm DNA (Catalogue no 15632011, Invitrogen) for 1 hr at room temperature before immunostaining. A conformation-specific anti-αS filament antibody, MJFR-14-6-4-2 (Abcam), was conjugated with a synthesised short single-stranded DNA (docking strand), and then it was with diluted by 10000× in the blocking solution and incubated with cells overnight at 4 °C. On the next day, the samples were rinsed three times with PBS, loaded in a cell chamber, and replaced with the imaging solution in the presence of Hoechst stain with 1:3000 dilution before imaging. The imaging solution was made by diluting a synthesized single-stranded DNA (imaging strand; contain a complementary sequence to docking strand) labelled with Cy3b fluorescent dye to 5 nM in the blocking solution.

AD Paint imaging was performed using a home-built TIRFM setup as described in Chapter 2.5 but with HILO (highly inclined and laminated optical) mode, where the laser is directed at a relatively sharper angle through the sample. This affords an imaging depth of ~5 μm in this case and hence increases illumination depth in neurites at an SNR only slightly lower than that of TIRF. Images were acquired in random fields of view at a frame rate of 50 ms and 100 frames for brightfield illumination, 100 frames for 405 nm channel, and 4000 frames for 561 nm channel, respectively. The subsequent image analysis was carried out with a custom-made Python script by Yukun Zuo. In brief, the individual images were filtered by fine-tuning the localisation thresholds of signals. The individual signals above the threshold were then calculated based on the proximity of each pair of signals, and the signals above a proximity threshold were determined as one object. The length of objects was measured using built-in algorithms by thinning individual objects and then calculated with the image pixel size of 98.6 nm.

Chapter 3 | The mechanism of prion-like spreading I: PrP aggregation

3.1 Introduction

Prion replication occurs by a nucleation-dependent polymerisation reaction, whereby growth of aggregated PrP nuclei is followed by fast elongation through recruitment of misfolded PrP monomers to the protein assemblies[175]. Several molecular events are proposed to play a key role in this process, including secondary nucleation and fibril fragmentation[186,187,190] (Figure 3.1a). Secondary nucleation allows the formation of new prion aggregates from existing template seeds with concomitant amplification of the total number of PrP^{Sc} assemblies[190]. Fibril fragmentation has been demonstrated to accelerate prion replication in yeast prion Sup35[184,187] and Ure2[178], as well as αS in PD[191], while few insights were provided from mammalian prion studies[310]. Significantly, there is no clear evidence that mammalian prions show a similar phenomenon of fragmentation in aggregation, although it has been long suggested that they amplify rapidly enough *in vivo* to confer transmissibility through fragmentation of existing PrP aggregates, entering neighbouring cells, and then acting as new seeds to initiate the aggregation of endogenous PrP[174,186,311,312]. Therefore, it is important to determine the mechanism and kinetics of how PrP aggregates grow and amplify, since these events will provide fundamental insights into how prions might spread in the brains of individuals affected by these conditions.

Dissecting the mechanism of prion propagation *in vivo* is difficult given the molecular and cellular complexity of the mammalian brain. As a consequence, this process has been increasingly studied with recombinant prion protein *in vitro*. Compared with conventional biochemical and biophysical approaches, single-molecule fluorescence microscopy serves as a powerful tool by resolving individual behaviour of protein aggregates that may be averaged in ensemble experiments. Recently, our group has developed 'single-aggregate' fluorescence imaging to visualise protein aggregates through the use of sensitive total internal reflection fluorescence (TIRF) microscopy in combination with thioflavin T (ThT)[276]. This method provides direct observation of the low-populated species such as oligomers, which are naturally heterogeneous, transient, and meta-stable during aggregation[180,191,195,313,314]. It also enables quantitative measurements of the change in the number of individual aggregates as a function of time. Furthermore, as ThT molecules transiently bind to protein aggregates in equilibrium, this

approach allows protein aggregates to be imaged for extended time lengths without photobleaching and for biochemical assays such as proteinase K (PK) resistance measurements to be performed on individual aggregates.

In this chapter, the single-aggregate fluorescence imaging has been adopted to visualise the aggregation process of recombinant PrP under native conditions. In this chapter, I have quantitatively measured PrP aggregation *in vitro* as a function of time. This has enabled determination of the elongation and fragmentation rate constants for PrP aggregation for the first time through the use of a kinetic modelling approach. These parameters thus were used for predicting the spread of PrP through the brain based on a simple model. In addition, it is found that during the aggregation reaction, PrP converts from a PK-sensitive to PK-resistant conformer. The fragmentation rate increases with fibril length, and this process results in the formation of PK-sensitive fragments.

3.2 The kinetic rate constants of PrP aggregation are determined from solution-seeded reactions

Kinetic rate constants for the elongation and fragmentation process of amyloidogenic proteins can be derived from quantitative measurements during aggregation[192]. To acquire the kinetic parameters for PrP aggregation, a set of seeded reactions of recombinant mouse PrP was performed in bulk solution under native conditions (Figure 3.1b, left).

To produce seeds, PrP aggregation was performed following a previously published protocol[292]. The morphologies of the PrP aggregates at different times were revealed using single-molecule TIRF imaging (Figure 3.2a). Small aggregates, as well as large fibrils, were obtained after 48 hr, when the reaction reached a plateaued. The fibrils obtained were further examined by transmission electron microscopy (TEM) (Figure 3.2b). A similar morphology was found between the structure formed in the current and those in the previous studies[292,315]. The aggregation mixture collected at 48 hr was then separated by centrifugation to obtain soluble aggregates from the supernatant (soluble seeds), or insoluble aggregates (insoluble seeds; acquired from sonication of the fibrillary species after pellet re-suspension). Control experiments showed that upon 1-minute sonication, most of the mature PrP fibrils formed after 48 hr were broken into small fragments with low ThT intensity (<10 a.u.) (Figure 3.3), consistent with the previous result with PrP fibrils that generated under the same buffer condition[315].

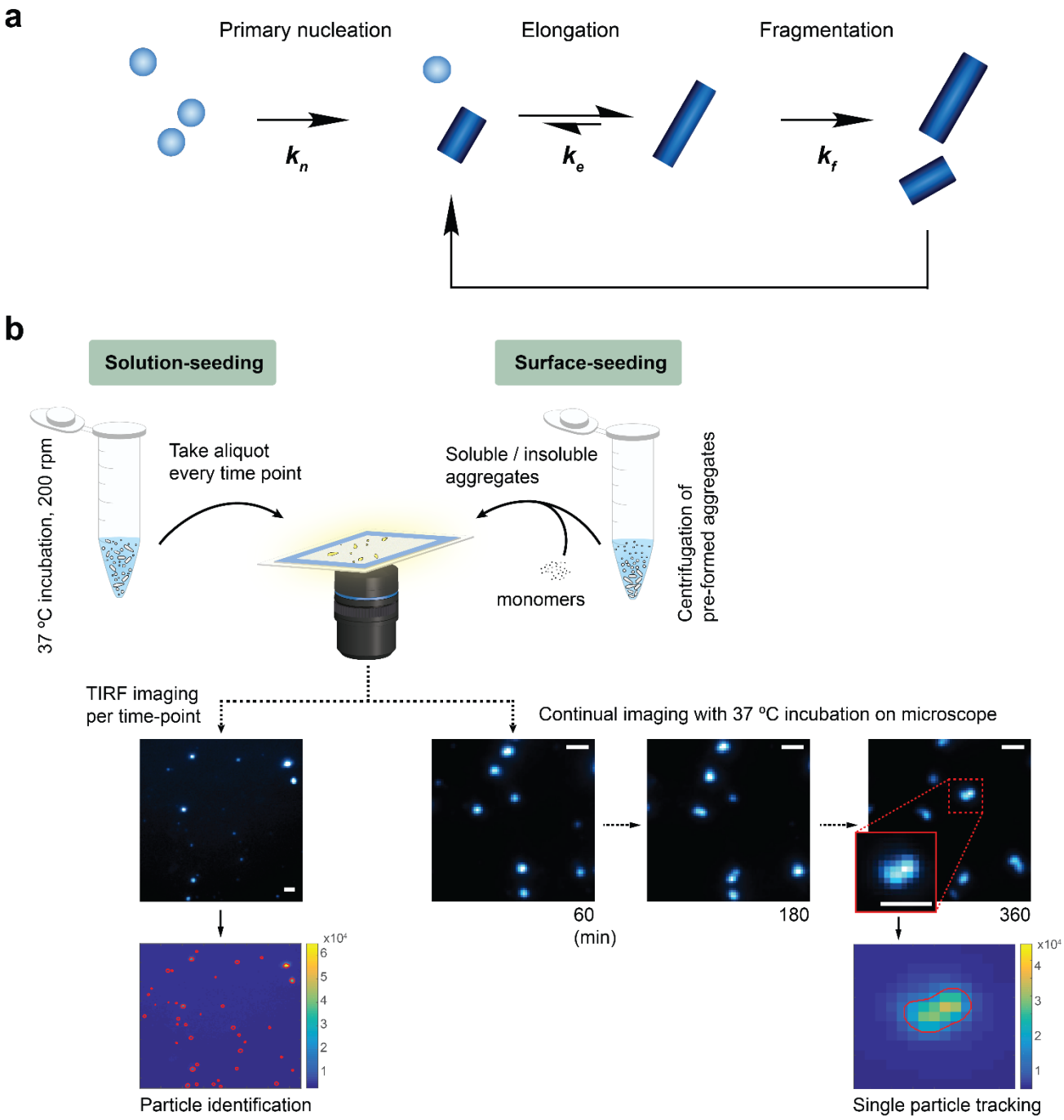

Figure 3.1 | Schematic description of the molecular processes of fibril formation and the experimental setup. (**a**) Amyloid fibril formation begins with slow primary nucleation that involves a range of structurally-diverse intermediates, followed by a fast growth of fibrils. The fibrils can break into smaller fragments and act as new templates for further growth. (**b**) In the bulk solution-seeded measurements (left), PrP aggregates were incubated in a 1.5-mL centrifuge tube. At various time points, aliquots were removed from the reaction mix and transferred to a solution containing ThT. The aggregates subsequently diluted to a nanomolar concentration. The PrP aggregates were visualised on a TIRF microscope with a 3×3 image grid at 3 random positions (i.e. 27 simultaneous images). The acquired images were analysed

with a Matlab-based script to identify individual aggregates (see Chapter 2.7 for details). For the surface-seeded measurements (right), pre-formed soluble or insoluble seeds were separated by centrifugation and then adsorbed onto a glass coverslip. After removal of residual solution, fresh PrP monomers and ThT were added to the glass coverslip and slide chamber sealed to prevent fluid evaporation. Images of individual aggregates were acquired over time in a single 3×3 image grid with fixed fields of view at 37 °C (i.e. 9 simultaneous images). All the scale bars represent 2 μm.

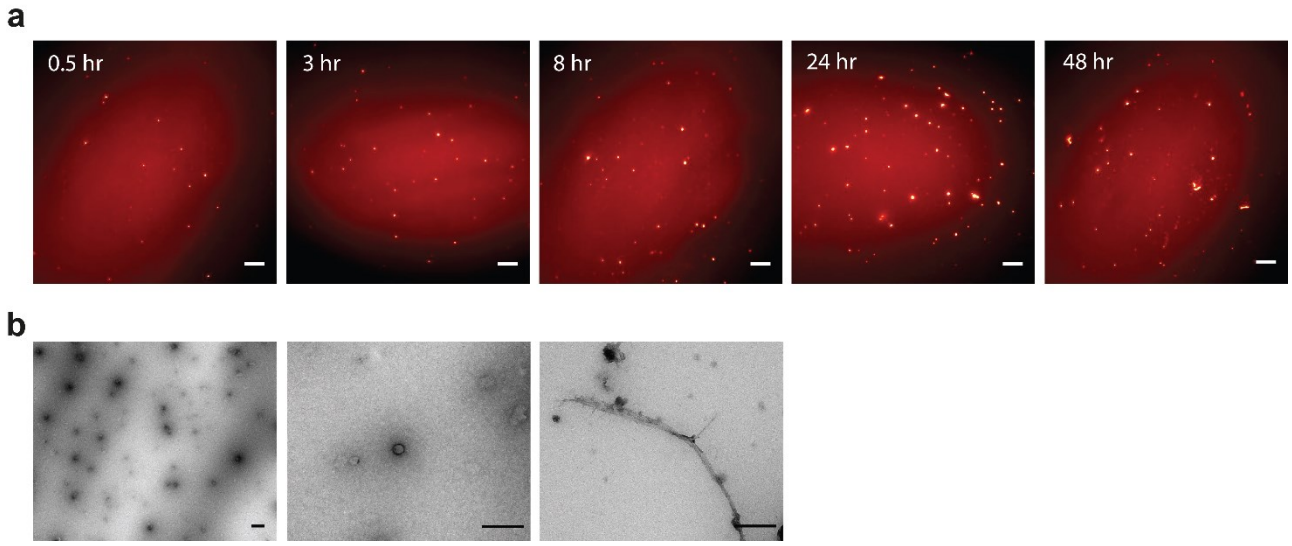

Figure 3.2 | Representative images of PrP aggregates in a semi-denaturing condition. (**a**) The TIRF images of PrP aggregates at 0.5 hr, 3 hr, 8 hr, 24 hr, and 48 hr in unseeded aggregation are revealed. Monomeric PrP was incubated in a 1.5-mL microcentrifugal tube in the presence of 2 M GdnHCl at 37 °C with 200 rpm. At different time points, an aliquot was removed from the reaction mix, diluted to a final concentration of 300 nM, and loaded onto a PLL-coated glass coverslip in the presence of 25 μM ThT for TIRF imaging. (**b**) TEM images of PrP aggregates at 48 hr when the reaction plateaued. The protein assemblies were fixed in carbon-coated copper grids and negatively stained with 2% (v/v) uranyl acetate. The scale bars in panel **a** and **b** represent 10 μm and 500 nm,

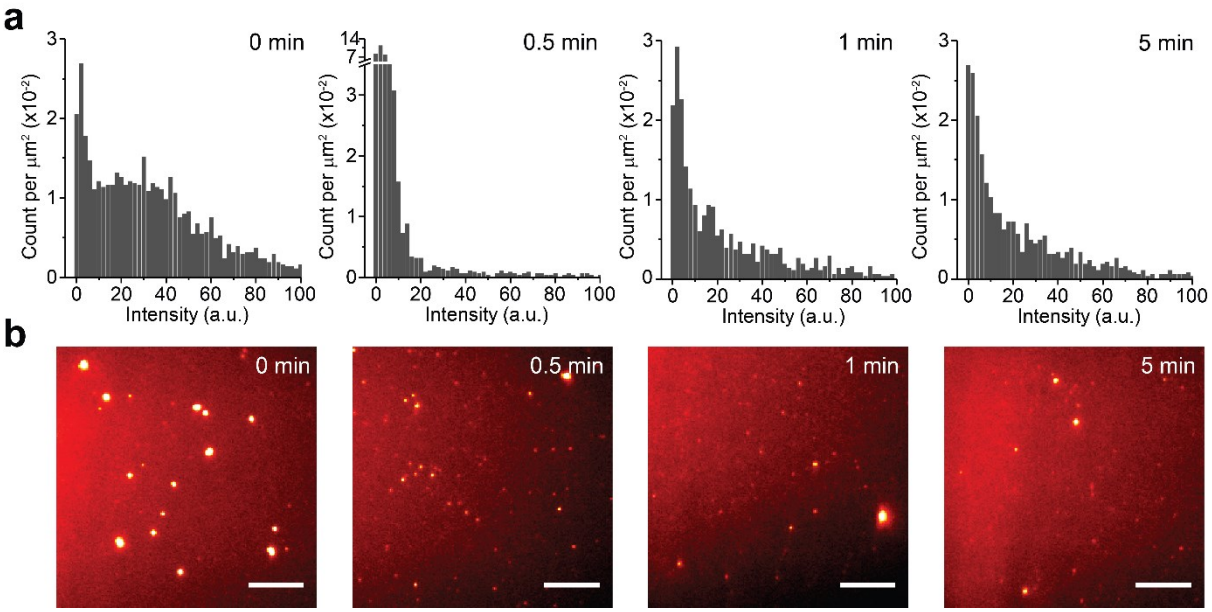

Figure 3.3 | Sonication effect to PrP fibrils. (**a**) Intensity distributions and (**b**) TIRF images of sonicated PrP fibrils for different sonication durations. PrP fibrils collected at 48 hr when the aggregation reaction plateaued were collected by centrifugation at 16,000 ×g for 30 min and resuspended in the reaction buffer. The PrP fibrils were either non-sonicated (0 min) or sonicated for 0.5, 1, or 5 min and imaged using a TIRF setup. The scale bars represent 10 μm.

Prior to seeded aggregation, an optimal condition for effective protein-dye binding was established. A serial dilution of thioflavin T (ThT) dye was prepared ranging from 0.01 to 100 μM, and then mixed with the aggregates collected at 48 hr to a final protein concentration of 300 nM. Using single-aggregate imaging with TIRF microscopy, the PrP aggregates were visualised at multiple fields of view, and the number at the respective fields of view was quantified as a function of ThT concentrations (Figure 3.4). The average number of the detected aggregates reached a maximum level at a ThT concentration of 25 μM, which indicated an optimal ThT concentration for the imaging setup. Next, the saturation effect of the PrP aggregates upon the poly L-lysine (PLL)-coated glass surface was examined. The number of PrP aggregates adsorbed onto a glass surface was found to be proportional to their solution concentration up to 300 nM, suggesting the surface was not saturated by the aggregates (Figure 3.5).

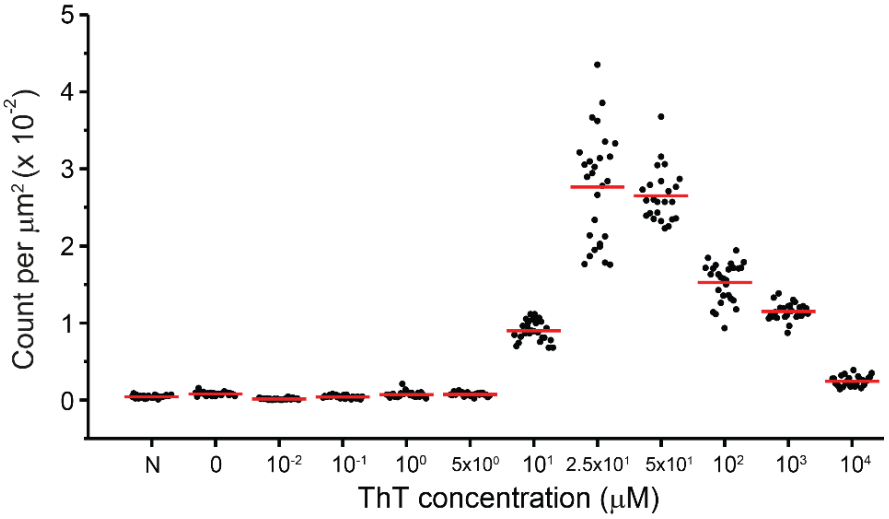

Figure 3.4 | Affinity of ThT to PrP aggregates as a function of concentration. ThT concentration was serially diluted and mixed with PrP aggregates formed at 48 hr at a fixed concentration of 300 nM. The samples were then imaged using a TIRF setup. The average of the count of PrP aggregates (red lines) increased at ThT concentrations that were over 10 μM. N: negative control of 25 μM ThT without PrP aggregates.

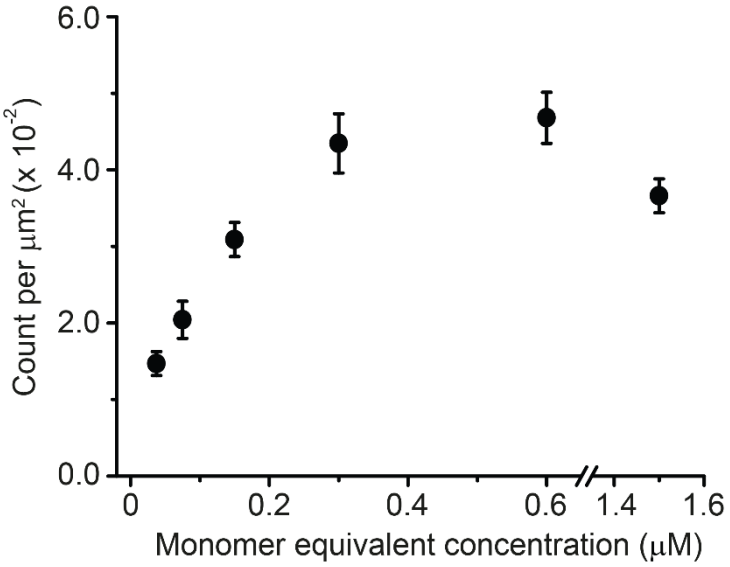

Figure 3.5 | Titration of PrP aggregate concentrations on a poly L-lysine (PLL)-coated glass coverslip surface. The 12-mer PrP aggregates at various concentrations were adsorbed on PLL-coated coverslips to determine when surface adsorption was saturated. Protein concentrations below 300 nM are linearly correlated to their counts with $R^2 = 0.97211$. The error bars represent standard deviations from three independent experiments with different batches of protein samples.

Bulk solution-seeded PrP aggregation was carried out using the soluble seed under native conditions (reaction buffer: 50 mM sodium phosphate buffer, pH 7.0) with a wide range of seed and monomer concentrations. At defined time points during the seeded aggregation reaction, aliquots were removed from the reaction mix, and the number of PrP aggregates quantified using ThT and TIRF microscopy (Figure 3.1b, left). At the single-aggregate level, seeded PrP aggregation was found to proceed through exponential amplification, as shown in Figure 3.6. Gentle shaking of the reaction mix was found to be required in order for PrP to form aggregates. This is consistent with conditions used for

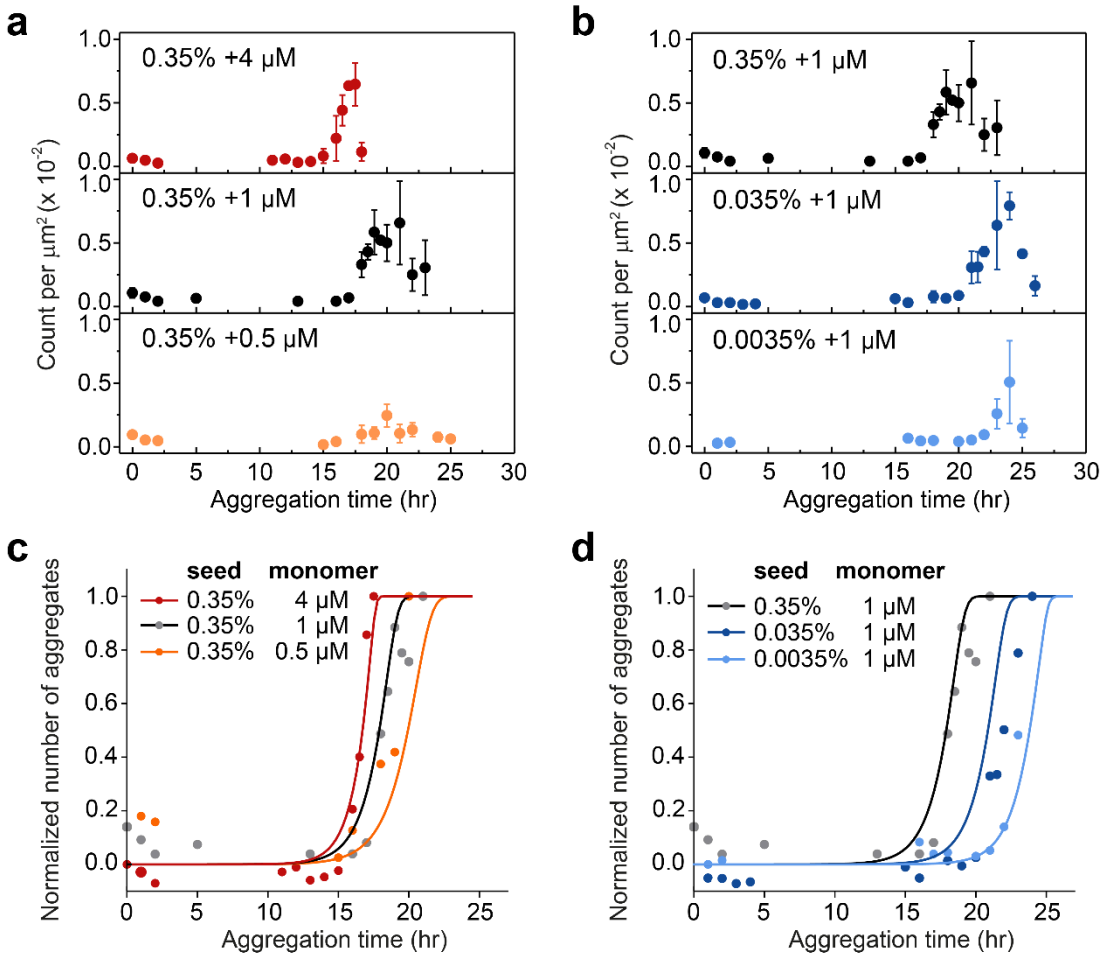

Figure 3.6 | Kinetics of solution-seeded PrP aggregation. (**a**) Representative TIRF images of 0.35% (v/v) soluble PrP seeds+ 1 μM monomers at different times are revealed. The scale bars represent 10 μm. Solution-seeded PrP aggregation was followed with various concentrations of (**b**) monomers or (**c**) soluble seeds in 50 mM sodium phosphate (pH7.0). The kinetics were followed by taking aliquots at various time points from the aggregation reaction mix that was incubated at 37 °C with shaking at 200 rpm. (**d** and **e**) Global fits of the kinetic profiles. The y-axis was normalised to the maximum value of each profile. The product of the rate constants $k_e k_f$ was 0.06 $M^{-1}s^{-2}$. The error bars represent standard deviations from three independent experiments with different batches of protein samples.

QuIC experiments[316] and was possibly due to a fraction of the aggregates adsorbed on the micro-centrifuge tube surface. Interestingly, fast disappearance of PrP aggregates was also observed after the reaction reached a plateau. Through the use of transmission electron microscopy (TEM), the PrP aggregates that disappeared in TIRF images were ThT-inactive and small fragments (< 50 nm) (Figure 3.7) that probably formed due to fragmentation.

To acquire kinetic parameters for PrP aggregation, the data were globally fitted to the nucleation-elongation-fragmentation kinetic model for protein aggregation that was published previously[186,193]. This model has two parameters: the elongation rate constant, k_e, and the fragmentation rate constant, k_f. When we consider the time required for a single misfolded PrP aggregate to elongate and fragment to form two aggregates, the doubling time t_2, is given by:

$$t_2 = \frac{ln2}{\sqrt{\left(2k_e k_f m\right)}} \qquad \text{(Eq. 3.1)}$$

where m is the monomer concentration. The solution-seeded data were fitted (Figure 3.6d) with the help from Dr Georg Meisl in the Department of Chemistry, Cambridge. The product of k_e and k_f was found to be 0.06 $M^{-1}s^{-2}$ (Table 3.1).

According to Equation 1, the doubling time t_2 for PrP amplification in a cell depends on

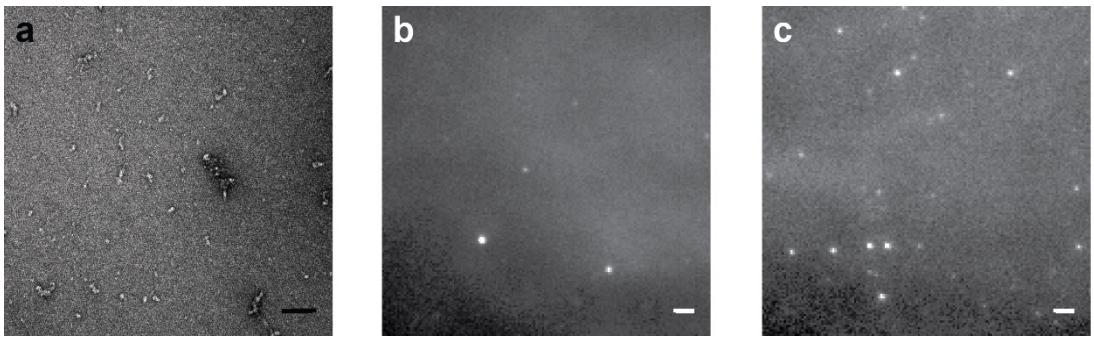

Figure 3.7 | ThT-inactive PrP aggregates. Solution-seeded aggregates incubated for 72 hr were visualised by TEM (**a**) and TIRFM (**b**) with 25 μM ThT. (**c**) Comparison of ThT-active PrP aggregates from solution-seeded aggregates incubated for 20 hr. The seeded aggregation was carried out with 1 μM monomer + 0.35% soluble seeds at 37 °C with 200 rpm. For TEM imaging, the protein assembles were fixed in carbon-coated copper grids and negatively stained with 2% (v/v) uranyl acetate. The scale bars represent 100 nm in **a** and 2 μm in **b** and **c**.

the rate constants, k_e and k_f, as well as subcellular PrP^C concentration (m) at the cellular location where PrP^C-PrP^{Sc} conversion takes place. Since this conversion site in cells is still debated[298–300,317], it is assumed that PrP aggregation occurs at the plasma membrane and the corresponding local PrP^C concentration is 60 nM (see Chapter 2.8.4 for details). Using the rate constants obtained from the solution-seeded reaction with soluble seeds, t_2 was estimated to be 2.2 hr for PrP assembly propagation on the plasma membrane. In comparison, if PrP aggregation is assumed to take place in the endosomal compartments, where the local PrP^C concentration is 15 nM, the estimated t_2 would slightly increase to 4.4 hr, showing that t_2 is not very sensitive to the monomer concentration (Table 3.1).

Protein	k_e ($M^{-1}s^{-1}$)	k_f (s^{-1})	$k_e k_f$ ($M^{-1}s^{-2}$)	m (nM)	t_2 (hr)	PK-sen→res conversion half-time
Soluble seeded PrP	~10^4 #	~10^{-6} #	0.06 ± 0.03	60 (PM) 15 (EC)	2.2 ± 1.1 4.4 ± 2.2	< 0.25 hr

Table 3.1 | Kinetic parameters for PrP aggregation in solution. k_e, elongation rate constant; k_f, fragmentation rate constant; m, local concentration of monomers in cells; t_2, doubling time required for a single protein aggregate to replicates into two aggregates during aggregation. PM, plasma membrane; EC, endosomal compartments. The errors represent uncertainties of the fitting parameters given the dataset.

Estimate is within the same order of magnitude

3.3 PrP fragmentation and elongation are directly observed from surface-seeded aggregation

Next, to study the fragmentation kinetics of PrP, surface-seeded aggregation reactions were performed under the same native conditions as above, which allowed continual measurements of fixed fields of view on a coverslip surface. Experiments were achieved by adsorbing either the soluble or insoluble seed onto a glass coverslip, removing the residual solution, followed by the addition of PrP monomers into the reaction mix. Changes in the morphology and the size of individual PrP aggregates were visualised over time by continual imaging of the same fields of view on a microscope stage at 37 °C (Figure 3.1b, right). There were more than 10000 aggregates measured from the surface-seeded reaction using the soluble or insoluble seed, respectively. Interestingly, 8.7% (soluble) and 4.4% (insoluble) of the PrP aggregates were observed to grow into longer fibrils (Figure 3.8a, upper two panels), while the majority of the existing PrP seeds showed no detectable change in length. Consistent with the observation of an increase in aggregate length, the ThT intensity of individual aggregates increased with length both in soluble and insoluble seeding cases (Figure 3.8c and d). The slower increase in the average length for insoluble seeds compared to soluble seeds could be due to structural differences of the seeds and thus growing into fibrils at different replication rates (Figure 3.8b).

Strikingly, fragmentation of PrP fibrils was directly observed that involved one fibrillar assembly break into two or more smaller-sized fragments. These fragments were shown to be capable of growing into longer fibrils at later times (Figure 3.8a, lower two panels). The fragmentation events account for only 0.4% (soluble) and 0.9% (insoluble) of the total events recorded for each type of seed. In addition, a fraction of the fragmented species disappeared during the aggregation reaction, which suggested that these small-sized assemblies were not detected by ThT. This is in agreement with the finding from solution-seeded experiments (Figure 3.6b and c) and TEM imaging (Figure 3.7) that PrP aggregates can fragment into ThT-inactive species. Centrifugation experiments demonstrated that fluorescence imaging with ThT was able to detect PrP aggregates of 12-mers or larger (Figure 3.9), which suggested the ThT-inactive species were smaller in size.

Although a similar real-time imaging approach has previously been used to follow fibril formation of β2-microglobulin[318] and Aβ[319], the molecular mechanism was not discussed or quantified despite the importance of understanding prion propagation. To measure the

kinetic rate constants for PrP aggregation on a surface, the average rate of increase of fibril length was fitted as a function of time (Figure 3.8b). The fragmentation rate constants were estimated as $k_{f\,(soluble)} \geq 5\times10^{-9}$ s^{-1} and $k_{f\,(insoluble)} \geq 1.6\times10^{-8}$ s^{-1} for soluble and insoluble seeding, respectively. In contrast, the elongation rate constants were estimated as $k_{e\,(soluble)} = 3.39\times10^{4}$ M^{-1}s^{-1} and $k_{e\,(insoluble)} = 1\times10^{4}$ M^{-1}s^{-1} (Table 3.2). The different rate constants for the soluble and insoluble seed is likely to result from the different structures. It should be noted that the sign '≥' was used for k_f values because of

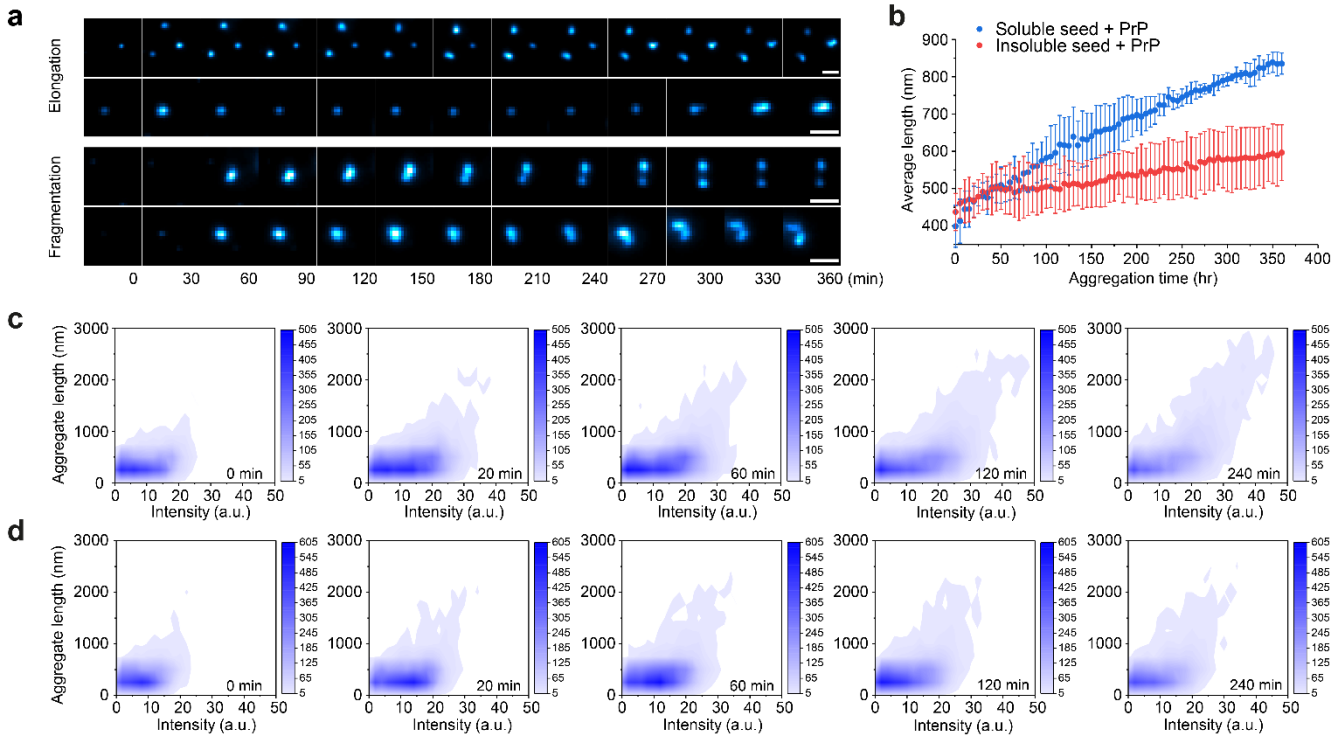

Figure 3.8 | Direct measurement of PrP fibril elongation and fragmentation. (**a**) The representative examples of PrP elongation (upper panels) and PrP fragmentation (lower panels) were recorded over a 6 hr period during surface-seeded aggregation with soluble seeds in 50 mM sodium phosphate (pH 7.0) at 37 °C. Individual particles were tracked over time by imaging with fixed fields of view every 5 minutes. The scale bars represent 2 μm. (**b**) Time-dependent change on average PrP assembly length for soluble- and insoluble-seeded aggregation. The error bars represent standard deviations from three independent experiments with different batches of protein samples. Correlation between intensity and length at different times during surface-seeded aggregation with (**c**) soluble or (**d**) insoluble seeds. Combined data of three independent measurements from different protein samples are shown. The obtained data were used to estimate the fragmentation and elongation rate constants (k_f and k_e), respectively. The $k_e k_f$ was $\geq1.5\times10^{-5}$ M^{-1}s^{-2} for PrP replication induced by soluble seeds and $\geq1.6\times10^{-5}$ M^{-1}s^{-2} when induced by insoluble seeds, respectively.

potential under-estimation, as there may be fragmentation events that were unable to be detected as shown in Figure 3.7. The product of k_e and k_f for the soluble seed was also observed to be $\geq$0.00017 $M^{-1}s^{-2}$ in surface-seeded reaction, which is slower than 0.06 $M^{-1}s^{-2}$ in bulk solution-seeded reaction by two orders of magnitude. This may reflect differences between aggregation in solution and on the surface, but may also be due to the under estimation of k_f obtained in the surface-seeded experiments, resulting in a lower $k_e k_f$. However, the slower surface-seeded reaction allowed the direct observation of fragmentation and the measurements in changes in PK resistance in the next section.

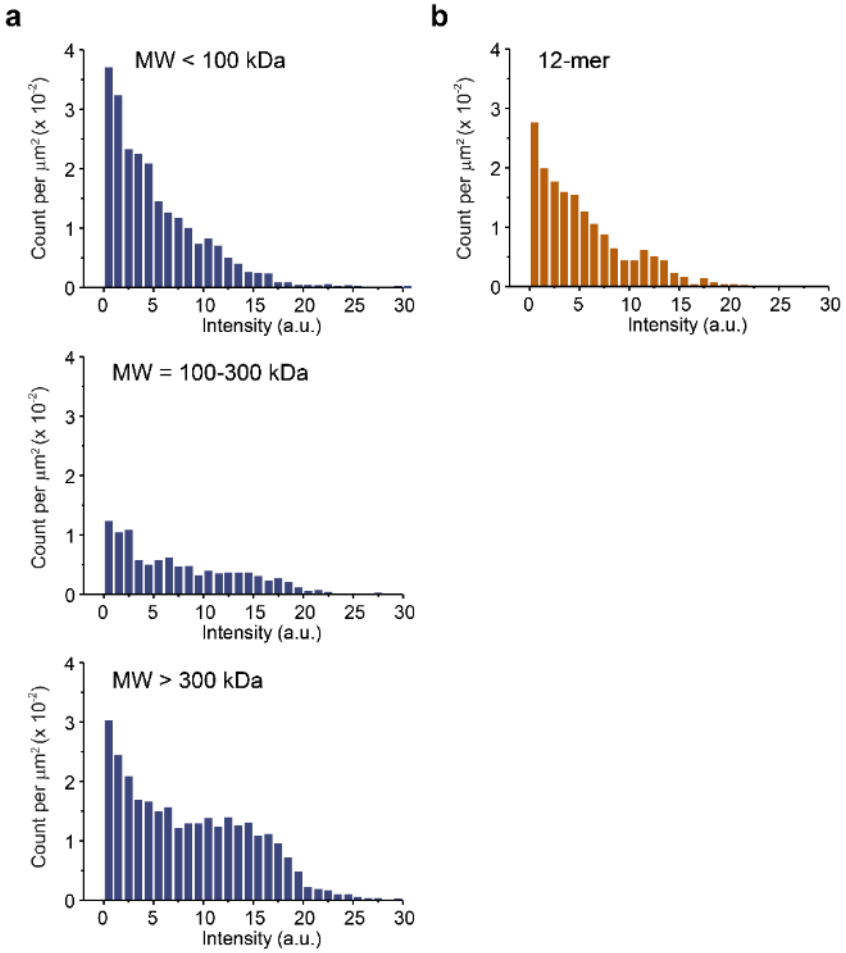

Figure 3.9 | Probing the size of PrP aggregates using TIRF imaging with ThT. (**a**) PrP that aggregated after 48 hr was separated sequentially by centrifugal filtration with 300 and 100 kDa cut-off and then subjected for TIRF imaging in the presence of 25 µM ThT. A significant increase is shown in the high-intensity range (>10 a.u.) for the species larger than 300 kDa. (**b**) The oligomeric species of 12-mer (~280 kDa), which is a known stable low-MW species, dominates in the lower intensity range as the filtered species smaller than 300 kDa. The oligomer was obtained by denaturation and reduction of the disulphide bond in PrP and then refolded by exchanging buffer as reported by Trevitt *et al*[295].

Seed type	k_e ($M^{-1}s^{-1}$)	k_f (s^{-1}) *	$k_e k_f$ ($M^{-1}s^{-2}$) *	*PK-sen → PK-res conversion half-time*
Soluble seeded PrP	$3.39 \pm 0.04 \times 10^4$	$\geq 5\times10^{-9}$	≥ 0.00017	0.25 hr
Insoluble seeded PrP	1×10^4	$\geq 1.6\times10^{-8}$	≥ 0.00016	

Table 3.2 | Kinetic parameters for surface-seeded PrP. k_e, elongation rate constant; k_f, fragmentation rate constant. The errors represent uncertainties of the fitting parameters given the dataset.

* Measured as the slowest value.

3.4 PrP aggregates undergo structural conversion from PK-sensitive to PK-resistant conformations

To assess the susceptibility of PrP aggregates to proteinase K (PK) digestion, proteolytic digestion was carried out at the single-aggregate level during surface-seeded aggregation with soluble seeds (Figure 3.10). This was achieved by the addition of PK at defined time points during the seeded aggregation reaction and subsequent measurement of the decrease of ThT intensity of individual PrP assemblies induced by proteolytic digestion.

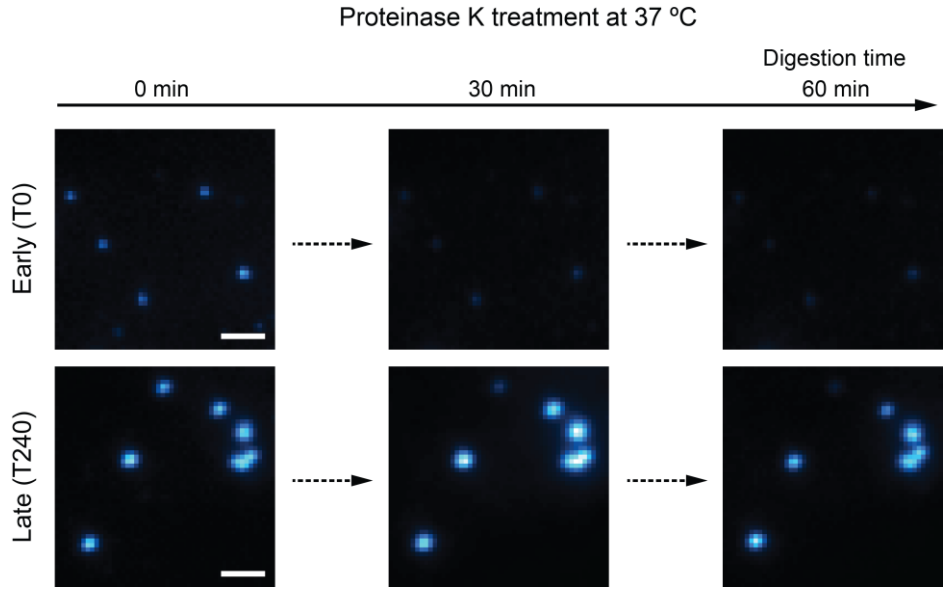

Figure 3.10 | Schematic description of single-molecule proteinase K (PK) digestion. PK digestion is combined with the surface-seeded measurements (Figure 3.1b, right) by applying a constant concentration of PK (2 μM for 300 nM PrP aggregates and 0.1 μM for 300 nM αS aggregates) into the aggregation mixture at defined time points. Sealed glass coverslips with surface-seeded aggregates were taken out from the incubator, unsealed, mixed with PK, re-sealed, and then loaded back onto the microscope stage with an incubator chamber at 37 °C. Proteolytic digestion of individual aggregates was followed over time in a single 3×3 image grid with fixed fields of view (i.e. 9 simultaneous images). In the upper panel, the majority of early PrP assemblies aggregated for 0 min are sensitive to PK and thus disappeared after 1-hour digestion. In contrast in the lower panel, a larger number of late PrP assemblies aggregated for 240 min shows increased resistance to PK and remained a high fraction compared to their initial intensity after 1-hour digestion. The scale bars represent 2 μm.

Initially, the soluble seeds were predominantly PK-sensitive (PK-sen), as very few PrP assemblies remained detectable after 1 hr digestion with PK. With increasing time, more aggregates maintained high ThT intensity after PK digestion (Figure 3.11). This suggested that accumulation of PK-resistant species (PK-res) occurred during PrP aggregation. Furthermore, compared to PK-sen species, the PK-res species possessed higher initial T intensity before PK digestion, which indicated these assemblies were also larger in size since the length-intensity relationship was demonstrated to be linear (Figure 3.12).

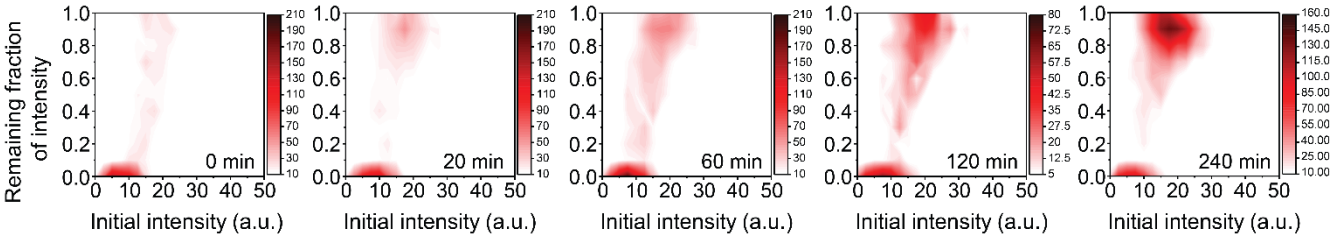

Figure 3.11 | PK resistance of PrP aggregates during surface-seeded aggregation. PK was added at different times to the glass surface that contained the PrP aggregates and slide chamber sealed to prevent fluid evaporation. The change in ThT intensity of individual aggregates was followed by continual imaging with fixed fields of view at 37 °C incubation. PK resistance was calculated as the fraction of the ThT intensity after 1 hr proteolytic digestion compared to that seen at the start of the experiment. Combined data of three independent measurements with different batches of protein samples are shown.

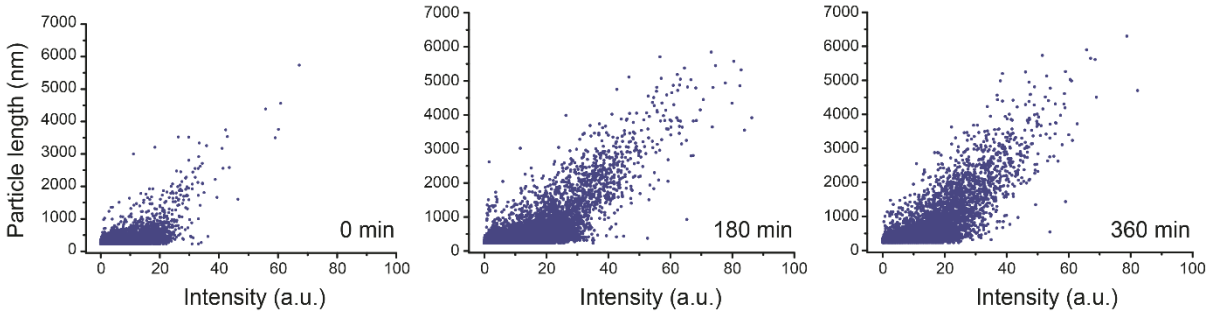

Figure 3.12 | Analysis to the length-intensity relationship of PrP aggregates in surface-seeded aggregation with soluble seeds. The scatter plots reveal that the length of the PrP aggregates follows a linear relationship against their ThT intensity over time. Hence, the intensity can be used for probing different sizes of PrP populations as shown in Figure 3.9.

Next, the fractions of the PK-sen and PK-res species were quantified with 2D Gaussian functions, and hence the kinetic profiles were acquired as shown in Figure 3.13. The number of PK-res aggregates showed a fast increase and reached a maximum level after 1 hr aggregation. This suggested a fast PK-sen → PK-res conversion reaction occurred with a half-time of ~0.25 hr (Table 3.2). As the replication rate of PrP was slower on the surface due to lower $k_e k_f$, this conversion rate on the surface was likely to be slower than that in bulk solution, which is expected to be <0.25 hr.

It is noted that solution deoxygenation was required for continual imaging. In surface-seeded aggregation and subsequent PK digestion, the reaction was found to be substantially inhibited by the presence of aerobic oxygen dissolved in solution (Figure 3.14). The inhibition effect was likely due to photo-oxygenation of amyloid proteins, which involves the covalent linkage of hydrophilic oxygen atoms to cross-β-sheet structure on residues upon protein surface[320,321]. This reaction was potentially catalysed

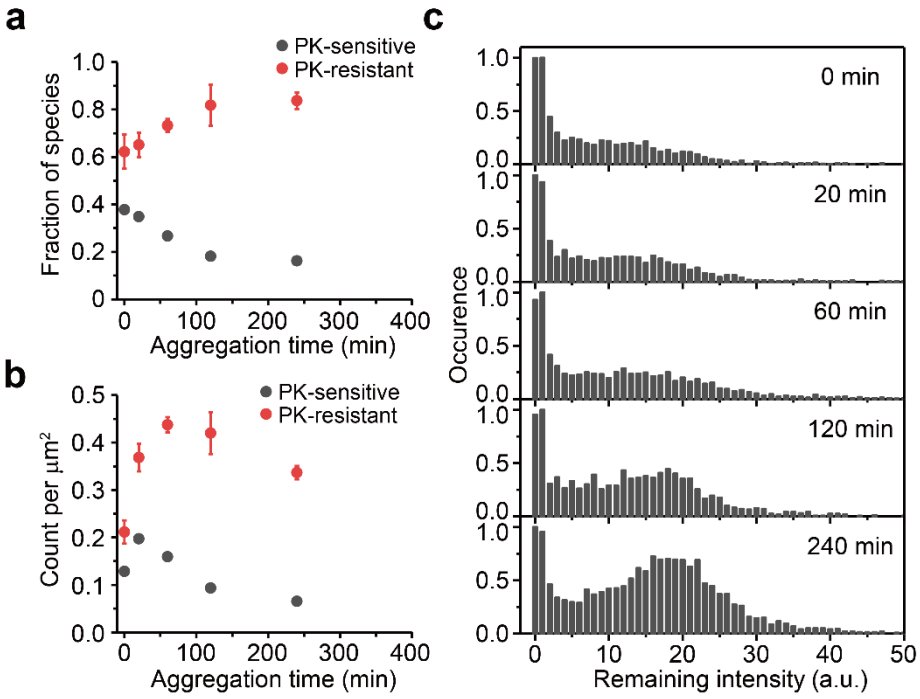

Figure 3.13 | Structural conversion of PrP aggregates. Temporal change in (**a**) the fraction and (**b**) the number of PK-sen and PK-res species of surface-seeded PrP aggregates using soluble seeds. The dataset from Figure 3.11 was globally fitted to 2D-Gaussian functions to obtain the fraction of PK-sen and PK-res populations. (**c**) Intensity distributions after PK-digestion for surface-seeded PrP aggregates at different time points. The error bars represent standard deviations from three independent experiments with different batches of protein samples.

by long-term exposure of high-powered laser source. To evacuate the oxygen from solutions, the deoxygenation efficiency of two common methods, vacuum degassing[322–324] and an enzymatic scavenging system (glucose oxidase in combination with catalase, GOC)[325–327], was estimated before PK digestion assay. From the results, both methods showed substantially increased rates during 1 hr proteolytic digestion with PK after removal of dissolved oxygen molecules in the reaction buffer, which suggested high efficiency of deoxygenation (Figure 3.14). As the glucose oxidase/catalase was likely to contribute false positive ThT signals and thus interfere image processing, the physical method of pump degassing was adopted throughout the continual measurements in this study.

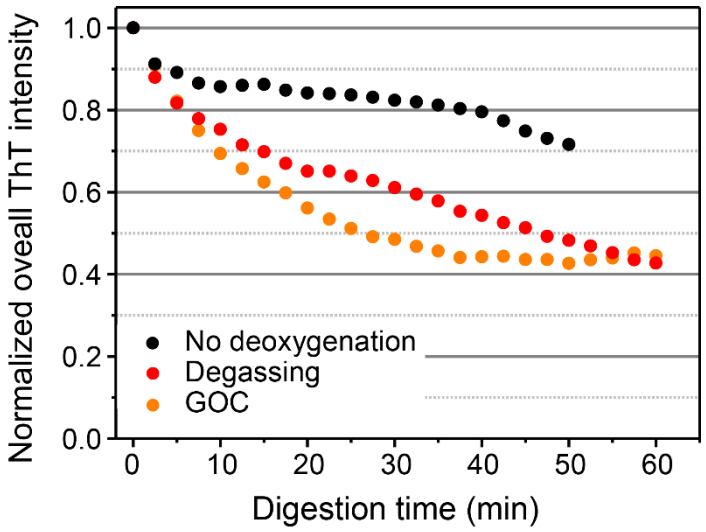

Figure 3.14 | Deoxygenation effect to PK digestion. Pump degassing and an enzymatic scavenging system (glucose oxidase in combination with catalase, GOC), were used for assessing the oxygen removal efficiency in solution. For pump degassing, four repeats of 1-minute vacuum cycle were applied in the buffer and ThT solutions, while in the GOC system, 7.5 U/mL of the oxidase and 1 kU/mL of catalase were directly added in the reaction mix. The changes in overall ThT intensity from PK-digested PrP aggregates (enzyme/PrP aggregate concentrations are 2 and 0.3 μM, individually) were followed by continual imaging with fixed fields of view at 37 °C incubation.

3.5 PrP fibril fragmentation is length-dependent and accompanied by loss of PK resistance

The fragmentation rate constant, k_f, in the nucleation-elongation-fragmentation kinetic model was defined per monomer in an aggregated assembly. A fibril may potentially fragment at random positions along its fibrillar axis, and hence the rate of fragmentation would be expected to increase with fibril length (i.e. a 1000-mer fibril is expected to have a fragmentation rate higher than the k_f value by 1000-fold). Since very few studies have demonstrated the molecular details of fibril fragmentation, I measured this process on the coverslip surface to probe the length-dependence. Fragmentation of individual PrP fibrils was followed continually over 72 hr in the fixed fields of view, and the decrease in the average fibril length (i.e. fragmentation) measured. A higher fragmentation rate was revealed with increasing fibril length (Figure 3.15). The kinetic profiles were in good agreement with the PrP fibril fragmentation fits based on the kinetic model, which suggested that the fragmentation rate of a fibril is proportional to its fibril length, and that our previous assumption was justified, where the fragmentation rate of a fibril is proportional to its length.

Next, the susceptibility of fragmented PrP fibrils to PK digestion was examined at defined time points (Figure 3.15c). Surprisingly, PrP fibrils rapidly lost resistance to PK despite the number of PK-sen aggregates remaining approximately constant (Figure 3.15b). The PK-res species which have a peak intensity at 10 a.u. became PK-sen, while the less intense PK-sen species that peaked at 5 a.u. disappeared, presumably due to fragmentation into smaller species that were not ThT-active. This suggested that the PK-sen aggregates at later times are more likely to be generated from the initially PK-res fibrils by a structural conversion.

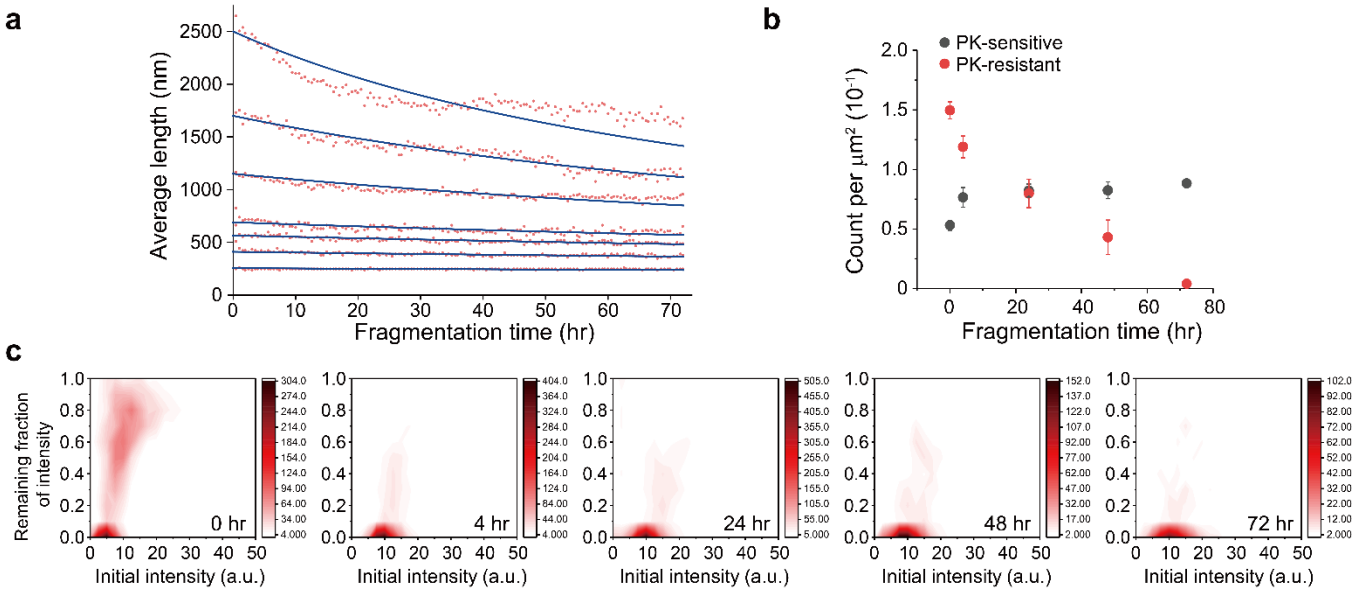

Figure 3.15 | PrP fibril fragmentation. (**a**) Time-dependent change on average PrP fibril length. The data shown correspond to the average of three independent experiments with different batches of protein samples. (**b**) Proteinase K (PK) resistance of PrP aggregates during surface-seeded aggregation. PK was added at different times to the glass surface that contained the PrP aggregates and slide chamber sealed to prevent fluid evaporation. The change in ThT intensity of individual particles was followed by continual imaging with the fixed fields of view at 37 °C incubation. PK resistance was calculated as the fraction of the ThT intensity after 1 hr proteolytic digestion compared to that seen at the start of the experiment. The error bars represent standard deviations from three independent experiments. (**c**) Temporal change in the fraction and the number of PK-sen and PK-res species of PrP fragments as a function of time. The dataset from (**b**) was globally fitted to 2D-Gaussian functions to obtain the fraction of PK-sen and PK-res populations as a function of time.

3.6 Estimation for PrP spreading in the brain from a kinetic approach

It has been demonstrated that the growth rate of different strains in yeast prion Sup35 can be predicted by a simple model which takes into account monomer concentration, the rate of cell division, and the elongation and fragmentation rates of different strains[184]. With a similar model, the spreading of tau replication in the brain was previously estimated using experimentally measured kinetic parameters, showing that tau accumulation in the brain is likely to follow an exponential behaviour resulting from fragmentation[192]. Here, I tested this spreading model with PrP using the kinetic parameters acquired in Table 3.1.

Sustainable spreading of protein aggregates in the cells involves both effective seeding and amplification[191]. In this scenario, a single PrP aggregate in a cell can grow and then fragment into two smaller assemblies. The two assemblies thus act as new templates and are able to enter neighbouring cells in order to support sustained spreading. Therefore, the accumulated number of PrP aggregates is exponential and given by:

$$f(n) = f_0 \cdot 2^n \qquad \text{(Eq. 3.2)}$$

where f_0 is the initial number of aggregates and n is the round of doubling required to reach a final number of aggregates $f(n)$. Based on the rounds of doubling (n) and doubling time (t_2) in Equation 1, one can calculate the hypothetical spreading time ($T_{spreading}$) required to obtain a certain number of aggregates in the brain:

$$T_{spreading} = n \cdot t_2 \qquad \text{(Eq. 3.3)}$$

Next, I determined how fast PrP aggregates would hypothetically spread in the mouse brain based on the kinetic parameters measured when a single aggregate is effectively seeded on the plasma membrane. According to the equations, the accumulation of PrP aggregates was plotted as a function of time and then calculated $T_{spreading}$ (Figure 3.15).

In a typical mouse brain, there are approximately 70 million neurons. To obtain one PrP

aggregate in every neuron on average, it would take 2.4 days for a wild-type *Prnp*$^{+/+}$ mouse through the exponential replication. For a Prnp$^{+/-}$ mouse (~0.5x PrP expression level) and a tg20 mouse (~8x PrP expression level), it would take 3.4 and 0.8 days, respectively (Table 3.3). As discussed in Chapter 3.2, PrP levels at different conversion sites only have a mild effect to t_2, and hence does not alter $T_{spreading}$ to a greater extent. The hypothetical calculation of PrP spreading agrees with the experimental incubation periods observed in mice models within two orders of magnitude. The experimentally determined incubation periods are 137 ± 1.5, 258 ± 24, and 59.5 ± 2 days for *Prnp*$^{+/+}$, *Prnp*$^{+/-}$, and tg20 mice, respectively[244]. Importantly, the relative ratios of $T_{spreading}$ between the three mouse strains (*Prnp*$^{+/-}$, *Prnp*$^{+/+}$, tg20) predicted from the model are very similar to those from animal experiments.

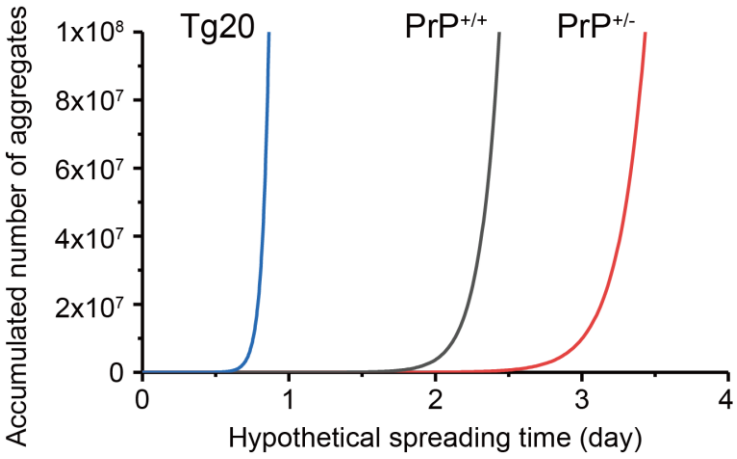

Figure 3.16 | Hypothetical spreading for PrP in the brain. The simulated kinetic profiles are based on the exponential replication mechanism and the kinetic parameters measured in Table 3.1.

PrP strain	t_2	f_0	f	n	Hypothetical $T_{spreading}$
PrP$^{+/-}$ mouse	3.1 hr				3.4 day
PrP$^{+/+}$ mouse	2.2 hr	1	7×10^7	26	2.4 day
Tg20 mouse	0.78 hr				0.8 day

Table 3.3 | Hypothetical spreading time ($T_{spreading}$) for PrP in the mouse brain. t_2: doubling time; f_0: initial number of aggregates; f: accumulated number of aggregates at t=$T_{spreading}$; n: round of doubling for PrP replication; $T_{spreading}$: time required to obtain one aggregate in every neuron on average.

3.7 Summary of the chapter

In this chapter, the elongation and fragmentation of murine PrP have been directly observed. Despite the fact that fragmentation has been proposed to be an important factor for sustained replication in protein aggregation, this is the first time that this mechanism has been directly confirmed. The results show that amplification of the number of PrP aggregates occurs by an elongation/fragmentation mechanism. Surface-seeded experiments reveal fibril fragmentation is proportional to fibril length, which suggested that larger-sized fibrils are more likely to break and thus produce new templates for further replication.

It was also observed that during the aggregation process PrP undergoes structural conversion from a PK-sen to PK-res conformer. This is consistent with previous studies in mice, where PK-res and PK-sen species accumulated during prion propagation[244,328]. However, in the current experiments, it was found that during fragmentation PrP fibrils rapidly lose PK resistance, possibly due to destabilisation of the fibrillar structure. This finding would argue that reversion of PK resistance occurs when the fibrillar structure becomes fragile. Despite the fragility of fibril fragments, they are able to form new fibrils as directly observed on the surface and regain resistance to PK. The observations partly explain the production of disease-related PK-sen species observed *in vivo*[244,246,329–331]. Fragmentation of large PrP fibrils at later times is likely to produce more PK-sen segments and thus exceed the formation of new PK-resistant fibrils, which may partly explain the finding that the PK-sen species may constitute the majority of the total disease-related PrP in some prion strains of mice[244,246] and in sCJD patients[248].

Through determination of the rate constants of k_e and k_f, one is able to calculate the t_2 for PrP replication at the physiological protein concentration in cells, and hence establish a simple spreading model based on these kinetic measurements. PrP aggregation shows fast elongation/fragmentation and results in an estimated t_2 of 2.2 hr if the aggregation occurs on the plasma membrane (Table 3.1), leading to spreading in a few days based on the hypothetical calculation of the mouse brain. The discrepancy between the theoretical estimation and the experimental data *in vivo* can be explained by several cellular mechanisms that were not considered in the spreading model. These include organelle confinement, the presence of membranes, and active clearance and degradation mechanisms. Furthermore, PrP glycoform ratio, especially the sialyation level, was demonstrated to affect the rate of PrP^{Sc} accumulation in PMCA[68,69]. A decrease in PrP^{C} sialylation levels resulted in a higher proportion of the diglycosylated form of PrP^{Sc} that is faster accumulated in PMCA by 10-10000 fold. Although these determinants were not

included in the calculations above, they would ultimately decelerate PrP spreading *in vivo* by either reducing the replication efficiency or increasing t_2.

Chapter 4 | Biophysical characterisation of PrP at the early aggregation stage

4.1 Introduction

In prion pathogenesis, it is increasingly recognised that there are multiple disease-related PrP conformers, such as proteinase K (PK)-sensitive species[244,246,329–331]. In particular, small soluble oligomeric intermediates, instead of the end product of amyloid fibrils, have been shown to be the most efficient mediators of infectivity[200,242] and exert higher cytotoxicity than mature fibrils both *in vitro* and *in vivo*[242]. The oligomeric aggregates have also been suggested to play key roles in other neurodegenerative diseases from various ensemble approaches[196,332–336]. It is fundamentally important to acquire detailed information on the formation, structure, and toxicity of these oligomers starting first with the oligomers formed *in vitro*. However, the studies in oligomers have raised a problem that is extremely challenging in investigating early events in protein aggregation, as these oligomeric species are transient and heterogeneous by nature. A recent study in yeast prion Ure2 has overcome the problem of structural heterogeneity with a single-molecule approach, identifying two structurally distinct oligomeric species before mature fibrils formed and establishing a temporal relationship between the oligomeric and mature fibrillar species[178]. In the particular case of mammalian PrP, prion infectivity and neurotoxicity have been proposed to be uncoupled[99,244,245] and to be different species appearing in two distinct kinetic phases by Sandberg *et al* [244,245], while the neurotoxic species in Phase 2 are still undefined. The proportional contribution of PK-sensitive disease-related conformers and PK-resistant PrP^{Sc} also remains unclear.

Given the structural heterogeneity of oligomers and the lack of physical studies at the early stage of PrP aggregation, I have studied the structural changes of the oligomeric species formed by recombinant mouse PrP as a function of time in this chapter. This characterisation has focused on molecular events before the exponential growth phase in bulk solution kinetics using a set of biophysical methods, including 1) TIRF imaging, 2) sPAINT imaging[284], 3) a single-vesicle calcium influx assay for probing membrane permeability[308], and 4) a single-aggregate PK resistance assay. These approaches have enabled observation of a range of different oligomeric species during early PrP aggregation. Furthermore, a kinetic scheme for PrP aggregation is established to provide insights into the key molecular mechanisms that lead to the formation of oligomers and identifies a key structural conversion process for PrP aggregation.

4.2 Single-aggregate imaging reveals the formation of small aggregates in early PrP aggregation

Mouse PrP aggregation was performed at 37 °C with 200 rpm under partially denaturing conditions of 2 M GdnHCl that facilitate fibril formation *in vitro*. With the use of the single-aggregate imaging based on TIRF microscopy[276], the aggregation reaction was followed over time by taking aliquots at different time points and then visualised in the presence of 25 μM ThT (Figure 3.2). At early aggregation time (t <8 hr), the overall intensity and the number of PrP aggregates were observed to gradually increase depending on initial protein concentrations (Figure 4.1a and b), and they were found to increase at different rates as discussed more in Chapter 4.6. Only small-sized aggregates were detected at early times, and fibrils were not detected until 24 hr. It is consistent with previously measured kinetics in bulk solution at the same condition[292], where the lag time was 10-15 hr and the plateau was reached after 30-35 hr.

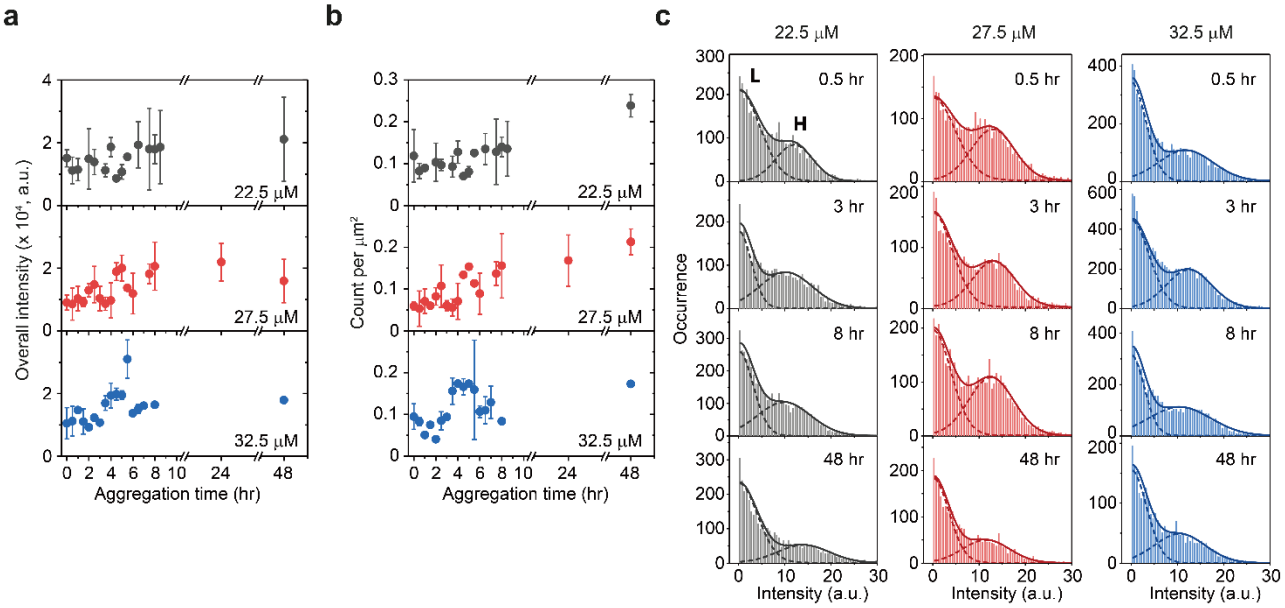

Figure 4.1 | Single-aggregate measurements of PrP aggregates at the early aggregation stage. (**a**) Overall ThT intensity and (**b**) number of PrP aggregates over time. The measurements were carried out from three independent experiments by taking aliquots at various time points from the aggregation reaction mix that was incubated at 37 °C with shaking at 200 rpm. The error bars represent standard deviations from three independent experiments. (**c**) Intensity histograms of ThT-active PrP aggregates at different time points. The PrP aggregates were split into two apparent ThT intensity groups: low-intensity (L species) and high-intensity (H species). Illustrative fits of the individual PrP species (dash) to Gaussian functions and their accumulative fits (solid) are shown. The traces correspond to three independent experiments with different batches of protein samples.

4.3 Early-formed PrP aggregates are structurally diverse oligomers by sPAINT imaging.

It has previously been shown that in sPAINT imaging, the fluorescence spectral shift of Nile red (NR) dye, which non-specifically and transiently binds to protein aggregates, allows super-resolution and measurement of relative surface hydrophobicity of individual protein aggregates[284]. In addition, combining with dual imaging with ThT dyes, the ThT-inactive aggregates can also be identified and thus provide more structural information compared with conventional ThT fluorescence measurements. To gain more structural insights at the early aggregation stage of PrP, sPaint was applied to visualise the morphology of PrP aggregates with spatial resolution of 40 nm, as well as to characterise the temporal change in surface hydrophobicity. With the help from Dr Ji-Eun Lee at the Department of Chemistry, Cambridge, an aliquot of PrP aggregates were collected from the same reaction mix at different time points, diluted to 0.1 μM of the

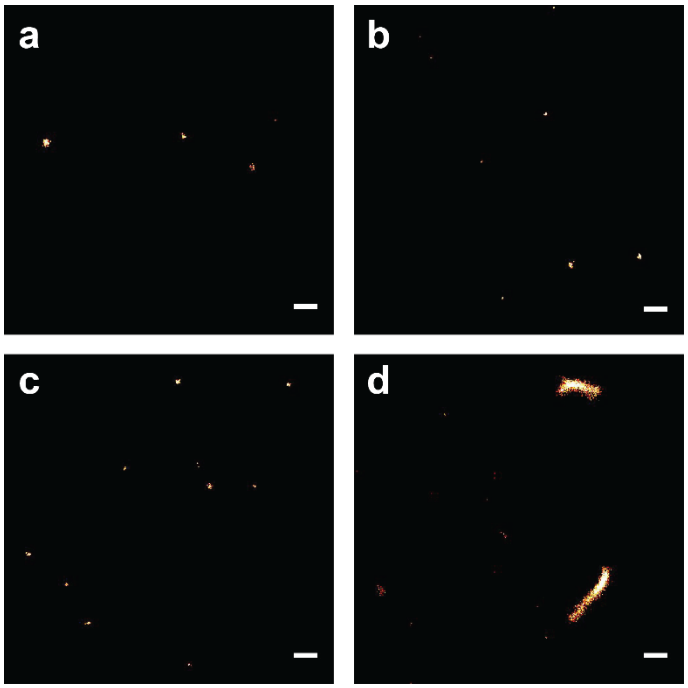

Figure 4.2 | Super-resolved sPAINT images of PrP aggregates with Nile red (NR) at different time stages. The morphology of PrP aggregates at (**a**) 0.5 hr, (**b**) 3 hr, (**c**) 8 hr, and (**d**) 48 hr are revealed. Monomeric PrP was incubated in a 1.5-mL microcentrifugal tube with 2 M GdnHCl at 37 °C with 250 rpm. At various time points, aliquots were removed from the reaction mix and adsorbed onto a glass coverslip for sPAINT imaging. The scale bars represent 500 nm.

equivalent monomer concentration, and then visualised with sPAINT imaging (Figure 4.2).

At early times, only small-sized oligomers were found in the super-resolved images, which is consistent with the TIRF data. Note that the oligow2mers in this study are defined as being smaller than 40 nm from the super-resolved images. The results in Figure 4.3c showed that ThT-inactive species were formed and only constituted a small fraction of all oligomeric aggregates over time. Based on the shift of median wavelengths of NR fluorescence (Figure 4.3a and b), the surface structure of ThT-inactive species was more hydrophobic compared to ThT-active species. The increase in surface hydrophobicity with time suggested that structural reorganization of ThT-inactive species takes place in early PrP aggregation (Figure 4.3d). In contrast, the dominant ThT-active aggregates showed no clear changes in hydrophobicity with time.

The patterns of surface hydrophobicity for ThT-inactive and ThT-active oligomers were more clearly distinguished by accumulating the plots over 0.5, 3, and 8 hr (Figure 4.4). ThT-inactive and ThT-active oligomers showed distinct patterns of surface hydrophobicity. ThT-inactive oligomers had low numbers of NR localisation, while ThT-active oligomers had broader numbers of NR localisation, indicating a higher diversity in molecular size. Furthermore, despite the number of NR localisation is lower, the pattern for ThT-active oligomers was close to that for mature fibrils collected at 48 hr, which generally possess higher number of NR localisation and hence high molecular size. This indicates that ThT-active oligomers were structurally more similar to mature fibrils.

The total number of PrP aggregates detected in sPAINT imaging showed only small changes with time (Figure 4.3c). Consistent with TIRF data (Figure 4.1b), it suggested that only a small fraction of PrP oligomers formed at the early stage of aggregation ultimately grew into mature fibrils. The ThT intensity distributions of ThT-active species showed the presence of two populations, high-intensity (H species, peak at ~15 a.u.) and low-intensity species (L species, peak at < 1 a.u.), with different temporal behaviours (Figure 4.1c). While the number of L species remained approximately constant over time, the number of H species decreased with time. Previous experiments have shown that the H species appeared to be larger in size with molecular weights > 300 kDa (i.e. >12 PrP molecules), while the L species was < 300 kDa (Figure 3.9). It is noted that PrP fibrils are not efficiently detected in this TIRF imaging system, possibly due to the structural fragility of PrP fibrils. Despite the inefficiency in fibril detection, these experiments provide structural insights into early-formed oligomers based on ThT intensity of individual PrP aggregates and their PK resistance as discussed below.

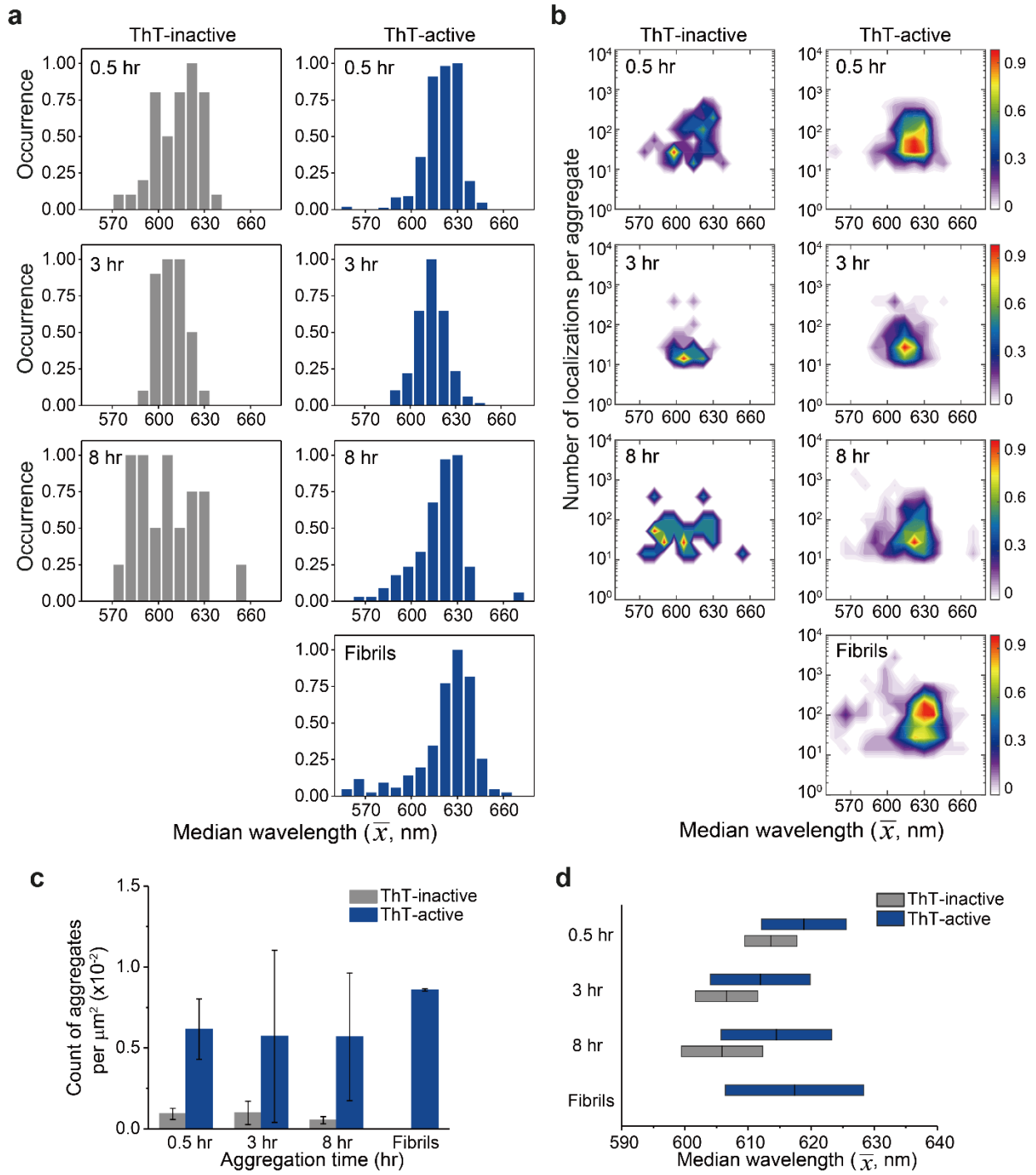

Figure 4.3 | sPAINT analysis. (**a**) Hydrophobicity distribution of ThT-inactive and -active PrP species at different time points. The median wavelength of NR fluorescence derived from all binding events to a single PrP aggregate was determined as hydrophobicity for individual aggregates. (**b**) Hydrophobicity landscapes of individual aggregates. The distributions shown correspond to the accumulation of three independent measurements with different batches of protein samples. (**c**) Number and (**d**) Median wavelength of NR fluorescence for individual aggregates as a function of time. The error bars represent mean values and standard deviations from three independent experiments with different batches of protein samples. The overall number of analysed PrP aggregates is as following. At 0.5 hr: $N_{ThT\text{-}inactive} = 44$, $N_{ThT\text{-}active} = 403$; at 3 hr: $N_{ThT\text{-}inactive} = 36$, $N_{ThT\text{-}active} = 199$; at 8 hr: $N_{ThT\text{-}inactive} = 24$, $N_{ThT\text{-}active} = 261$; for fibrils at 48 hr: $N_{ThT\text{-}active} = 341$.

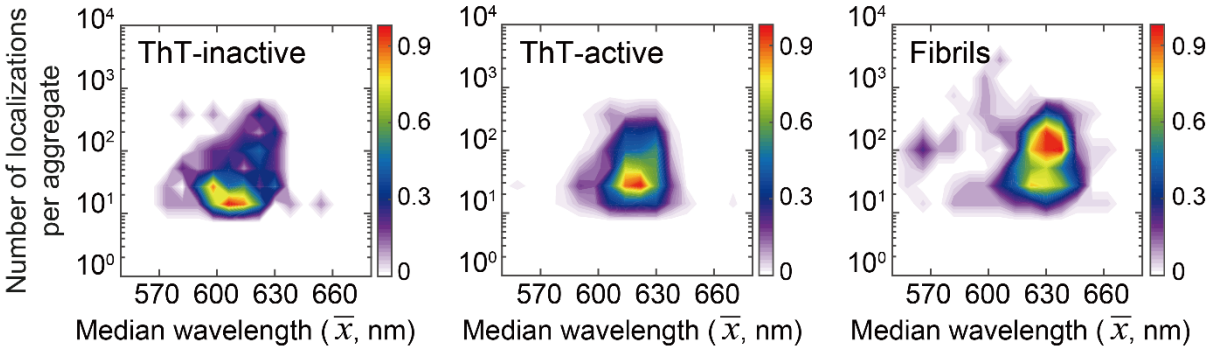

Figure 4.4 | Different aggregated species of PrP show distinct accumulated hydrophobicity distributions. Hydrophobicity distributions were accumulated over all time points in each PrP species. ThT-active oligomers share a similar pattern with mature fibrils formed after 48 hr aggregation, despite the NR localisation for fibrils are higher. In contrast, ThT-inactive oligomers possess lower median wavelength and hence more hydrophobic. The number of NR localisations of ThT-inactive oligomers is low. The overall number of analysed PrP aggregates is as following: $N_{ThT\text{-}inactive} = 103$, $N_{ThT\text{-}active} = 863$, $N_{ThT\text{-}active}$ for fibrils at 48 hr $= 341$.

4.4 PrP oligomers undergo PK-sensitive to PK-resistant structural conversion

Next, the PK susceptibility of the ThT-active PrP oligomers was examined as a function of time using TIRF microscopy. The decrease of ThT intensity of individual oligomers at defined time points was measured after 1 hr-proteolytic digestion (Figure 4.5a-c). Most of the ThT-active oligomers were PK-sensitive (PK-sen), and PK-resistant species (PK-res) developed rapidly (Figure 4.5c). The initial ThT intensity of the oligomers before PK

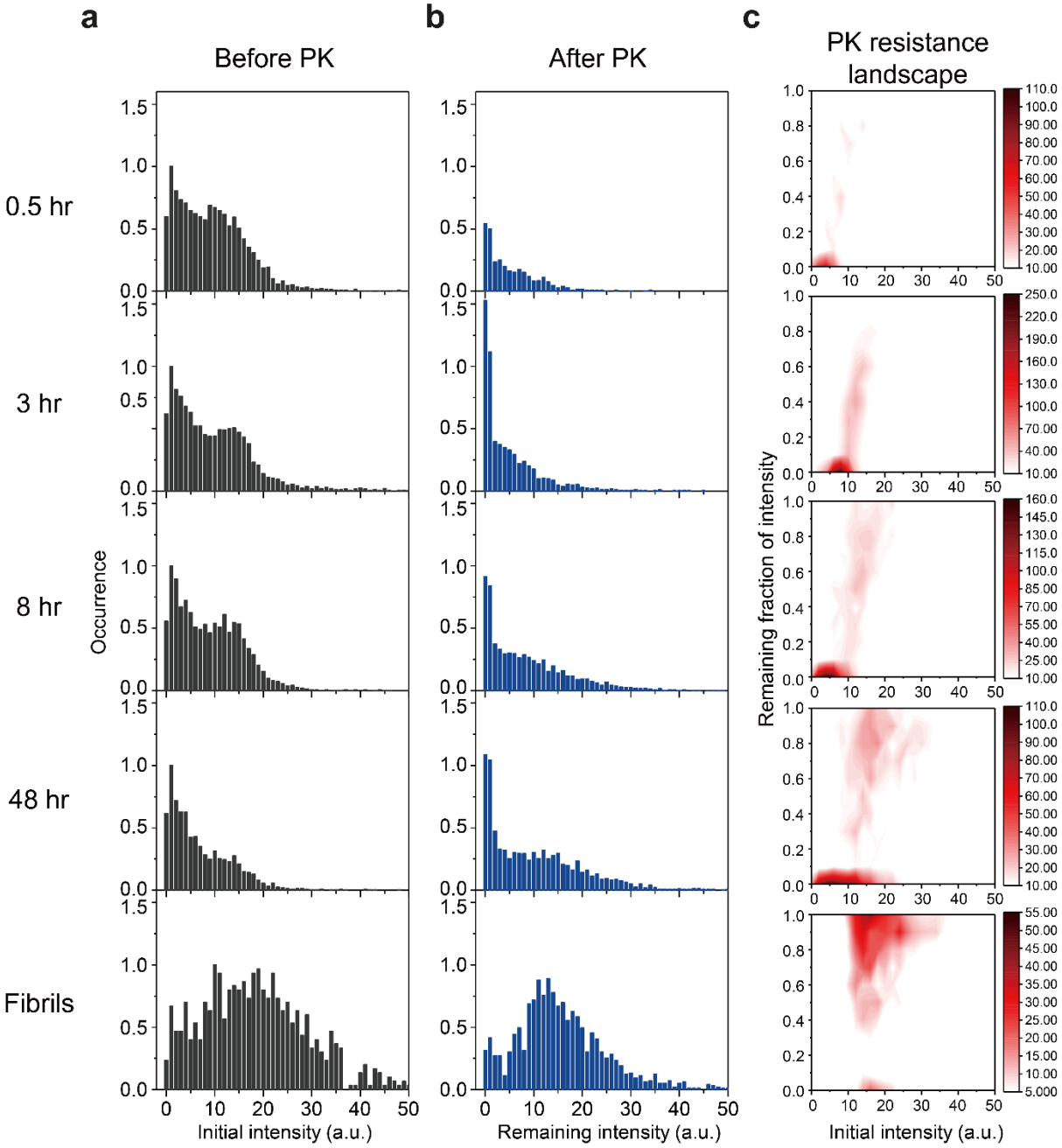

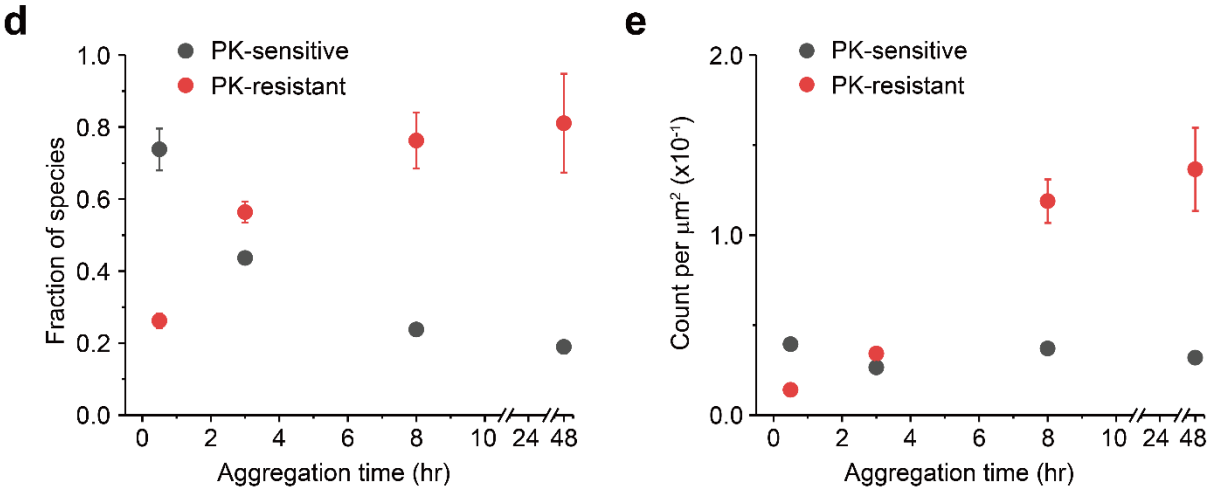

Figure 4.5 | Time-dependent increase of PK resistance during PrP aggregation. The ThT intensity distributions of PrP aggregates at different time points (**a**) before and (**b**) after PK treatment were shown. PK was added at different times to the glass surface that contained the PrP aggregates and slide chamber sealed to prevent fluid evaporation. The change in ThT intensity of individual particles was followed by continual imaging with the fixed fields of view at 37 °C incubation. PK resistance was calculated as the fraction of the ThT intensity after 1-hr proteolytic digestion compared to that seen at the start of the measurement. Note that in each set of histograms at defined time points in (**a**) and (**b**), the occurrence was set to 1 in respective of the highest bin count before PK treatment. (**c**) The PK resistance of individual aggregates against their initial intensity. The plots shown correspond to the accumulation of three independent measurements. The dataset of the PK resistance landscape plots was globally fitted to 2D-Gaussian functions to estimate the fraction of PK-sen and PK-res species. Changes in (**d**) the fraction and (**e**) the number of PK-sen and PK-res species of PrP aggregates shown as a function of time. The error bars represent standard deviations from three independent experiments with different batches of protein samples.

treatment increased over time, suggesting the molecular size of PrP oligomers increased over time, which is consistent with the TIRF and sPAINT data. Interestingly, the relationship between PK resistance and their initial ThT intensity in Figure 4.5c also suggested that the H species of PrP aggregates were comprised of both PK-sen and PK-res species. The PK resistance data was quantified by fitting to 2D-Gaussian functions at different time points and acquired the fraction and the number of the PK-sen/PK-res species (Figure 4.5d and e).

To gain more insight from the correlation between PK resistance and ThT intensity, I combined the PK resistance data (Figure 4.5d) with the ThT intensity distributions (Figure 4.1c). The PK-sen and PK-res oligomers could be further sub-classified based on their ThT intensity, either L or H. Therefore, four oligomeric species were identified: (1) PK-sen/low-intensity, (S_L); (2) PK-sen/high-intensity (S_H); (3) PK-res/low-intensity (R_L); and (4) PK-res/high-intensity (R_H). According to Figure 4.6, R_L and R_H formed later than S_L and S_H formation, and hence the production of R_L and R_H could either convert from S_L and S_H, or be nucleated directly from monomers. From the observations, R_L shares a similar ThT intensity profile with S_L (and likewise, in the R_H and S_H pair) (Figure 4.1c), and the increase of the fraction of the PK-res species was at the same rate as that of the decrease of the PK-sen species (Figure 4.5d). Therefore, it is highly likely that there was a direct structural conversion from PK-sen to PK-res conformations.

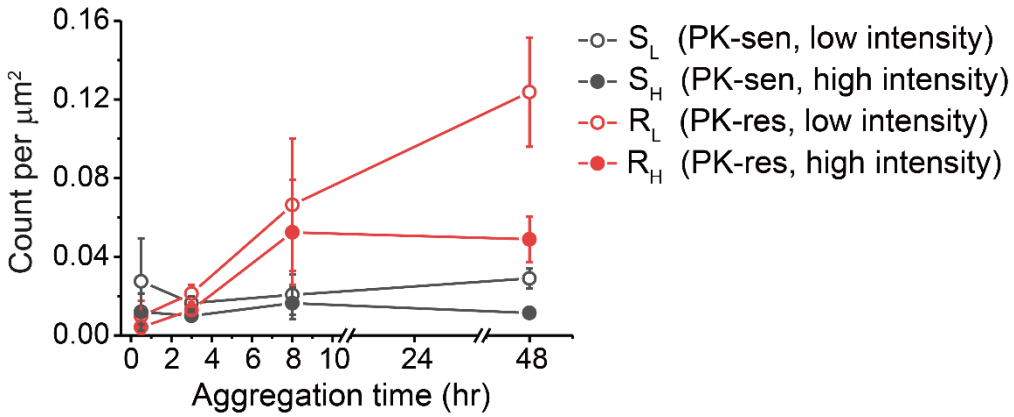

Figure 4.6 | Temporal change in the number of the four identified ThT-active PrP aggregate species. Combining the intensity histograms and their PK resistance, the PrP aggregates were characterised into four species: low-intensity PK-sensitive (L-sen), low-intensity PK-resistant (L-res), high-intensity PK-sensitive (H-sen), high-intensity PK-resistant (H-res). The error bars represent standard deviations from three independent experiments with different batches of protein samples.

4.5 PK-sensitive oligomers are more capable of disrupting the lipid membrane than fibrils

The oligomeric aggregates of PrP have been shown to confer higher toxicity compared to fibrils both *in vitro* and *in vivo* [6,7,30,181,196–200]. Despite the complexity of the origin of toxicity, non-specific membrane disruption induced by protein aggregates is suggested to cause toxicity [6,181,231–236]. This aberrant interaction is shown to partially permeabilise the lipid membrane, resulting in Ca^{2+} influx and the disruption of cellular homeostasis[6,180,181,205,234,235,238]. To study the potentially damaging effects of protein aggregates on the lipid membrane, a single-vesicle assay has recently been developed to

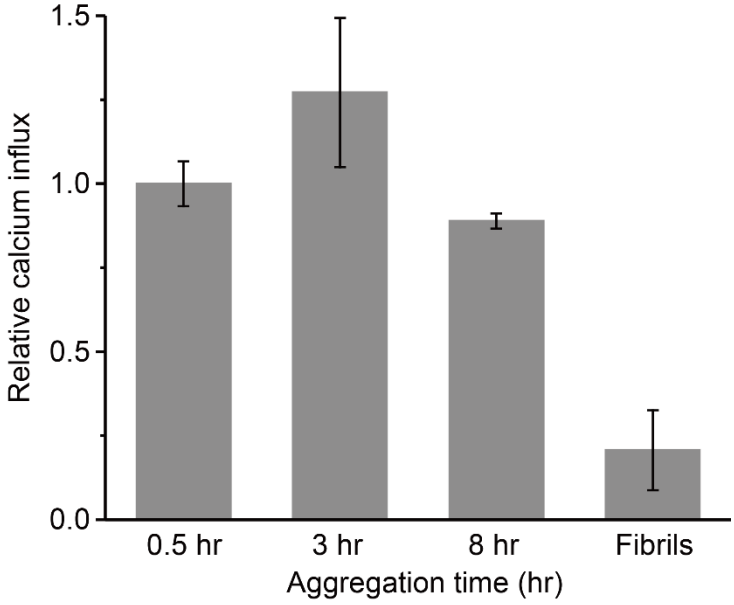

Figure 4.7 | Membrane permeability per PrP aggregate as a function of time. Monomeric PrP was aggregated at a concentration of 27.5 μM in the presence of 2 M GdnHCl at 37 °C with shaking at 200 rpm. At each time point, an aliquot was taken, diluted to a final concentration of 50 nM, and loaded onto a liposome-attached slide surface. The fibrils were collected at 48 hr of aggregation by centrifugation. The increase of Cal-520 (Ca^{2+}-binding dye) fluorescence was determined as Ca^{2+} influx and was calibrated with the blank background and ionomycin control as described in the Methods. The Ca^{2+} influx from individual experiments was then normalised with the number of ThT-active PrP aggregates observed from TIRF images. The relative influx level at 0.5 hr is set as 1. The error bars represent standard deviations from three independent experiments with different batches of protein samples.

quantify the ability to permeabilise the liposome membrane by measuring the influx of external Ca^{2+} ions with liposome-encapsulated Ca^{2+}-binding dye[308]. The membrane permeability assay provides a reliable and ultrasensitive approach to characterise the various PrP species identified from a structural insight. With the help from Dr Suman De at the Department of Chemistry, Cambridge, PrP aggregates were applied at defined time points onto a liposome-attached coverslip surface, and the resulting fluorescence induced by Ca^{2+} influx was determined as membrane permeability.

In Figure 4.7, the membrane permeability was normalised to the average number of PrP aggregates observed in TIRF images (Figure 4.1b). Mature PrP fibrils collected after 48 hr were shown to be inefficient in permeabilising the lipid membrane compared with early-formed oligomers. In contrast, the membrane permeability per aggregate showed little change at early aggregation times. This constant permeability suggested that the PK-res oligomers (R_L and R_H) were less likely to be responsible for the disruption of the lipid membrane, as their numbers increased over time (Figure 4.5e). Instead, the PK-sen oligomers (S_L and S_H) and ThT-inactive oligomers, which both remained constant number over time (Figure 4.3c and 4.5e), are more likely to permeabilise the membrane.

4.6 Modelling the kinetics of PrP aggregation

The aggregation kinetics of recombinant PrP at early stages under partially denaturing conditions has been explored[180,191,337,338]. To acquire more insights into the early events of PrP aggregation, the quantitative TIRF data were further analysed by fitting them to a kinetic model for protein aggregation for protein aggregation, with the help from Dr Georg Meisl at the Department of Chemistry, Cambridge [186,193] (see Chapter 2.8.6 for the derivation of the model).

According to the original kinetic scheme for PrP aggregation (Figure 4.1b), the number of the PK-sen oligomers, S_L and S_H, remained unchanged over the measurement period, which is likely to be at equilibrium with monomers. The possibility of the steady state of the aggregation reaction was ruled out, as there were insufficient numbers of PK-res oligomers or fibrils to be consistent with a steady state scenario. As discussed in Chapter 4.4, the production of R_H and R_L are very likely due to a direct conversion from S_H and S_L. Therefore, the kinetic model here was considered to be the nucleation of PK-sensitive species from the monomer (m) is at equilibrium, followed by a structural conversion reaction from PK-sen (S) to PK-res (R) populations (Figure 4.8a). Compared to the previously established model for α-Synuclein aggregation *in vitro*, the current model for PrP aggregation follows a nucleation-dissociation-conversion model, which contains reversible reaction steps that cannot be neglected.

S_L and S_H share similar kinetic parameters, as do R_L and R_H (Table 4.1), which is consistent with the ThT intensity distribution of PrP aggregates that L and H species share a similar kinetic profile at the early stage of aggregation (Figure 4.1c). This suggests that the L and H species are likely to interconvert on the similar time scale of the measurements. Therefore, for convenience, the scheme can be simplified to that shown in Figure 4.8b, where S_L and S_H are treated as a single species, as are R_L and R_H. Based on this scheme, the fitted kinetic parameters are shown in Table 4.2. This means the half-life for PK-sen → PK-res conversion is roughly 1 hr under current aggregation condition.

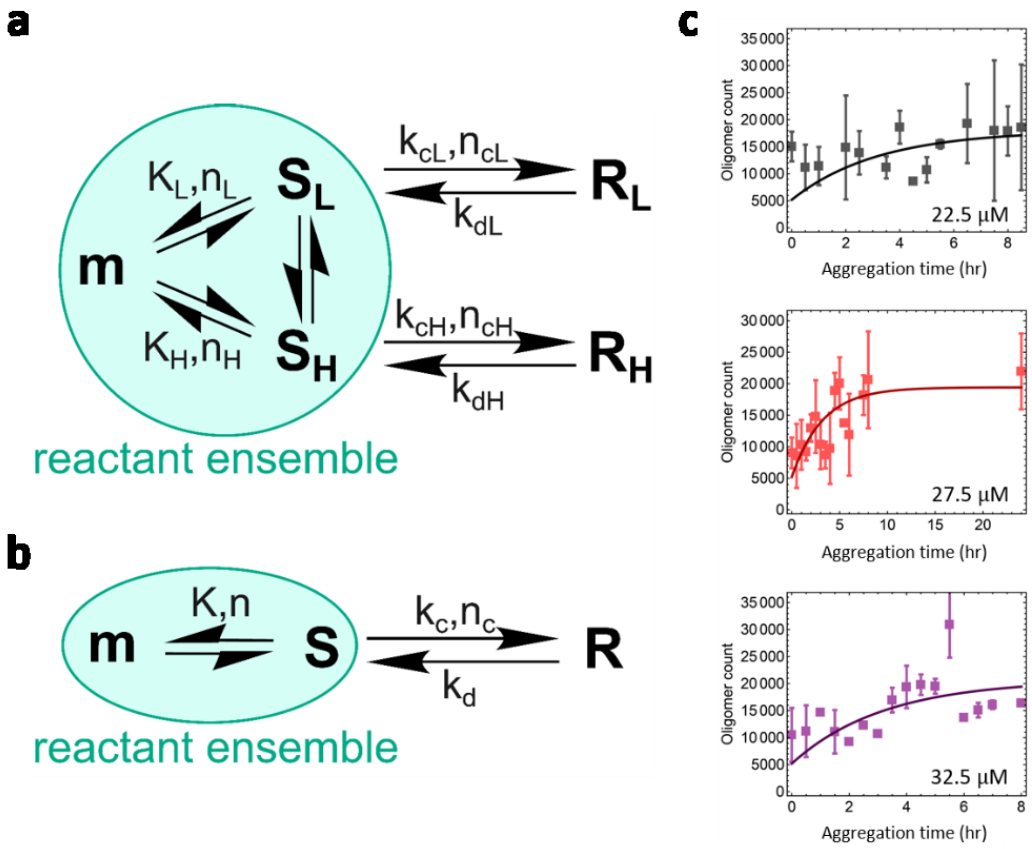

Figure 4.8 | Modelling the kinetics of PrP aggregation. (**a**) The kinetic model considers the nucleation of PK-sensitive species from the monomer (m) is in equilibrium, and a structural conversion reaction happens between PK-sensitive (S) to PK-resistant (R) populations. (**b**) A simplified kinetic model that considers a single S → R population, as L and H shares similar kinetic parameters. The S species includes S_L (low-intensity) and S_H (high-intensity), while the R species includes R_L (low-intensity) and R_H (high-intensity). (**c**) Global fits of the TIRF kinetic profiles in Figure 4.1b using a single S → R population. *K*, equilibrium constant; *n*, reaction order of nucleation; k_c, rate constant of conversion from S to R; n_c, reaction order of conversion; k_d, rate constant of reverse reaction of conversion.

PrP Species	K (count/μM)	n	k_c (hr^{-1})	n_c	k_d (hr^{-1})
L	120	1	0.80	0	0.40
H	69	1	0.93	0	0.23

Table 4.1 | Fitted parameters for the kinetic model of PrP aggregation. In this model, the L and H species are nucleated from monomers and have independent aggregation reactions (i.e. $S_L \rightarrow R_L$; $S_H \rightarrow R_H$). *K*, equilibrium constant; *n*, reaction order of nucleation; k_c, rate constant of PK-sen → PK-res conversion; n_c, reaction order of conversion; k_d, rate constant of reverse reaction of conversion.

PrP Species	K (count/μM)	n	k_c (hr^{-1})	n_c	k_d (hr^{-1})
Total (L+H)	189	1	0.77	0	0.27

Table 4.2 | Fitted parameters for the simplified kinetic model of PrP aggregation. In the simplified model, the L and H species are treated as a single species due to their similar kinetics. The PK-sensitive species is formed by monomer nucleation and then converts to PK-resistant species. *K*, equilibrium constant; *n*, reaction order of nucleation; k_c, rate constant of PK-sen → PK-res conversion; n_c, reaction order of conversion; k_d, rate constant of reverse reaction of conversion.

4.7 Summary of the chapter

The spatial distribution and temporal evolution of the infectious and toxic species are important in the research in PrP neuropathology, and they require direct studies of infectivity and toxicity and identification of the species responsible. However, such physical characterisation is proving technically challenging due to the complicated nature of protein aggregation. The single-aggregate imaging methods provide an *in vitro* approach to characterise the various species of PrP aggregates from a structural perspective.

The aggregation kinetics of recombinant PrP at the early stage has been explored under a semi-denaturing condition. According to the single-aggregate measurements, five oligomeric species with distinct structural characteristics have been identified: (1) ThT-inactive oligomers, (2) PK-sen low-ThT intensity oligomers (S_L), (3) PK-sen high-intensity oligomers (S_H), (4) PK-res low-intensity oligomers (R_L), and (5) PK-res high-intensity oligomers (R_H). The presence of S_L, S_H, and ThT-inactive oligomers at early times and their constant numbers during aggregation suggests that they are in kinetic equilibrium with monomers. In contrast, from the temporal change of PK-sen and PK-res species in Figure 4.5d, it is suggested that S_L and S_H undergo structural conversion to R_L and R_H, independently, despite the L and H species seem to have a similar kinetic behaviour at early aggregation times within 10 hr (Figure 4.1c and 4.6).

The small changes in the number and the ThT intensity of total oligomeric populations formed at the early stage of aggregation (Figure 4.1a and b), and no clear shift of the peak to higher intensity in the ThT intensity distribution (Figure 4.1c) suggest that many of the PrP oligomers in the early stage of aggregation remain in the soluble states, and only a minor fraction of the PK-res oligomers grows into mature fibrils under the semi-denaturing condition. Despite the L and H species showing similar kinetics, the fraction of the H species decreased at 48 hr when fibril formation reached a plateau (Figure 4.1c), suggesting that the H species, possibly larger-sized R_H (> 300 kDa), that ultimately grows to mature fibrils.

According to the modelling to PrP aggregation, the half-life of PK-sen → PK-res conversion in PrP aggregation is about 1 hr. Compared to our previous measurement for αS^{180} that plays a key role in Parkinson's disease, the half-life of PK-sen → PK-res conversion for αS is about 36 hr, which is slower than that for PrP by more than an order of magnitude. The fast conversion rate for PrP may be partially due to the denaturing condition, but still, it reflects the conversion rate is fundamentally faster in the PrP case.

Although the origin of toxicity induced by aggregated proteins might be complicated, it appears to highly correlate to the disruption of the lipid membrane of cellular components. The membrane permeability assay is the first attempt to quantitatively measure the damaging ability of PrP aggregates to the lipid membrane and to probe the responsible species from a structural perspective. The data shows that early-formed PrP oligomers possess higher membrane permeability than mature fibrils and that ThT-inactive or PK-sen oligomers are likely to be responsible for inducing calcium influx in membranes. This is consistent with the previous finding that toxic oligomers are structurally loosely-packed[181], as well as the observation from mouse models that the toxicity may result from PK-sen species[244]. It also suggests that the aggregate species of PrP that caused the disruption of the membrane may include ThT-inactive species, which are in a low level, relatively small in size, and technically difficult to detect.

Overall, this chapter reveals that at least five types of aggregates can co-exist during PrP aggregation. The ThT-inactive oligomers and PK-sen oligomers remain constant number over time and are more capable of disrupting the lipid membrane and inducing Ca^{2+} influx. In contrast, PK-res oligomers are formed by a structural conversion from the PK-sen species and are likely to form fibrils. According to ThT intensity, the structurally different PK-sen/PK-res species can be sub-divided into the L and H species, individually, which are different in size and yet share a similar kinetic behaviour. Therefore, PrP amplification and lipid membrane disruption are likely mediated by different aggregate species with separate structural properties. Intervention in the formation of these specific targets during PrP propagation can be potentially important to inhibit the aggregation process.

Chapter 5 | The mechanism of prion-like spreading II: αS aggregation

5.1 Introduction

Parkinson's disease, like other neurodegenerative diseases, is associated with protein aggregation. The hallmark of this disease is the insoluble aggregates of αS and its deposits in the brain, known as Lewy bodies[339]. According to previous immunohistochemical studies in PD brains, the development of PD has been found to accompany with the accumulation of αS inclusions before the appearance of clinical symptoms, and a mutation, A53T, in the αS gene is identified to accelerate the disease development[114,115,340]. It has been reported that Lewy bodies propagate from host to transplanted embryonic neurons in PD brains, suggesting that αS aggregates could spread to neighbouring cells[341–343]. Furthermore, WT and transgenic mouse experiments have shown that injection of recombinant αS fibrils could lead to endogenous αS aggregation[258,259,344]. This suggests that αS aggregation can be accelerated by seeding and follows the nucleation-dependent polymerisation mechanism as observed from PrP studies. From *in vivo* studies, clinical signs of synucleinopathies are demonstrated to be able to be triggered in transgenic A53T mice after intracerebral inoculation of brain homogenates from old mice with synucleinopathy[345] or from MSA patients[346]. These findings provide strong evidence of αS transmissibility among cells and organisms, which is the prerequisite for *bona fide* prions. Based on the above observations from the intercellular spread and seeded propagation, αS aggregates have been suggested to possess 'prion-like' properties[257,261,347,348].

However, some have argued that Lewy pathology has not been detected in all transplanted cells[260], and no interorganismal infectivity was reported in human PD[256]. The reason may be partially due to a low protein level *in vivo* and low fragmentation rates of αS fibrils that may lead to inefficient spreading of αS aggregates, so that αS amplification and transmission have not been detected in a reasonable time period. The prion-like hypothesis of αS in PD pathology requires further studies. In this chapter, I have explored the propagation characteristics of WT and A53T αS aggregates using the single-aggregate imaging with TIRF microscopy and made quantitative comparison between αS and PrP based on the kinetic rate constants determined. The kinetic constants measured have allowed the estimation for the hypothetical spreading of αS throughout the brain and thus examined the validity of the spreading model with αS aggregates.

5.2 Single-aggregate studies of WT αS aggregation from bulk solutions

The propagation characteristics of WT human αS was investigated with the same approach as in the PrP study in Chapter 3. Seeded or unseeded αS aggregation reactions were performed in bulk solution under native conditions to determine the change in aggregate length with respect to time (Figure 3.1, left and Figure 5.1). The αS seed was generated from sonication of fibrils formed by WT αS, which were typically broken into small fragments below the detection limit of ~450 nm and is consistent with a previous finding[349]. In unseeded αS aggregation, an initial increase in the average aggregate length was observed, followed by a slow decrease at later times over a long period of several weeks. The decrease of aggregate length was shown not to be due to proteolysis (Figure 5.2), which suggested it is likely to result from fragmentation of αS fibrils. To extract the kinetic parameters of αS aggregation, the kinetic profiles were fitted again with the help

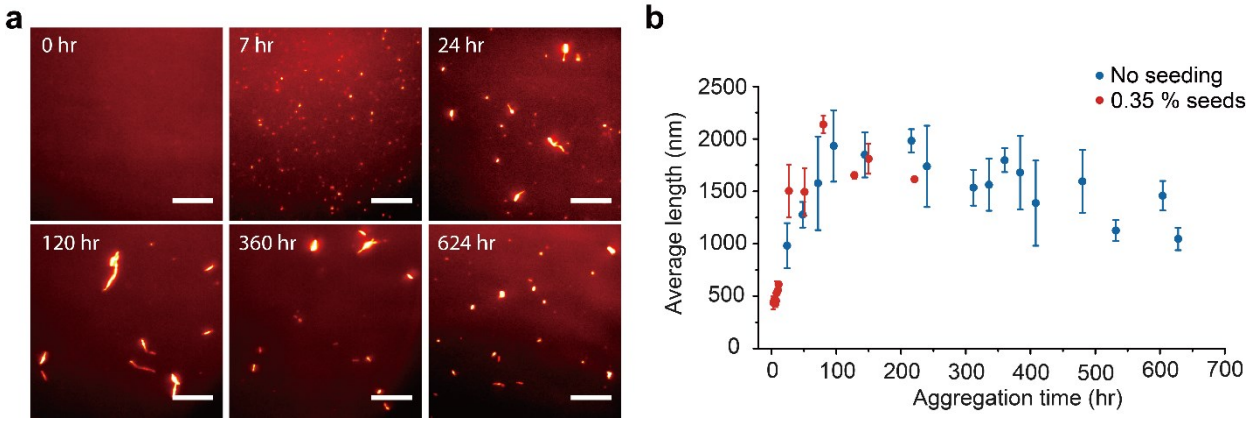

Figure 5.1 | Kinetics of WT αS aggregation in bulk solution. (**a**) Representative TIRF images of non-seeded αS aggregation at a protein concentration of 70 μM at different times were revealed using TIRF imaging. The scale bars represent 10 μm. (**b**) The change on average aggregate length of non-seeded and 0.35% (v/v) seeded αS aggregation at a protein concentration of 70 μM in PBS (pH 7.0) supplemented with 0.01% (v/v) NaN_3. Reaction kinetics were measured by taking aliquots at various time points from the aggregation reaction mix that was incubated at 37 °C with shaking at 200 rpm. The kinetic data obtained were used to estimate the fragmentation and elongation rate constants k_e and k_f, respectively. The product of rate constants $k_e k_f$ is 6.9×10^{-9} $M^{-1}s^{-2}$. The error bars represent standard deviations from three independent experiments with different batches of protein samples.

from Dr Georg Meisl at the Department of Chemistry, Cambridge. The product of k_e and k_f was estimated to be 6.9×10^{-9} $M^{-1}s^{-2}$, which is lower than the equivalent value for PrP in solution by a factor of 10^7 (Table 5.1). Given the αS concentration of neuron synapses in the mouse brain is 2 μM [350], the derived doubling time t_2 for αS is 48 days. This suggested that the time for αS to replicate was approximately 1000-fold longer than that for PrP. This calculation provides a quantitative approach to estimate to what extent αS is 'prion-like' through the kinetic parameters measured.

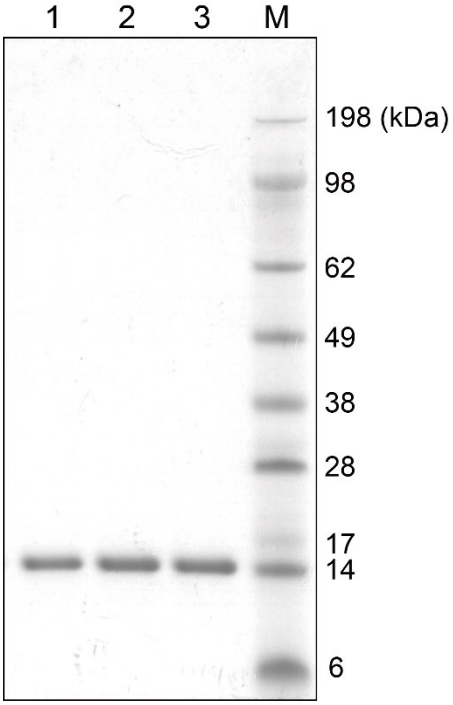

Figure 5.2 | Structural integrity of unseeded WT αS aggregates using SDS-PAGE. αS was aggregated in PBS with the supplement of 0.01% NaN_3 at 37 °C with 200 rpm. An aliquot was taken for analysis at defined time points. After boiling for 10 min, 2 μg of the aggregates were separated by 4-12% Bis-Tris NuPage gel. The result shows a single band with similar intensity over long-term incubation, suggesting no obvious degradation over time. No large-sized species was observed remaining above the wells. 1: 0 hr; 2: 168 hr; 3: 2000 hr; M: protein marker.

Protein	k_e # ($M^{-1}s^{-1}$)	k_f # (s^{-2})	k_ek_f ($M^{-1}s^{-2}$)	m (nM)	t_2 (day)	*PK-sen→res conversion half-time*
WT αS	43±7	$1.6 \pm 0.2 \times10^{-10}$	$6.9 \pm 1.4\times10^{-9}$	2000 (SN)	48 ± 2	39.5 ± 7.3 hr

Table 5.1 | Kinetic parameters for WT αS aggregation in solution. k_e, elongation rate constant; k_f, fragmentation rate constant; m, local concentration of monomers in cells; t_2, doubling time required for a single protein aggregate replicates into two aggregates during aggregation. SN: synapse. The errors represent uncertainties of the fitting parameters given the dataset.

The PK resistance for αS assemblies was analysed at defined time points (Figure 5.3). It was found that αS aggregates were initially PK-sensitive and subsequently acquired PK resistance as the assemblies grew in length into longer fibrils. To acquire more insights, the fractions of the PK-sen and PK-res species of αS were quantified with 2D Gaussian functions and hence kinetic profiles acquired. The fraction of PK-res aggregates increased rapidly and reached a plateau after 2 days (Figure 5.4a), while the number of these assemblies increased continuously over time (Figure 5.4b). The conversion from PK-sen to PK-res was determined to have a half time of ~39.5 hr, which is in good agreement with the previous FRET measurements[180]. In comparison with the half-time for PrP conversion, αS aggregates required significant >100 fold more time for structural conversion (Table 3.1 and 5.1) despite the fact that the aggregation would appear to occur by a similar mechanism.

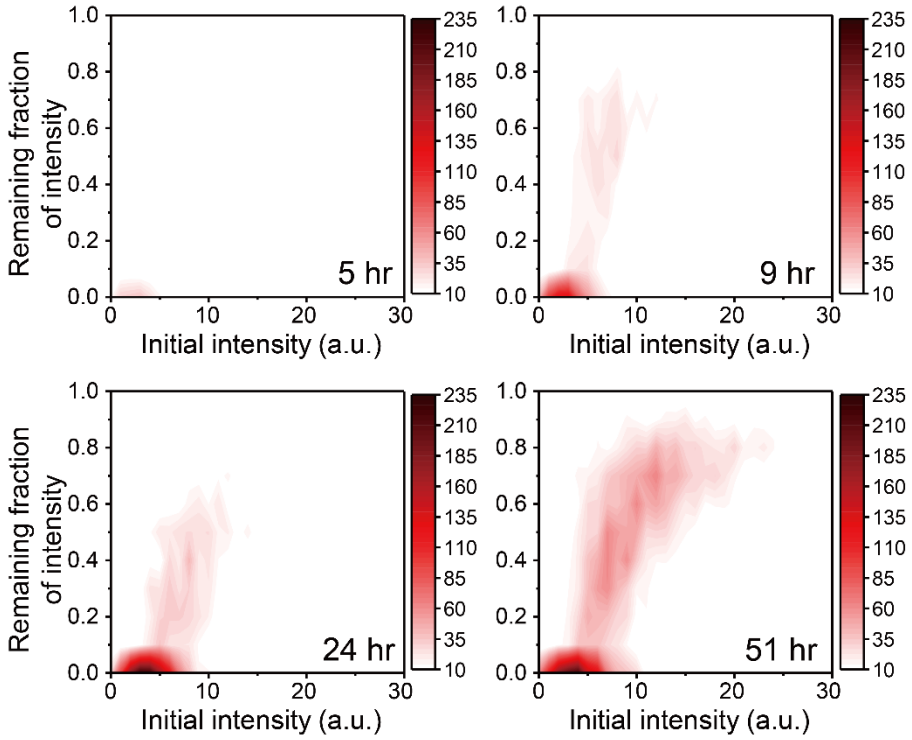

Figure 5.3 | PK resistance of unseeded WT αS aggregates. αS was aggregated in PBS with the supplement of 0.01% NaN_3 at 37 °C with 200 rpm. At various time points, aliquots were removed from the reaction mix and adsorbed onto a glass coverslip. PK was added at different times to the glass coverslip and slide chamber sealed to prevent fluid evaporation. The change in ThT intensity of individual particles was followed by continual imaging with the fixed fields of view at 37 °C incubation. PK resistance was calculated as the fraction of the ThT intensity after 1 hr proteolytic digestion compared to that seen at the start of the experiment. Combined data of three independent measurements with different batches of protein samples were shown.

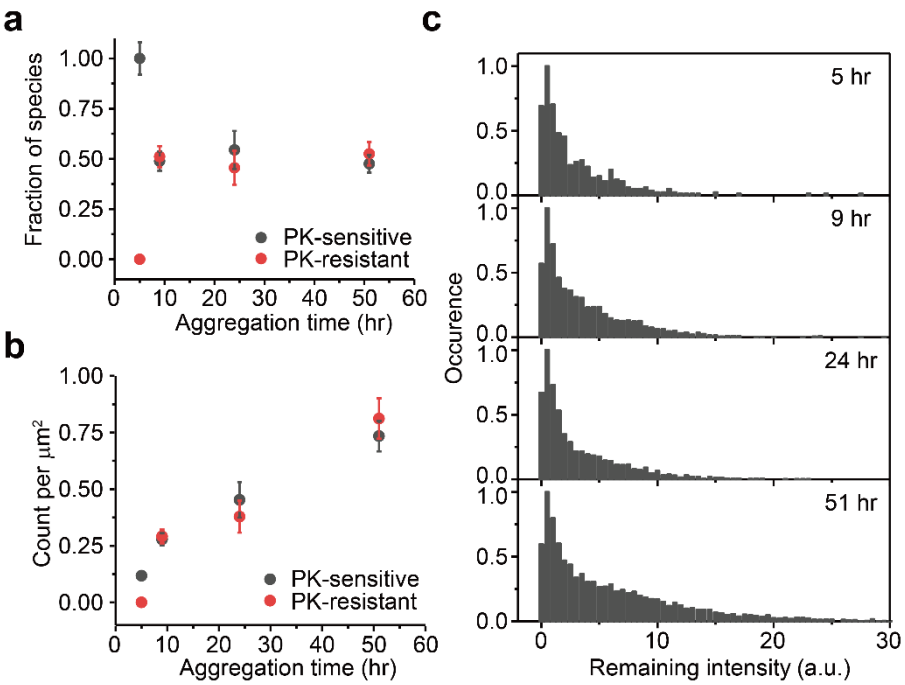

Figure 5.4 | Structural conversion of αS aggregates. Temporal change in (**a**) the fraction and (**b**) the number of PK-sen and PK-res species of αS aggregates as a function of time. The dataset from Figure 5.3 was globally fitted to 2D-Gaussian functions to obtain the fraction of PK-sen and PK-res populations as a function of time. (**c**) Intensity distributions after PK-digestion at different time points.

5.3 Estimation for WT αS spreading in the brain from a kinetic approach

Protein inclusions of αS are the neuropathological hallmark of Parkinson's disease (PD) and related synucleinopathies including dementia with Lewy bodies (DLB) and multiple system atrophy (MSA). In the development of the synucleinopathies, αS aggregates are reported to exhibit transcellular spread by a prion-like mechanism[256,257,261]. With the same rationale of estimation for PrP spreading in Chapter 3.6, I repeated the calculations for spreading in the brain based on the rate constants obtained for WT human αS (Figure 5.5a).

As the fits to the kinetic profiles for αS obtained a t_2 of 48 days in the mouse brain, $T_{spreading}$ for αS was predicted to be ~3.4 years in order to spread through an entire mouse brain (Figure 5.5). This is in good agreement with the experimental results of 15 months duration, when phosphorylated αS pathology was distributed throughout the brain after intracerebral injection with the human αS seed[258].

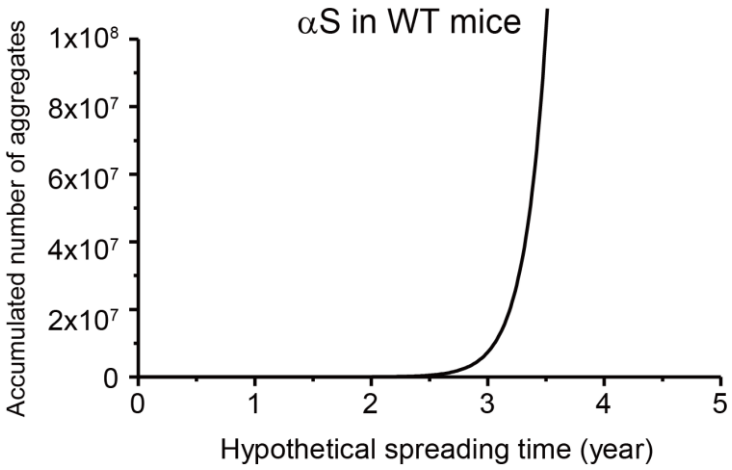

Figure 5.5 | Hypothetical spreading for human WT αS in the mouse brain. The simulated kinetic profiles are based on the exponential replication mechanism and the kinetic parameters measured in Table 5.1.

αS strain	t_2	f_0	f	n	Hypothetical $T_{spreading}$
WT αS in WT mice	48 day	1	7×10^7	26	3.4 year

Table 5.2 | Hypothetical spreading time ($T_{spreading}$) for human WT αS in the mouse brain. t_2: doubling time; f_0: initial number of aggregates; f: accumulated number of aggregates at $t=T_{spreading}$; n: round of doubling for αS replication; $T_{spreading}$: time required to obtain one aggregate in every neuron on average.

5.4 Kinetic studies of a disease-related αS mutant A53T

Chapter 3 has discussed that the difference among prion strains can be explained with the exponential replication in the spreading model. In this context, prion strains with unique conformational states may be differentiated by different kinetic parameters acquired from single-molecule studies. In αS studies, there is no clear evidence for the existence of αS strains, and there is no specific definition of them. However, the existence of αS strains may potentially explain the distinct clinical and pathological disease

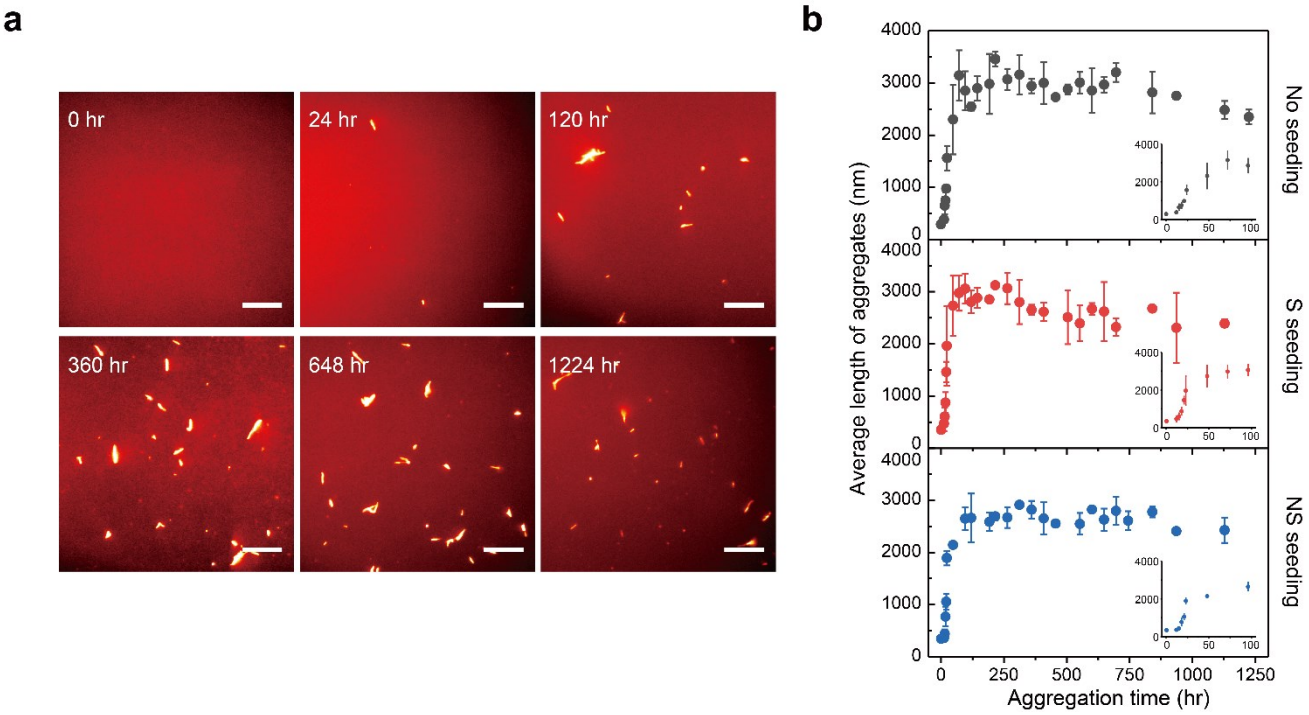

Figure 5.6 | Kinetics of A53T αS aggregates with S or NS strain seeds. (**a**) Representative images of non-seeded A53T aggregation at a protein concentration of 70 μM at different times were revealed using TIRF imaging. The scale bars represent 10 μm. The change on average aggregate length of (**b**) non-seeded, salt seeded (S), and non-salt seeded (NS) A53T aggregation at a protein concentration of 70 μM with 0.35% (v/v) seeds in PBS (pH7.0) supplemented with 0.01% (v/v) NaN_3. Reaction kinetics were measured by taking aliquots at various time points from the aggregation reaction mix that was incubated at 37 °C with shaking at 200 rpm. The kinetic data obtained were used to estimate the fragmentation and elongation rate constants k_e and k_f, respectively. The product of rate constants $k_e k_f$ is 4.8×10^{-5} and 1.3×10^{-5} $M^{-1}s^{-2}$ for S and NS strain-seeded reaction, respectively. The error bars represent standard deviations from three independent experiments with the same batch of protein samples.

phenotypes observed amongst the human synucleinopathies. Several recent studies have provided evidence that αS aggregates may exhibit strain-like behaviour *in vitro* and in mice[169,351–353]. Here I test the hypothesis with, A53T, is a PD-associated αS mutant that has been identified to exist in two distinct aggregated strains[169,353] and to accelerate the aggregation compared to the WT protein[354].

Two human A53T αS strains were obtained by varying the buffer conditions during fibril formation, in either the presence or absence of 100 mM NaCl to generate Salt (S) and No Salt (NS) fibrils, respectively. For the seeded reactions, pre-formed S or NS fibrils were sonicated as seeds, respectively. To measure the A53T αS aggregation kinetics, A53T αS was aggregated in bulk solution in the presence or absence of seeds over a long period of several weeks. A similar morphology was found between the WT and A53T aggregates formed in the same condition using TIRF imaging (Figure 5.6a). In contrast to WT, A53T aggregated faster and formed fibrils with longer average lengths (Figure 5.6b). Comparing the two strains, S fibrils were found to fragment more rapidly than NS fibrils. To determine the kinetic parameters of A53T aggregation, the TIRF data was fitted to the nucleation-elongation-fragmentation kinetic model. The derived k_e for both S and NS strains was substantially higher than that of WT by 10^4 fold, while k_f did not show an obvious difference (Table 5.3). The product of k_e and k_f was calculated to be 4.8×10^{-5} and 1.3×10^{-5} for S and NS seeding, respectively, which are both substantially higher than the equivalent value for WT (6.9×10^{-9} $M^{-1}s^{-2}$).

Protein	k_e # ($M^{-1}s^{-1}$)	k_f # (s^{-1})	k_ek_f ($M^{-1}s^{-2}$)	m (μM)	t_2
WT-seeded WT monomer	$4.3 \pm 0.7 \times10^{1}$	$1.6 \pm 0.2 \times10^{-10}$	$6.9 \pm 1.4 \times10^{-9}$	2	48 ± 2 (day)
S strain-seeded A53T monomer	$3.4 \pm 0.3\times10^{5}$	$1.4 \pm 1.1 \times10^{-10}$	$4.8 \pm 3.9\times10^{-5}$	2	13.8 ± 11.2 (hr)
				1	19.5 ± 15.8 (hr)
NS strain -seeded A53T monomer	$2.9 \pm 0.1\times10^{5}$	$4.4 \pm 3.0 \times10^{-11}$	$1.3 \pm 0.9\times10^{-5}$	2	26.5 ± 18.4 (hr)
				1	37.5 ± 26.0 (hr)

Table 5.3 | Comparison of kinetic parameters for WT and A53T αS aggregation in solution. The WT-seeded aggregation data is derived from Table 5.1. k_e, elongation rate constant; k_f, fragmentation rate constant; m, local concentration of monomers in cells; t_2, doubling time required for a single protein aggregate replicates into two aggregates during aggregation. The errors represent uncertainties of the fitting parameters given the dataset.

Despite the lack of information on the A53T αS concentration *in vivo*, at the same protein concentration of 2 μM, the doubling time t_2 was hence 13.8 hr and 26.5 hr, respectively, compared to that of 43 days for WT. The difference in t_2 between A53T and WT was shown to be roughly 10-100 fold.

In collaboration with Dr Joel Watts at the Tanz Centre for Research in Neurodegenerative Diseases, University of Toronto, I was able to compare the hypothetical spreading of A53T with the experimental results from hemizygous TgM83 mice (*M83*$^{+/-}$, ~0.5x expression level) after intracerebral inoculation with the A53T seed (Figure 5.7). As the A53T expression level was estimated to be half (i.e. 1 μM) in *M83*$^{+/-}$ mice than that in *M83*$^{+/+}$ mice, $T_{spreading}$ for the S and the NS seed-inoculated *M83*$^{+/-}$ mice was predicted to be 22 and 42 days, respectively (Table 5.4), in order to spread through an entire mouse brain. In comparison, the experimentally determined incubation periods for S strain and NS strain-inoculated mice were 142 ± 2 days and 375 ± 63 days, respectively[355], which agree with the estimated $T_{spreading}$ within an order of magnitude. Importantly, the relative ratios of $T_{spreading}$ between the two A53T strains (S and NS) predicted from the spreading model are very similar to those from the mice experiments.

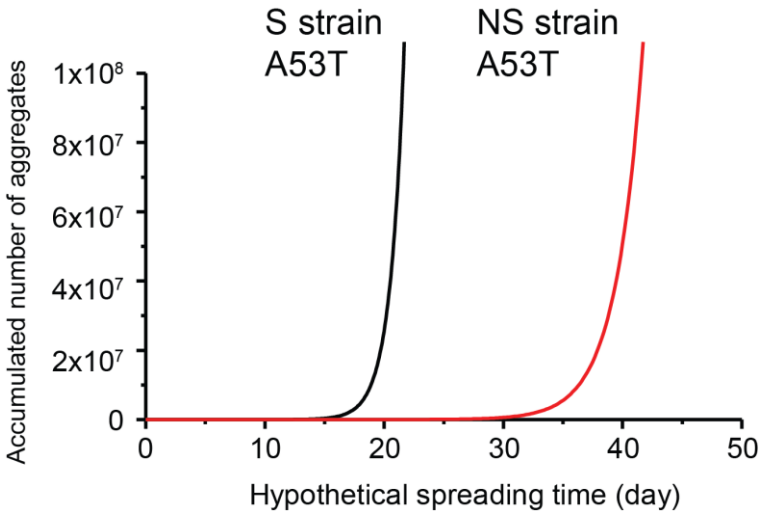

Figure 5.7 | Hypothetical spreading for human A53T αS in the mouse brain. The simulated kinetic profiles are based on the exponential replication mechanism and the kinetic parameters measured in Table 5.1.

αS strain	t_2	f_0	f	n	Hypothetical $T_{spreading}$
S strain A53T in mice	19.5 hr	1	7×10^7	26	22 day
S strain A53T in mice	37.5 hr	1	7×10^7	26	42 day

Table 5.4 | Hypothetical spreading time ($T_{spreading}$) for human A53T αS in the mouse brain. t_2: doubling time; f_0: initial number of aggregates; f: accumulated number of aggregates at $t=T_{spreading}$; n: round of doubling for αS replication; $T_{spreading}$: time required to obtain one aggregate in every neuron on average.

5.5 Disaggregation of αS assemblies by the proteasome

Although the formation of aggregates has been researched extensively, little is known about their removal. Aggregate degradation *via* both the proteasomal and the lysosomal systems has been described in the literature[356,357]. Whereas larger aggregates are believed to be cleared by lysosomes, removal of smaller oligomers has been attributed to the proteasome[358]. The 26S proteasome holoenzyme is an abundant multi-subunit protein complex responsible for the regulation of many key signalling pathways and general cell homeostasis[359]. This complex consists of a 20S core particle (CP) and one or two 19S regulatory particles (RP) that cap the CP at either end. Degradation activity of the proteasome is provided by several proteases that require ATP hydrolysis within the interior of the CP, while the RP is responsible for the recognition of ubiquitin-conjugated substrates, which are subsequently unfolded and translocated into the CP[360]. In cells, both tau and αS have been reported to be degraded by the proteasome[361,362], while their aggregated forms were not observed to be subjects of the proteasome *in vitro*. It is further possible that distinct aggregate conformations of sufficient size and stability may be recognised but not processed by the proteasome and thus inhibit its activity, as has been suggested for Aβ, tau, αS, and PrP aggregates[210,363–365]. Here I show preliminary data that large αS fibrils were predominantly removed by the proteasome in an ATP-dependent manner[366].

To test whether αS fibrils may also be targeted by the proteasome holoenzyme, human WT αS aggregates after 24 hrs of aggregation reaction were collected and treated with the proteasome or an ATP-containing buffer control with the help from Dr Yu Ye and Rachel Cliffe at the Department of Chemistry, Cambridge. The reaction mix was visualised with single-aggregate TIRF microscopy combining with pentameric formylthiophene acetic acid (pFTAA), a fluorescent dye that significantly increases the fluorescence quantum yield upon binding to amyloid structures[367]. An ATP regeneration system (see Chapter 2.13) was added to both the control and proteasome-treated samples to maintain the ATP concentration during the assay.

According to TIRF images, the length of individual pFTAA-active aggregates was plotted against their intensity (Figure 5.8a and b). Large αS fibrils (length >1 μm) were still detected even after 20 hrs of incubation in the degradation buffer without the proteasome. These fibrils constituted about 28% of all aggregates (471±14 counts), while the level of small aggregates (length <1 μm) is 72% (1227±318 counts). In comparison, incubation with the proteasome significantly removed αS fibrils (259±109 counts, or 8%), while the level of small aggregates increased (3094±255 counts, or 92%). This result suggests that

the proteasome can disassemble large fibrils into small aggregates. It is noted that proteasomes did not bind pFTAA and therefore could not contribute to any fluorescence signals detected.

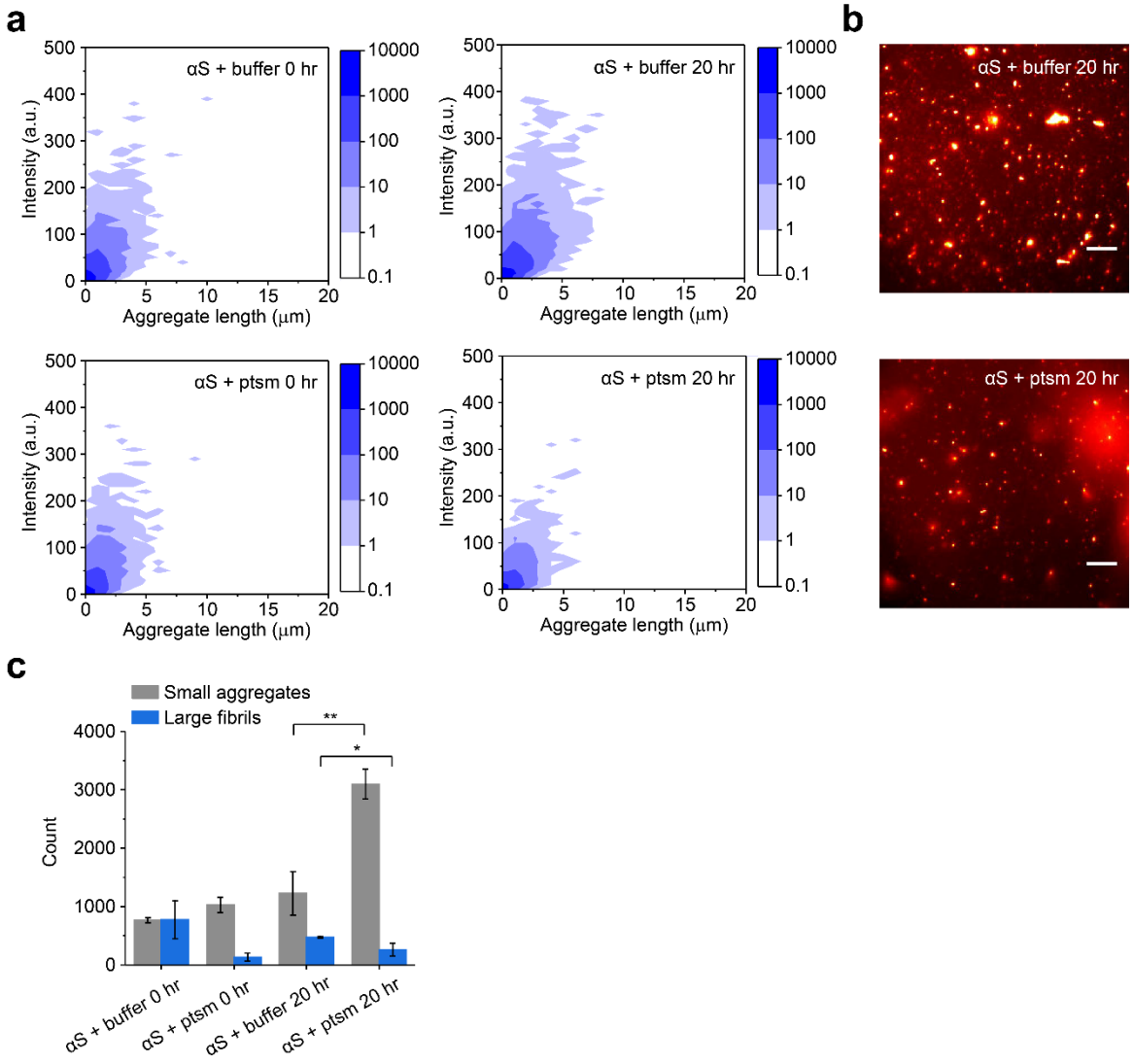

Figure 5.8 | Proteasome disaggregates αS fibrils into small-sized fragments. αS aggregates were assembled from monomers for 24 hrs, subsequently incubated with an ATP-containing buffer or proteasome holoenzyme for 20 hr, and then imaged with TIRF microscopy in the presence of 30 nM pFTAA. (**a**) Particle length and intensity of individual αS aggregates at 0 hr (upper) and 20 hr (middle) after buffer or proteasome treatment were revealed with contour plots. The combined data of three independent measurements with different batches of protein samples are shown. (**b**) TIRF images of the αS aggregates after 20 hr incubation in the presence or absence of the proteasome treatment. The scale bars represent 10 μm. (**c**) Quantification of the number of αS aggregates. The aggregates with length >1 μm are categorised as large fibrils, while those with length < 1 μm are categorised as small aggregates. The error bars represent standard deviations from three independent experiments with the same batch of protein samples. *P< 0.05, **P< 0.01, two-tailed t-test. Data acquired from the collaboration with Dr Yu Ye and Rachel Cliffe in Ref. 366.

5.6 Summary of the chapter

In this chapter, the elongation and fragmentation of WT and A53T mutant of human αS have been studied. The results show that replication of WT and A53T αS aggregates follows a similar elongation/fragmentation mechanism as in the PrP case, and αS fibrils fragment with a substantially slower rate constant compared with PrP.

Through the measurements of the kinetic parameters, the t_2 for αS replication is determined at the physiological protein concentration in cells. Hence, the spreading model established in Chapter 3 can be tested based on the experimental observations of αS aggregation. WT αS shows substantially slower elongation/fragmentation than PrP and results in $t_2 = 48$ days, leading to a hypothetical spreading time of 3.4 years based on our calculation in the mouse brain. The estimation for the hypothetical spreading time in the brain is in good agreement with the results from animal experiments within an order of magnitude. Therefore, WT αS accumulation in the brain is likely to follow the same exponential behaviour resulting from fragmentation like PrP in Chapter 3 and tau[192]. Based on the observation of longer t_2, it is predicted that WT αS aggregates would spend significant time in cells without degradation as has recently been observed[368].

The study in A53T αS strains shows that small differences in the product of k_e and k_f by ~4 fold between the S and NS strain of the A53T aggregates, resulting in a difference in t_2 by roughly 2 fold. In contrast to WT αS aggregates, S and NS A53T αS strains had faster t_2 by approximately 100 fold. Despite the lack of information about the A53T expression levels in transgenic mice, the estimations for the hypothetical spreading time of A53T in the brain are in good agreement with the results from animal experiments within an order of magnitude, assuming the expression level is the same as that in WT mice. Furthermore, the relative ratios of t_2 between the S and NS strain aggregates predicted from the spreading model are very similar to that from animal experiments[355]. This is consistent with the estimation of the spreading model that the diversity among prion or prion-like strains can be explained from a kinetic perspective as discussed in Chapter 3. Together with the estimations from WT and A53T αS, the results suggest that the prion-like property can be quantified and thus compared among strains or proteins with the same spreading model, and it may be extended to other aggregation-prone proteins as well.

Preliminary measurements in the proteasome holoenzyme reveal a potential novel disaggregase function of the proteasome. The proteasome is shown to disaggregate αS fibrils up to ~20 μm in length independently of ubiquitin conjugation, resulting in a substantially higher amount of small aggregates with length < 1 μm. The proteasome

assay has been conducted with tau in our group as well and shown a consistent result[366]. Combining with the data from gel electrophoresis and TEM images, it implies that the proteasome is able to disaggregate stable fibrillar structures that are larger than itself by several orders of magnitude, and this disaggregation ability is not restricted to a particular protein. This finding is in agreement with recent studies on proteasome recruitment to aggresomes in cultured cells[369,370] and to poly-GA aggregates in neurons[371]. In this context, it may partially be true that in the cellular environment protein aggregates without modifications are disaggregated by the proteasome and hence generated more templates as new seeds, resulting in acceleration of the aggregation process.

Furthermore, the current study has focused on the fibril disaggregase activity of proteasome holoenzyme on unmodified recombinant αS. In physiological conditions, protein aggregates with distinct modifications (e.g. ubiquitination) may be targeted by the proteasome through alternative cellular mechanisms for disaggregation. This may also explain the inhibitory effect of protein aggregates upon the proteasome in previous reports[210,363–365,372]. The cellular mechanisms for disaggregation and the aggregated species responsible for proteasomal inhibition remain to be studied.

Chapter 6 | Prion-like spreading in cells

6.1 Introduction

In the previous chapters, I have demonstrated PrP and αS replication *in vitro* at the single-molecule level and how this process is accelerated by fibril fragmentation. In this context, mammalian prions and other prion-like proteins may propagate *in vivo* through fragmentation as well, to confer transmissibility *via* the transcellular spread of seeds that initiate the misfolding and aggregation in recipient cells. As PrP is generally accepted to transmit among cells and organisms[186,312], growing evidence has been provided for the cell-to-cell transmissibility of many proteins associated with other neurodegenerative diseases, including αS[373,374], tau[373,375], SOD-1[376], and TDP-43[377]. The newly emerged 'transmission hypothesis' for the prion-like property offers a link to the common mechanism underlying the onset and progression of various neurodegenerative diseases. This also explains the pathological spreading patterns that have long been observed in these diseases[174,250,378,379].

Current approaches with the cell work in neurodegenerative diseases have been essentially qualitative. Furthermore, no observations were achieved to proteins at physiological levels in non-transfected cells. To understand the exact molecular basis of aggregation in cells, in this chapter I describe the observations from endogenous αS amplification after cellular uptake of the external seed. This ongoing project has been exploiting an advanced super-resolution microscopy, AD Paint, to quantitatively follow the spatio-temporal evolution of αS aggregates in cells and spreading to recipient cells.

6.2 Endogenous αS amplification is visualised in cultured cells with time using AD Paint imaging

To follow the αS amplification with the seed in cultured cells, the efficiency of seed transduction into cells was first assessed using different delivery methods. The αS seed was produced by sonication of fibrils formed by WT αS labelled with Alexa 594 (A594), which were typically broken into small fragments below the detection limit of ~450 nm and is consistent with a previous finding[349]. The sonicated αS fibrils were then transduced to SH-SY5Y cells for 4 hr without (Naked) or with a delivery mediator (Bioporter), which is a non-covalent lipid-based delivery system into living cells[373,380]. The cells were visualised using conventional epi-fluorescence microscopy. Bioporter-mediated αS-A594 seeds (green) showed higher co-localisation with the plasma membrane (red) and were more efficiently internalised by the cells after seed transduction. In contrast, cell

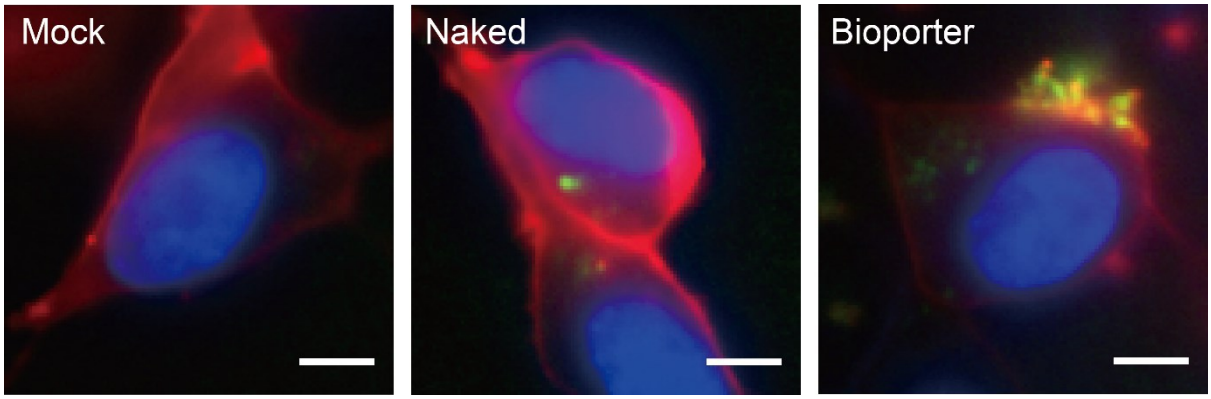

Figure 6.1 | Seed transduction in cultured cells with different methods. Representative images of transduced αS-A594 in SH-SY5Y cell line were acquired with epi-illumination (wide-field) mode after 4 hr mock or seed transduction. Pre-formed αS fibrils were sonicated and incubated with the cells for 4 hr. After transduction, the medium was removed, washed with PBS, and imaged with three illumination channels. Blue: Hoechst dye staining of DNA in nuclei; green: pre-formed αS seeds labelled with Alexa 594 dye; red: CellMask dye staining of the plasma membrane. Mock: PBS; Naked: αS-A594 without delivery mediators; Bioporter: αS-A594 mediated with the Bioporter lipid vesicles. In the Bioporter image, the co-localisation of yellow puncta surrounding the plasma membrane and the higher number of green puncta in the cytosol indicate a high proportion of lipid vesicle-packed αS-A594 were internalised by the neurons and released into the cytosol. The scale bars represent 5 μm.

internalisation of the seed was substantially lower without the mediator (Figure 6.1).

AD Paint is a super-resolution imaging technique aiming to observe protein aggregates in fixed cells. It requires the transient binding between the docking strand and the imaging strand as described in Figure 1.12. In the present study, endogenous αS filaments in the cells induced by the internalised αS seed were recognised by the antibody-labelled docking strand at defined time points, subsequently visualised with the Cy3b dye-labelled imaging strand using a TIRF setup. The localisation events from the individual fluorophores shown on the images were used to probe the morphology of individual aggregates, as well as to quantify the number and the aggregate length.

Next, the seeded αS aggregation in SH-SY5Y cells was followed in respect of time using AD Paint imaging with the assistance from Yukun Zuo at the Department of Chemistry, Cambridge. After Bioporter-mediated seed transduction, endogenous αS showed a substantial accumulation of aggregates in respect of time (Figure 6.2). As the observed αS inclusions were detected by binding with the conformation-specific MJFR-14-6-4-2 antibody that recognises filament forms of αS, it suggests that αS present within inclusions shares a similar conformation similar to the misfolded αS in the pathological Lewy bodies of Parkinson's disease, but different from normal cellular αS. Interestingly, a time-dependent change in the spatial distribution of αS aggregation was also observed. Endogenous αS aggregates at early times were spread around outside of the nucleus, while at later times, most of them formed large inclusions and localised in close proximity of the plasma membrane. In contrast, in the control group with PBS, only the background signal was seen over time (Figure 6.3).

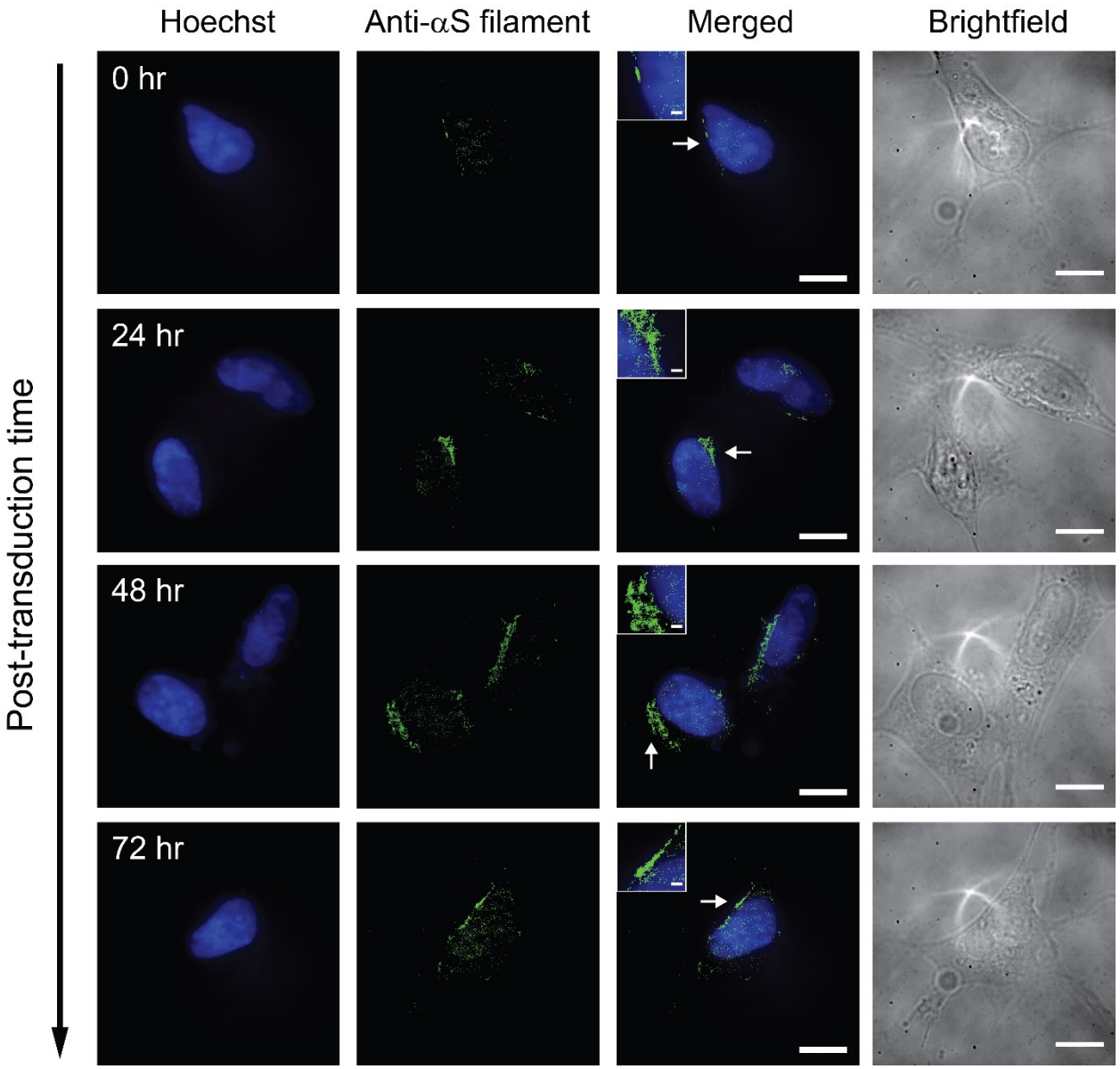

Figure 6.2 | Time-dependent amplification of the endogenous αS aggregates in seeded cells. Super-resolved images of the endogenous αS aggregates in neurons were acquired at defined time points after seed transduction with HILO (highly inclined and laminated optical) illumination mode using AD Paint imaging. Pre-formed αS fibrils were sonicated and incubated with SH-SY5Y cells for 4 hr. After seed transduction, the medium was removed and washed with PBS. At defined time points, cells were fixed with 4% paraformaldehyde, permeabilised with 0.5% Triton X-100, and then immunostained with an anti-αS filament antibody, MJFR-14-6-4-2, which is conjugated with a 9 bp single-stranded docking DNA sequence. The docking strand is recognised by its complementary strand in the single-stranded imaging DNA sequence, which is labelled with Cy3b fluorescent dye. (blue) Hoechst dye staining of DNA in nuclei; (green) super-resolved αS aggregates. The arrows indicate the enlarged area shown in the inlets. The scale bars represent 10 μm and those in the inlets are 1 μm.

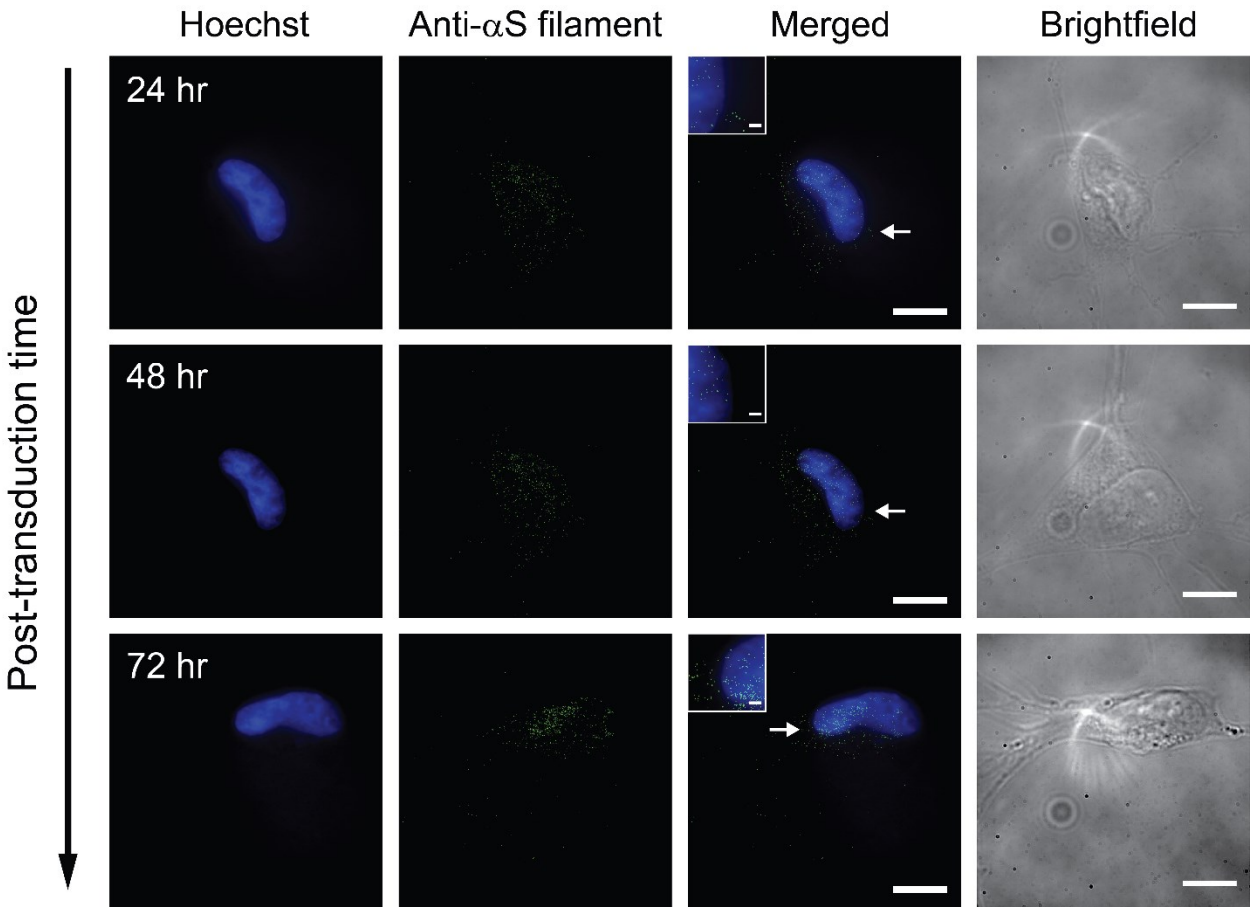

Figure 6.3 | Endogenous αS does not self-aggregate in mock cells. Super-resolved images of the endogenous αS in neurons were acquired at defined time points after seed transduction with HILO (highly inclined and laminated optical) illumination mode using AD Paint imaging. The mock solution of PBS was incubated with SH-SY5Y cells for 4 hr. After incubation, the medium was removed and washed with PBS. At defined time points, cells were fixed with 4% paraformaldehyde, permeabilised with 0.5% Triton X-100, and then immunostained with an anti-αS filament antibody, MJFR-14-6-4-2, which is conjugated with a 9 bp single-stranded docking DNA sequence. The docking strand is recognised by its complementary strand in the single-stranded imaging DNA sequence, which is labelled with Cy3b fluorescent dye. (blue) Hoechst dye staining of DNA in nuclei; (green) super-resolved αS aggregates. The arrows indicate the enlarged area showing in the inlets. The scale bars represent 10 μm and those in the inlets are 1 μm.

6.3 Quantitative analysis of αS amplification in the cells

There are several approaches available to analyse the aggregation kinetics in cells. For further analysis, the average aggregate length was unreliable according to the cell images, because large αS clusters were formed at later times. As a result, the length of individual events (i.e. individual aggregates and inclusions) at each time point showed non-linear relationships with their localisation values (Figure 6.4). These events with molecular size > 500 nm were mostly constituted by large αS inclusions and thus caused a large discrepancy in the measurement. In contrast, the events with small molecular size (30-500 nm) were mainly individual aggregates. Hence, it is extremely difficult to analyse the length distribution of overall aggregate populations. For the small-sized αS aggregate populations that < 500 nm, the typical length of them in each cell was ~90 nm on average (Figure 6.5). Furthermore, the average length of these small-sized aggregates did not show obvious changes during the measurement period, which suggested that αS aggregates in cells did not form long fibrillar species. It is noted that the resolution for AD Paint imaging is approximately 30 nm.

The determination of the number of aggregates is likely to under-estimate the precise number, due to the formation of large αS inclusions. However, the trend of the increase

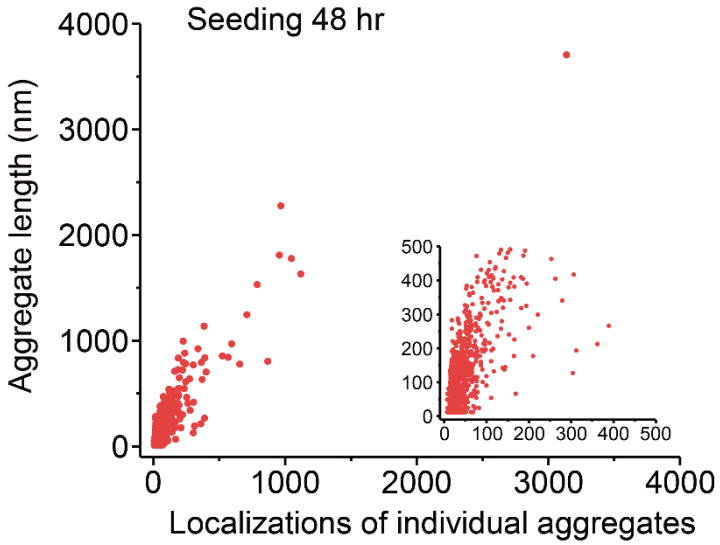

Figure 6.4 | Length- localisation relationship of individual aggregates is not linear. The analysis in the seeded cells after 48 hr shows that the events of > 500 nm possessing high localisation values are relatively shorter in their apparent length compared to those of < 500 nm. It may be due to large aggregated clusters which exhibit relatively low apparent size but with high localisation.

may be similar to the real situation, since large inclusions contributed less to the detected number of aggregates (i.e. counted as 1 for a single inclusion) than to the detected length (i.e. measured as 500-4000 nm for a single inclusion).

The total localisation value in single cells can be used to analyse the aggregation kinetics quantitatively, as it does not require one to recognise single aggregates. The temporal change in the number of αS aggregates and the total localisation per cell were shown in Figure 6.6 (cell number = 10 in each time point). After seed transduction, a clear increase in the number, as well as the total localisation, was seen over time, while no detectable increase was found in the mock control cells. Interestingly, αS aggregates were observed to remain undetectable in a fraction of cells, suggesting that the seeds were absent in these cells and thus unable to induce endogenous αS aggregation. As the number of this cell population decreased over time, more cells showed accumulation of αS aggregates. The newly-emerged cells that contained aggregates were unlikely to result from initial seeding since the seed should be detectable at time=0. The data suggested that the newly-formed αS aggregates were induced by initial seeding and that the αS aggregates were able to spread to neighbouring cells over time.

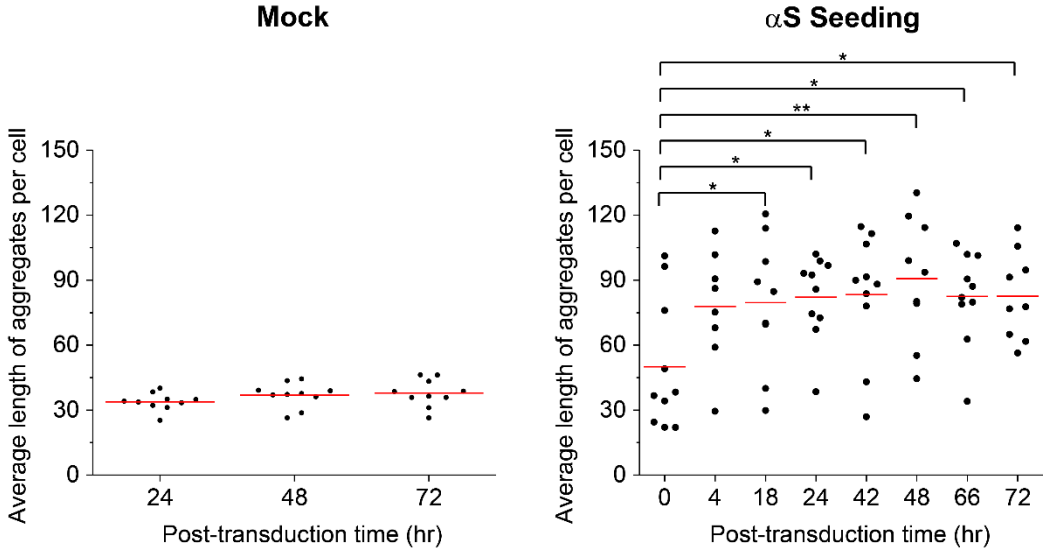

Figure 6.5 | Average aggregate length of αS does not increase during amplification in cells. At each time point, ten cell images were acquired from ten random fields of view using AD Paint. The images for single cells were analysed and quantified with a custom-made Python script. The dot distribution shows that αS aggregates remain constant length on average in the cells after seed uptake. The red lines represent the mean values of the average length of αS aggregates among the ten cells at defined time points. $*P < 0.05$, $**P < 0.01$, two-tailed t-test.

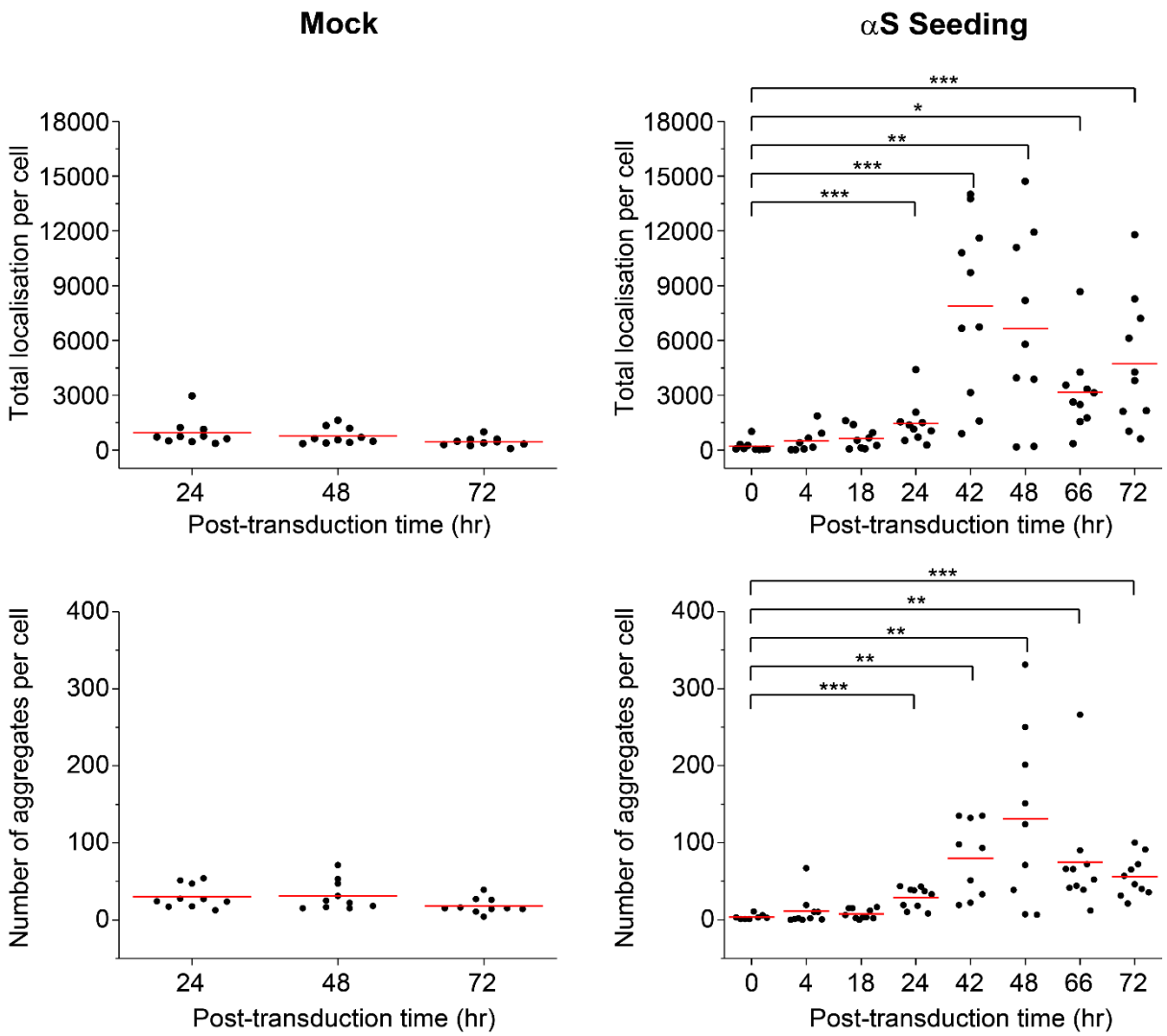

Figure 6.6 | αS aggregate amplification in respect of time. At each time point, ten cell images were acquired from ten random fields of view using AD Paint. The images for single cells were analysed and quantified with a custom-made Python script. The dot distribution shows that the cells initially contain a low level of αS aggregates, and a fraction of them gradually accumulate αS aggregates with time after seed transduction, while aggregates remain undetectable in control cells. The red lines represent the average of the number or the total localisation of αS aggregates among the ten cells at defined time points. *$P < 0.05$, **$P < 0.01$, ***$P < 0.001$, two-tailed t-test.

To better study the αS amplification in those transmitted cells, I separated the transmitted cell group from the non-transmitted cell group by setting a threshold according to the localisation value. Among all cells, those cells observed with upper 25% localisation values (i.e. higher than the third quartile Q3 in statistics) were categorised as 'transmitted cells', while the cells with lower 25% localisation values (i.e. lower than the first quartile Q1 in statistics) were categorised as 'non-transmitted cells'. Based on this analysis, the aggregation kinetics of the transmitted cells can be plotted as shown in Figure 6.7. The number of αS aggregates per cell increased with time and reached a maximum at 40-48 hr post-transduction, followed by a decrease at 72 hr. The total localisation per cell had a similar pattern and reached a plateau without further decrease. The results suggested that the formation of αS aggregates had reached a maximum level in 2 days post-transduction when a large fraction of them formed large inclusions, which is consistent with the observation that large inclusions occurred at 72 hr in Figure 6.2.

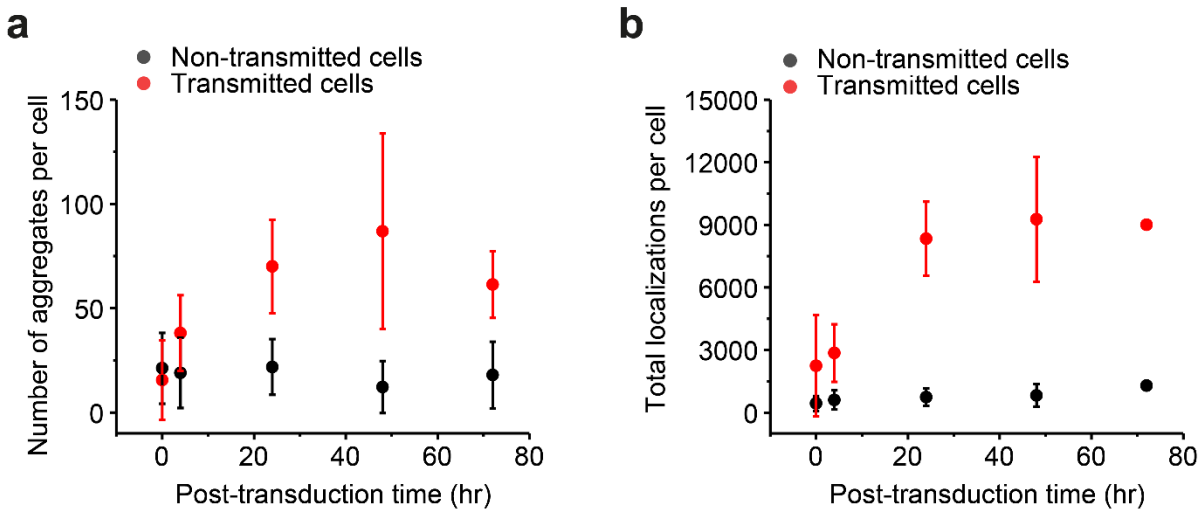

Figure 6.7 | Kinetic analysis of endogenous αS aggregation in cultured cells after seed transduction. The number (**a**) or the localisations (**b**) of αS aggregates as a function of time after seed transduction. The seeded cells are divided into two categories: non-transmitted and transmitted cells. At each time point, ten cell images from random fields of view were acquired. Those cells containing the lower 25% (i.e. lower than the first quartile Q1 in statistics) localisation values are grouped as the non-transmitted cells, while the cells containing the upper 25% (i.e. higher than the third quartile Q3 in statistics) localisation values are grouped as the transmitted cells. Analysis of the transmitted cells shows that both the overall localisation and number of αS aggregates per cell increase with time and reach a plateau around 48 hr. The error bars represent standard deviations from three independent experiments with different batches of αS seeds and cells.

Next, to estimate the spreading of αS aggregates among cells, the percentage of the cells that were developing aggregates was analysed as a function of time. This was achieved by determining the fraction of cells containing more aggregates than the initially seeded cells (i.e. localisation value above the third quartile Q3 at time=0). As shown in Figure 6.8, the initially seeded cells accounted for ~30% at time=0, and the cells containing αS aggregates increased to ~80% of the total cell population in 2 days post-transduction with spreading half-time of 23 hr. The spreading plateau after 2 days may result from either the aggregate-induced cell death or simply the accumulation of by-products during cellular metabolism as the cell medium was not replaced.

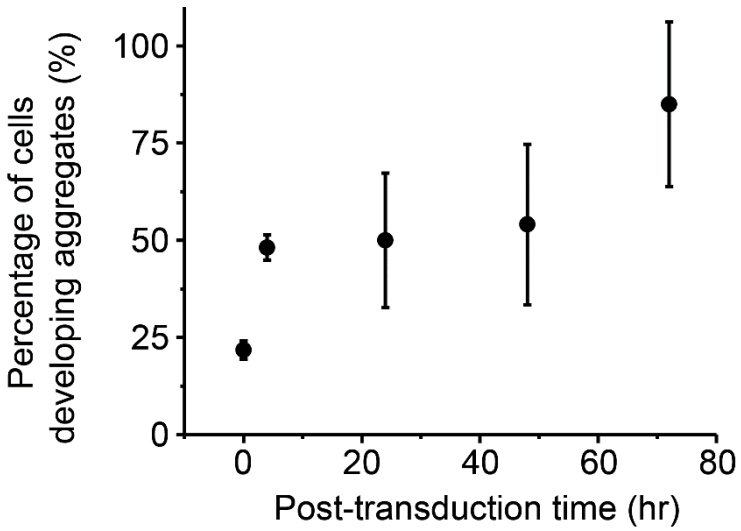

Figure 6.8 | Fraction of cells developing αS aggregates. The fraction of cells developing αS aggregates is shown as a function of time. The upper 25% (i.e. higher than the third quartile Q3 in statistics) localisation value at time=0 was arbitrarily used as a threshold to calculate the fraction of transmitted cell at each time point.

6.4 Summary of the chapter

In this chapter, the amplification of αS aggregates has been quantitatively measured in cultured cells with AD Paint imaging. The preliminary results suggest that after seed transduction, αS aggregates are accumulated rapidly around the nucleus within 2 days, and formation of large aggregate inclusions can be seen along the plasma membrane as time advances. This is in agreement with previous findings that in the presence of αS fibrillar seeds, the accumulation of exogenous αS fibrils takes place inside the cytoplasm within close proximity of the nucleus at early times[381], and that abundant large αS inclusions occupy the cytoplasm and displace the nucleus at later times[373]. The use of super-resolution microscopy enables detailed observation of αS aggregation compared to conventional confocal microscopy. The average aggregate length of αS is ~90 nm and does not show obvious change with time. In contrast, large inclusions are typically >1 μm, which are likely to be the early formation of Lewy bodies that are normally observed to be 5-25 μm in diameter. Ultrastructure of the large αS inclusions from immunoelectron microscopy also reveals that they are composed of small filamentous structures that are ~100 nm in size[373], which is consistent with the present finding.

Current observation of the αS aggregation kinetics in cells is found to be slower than that from previous seeding experiments[368,380]. This may result from the use of non-transfected cells in this study, in which the endogenous αS expression level is typically lower by several folds compared to transfected cells. Current data suggest that exogenous αS seeds are able to induce αS aggregate amplification by recruiting endogenous monomers. In comparison with my previous *in vitro* measurements of WT αS aggregation in Chapter 5.2 (t_2 =48 days), the αS replication rate in cells appears to be substantially faster. This discrepancy may be partially due to the proteasomal system in cells. Based on the observation of the disaggregase activity of the proteasome in Chapter 5.5, the proteasome may disaggregate non-ubiquitinated αS fibrils in the cytosol and thus produce a large amount of small-sized fibrillar segments, acting as new seeds for further amplification. This partially explains the observation that the average aggregate length of αS in the cells remains short ~90 nm.

In addition, the results also show that αS aggregates are likely to spread to neighbouring cells in a reasonably fast manner, despite the fact that the cell line used is physiologically different from primary neurons and proliferates with time. In this sense, it might lead to under-estimation of the αS spreading rate. The current data cannot rule out that the spreading of aggregates observed is through cell proliferation rather than cell-to-cell transmission, although it is rather unlikely due to the relatively slow doubling time of SH-

SY5Y cells (55 hr; CLDB database) compared to the observed spreading rate (half time = 23 hr). To take into account of proliferation and apoptosis of cells, further experiments with non-proliferating cells, such as iPS neurons, are required.

Chapter 7 | Concluding remarks and future directions

This dissertation summarises work done in the last four years on understanding prion and prion-like aggregation at the molecular level. The single-molecule techniques have shown the ability to unravel the molecular details of the self-assembly process of PrP and αS and the structural diversity of the aggregated species. This study highlights some of the key determinants in prion and prion-like replication and provides quantitative insights into the spreading of protein aggregates in the brain.

7.1 The basis of prion-like spreading

The current study has utilised a single-aggregate TIRF imaging method to observe PrP and αS aggregation under native conditions, revealing a possible aggregation mechanism which is described by an elongation-fragmentation reaction. Despite fragmentation having been considered important for sustained replication in protein aggregation, this is the first time that the mechanism has been directly confirmed. The rate of PrP fragmentation is revealed to be proportional to fibril length, and this process induces the generation of PK-sen segments, possibly due to destabilisation of the fibrillar structure. This suggests that large-sized PrP aggregates are more likely to fragment, thus producing more seeds for further amplification. In previous studies with PrP 27-30 purified from prion-infected hamster brains, sonication of large fibrillar PrP27-30 has been shown to decrease the average fibril length and increase the ability to convert PrP^{C} [242]. In another study, sonication of PrP27-30 in the presence of phospholipids can increase scrapie infectivity levels[382]. Consistent with the current observation that the small-sized fragments of PrP fibrils are capable of being seeds and elongating to new fibrils *in vitro*, these findings together suggest that fibril fragmentation may play a key role in the generation of the infectious form of PrP aggregates.

The results also show that WT αS fibrils fragment with a substantially slower rate compared with PrP fibrils. It suggests that the difference in aggregation rates among proteins can be quantitatively compared with the same spreading model. Through the measurements of kinetic parameters for PrP and other protein aggregates under similar experimental conditions, their aggregation characteristics can be summarised by plotting their elongation rate constant (k_e) against the fragmentation rate constants (k_f)

measured *in vitro* (Figure 7.1). Since the doubling time t_2 for protein aggregation depends on the product of k_e and k_f, the higher $k_e k_f$ leads to higher aggregation rate that falls in the 'dangerous zone' (red), while the opposite direction represents low replication rate, or 'safe zone' (canary yellow). This plot provides a quantitative approach to explain the potential of proteins aggregates replicating through an elongation-fragmentation mechanism. Interestingly, PrP aggregates (measured in solution) is located in the dangerous zone, showing unusually high values for k_e and k_f. Therefore, it is predicted to replicate much faster than other proteins. Together with the kinetic data of WT and P301S tau obtained from Kundel *et al*[192], the disease-related mutant forms of tau and αS aggregates, P301S tau and A53T αS, are possible to achieve efficient aggregation through the combination of fast k_e and slow k_f, compared to their WT forms which have slow rate constants. On the other hand, as discussed in Chapter 5, the kinetic difference between the S and NS strain of A53T αS lies on the fragmentation rate.

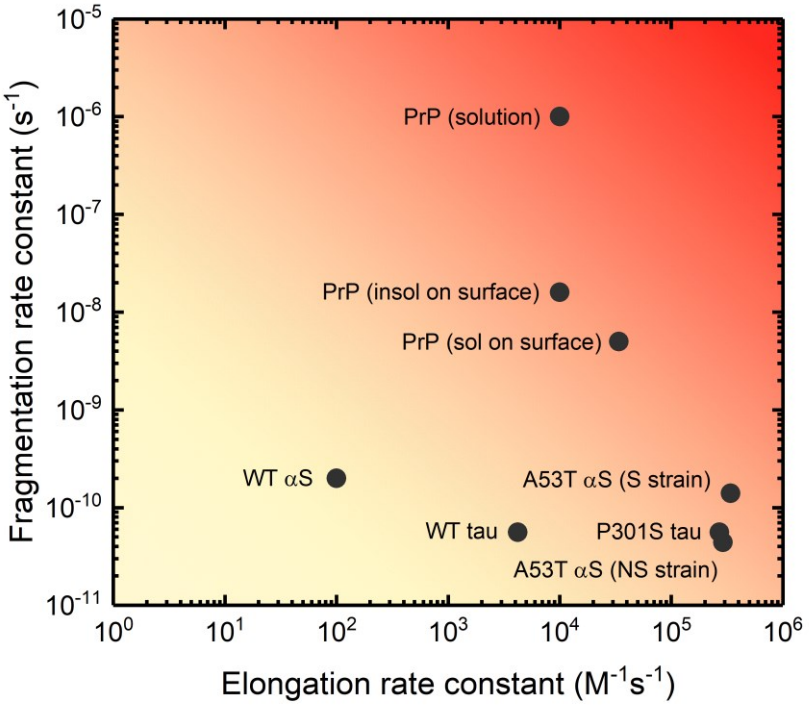

Figure 7.1 | Elongation-fragmentation relationship. The elongation rate constant (k_e) of prion-like proteins is plotted against their fragmentation rate constants (k_f) measured *in vitro*. The higher product of k_e and k_f leads to higher replication rate that falls in the 'dangerous zone' (red), while the opposite direction represents low replication rate, or 'safe zone' (canary yellow). The kinetic data of WT and P301S tau are obtained from Kundel *et al* [192]. Note that k_e and k_f are measured as the rate constants per monomer.

Prion strains are defined as prion isolates that encode the same polypeptide sequence and yet cause distinct heritable clinico-pathological phenotypes and incubation periods when transmitted to identical hosts[25,383]. Inoculation of different prion strains in mice usually results in different and reproducible incubation periods[384–386]. Accumulating biochemical and biophysical evidence have associated the diversity of prion strains with different conformational states of PrP^{Sc} [331,383,387–391]. The structural fragility of yeast prions has been found to determine the strength of their strain phenotype[184]. In this sense, prion strains may adopt different conformations and hence replicate at different rates, resulting in different incubation times *in vivo*. With the kinetic approach described in Chapter 3, the difference of the replication rate among prion strains can be explained by the concept of doubling times. Considering that a given prion strain (F) has faster t_2 (i.e. higher k_e or k_f value) than a slow strain (S), based on Equation 1, the resulting PrP replication for prion strain F would be substantially greater than that of prion strain S (see Chapter 2.8.5 for calculations). For example, if strain F has 10% lower t_2 (i.e. approximately 20% higher in $k_e k_f$), after the same duration of $T_{spreading}$ in mice, a 5-fold excess of strain F aggregates will be produced. Therefore, small differences in kinetic rate constants or replication efficiency would appear to be able to contribute to an explanation of the diversity in prion strains. The minor change in fragmentation/elongation rates is likely to result in a substantial difference in the accumulation of protein aggregates. In αS studies, although the strain is not well-defined, the A53T αS aggregates have been shown to adopt in two distinct conformations under different buffer conditions, S and NS, and result in different incubation periods in mice[355]. In Chapter 5.4, the kinetic measurements of the S and NS strains suggest the S and NS strain has distinct kinetic rate constants despite the same batch of protein samples.

The observation of the difference in rate constants between WT and mutant forms, or between the A53T αS strains, can be associated with a difference of their physical conformations. The A53T mutation of αS was demonstrated to play a dominant role in increasing the growth rate of A53T αS fibrils by altering the propensity of secondary structure formation[392], which is consistent with the current finding. The combination of P301 and S320 mutation in tau increases the structural propensities for aggregation[393], which at least partially explains the increased k_e of P301S tau. Another study in two variants (strains) of superoxide dismutase-1 (SOD1) aggregates with distinct growth kinetics, generated under different experimental conditions, has shown that the strains possess distinct structural properties[394]. It was found that the structurally fragile strain of SOD1 aggregates has a higher tendency of fragmentation and causes rapid aggregation *in vivo*. This result agrees with the current finding from the measurements of A53T αS strains.

Due to the exponential nature of fibril fragmentation, a simple model has been established and enables the estimation of aggregate spreading in the brain. Despite the spreading of aggregates *in vivo* depends on many factors as discussed in Chapter 3, the hypothetical model has shown the ability to estimate the spreading time of PrP and αS in the brain. Together with a previous study on tau filament replication[192], this suggests that exponential replication through fragmentation can be the basis for prion-like spreading in the pathogenesis of these diseases. By applying the rate constants obtained into the same kinetic model, the spreading time of the two strains of A53T αS was estimated in the brain and comparable to the results from animal experiments[355].

The aggregation kinetics *in vivo* is determined by multiple factors as discussed in Chapter 3.7. These key factors include post-translational modifications, cellular clearance mechanisms, and the disaggregase function of the proteasome that is currently studied. The conformations between intracellular and recombinant protein aggregates may also differ due to hyper-phosphorylation or glycosylation. These factors are likely to determine the spread of aggregates *in vivo* by either altering t_2 or replication efficiency, thus generating a discrepancy between theoretical values and *in vivo* observations. However, these factors could not be included in the spreading model, because the aggregation kinetics were modelled based on experimental measurements. From the results, the discrepancy is constrained in a reasonable range and the relative ratios of the estimations are similar to the data from mouse experiments, the elongation-fragmentation mechanism is likely to be one of the key determinants for protein aggregation. While not covered the cellular factors, the kinetic approach provides insights into the key factors that will likely affect spreading rates of protein aggregates.

7.2 PrP forms a range of oligomers during aggregation

Structural information in early PrP aggregation is provided by a combination of several biophysical and biochemical assays. The early-formed PrP oligomers have been characterised under semi-denaturing conditions with respect to time and shown to comprise of five species with distinct structures and sizes: (1) ThT-inactive oligomers, (2) PK-sen low-ThT intensity oligomers (S_L), (3) PK-sen high-intensity oligomers (S_H), (4) PK-res low-intensity oligomers (R_L), and (5) PK-res high-intensity oligomers (R_H). PrP aggregates are found to form into two oligomeric species with distinct molecular sizes (i.e. L is <300 kDa and H is >300 kDa), and they undergo a PK-sen → PK-res structural conversion, despite the surface hydrophobicity remains unchanged. The number of the PK-res species, R_L and R_H, increases over time, while that of the PK-sen, S_L and S_H, and ThT-inactive oligomers remains stable.

It is not surprising that in the absence of a PrP^{Sc} template, the aggregation of recombinant PrP results in a range of abnormal β-sheet-rich isoforms. Many biochemical works have been carried out to generate and characterise PrP oligomers *in vitro*, although these oligomers were often obtained under various aggregation conditions and from different versions of PrP. PrP oligomers can be obtained by incubating truncated mouse PrP (90-231) with 1 M GdnHCl, 3 M urea, 150 mM NaCl and then dialysing against 10 mM sodium acetate (pH 3.7)[395,396]. In the dialysis step, PrP was demonstrated to form soluble oligomers at low pH (<5.5) or to assemble into amyloid fibrils at mildly acidic pH (>5.5)[395]. Alternatively, PrP oligomers have been generated by denaturing and then reducing truncated human PrP (91-231) with 6 M GdnHCl and DTT (pH 8.0), then refolding the protein under an acidic condition (pH 4.0)[397–399]. Interestingly, the same group found that the N-terminus of mouse PrP (23-231) reduces the structural complexity and maintains a distinct conformation of oligomers with ~280kDa, despite the lack of toxicity and infectivity[295]. However, the above two versions of PrP oligomers have been shown to be kinetically stable and do not form fibrils. The conditions used above are different to what is currently used in this thesis, which is kinetically favoured the formation of amyloid fibrils. It is possible that after the dialysis and structure refolding, recombinant PrP is more likely to be trapped in kinetic local maxima. Furthermore, the truncated versions of PrP, the lack of co-factors may together contribute to the chance of being trapped in local maxima as well.

Since the semi-denaturing condition used in this thesis allows the formation of amyloid fibrils, at least a part of the oligomeric species I observed is likely to be on-pathway intermediates during fibril formation. A previous study reports that off-pathway PrP

oligomers do not bind to ThT[400], which is different from the currently observed ThT-inactive species. The ThT-inactive species described in Chapter 4 shows a structural transition to a more hydrophobic conformation during the measurement period. Instead of being an end product that should accumulate its number over time, the unchanged number of the ThT-inactive species suggests that ThT-inactive species may be at equilibrium with other aggregate species, such as the PK-sen species, or monomers, which suggested to be on the pathway to the formation of fibrils. Furthermore, as discussed in Chapter 4.4, R_L shares a similar ThT intensity profile with S_L (and likewise, in the R_H and S_H pair) in the ThT intensity distribution, and the increase of the fraction of the PK-res species was at the same rate as that of the decrease of the PK-sen species (Figure 4.5d). Hence, it is highly likely that the PK-sen species undergo a structural conversion to PK-res species under the current condition.

It is unknown which PK-res species (i.e. R_L and R_H), or both, are capable of growing into mature fibrils, and the possibility that one of the PK-res species is an off-pathway product in the aggregation kinetics cannot be ruled out. It is noted that only the early stage of PrP fibril formation was included in the quantitative kinetic model in Figure 4.8, and no fibrils were detected during this time period. According to the working model, L (<300 kDa) and H (>300 kDa) species are kinetically similar and share similar primary nucleation rate and conversion rate. Apart from the molecular size (based on the observation from ThT intensity distribution), it is difficult to distinguish them from other structural approaches, such as surface hydrophobicity or PK resistance, indicating a similar conformation between L and H species. From studies of the purified hamster PrP^{Sc}, the oligomeric species appear to form two forms with different molecular sizes. The molecular weight of the most infectious PrP aggregates was found to be around 600 kDa[242,330], while the smaller oligomeric species comprising 4-6 PrP molecules (~100-150 kDa) was not infectious[242,401]. The current work provides a link PrP oligomers between *in vitro* and *in vivo* observations, and it would be interesting to examine the seeding ability of L and H species observed.

Cell death induced by protein aggregation has been suggested to come from various causes, including apoptosis[200,215,216], hyper-activity of the excitatory amino acid transmitters (e.g. glutamate)[217–220], ER stress[221–223], autophagy[224–229], and non-specific membrane disruption[6,181,231–236]. The commonly used colourimetric methods for measuring cytotoxicity include MTT assay, LDH assay, and alamarBlue assay (detecting mitochondrial enzymatic activity, detecting lactate dehydrogenase released from the disrupted plasma membrane, and measuring cell metabolic activity for resazurin, respectively). However, the colourimetric assays often require a large amount of protein samples. In addition, they are relatively insensitive to examine the effect induced by low-

abundant oligomeric aggregates. To solve this problem, an ultra-sensitive single-vesicle assay has been applied to examine the disruption of lipid membranes induced by protein aggregates. The results for PrP oligomers show that at the early stage of aggregation, the PK-sen species, S_L and S_H, perhaps ThT-inactive oligomers as well, are more likely to be capable of disrupting lipid membranes than the PK-res species, R_L and R_H. This is not to say that these species are necessarily toxic to cells, but the single-vesicle assay provides a direction for further cytotoxicity studies.

7.3 Prion-like spreading in cells

The current data of SH-SY5Y cells with fibrillar αS seeding has suggested that αS aggregates can be internalised by cells and that amplification of endogenous αS aggregates develops in a time-dependent manner. It is observed that the proportion of SH-SY5Y cells containing αS aggregates increases with time, which suggested that αS aggregates are likely to spread to neighbouring cells in a reasonably fast manner. This is consistent with previous studies[368,373,374,381,402–405] and supports that cell-to-cell transmission is the underlying mechanism for the spread of αS in cells. However, to enter neighbouring cells, a transmission route is required for the aggregates. Different routes of internalisation have been proposed for various neurodegenerative diseases, such as direct release and penetration through the plasma membrane, lipid raft-dependent micropinocytosis, endocytosis, or synaptic transmission through exosomes or nanotubes that connect two cells[250,378]. Therefore, it is worthwhile to utilise AD Paint imaging to study the cellular localisations of αS aggregates and how these aggregates might move between cells, such as measurements of the aggregate level in the cell medium.

The SH-SY5Y neuroblastoma cells used in the study is physiologically different from neurons and proliferates with time. Hence, the spreading rate of aggregates in Figure 6.8 might be under-estimated. The current data cannot rule out that the spread of aggregates observed is through cell proliferation rather than cell-to-cell transmission as discussed in Chapter 6.4, although it is an unlikely event due to the relatively slow doubling time of the number of SH-SY5Y cells (55 hr; CLDB database), compared to the observed spreading rate (half time = 23 hr). The combination of cell seeding AD Paint imaging appears to be a good system for investigating protein aggregation in cells. It would be important to take into account of cell proliferation and extend the experiment to non-proliferating cells, such as iPSC (induced pluripotent stem cells)-derived neurons. In addition, the current study is based on the use of MJFR-14-6-4-2 antibody that recognises the filament form of αS. It is possible that the observed αS amplification was due to cellular uptake of αS seeds over time. Despite the fact that the low-amount seeds were included in the lipid-based reagent Bioporter that can be removed by cell rinsing and were generally undetectable at time=0, to rule out the possibility, an alternative anti-αS antibody that recognises phosphorylated S129 residue can be used[406]. S129 residue has been shown selectively and extensively phosphorylated in pathological lesions *in vivo* [407,408], and it would be a good candidate to distinguish the endogenous αS aggregates from the seeds that are generated with recombinant αS.

Compared to the previous αS seeding experiment in SH-SY5Y cells[381], the aggregation

kinetics currently observed in cells is found to be slower and does not yet form large Lowy body-like inclusions. This may result from the use of non-transfected cells in this study, in which the endogenous αS expression level is typically lower by several folds compared to transfected cells. However, when compared to *in vitro* aggregation experiments in Chapter 5, αS aggregation in cells shows a substantially higher amplification rate. The rate discrepancy may be partly explained by S129 phosphorylation of αS aggregates in cells, which has been shown to promote αS aggregation and generate more insoluble aggregates than non-phosphorylated αS *in vitro* [409]. The physiological nature of SH-SY5Y cells is also likely to cause a different aggregation pattern compared to primary neurons. The cell line was obtained as a neuroblastoma derivative and thus has cancerous properties that influence its differentiation fate, viability, growth performance, metabolic properties and genomic stability. Furthermore, the possible disaggregation effects of the proteasome may also contribute to the discrepancy. It is hypothesised that the aggregates can be disassembled to many smaller-sized templates for further replication in cells. This can be tested by measuring the aggregation kinetics with inhibition of the proteasomal activity in cells. If the proteasomal disaggregation plays an important role in αS aggregation in cells, the addition of proteasome inhibitors, such as MG132 or carfilzomib, would reduce the amount of αS aggregates observed in cells.

The seeded αS aggregates are found to accumulate inside the cytoplasm within close proximity of the nucleus at early times. At later stages, abundant large αS inclusions, develop in the cytoplasm and displace the nucleus. These findings are consistent with previous seeding experiments with cell lines[373,381]. Apart from large inclusions that are typically $>$ 500 nm in size, the quantitative analysis has shown that the average length of the small-sized aggregates ($<$500 nm) do not show obvious changes over time and remained ~90 nm on average, which suggested that αS aggregates in cells did not form long fibrillar species. This average length is in agreement with a previous finding from immunoelectron microscopy that the large αS inclusions are composed of small aggregates of ~100 nm[373]. Consistently, a recent study using dSTORM super-resolution imaging also reports that seeded αS aggregates in SH-SY5Y cells appear to be ~80-100 nm in the endosomal system[349]. However, large inclusions were not observed in this study, possibly due to a relatively low amount of seeds in the cell line and thus most of them efficiently degraded in lysosomes. In addition, the small size currently observed may suggest that it is the critical length of αS aggregates entering a cell through endocytosis (the size of endosomes and lysosomes ranges between 50-400 nm[410]), or may reflect that most of the aggregates degraded in lysosomes. Similar studies are needed in non-transfected neurons, where the αS expression level is higher at presynaptic terminals and the formation of PD-like αS inclusions is more efficient than neuroblastoma cells[374,403].

7.4 Directions for future research

The phenomenon of protein aggregation is fundamentally important in scientific disciplines ranging from biology and medicine to physics and chemistry. Although this subject has been investigated for over 30 years, many issues remain unclear. To establish a more convincing link between aggregate species and pathogenesis, I have been studying protein aggregation in cultured cells, as well as the role of the proteasome. Still, many questions remain to be answered. In the above discussion in this chapter, I have reviewed the current results and how the work might be continued. The possible directions that stem from the current study can be summarised as: (i) verifying the work of endogenous αS aggregation and exploring the likely mechanism of aggregate spreading in neurons, (ii) studying how the cellular clearance machinery fails to disassemble the misfolded aggregates, especially the cellular response after inhibiting the proteasomal activity, and (iii) characterising the damaging pathways of the toxic aggregate species to neurons. (iv) extending the cell study to other neurodegenerative proteins, such as PrP and tau. The findings from the above work should contribute to our understanding of aggregation mechanisms in cells and establish a realistic framework for studying disease spreading in the brain. Furthermore, the described approach may also benefit the design of potential treatments for dementia in the future.

References

(1) Anfinsen, C. B. Principles That Govern the Folding of Protein Chains. *Science* **1973**, *181* (4096), 223–230.

(2) Hartl, F. U.; Hayer-Hartl, M. Converging Concepts of Protein Folding in Vitro and in Vivo. *Nat. Struct. Mol. Biol.* **2009**, *16* (6), 574–581.

(3) Dobson, C. M. Protein Misfolding, Evolution and Disease. *Trends Biochem. Sci.* **1999**, *24* (9), 329–332.

(4) Greenwald, J.; Riek, R. On the Possible Amyloid Origin of Protein Folds. *J. Mol. Biol.* **2012**, *421* (4–5), 417–426.

(5) DePas, W. H.; Chapman, M. R. Microbial Manipulation of the Amyloid Fold. *Res. Microbiol.* **2012**, *163* (9–10), 592–606.

(6) Knowles, T. P. J.; Vendruscolo, M.; Dobson, C. M. The Amyloid State and Its Association with Protein Misfolding Diseases. *Nat. Rev. Mol. Cell Biol.* **2014**, *15* (6), 384–396.

(7) Chiti, F.; Dobson, C. M. Protein Misfolding, Functional Amyloid, and Human Disease. *Annu. Rev. Biochem.* **2006**, *75*, 333–366.

(8) Dobson, C. M. Protein Folding and Misfolding. *Nature* **2003**, *426* (6968), 884–890.

(9) Balchin, D.; Hayer-Hartl, M.; Hartl, F. U. In Vivo Aspects of Protein Folding and Quality Control. *Science* **2016**, *353* (6294), aac4354.

(10) Dobson, C. M.; Šali, A.; Karplus, M. Protein Folding: A Perspective from Theory and Experiment. *Angew. Chem. Int. Ed. Engl.* **1998**, *37* (7), 868–893.

(11) Dill, K. A.; Chan, H. S. From Levinthal to Pathways to Funnels. *Nat. Struct. Biol.* **1997**, *4* (1), 10–19.

(12) Onuchic, J. N.; Luthey-Schulten, Z.; Wolynes, P. G. Theory of Protein Folding: The Energy Landscape Perspective. *Annu. Rev. Phys. Chem.* **1997**, *48* (1), 545–600.

(13) Brockwell, D. J.; Radford, S. E. Intermediates: Ubiquitous Species on Folding Energy Landscapes? *Curr. Opin. Struct. Biol.* **2007**, *17* (1), 30–37.

(14) Ellis, R. J.; Minton, A. P. Protein Aggregation in Crowded Environments. *Biol. Chem.* **2006**, *387* (5), 485–497.

(15) White, D. A.; Buell, A. K.; Knowles, T. P. J.; Welland, M. E.; Dobson, C. M. Protein Aggregation in Crowded Environments. *J. Am. Chem. Soc.* **2010**, *132* (14), 5170–5175.

(16) Bartlett, A. I.; Radford, S. E. An Expanding Arsenal of Experimental Methods Yields an Explosion of Insights into Protein Folding Mechanisms. *Nat. Struct. Mol. Biol.* **2009**, *16* (6), 582–588.

(17) Geddes, A. J.; Parker, K. D.; Atkins, E. D.; Beighton, E. "Cross-β" Conformation in Proteins. *J. Mol. Biol.* **1968**, *32* (2), 343–358.

(18) Buxbaum, J. N.; Linke, R. P. A Molecular History of the Amyloidoses. *J. Mol. Biol.* **2012**, *421* (2–3), 142–159.

(19) Sipe, J. D.; Cohen, A. S. Review: History of the Amyloid Fibril. *J. Struct. Biol.* **2000**, *130* (2–3), 88–98.

(20) Wyss-Coray, T. Ageing, Neurodegeneration and Brain Rejuvenation. *Nature* **2016**, *539* (7628), 180–186.

(21) Prusiner, S. B. Novel Proteinaceous Infectious Particles Cause Scrapie. *Science* **1982**, *216* (4542), 136–144.

(22) Aguzzi, A.; Nuvolone, M.; Zhu, C. The Immunobiology of Prion Diseases. *Nat. Rev. Immunol.* **2013**, *13* (12), 888–902.

(23) Cobb, N. J.; Surewicz, W. K. Prion Diseases and Their Biochemical Mechanisms. *Biochemistry* **2009**, *48* (12), 2574–2585.

(24) Prusiner, S. B. Prions. *Proc. Natl. Acad. Sci. U. S. A.* **1998**, *95* (23), 13363–13383.

(25) Collinge, J. Prion Diseases of Humans and Animals: Their Causes and Molecular Basis. *Annu. Rev. Neurosci.* **2001**, *24* (1), 519–550.

(26) Aguzzi, A.; Polymenidou, M. Mammalian Prion Biology. *Cell* **2004**, *116* (2), 313–327.

(27) Colby, D. W.; Prusiner, S. B. Prions. *Cold Spring Harb. Perspect. Biol.* **2011**, *3* (1), a006833.

(28) Prusiner, S. B.; Scott, M. R.; DeArmond, S. J.; Cohen, F. E. Prion Protein Biology. *Cell* **1998**, *93* (3), 337–348.

(29) Prusiner, S. B.; McKinley, M. P.; Bowman, K. A.; Bolton, D. C.; Bendheim, P. E.; Groth, D. F.; Glenner, G. G. Scrapie Prions Aggregate to Form Amyloid-like Birefringent Rods. *Cell* **1983**, *35* (2 Pt 1), 349–358.

(30) Caughey, B.; Lansbury, P. T. Protofibrils, Pores, Fibrils, and Neurodegeneration: Separating the Responsible Protein Aggregates from the Innocent Bystanders. *Annu. Rev. Neurosci.* **2003**, *26*, 267–298.

(31) Brown, P.; Bradley, R. 1755 and All That: A Historical Primer of Transmissible Spongiform Encephalopathy. *Br. Med. J.* **1998**, *317* (7174), 1688–1692.

(32) Chesebro, B. Introduction to the Transmissible Spongiform Encephalopathies or Prion Diseases. *Br. Med. Bull.* **2003**, *66*, 1–20.

(33) Chandler, R. L. Encephalopathy in Mice Produced by Inoculation with Scrapie Brain Material. *Lancet* **1961**, *1* (7191), 1378–1379.

(34) Gajdusek, D. C.; Zigas, V. Degenerative Disease of the Central Nervous System in New Guinea. *N. Engl. J. Med.* **1957**, *257* (20), 974–978.

(35) Hadlow, W. J. Scrapie and Kuru. *Lancet* **1959**, *274* (7097), 289–290.

(36) Coulthart, M. B.; Cashman, N. R. Variant Creutzfeldt-Jakob Disease: A Summary of Current Scientific Knowledge in Relation to Public Health. *Can. Med. Assoc. J.* **2001**, *165* (1), 51–58.

(37) Will, R. .; Ironside, J. .; Zeidler, M.; Estibeiro, K.; Cousens, S. .; Smith, P. .; Alperovitch, A.; Poser, S.; Pocchiari, M.; Hofman, A. A New Variant of Creutzfeldt-Jakob Disease in the UK. *Lancet* **1996**, *347* (9006), 921–925.

(38) Linden, R.; Martins, V. R.; Prado, M. a M.; Cammarota, M.; Izquierdo, I.; Brentani, R. R. Physiology of the Prion Protein. *Physiol. Rev.* **2008**, *88* (2), 673–728.

(39) Wilson, D. R.; Anderson, R. D.; Smith, W. Studies in Scrapie. *J. Comp. Pathol. Ther.* **1950**, *60* (4), 267-IN12.

(40) Griffith, J. S. Nature of the Scrapie Agent: Self-Replication and Scrapie. *Nature* **1967**, *215* (5105), 1043–1044.

(41) Aguzzi, A.; Calella, A. M. Prions: Protein Aggregation and Infectious Diseases. *Physiol. Rev.* **2009**, *89* (4), 1105–1152.

(42) Nazor, K. E.; Kuhn, F.; Seward, T.; Green, M.; Zwald, D.; Pürro, M.; Schmid, J.; Biffiger, K.; Power, A. M.; Oesch, B.; Raeber, A. J.; Telling, G. C. Immunodetection of Disease-Associated Mutant PrP, Which Accelerates Disease in GSS Transgenic Mice. *EMBO J.* **2005**, *24* (13), 2472–2480.

(43) Hsiao, K. K.; Groth, D.; Scott, M.; Yang, S. L.; Serban, H.; Rapp, D.; Foster, D.; Torchia,

M.; Dearmond, S. J.; Prusiner, S. B. Serial Transmission in Rodents of Neurodegeneration from Transgenic Mice Expressing Mutant Prion Protein. *Proc. Natl. Acad. Sci. U. S. A.* **1994**, *91* (19), 9126–9130.

(44) Hsiao, K. K.; Scott, M.; Foster, D.; Groth, D. F.; DeArmond, S. J.; Prusiner, S. B. Spontaneous Neurodegeneration in Transgenic Mice with Mutant Prion Protein. *Science* **1990**, *250* (4987), 1587–1590.

(45) Zhang, Z.; Zhang, Y.; Wang, F.; Wang, X.; Xu, Y.; Yang, H.; Yu, G.; Yuan, C.; Ma, J. De Novo Generation of Infectious Prions with Bacterially Expressed Recombinant Prion Protein. *FASEB J.* **2013**, *27* (12), 4768–4775.

(46) Wang, F.; Wang, X.; Yuan, C.-G. C.-G.; Ma, J. Generating a Prion with Bacterially Expressed Recombinant Prion Protein. *Science* **2010**, *327* (5969), 1132–1135.

(47) Deleault, N. R.; Harris, B. T.; Rees, J. R.; Supattapone, S. Formation of Native Prions from Minimal Components in Vitro. *Proc. Natl. Acad. Sci. U. S. A.* **2007**, *104* (23), 9741–9746.

(48) Castilla, J.; Saá, P.; Hetz, C.; Soto, C. In Vitro Generation of Infectious Scrapie Prions. *Cell* **2005**, *121* (2), 195–206.

(49) Legname, G.; Baskakov, I. V; Nguyen, H.-O. B.; Riesner, D.; Cohen, F. E.; DeArmond, S. J.; Prusiner, S. B. Synthetic Mammalian Prions. *Science* **2004**, *305* (5684), 673–676.

(50) Prusiner, S. B. A Unifying Role for Prions in Neurodegenerative Diseases. *Science* **2012**, *336* (6088), 1511–1513.

(51) Prusiner, S. B. Biology and Genetics of Prions Causing Neurodegeneration. *Annu. Rev. Genet.* **2013**, *47*, 601–623.

(52) Walker, L. C.; Jucker, M. Neurodegenerative Diseases: Expanding the Prion Concept. *Annu. Rev. Neurosci.* **2015**, *38* (1), 87–103.

(53) Riesner, D. Biochemistry and Structure of PrP(C) and PrP(Sc). *Br. Med. Bull.* **2003**, *66* (ii), 21–33.

(54) Riek, R.; Hornemann, S.; Wider, G.; Billeter, M.; Glockshuber, R.; Wüthrich, K. NMR Structure of the Mouse Prion Protein Domain PrP(121-231). *Nature* **1996**, *382* (6587), 180–182.

(55) Wells, M. A.; Jackson, G. S.; Jones, S.; Hosszu, L. L. P.; Craven, C. J.; Clarke, A. R.; Collinge, J.; Waltho, J. P. A Reassessment of Copper(II) Binding in the Full-Length Prion Protein. *Biochem. J.* **2006**, *399* (3), 435–444.

(56) Ott, D.; Taraborrelli, C.; Aguzzi, A. Novel Dominant-Negative Prion Protein Mutants Identified from a Randomized Library. *Protein Eng. Des. Sel.* **2008**, *21* (10), 623–629.

(57) Prusiner, S. B. Scrapie Prions. *Annu. Rev. Microbiol.* **1989**, *43* (1), 345–374.

(58) Lysek, D. A.; Schorn, C.; Nivon, L. G.; Esteve-Moya, V.; Christen, B.; Calzolai, L.; von Schroetter, C.; Fiorito, F.; Herrmann, T.; Güntert, P.; Wüthrich, K. Prion Protein NMR Structures of Cats, Dogs, Pigs, and Sheep. *Proc. Natl. Acad. Sci. U. S. A.* **2005**, *102* (3), 640–645.

(59) Sang, J. C.; Lee, C.-Y.; Luh, F. Y.; Huang, Y.-W.; Chiang, Y.-W.; Chen, R. P.-Y. Slow Spontaneous α-to-β Structural Conversion in a Non-Denaturing Neutral Condition Reveals the Intrinsically Disordered Property of the Disulfide-Reduced Recombinant Mouse Prion Protein. *Prion* **2012**, *6* (5), 489–497.

(60) Bjorndahl, T. C.; Zhou, G.-P.; Liu, X.; Perez-Pineiro, R.; Semenchenko, V.; Saleem, F.; Acharya, S.; Bujold, A.; Sobsey, C. A.; Wishart, D. S. Detailed Biophysical Characterization of the Acid-Induced PrP(c) to PrP(β) Conversion Process. *Biochemistry* **2011**, *50* (7), 1162–1173.

(61) Hosszu, L. L. P.; Trevitt, C. R.; Jones, S.; Batchelor, M.; Scott, D. J.; Jackson, G. S.; Collinge, J.; Waltho, J. P.; Clarke, A. R. Conformational Properties of β-PrP. *J. Biol. Chem.* **2009**, *284* (33), 21981–21990.

(62) Yang, C.; Lo, W.; Kuo, Y.; Sang, J. C.; Lee, C.; Chiang, Y.; Chen, R. P.-Y. Revealing Structural Changes of Prion Protein during Conversion from α-Helical Monomer to β-Oligomers by Means of ESR and Nanochannel Encapsulation. *ACS Chem. Biol.* **2015**, *10* (2), 493–501.

(63) Rudd, P. M.; Endo, T.; Colominas, C.; Groth, D.; Wheeler, S. F.; Harvey, D. J.; Wormald, M. R.; Serban, H.; Prusiner, S. B.; Kobata, A.; Dwek, R. A. Glycosylation Differences between the Normal and Pathogenic Prion Protein Isoforms. *Proc. Natl. Acad. Sci. U. S. A.* **1999**, *96* (23), 13044–13049.

(64) Pan, T.; Li, R.; Wong, B.-S.; Liu, T.; Gambetti, P.; Sy, M.-S. Heterogeneity of Normal Prion Protein in Two- Dimensional Immunoblot: Presence of Various Glycosylated and Truncated Forms. *J. Neurochem.* **2002**, *81* (5), 1092–1101.

(65) Beringue, V.; Mallinson, G.; Kaisar, M.; Tayebi, M.; Sattar, Z.; Jackson, G.; Anstee, D.; Collinge, J.; Hawke, S. Regional Heterogeneity of Cellular Prion Protein Isoforms in the Mouse Brain. *Brain* **2003**, *126* (Pt 9), 2065–2073.

(66) Monnet, C.; Marthiens, V.; Enslen, H.; Frobert, Y.; Sobel, A.; Mège, R. M. Heterogeneity and Regulation of Cellular Prion Protein Glycoforms in Neuronal Cell Lines. *Eur. J. Neurosci.* **2003**, *18* (3), 542–548.

(67) Novitskaya, V.; Makarava, N.; Sylvester, I.; Bronstein, I. B.; Baskakov, I. V. Amyloid Fibrils of Mammalian Prion Protein Induce Axonal Degeneration in NTERA2-Derived Terminally Differentiated Neurons. *J. Neurochem.* **2007**, *102* (2), 398–407.

(68) Katorcha, E.; Makarava, N.; Savtchenko, R.; D'Azzo, A.; Baskakov, I. V. Sialylation of Prion Protein Controls the Rate of Prion Amplification, the Cross-Species Barrier, the Ratio of PrPSc Glycoform and Prion Infectivity. *PLoS Pathog.* **2014**, *10* (9), e1004366.

(69) Katorcha, E.; Makarava, N.; Savtchenko, R.; Baskakov, I. V. Sialylation of the Prion Protein Glycans Controls Prion Replication Rate and Glycoform Ratio. *Sci. Rep.* **2015**, *5* (August), 16912.

(70) Katorcha, E.; Daus, M. L.; Gonzalez-Montalban, N.; Makarava, N.; Lasch, P.; Beekes, M.; Baskakov, I. V. Reversible off and on Switching of Prion Infectivity via Removing and Reinstalling Prion Sialylation. *Sci. Rep.* **2016**, *6* (1), 33119.

(71) Büeler, H.; Fischer, M.; Lang, Y.; Bluethmann, H.; Lipp, H. P.; DeArmond, S. J.; Prusiner, S. B.; Aguet, M.; Weissmann, C. Normal Development and Behaviour of Mice Lacking the Neuronal Cell-Surface PrP Protein. *Nature* **1992**, *356* (6370), 577–582.

(72) Bremer, J.; Baumann, F.; Tiberi, C.; Wessig, C.; Fischer, H.; Schwarz, P.; Steele, A. D.; Toyka, K. V; Nave, K.-A.; Weis, J.; Aguzzi, A. Axonal Prion Protein Is Required for Peripheral Myelin Maintenance. *Nat. Neurosci.* **2010**, *13* (3), 310–318.

(73) Sunde, M.; Serpell, L. C.; Bartlam, M.; Fraser, P. E.; Pepys, M. B.; Blake, C. C. Common Core Structure of Amyloid Fibrils by Synchrotron X-Ray Diffraction. *J. Mol. Biol.* **1997**, *273* (3), 729–739.

(74) Tycko, R. Progress towards a Molecular-Level Structural Understanding of Amyloid Fibrils. *Curr. Opin. Struct. Biol.* **2004**, *14* (1), 96–103.

(75) Fitzpatrick, A. W. P.; Debelouchina, G. T.; Bayro, M. J.; Clare, D. K.; Caporini, M. a; Bajaj, V. S.; Jaroniec, C. P.; Wang, L.; Ladizhansky, V.; Müller, S. a; MacPhee, C. E.; Waudby, C. a; Mott, H. R.; De Simone, A.; Knowles, T. P. J.; Saibil, H. R.; Vendruscolo, M.; Orlova, E. V; Griffin, R. G.; Dobson, C. M. Atomic Structure and Hierarchical Assembly of a Cross-β Amyloid Fibril. *Proc. Natl. Acad. Sci. U. S. A.* **2013**, *110* (14), 5468–5473.

(76) Wille, H.; Michelitsch, M. D.; Guenebaut, V.; Supattapone, S.; Serban, A.; Cohen, F. E.;

Agard, D. a; Prusiner, S. B. Structural Studies of the Scrapie Prion Protein by Electron Crystallography. *Proc. Natl. Acad. Sci. U. S. A.* **2002**, *99* (6), 3563–3568.

(77) Govaerts, C.; Wille, H.; Prusiner, S. B.; Cohen, F. E. Evidence for Assembly of Prions with Left-Handed β-Helices into Trimers. *Proc. Natl. Acad. Sci. U. S. A.* **2004**, *101* (22), 8342–8347.

(78) DeMarco, M. L.; Daggett, V. From Conversion to Aggregation: Protofibril Formation of the Prion Protein. *Proc. Natl. Acad. Sci. U. S. A.* **2004**, *101* (8), 2293–2298.

(79) Cobb, N. J.; Sönnichsen, F. D.; McHaourab, H.; Surewicz, W. K. Molecular Architecture of Human Prion Protein Amyloid: A Parallel, in-Register β-Structure. *Proc. Natl. Acad. Sci. U. S. A.* **2007**, *104* (48), 18946–18951.

(80) Hafner-Bratkovic, I.; Bester, R.; Pristovsek, P.; Gaedtke, L.; Veranic, P.; Gaspersic, J.; Mancek-Keber, M.; Avbelj, M.; Polymenidou, M.; Julius, C.; Aguzzi, A.; Vorberg, I.; Jerala, R. Globular Domain of the Prion Protein Needs to Be Unlocked by Domain Swapping to Support Prion Protein Conversion. *J. Biol. Chem.* **2011**, *286* (14), 12149–12156.

(81) Knaus, K. J.; Morillas, M.; Swietnicki, W.; Malone, M.; Surewicz, W. K.; Yee, V. C. Crystal Structure of the Human Prion Protein Reveals a Mechanism for Oligomerization. *Nat. Struct. Biol.* **2001**, *8* (9), 770–774.

(82) Diaz-Espinoza, R.; Soto, C. High-Resolution Structure of Infectious Prion Protein: The Final Frontier. *Nat. Struct. Mol. Biol.* **2012**, *19* (4), 370–377.

(83) Vázquez-Fernández, E.; Vos, M. R.; Afanasyev, P.; Cebey, L.; Sevillano, A. M.; Vidal, E.; Rosa, I.; Renault, L.; Ramos, A.; Peters, P. J.; Fernández, J. J.; van Heel, M.; Young, H. S.; Requena, J. R.; Wille, H. The Structural Architecture of an Infectious Mammalian Prion Using Electron Cryomicroscopy. *PLoS Pathog.* **2016**, *12* (9), e1005835.

(84) Lu, X.; Wintrode, P. L.; Surewicz, W. K. β-Sheet Core of Human Prion Protein Amyloid Fibrils as Determined by Hydrogen/Deuterium Exchange. *Proc. Natl. Acad. Sci. U. S. A.* **2007**, *104* (5), 1510–1515.

(85) Tycko, R.; Savtchenko, R.; Ostapchenko, V. G.; Makarava, N.; Baskakov, I. V. The α-Helical C-Terminal Domain of Full-Length Recombinant PrP Converts to an in-Register Parallel β-Sheet Structure in PrP Fibrils: Evidence from Solid State Nuclear Magnetic Resonance. *Biochemistry* **2010**, *49* (44), 9488–9497.

(86) Groveman, B. R.; Dolan, M. A.; Taubner, L. M.; Kraus, A.; Wickner, R. B.; Caughey, B. Parallel In-Register Intermolecular β-Sheet Architectures for Prion-Seeded Prion

Protein (PrP) Amyloids. *J. Biol. Chem.* **2014**, *289* (35), 24129–24142.

(87) Apostol, M. I.; Perry, K.; Surewicz, W. K. Crystal Structure of a Human Prion Protein Fragment Reveals a Motif for Oligomer Formation. *J. Am. Chem. Soc.* **2013**, *135* (28), 10202–10205.

(88) Choi, J.-K.; Cali, I.; Surewicz, K.; Kong, Q.; Gambetti, P.; Surewicz, W. K. Amyloid Fibrils from the N-Terminal Prion Protein Fragment Are Infectious. *Proc. Natl. Acad. Sci. U. S. A.* **2016**, *113* (48), 13851–13856.

(89) Theint, T.; Nadaud, P. S.; Surewicz, K.; Surewicz, W. K.; Jaroniec, C. P. 13C and 15N Chemical Shift Assignments of Mammalian Y145Stop Prion Protein Amyloid Fibrils. *Biomol. NMR Assign.* **2017**, *11* (1), 75–80.

(90) Wille, H.; Bian, W.; McDonald, M.; Kendall, A.; Colby, D. W.; Bloch, L.; Ollesch, J.; Borovinskiy, A. L.; Cohen, F. E.; Prusiner, S. B.; Stubbs, G. Natural and Synthetic Prion Structure from X-Ray Fiber Diffraction. *Proc. Natl. Acad. Sci. U. S. A.* **2009**, *106* (40), 16990–16995.

(91) Smirnovas, V.; Baron, G. S.; Offerdahl, D. K.; Raymond, G. J.; Caughey, B.; Surewicz, W. K. Structural Organization of Brain-Derived Mammalian Prions Examined by Hydrogen-Deuterium Exchange. *Nat. Struct. Mol. Biol.* **2011**, *18* (4), 504–506.

(92) Piro, J. R.; Wang, F.; Walsh, D. J.; Rees, J. R.; Ma, J.; Supattapone, S. Seeding Specificity and Ultrastructural Characteristics of Infectious Recombinant Prions. *Biochemistry* **2011**, *50* (33), 7111–7116.

(93) Sevillano, A. M.; Fernández-Borges, N.; Younas, N.; Wang, F.; R Elezgarai, S.; Bravo, S.; Vázquez-Fernández, E.; Rosa, I.; Eraña, H.; Gil, D.; Veiga, S.; Vidal, E.; Erickson-Beltran, M. L.; Guitián, E.; Silva, C. J.; Nonno, R.; Ma, J.; Castilla, J.; R Requena, J. Recombinant PrPSc Shares Structural Features with Brain-Derived PrPSc: Insights from Limited Proteolysis. *PLoS Pathog.* **2018**, *14* (1), e1006797.

(94) Wille, H.; Requena, J. R. The Structure of PrPSc Prions. *Pathogens* **2018**, *7* (1), 20.

(95) Zweckstetter, M.; Requena, J. R.; Wille, H. Elucidating the Structure of an Infectious Protein. *PLoS Pathog.* **2017**, *13* (4), 1–6.

(96) Flores-Fernández, J.; Rathod, V.; Wille, H. Comparing the Folds of Prions and Other Pathogenic Amyloids. *Pathogens* **2018**, *7* (2), 50.

(97) Mizuno, N.; Baxa, U.; Steven, A. C. Structural Dependence of HET-s Amyloid Fibril Infectivity Assessed by Cryoelectron Microscopy. *Proc. Natl. Acad. Sci. U. S. A.* **2011**,

108 (8), 3252–3257.

(98) Yoder, M. D.; Jurnak, F. Protein Motifs. 3. The Parallel Beta Helix and Other Coiled Folds. *FASEB J.* **1995**, *9* (5), 335–342.

(99) Collinge, J.; Clarke, A. R. A General Model of Prion Strains and Their Pathogenicity. *Science* **2007**, *318* (5852), 930–936.

(100) Jankovic, J. Parkinson's Disease: Clinical Features and Diagnosis. *J. Neurol. Neurosurg. Psychiatry* **2008**, *79* (4), 368–376.

(101) Hoehn, M. M.; Yahr, M. D. Parkinsonism: Onset, Progression and Mortality. *Neurology* **1967**, *17* (5), 427–442.

(102) Hirtz, D.; Thurman, D. J.; Gwinn-Hardy, K.; Mohamed, M.; Chaudhuri, A. R.; Zalutsky, R. How Common Are the "Common" Neurologic Disorders? *Neurology* **2007**, *68* (5), 326–337.

(103) Tysnes, O.-B.; Storstein, A. Epidemiology of Parkinson's Disease. *J. Neural Transm.* **2017**, *124* (8), 901–905.

(104) de Lau, L. M. L.; Breteler, M. M. B. Epidemiology of Parkinson's Disease. *Lancet Neurol.* **2006**, *5* (6), 525–535.

(105) Samii, A.; Nutt, J. G.; Ransom, B. R. Parkinson's Disease. *Lancet* **2004**, *363* (9423), 1783–1793.

(106) de Rijk, M. C.; Launer, L. J.; Berger, K.; Breteler, M. M.; Dartigues, J. F.; Baldereschi, M.; Fratiglioni, L.; Lobo, A.; Martinez-Lage, J.; Trenkwalder, C.; Hofman, A. Prevalence of Parkinson's Disease in Europe: A Collaborative Study of Population-Based Cohorts. Neurologic Diseases in the Elderly Research Group. *Neurology* **2000**, *54* (11 Suppl 5), S21-3.

(107) de Rijk, M. C.; Breteler, M. M.; Graveland, G. A.; Ott, A.; Grobbee, D. E.; van der Meché, F. G.; Hofman, A. Prevalence of Parkinson's Disease in the Elderly: The Rotterdam Study. *Neurology* **1995**, *45* (12), 2143–2146.

(108) Ascherio, A.; Schwarzschild, M. A. The Epidemiology of Parkinson's Disease: Risk Factors and Preventioan. *Lancet Neurol.* **2016**, *15* (12), 1257–1272.

(109) Parkinson, J. An Essay on the Shaking Palsy. *J. Neuropsych. Clin. Neurosci.* **2002**, *14* (2), 223–236.

(110) Lees, A. J. Unresolved Issues Relating to the Shaking Palsy on the Celebration of

James Parkinson's 250th Birthday. *Mov. Disord.* **2007**, *22 Suppl 1* (SUPPL. 17), S327-34.

(111) Lewy, F. H. Paralysis Agitans. In *Handbuch der Neurologie*; Lewandowsky, M., Ed.; Springer-Verlag, Berlin, 1912; pp 920–933.

(112) Schulz-Schaeffer, W. J. The Synaptic Pathology of α-Synuclein Aggregation in Dementia with Lewy Bodies, Parkinson's Disease and Parkinson's Disease Dementia. *Acta Neuropathol.* **2010**, *120* (2), 131–143.

(113) Forno, L. S. Neuropathology of Parkinson's Disease. *J. Neuropathol. Exp. Neurol.* **1996**, *55* (3), 259–272.

(114) Spillantini, M. G.; Schmidt, M. L.; Lee, V. M.-Y.; Trojanowski, J. Q.; Jakes, R.; Goedert, M. α-Synuclein in Lewy Bodies. *Nature* **1997**, *388* (6645), 839–840.

(115) Polymeropoulos, M. H.; Lavedan, C.; Leroy, E.; Ide, S. E.; Dehejia, A.; Dutra, A.; Pike, B.; Root, H.; Rubenstein, J.; Boyer, R.; Stenroos, E. S.; Chandrasekharappa, S.; Athanassiadou, A.; Papapetropoulos, T.; Johnson, W. G.; Lazzarini, A. M.; Duvoisin, R. C.; Di Iorio, G.; Golbe, L. I.; Nussbaum, R. L. Mutation in the α-Synuclein Gene Identified in Families with Parkinson's Disease. *Science* **1997**, *276* (5321), 2045–2047.

(116) Goedert, M. Alzheimer's and Parkinson's Diseases: The Prion Concept in Relation to Assembled Aβ, Tau, and α-Synuclein. *Science* **2015**, *349* (6248), 1255555.

(117) Bisaglia, M.; Mammi, S.; Bubacco, L. Structural Insights on Physiological Functions and Pathological Effects of α-Synuclein. *FASEB J.* **2009**, *23* (2), 329–340.

(118) Maroteaux, L.; Campanelli, J. T.; Scheller, R. H. Synuclein: A Neuron-Specific Protein Localized to the Nucleus and Presynaptic Nerve Terminal. *J. Neurosci.* **1988**, *8* (8), 2804–2815.

(119) George, J. M. The Synucleins. *Genome Biol.* **2002**, *3* (1), reviews3002.1–3002.6.

(120) Bodner, C. R.; Dobson, C. M.; Bax, A. Multiple Tight Phospholipid-Binding Modes of α-Synuclein Revealed by Solution NMR Spectroscopy. *J. Mol. Biol.* **2009**, *390* (4), 775–790.

(121) Davidson, W. S.; Jonas, A.; Clayton, D. F.; George, J. M. Stabilization of α-Synuclein Secondary Structure upon Binding to Synthetic Membranes. *J. Biol. Chem.* **1998**, *273* (16), 9443–9449.

(122) Ulmer, T. S.; Bax, A.; Cole, N. B.; Nussbaum, R. L. Structure and Dynamics of Micelle-

Bound Human α-Synuclein. *J. Biol. Chem.* **2005**, *280* (10), 9595–9603.

(123) Eliezer, D.; Kutluay, E.; Bussell, R.; Browne, G. Conformational Properties of α-Synuclein in Its Free and Lipid-Associated States. *J. Mol. Biol.* **2001**, *307* (4), 1061–1073.

(124) Necula, M.; Chirita, C. N.; Kuret, J. Rapid Anionic Micelle-Mediated α-Synuclein Fibrillization in Vitro. *J. Biol. Chem.* **2003**, *278* (47), 46674–46680.

(125) Middleton, E. R.; Rhoades, E. Effects of Curvature and Composition on α-Synuclein Binding to Lipid Vesicles. *Biophys. J.* **2010**, *99* (7), 2279–2288.

(126) Varkey, J.; Isas, J. M.; Mizuno, N.; Jensen, M. B.; Bhatia, V. K.; Jao, C. C.; Petrlova, J.; Voss, J. C.; Stamou, D. G.; Steven, A. C.; Langen, R. Membrane Curvature Induction and Tubulation Are Common Features of Synucleins and Apolipoproteins. *J. Biol. Chem.* **2010**, *285* (42), 32486–32493.

(127) Westphal, C. H.; Chandra, S. S. Monomeric Synucleins Generate Membrane Curvature. *J. Biol. Chem.* **2013**, *288* (3), 1829–1840.

(128) Ferreon, A. C. M.; Gambin, Y.; Lemke, E. A.; Deniz, A. A. Interplay of α-Synuclein Binding and Conformational Switching Probed by Single-Molecule Fluorescence. *Proc. Natl. Acad. Sci. U. S. A.* **2009**, *106* (14), 5645–5650.

(129) Krüger, R.; Kuhn, W.; Müller, T.; Woitalla, D.; Graeber, M.; Kösel, S.; Przuntek, H.; Epplen, J. T.; Schöls, L.; Riess, O. Ala30Pro Mutation in the Gene Encoding α-Synuclein in Parkinson's Disease. *Nat. Genet.* **1998**, *18* (2), 106–108.

(130) Zarranz, J. J.; Alegre, J.; Gómez-Esteban, J. C.; Lezcano, E.; Ros, R.; Ampuero, I.; Vidal, L.; Hoenicka, J.; Rodriguez, O.; Atarés, B.; Llorens, V.; Gomez Tortosa, E.; Del Ser, T.; Muñoz, D. G.; De Yebenes, J. G. The New Mutation, E46K, of α-Synuclein Causes Parkinson and Lewy Body Dementia. *Ann. Neurol.* **2004**, *55* (2), 164–173.

(131) Martikainen, M. H.; Päivärinta, M.; Hietala, M.; Kaasinen, V. Clinical and Imaging Findings in Parkinson Disease Associated with the A53E SNCA Mutation. *Neurol. Genet.* **2015**, *1* (4), 1–4.

(132) Pasanen, P.; Myllykangas, L.; Siitonen, M.; Raunio, A.; Kaakkola, S.; Lyytinen, J.; Tienari, P. J.; Pöyhönen, M.; Paetau, A. Novel α-Synuclein Mutation A53E Associated with Atypical Multiple System Atrophy and Parkinson's Disease-Type Pathology. *Neurobiol. Aging* **2014**, *35* (9), 2180.e1-5.

(133) Proukakis, C.; Dudzik, C. G.; Brier, T.; MacKay, D. S.; Cooper, J. M.; Millhauser, G. L.;

Houlden, H.; Schapira, A. H. A Novel α-Synuclein Missense Mutation in Parkinson Disease. *Neurology* **2013**, *80* (11), 1062–1064.

(134) Appel-Cresswell, S.; Vilarino-Guell, C.; Encarnacion, M.; Sherman, H.; Yu, I.; Shah, B.; Weir, D.; Thompson, C.; Szu-Tu, C.; Trinh, J.; Aasly, J. O.; Rajput, A.; Rajput, A. H.; Jon Stoessl, A.; Farrer, M. J. Alpha-Synuclein p.H50Q, a Novel Pathogenic Mutation for Parkinson's Disease. *Mov. Disord.* **2013**, *28* (6), 811–813.

(135) Kiely, A. P.; Asi, Y. T.; Kara, E.; Limousin, P.; Ling, H.; Lewis, P.; Proukakis, C.; Quinn, N.; Lees, A. J.; Hardy, J.; Revesz, T.; Houlden, H.; Holton, J. L. α-Synucleinopathy Associated with G51D SNCA Mutation: A Link between Parkinson's Disease and Multiple System Atrophy? *Acta Neuropathol.* **2013**, *125* (5), 753–769.

(136) Lesage, S.; Anheim, M.; Letournel, F.; Bousset, L.; Honoré, A.; Rozas, N.; Pieri, L.; Madiona, K.; Dürr, A.; Melki, R.; Verny, C.; Brice, A. G51D α-Synuclein Mutation Causes a Novel Parkinsonian-Pyramidal Syndrome. *Ann. Neurol.* **2013**, *73* (4), 459–471.

(137) Venda, L. L.; Cragg, S. J.; Buchman, V. L.; Wade-Martins, R. α-Synuclein and Dopamine at the Crossroads of Parkinson's Disease. *Trends Neurosci.* **2010**, *33* (12), 559–568.

(138) Deleersnijder, A.; Gerard, M.; Debyser, Z.; Baekelandt, V. The Remarkable Conformational Plasticity of Alpha-Synuclein: Blessing or Curse? *Trends Mol. Med.* **2013**, *19* (6), 368–377.

(139) Kessler, J. C.; Rochet, J.-C.; Lansbury, P. T. The N-Terminal Repeat Domain of α-Synuclein Inhibits β-Sheet and Amyloid Fibril Formation. *Biochemistry* **2003**, *42* (3), 672–678.

(140) Koo, H.-J.; Lee, H.-J.; Im, H. Sequence Determinants Regulating Fibrillation of Human α-Synuclein. *Biochem. Biophys. Res. Commun.* **2008**, *368* (3), 772–778.

(141) Dikiy, I.; Eliezer, D. Folding and Misfolding of Alpha-Synuclein on Membranes. *Biochim. Biophys. Acta* **2012**, *1818* (4), 1013–1018.

(142) el-Agnaf, O. M. A.; Irvine, G. B. Aggregation and Neurotoxicity of α-Synuclein and Related Peptides. *Biochem. Soc. Trans.* **2002**, *30* (4), 559–565.

(143) Guerrero-Ferreira, R.; Taylor, N. M.; Mona, D.; Ringler, P.; Lauer, M. E.; Riek, R.; Britschgi, M.; Stahlberg, H. Cryo-EM Structure of Alpha-Synuclein Fibrils. *Elife* **2018**, *7*.

(144) Serpell, L. C.; Berriman, J.; Jakes, R.; Goedert, M.; Crowther, R. A. Fiber Diffraction of

Synthetic α-Synuclein Filaments Shows Amyloid-like Cross-β Conformation. *Proc. Natl. Acad. Sci. U. S. A.* **2000**, *97* (9), 4897–4902.

(145) Miake, H.; Mizusawa, H.; Iwatsubo, T.; Hasegawa, M. Biochemical Characterization of the Core Structure of α-Synuclein Filaments. *J. Biol. Chem.* **2002**, *277* (21), 19213–19219.

(146) Der-Sarkissian, A.; Jao, C. C.; Chen, J.; Langen, R. Structural Organization of α-Synuclein Fibrils Studied by Site-Directed Spin Labeling. *J. Biol. Chem.* **2003**, *278* (39), 37530–37535.

(147) Heise, H.; Hoyer, W.; Becker, S.; Andronesi, O. C.; Riedel, D.; Baldus, M. Molecular-Level Secondary Structure, Polymorphism, and Dynamics of Full-Length α-Synuclein Fibrils Studied by Solid-State NMR. *Proc. Natl. Acad. Sci. U. S. A.* **2005**, *102* (44), 15871–15876.

(148) Del Mar, C.; Greenbaum, E. A.; Mayne, L.; Englander, S. W.; Woods, V. L. Structure and Properties of α-Synuclein and Other Amyloids Determined at the Amino Acid Level. *Proc. Natl. Acad. Sci. U. S. A.* **2005**, *102* (43), 15477–15482.

(149) Du, H.-N.; Tang, L.; Luo, X.-Y.; Li, H.-T.; Hu, J.; Zhou, J.-W.; Hu, H.-Y. A Peptide Motif Consisting of Glycine, Alanine, and Valine Is Required for the Fibrillization and Cytotoxicity of Human α-Synuclein. *Biochemistry* **2003**, *42* (29), 8870–8878.

(150) Giasson, B. I.; Murray, I. V; Trojanowski, J. Q.; Lee, V. M. A Hydrophobic Stretch of 12 Amino Acid Residues in the Middle of α-Synuclein Is Essential for Filament Assembly. *J. Biol. Chem.* **2001**, *276* (4), 2380–2386.

(151) Park, S. M.; Jung, H. Y.; Chung, K. C.; Rhim, H.; Park, J. H.; Kim, J. Stress-Induced Aggregation Profiles of GST-α-Synuclein Fusion Proteins: Role of the C-Terminal Acidic Tail of α-Synuclein in Protein Thermosolubility and Stability. *Biochemistry* **2002**, *41* (12), 4137–4146.

(152) Qin, Z.; Hu, D.; Han, S.; Hong, D.-P.; Fink, A. L. Role of Different Regions of α-Synuclein in the Assembly of Fibrils. *Biochemistry* **2007**, *46* (46), 13322–13330.

(153) Hong, D.-P.; Xiong, W.; Chang, J.-Y.; Jiang, C. The Role of the C-Terminus of Human α-Synuclein: Intra-Disulfide Bonds between the C-Terminus and Other Regions Stabilize Non-Fibrillar Monomeric Isomers. *FEBS Lett.* **2011**, *585* (3), 561–566.

(154) Crowther, R. A.; Jakes, R.; Spillantini, M. G.; Goedert, M. Synthetic Filaments Assembled from C-Terminally Truncated α-Synuclein. *FEBS Lett.* **1998**, *436* (3), 309–312.

(155) Hoyer, W.; Cherny, D.; Subramaniam, V.; Jovin, T. M. Impact of the Acidic C-Terminal Region Comprising Amino Acids 109-140 on α-Synuclein Aggregation in Vitro. *Biochemistry* **2004**, *43* (51), 16233–16242.

(156) Jakes, R.; Spillantini, M. G.; Goedert, M. Identification of Two Distinct Synucleins from Human Brain. *FEBS Lett.* **1994**, *345* (1), 27–32.

(157) Liu, G.; Zhang, C.; Yin, J.; Li, X.; Cheng, F.; Li, Y.; Yang, H.; Uéda, K.; Chan, P.; Yu, S. α-Synuclein Is Differentially Expressed in Mitochondria from Different Rat Brain Regions and Dose-Dependently down-Regulates Complex I Activity. *Neurosci. Lett.* **2009**, *454* (3), 187–192.

(158) Bellani, S.; Sousa, V. L.; Ronzitti, G.; Valtorta, F.; Meldolesi, J.; Chieregatti, E. The Regulation of Synaptic Function by α-Synuclein. *Commun. Integr. Biol.* **2010**, *3* (2), 106–109.

(159) Chandra, S.; Gallardo, G.; Fernández-Chacón, R.; Schlüter, O. M.; Südhof, T. C. α-Synuclein Cooperates with CSPalpha in Preventing Neurodegeneration. *Cell* **2005**, *123* (3), 383–396.

(160) Burré, J.; Sharma, M.; Tsetsenis, T.; Buchman, V.; Etherton, M. R.; Südhof, T. C. α-Synuclein Promotes SNARE-Complex Assembly in Vivo and in Vitro. *Science* **2010**, *329* (5999), 1663–1667.

(161) Perlmutter, J. D.; Braun, A. R.; Sachs, J. N. Curvature Dynamics of α-Synuclein Familial Parkinson Disease Mutants: Molecular Simulations of the Micelle- and Bilayer-Bound Forms. *J. Biol. Chem.* **2009**, *284* (11), 7177–7189.

(162) Davies, P.; Moualla, D.; Brown, D. R. Alpha-Synuclein Is a Cellular Ferrireductase. *PLoS One* **2011**, *6* (1), e15814.

(163) Quilty, M. C.; King, A. E.; Gai, W.-P.; Pountney, D. L.; West, A. K.; Vickers, J. C.; Dickson, T. C. Alpha-Synuclein Is Upregulated in Neurones in Response to Chronic Oxidative Stress and Is Associated with Neuroprotection. *Exp. Neurol.* **2006**, *199* (2), 249–256.

(164) Abeliovich, A.; Schmitz, Y.; Fariñas, I.; Choi-Lundberg, D.; Ho, W. H.; Castillo, P. E.; Shinsky, N.; Verdugo, J. M.; Armanini, M.; Ryan, A.; Hynes, M.; Phillips, H.; Sulzer, D.; Rosenthal, A. Mice Lacking α-Synuclein Display Functional Deficits in the Nigrostriatal Dopamine System. *Neuron* **2000**, *25* (1), 239–252.

(165) Chandra, S.; Fornai, F.; Kwon, H.-B.; Yazdani, U.; Atasoy, D.; Liu, X.; Hammer, R. E.; Battaglia, G.; German, D. C.; Castillo, P. E.; Südhof, T. C. Double-Knockout Mice for α-

and β-Synucleins: Effect on Synaptic Functions. *Proc. Natl. Acad. Sci. U. S. A.* **2004**, *101* (41), 14966–14971.

(166) Breydo, L.; Wu, J. W.; Uversky, V. N. α-Synuclein Misfolding and Parkinson's Disease. *Biochim. Biophys. Acta* **2012**, *1822* (2), 261–285.

(167) Rodriguez, J. A.; Ivanova, M. I.; Sawaya, M. R.; Cascio, D.; Reyes, F. E.; Shi, D.; Sangwan, S.; Guenther, E. L.; Johnson, L. M.; Zhang, M.; Jiang, L.; Arbing, M. A.; Nannenga, B. L.; Hattne, J.; Whitelegge, J.; Brewster, A. S.; Messerschmidt, M.; Boutet, S.; Sauter, N. K.; Gonen, T.; Eisenberg, D. S. Structure of the Toxic Core of α-Synuclein from Invisible Crystals. *Nature* **2015**, *525* (7570), 486–490.

(168) Tuttle, M. D.; Comellas, G.; Nieuwkoop, A. J.; Covell, D. J.; Berthold, D. A.; Kloepper, K. D.; Courtney, J. M.; Kim, J. K.; Barclay, A. M.; Kendall, A.; Wan, W.; Stubbs, G.; Schwieters, C. D.; Lee, V. M. Y.; George, J. M.; Rienstra, C. M. Solid-State NMR Structure of a Pathogenic Fibril of Full-Length Human α-Synuclein. *Nat. Struct. Mol. Biol.* **2016**, *23* (5), 409–415.

(169) Bousset, L.; Pieri, L.; Ruiz-Arlandis, G.; Gath, J.; Jensen, P. H.; Habenstein, B.; Madiona, K.; Olieric, V.; Böckmann, A.; Meier, B. H.; Melki, R. Structural and Functional Characterization of Two Alpha-Synuclein Strains. *Nat. Commun.* **2013**, *4*, 2575.

(170) Roeters, S. J.; Iyer, A.; Pletikapić, G.; Kogan, V.; Subramaniam, V.; Woutersen, S. Evidence for Intramolecular Antiparallel Beta-Sheet Structure in Alpha-Synuclein Fibrils from a Combination of Two-Dimensional Infrared Spectroscopy and Atomic Force Microscopy. *Sci. Rep.* **2017**, *7* (December 2016), 41051.

(171) Kim, H.-Y.; Cho, M.-K.; Kumar, A.; Maier, E.; Siebenhaar, C.; Becker, S.; Fernandez, C. O.; Lashuel, H. A.; Benz, R.; Lange, A.; Zweckstetter, M. Structural Properties of Pore-Forming Oligomers of α-Synuclein. *J. Am. Chem. Soc.* **2009**, *131* (47), 17482–17489.

(172) Vilar, M.; Chou, H.; Lührs, T.; Maji, S. K.; Riek-Loher, D.; Verel, R.; Manning, G.; Stahlberg, H.; Riek, R. The Fold of α-Synuclein Fibrils. *Proc. Natl. Acad. Sci. U. S. A.* **2008**, *105* (25), 8637–8642.

(173) Li, B.; Ge, P.; Murray, K. A.; Sheth, P.; Zhang, M.; Nair, G.; Sawaya, M. R.; Shin, W. S.; Boyer, D. R.; Ye, S.; Eisenberg, D. S.; Zhou, Z. H.; Jiang, L. Cryo-EM of Full-Length α-Synuclein Reveals Fibril Polymorphs with a Common Structural Kernel. *Nat. Commun.* **2018**, *9* (1), 1–10.

(174) Jucker, M.; Walker, L. C. Self-Propagation of Pathogenic Protein Aggregates in Neurodegenerative Diseases. *Nature* **2013**, *501* (7465), 45–51.

(175) Jarrett, J. T.; Lansbury, P. T. Seeding "One-Dimensional Crystallization" of Amyloid: A Pathogenic Mechanism in Alzheimer's Disease and Scrapie? *Cell* **1993**, *73* (6), 1055–1058.

(176) Serio, T. R.; Cashikar, A. G.; Kowal, A. S.; Sawicki, G. J.; Moslehi, J. J.; Serpell, L.; Arnsdorf, M. F.; Lindquist, S. L. Nucleated Conformational Conversion and the Replication of Conformational Information by a Prion Determinant. *Science* **2000**, *289* (5483), 1317–1321.

(177) Lee, J.; Culyba, E. K.; Powers, E. T.; Kelly, J. W. Amyloid-β Forms Fibrils by Nucleated Conformational Conversion of Oligomers. *Nat. Chem. Biol.* **2011**, *7* (9), 602–609.

(178) Yang, J.; Dear, A. J.; Michaels, T. C. T.; Dobson, C. M.; Knowles, T. P. J.; Wu, S.; Perrett, S. Direct Observation of Oligomerization by Single Molecule Fluorescence Reveals a Multistep Aggregation Mechanism for the Yeast Prion Protein Ure2. *J. Am. Chem. Soc.* **2018**, *140* (7), 2493–2503.

(179) Lorenzen, N.; Nielsen, S. B.; Buell, A. K.; Kaspersen, J. D.; Arosio, P.; Vad, B. S.; Paslawski, W.; Christiansen, G.; Valnickova-Hansen, Z.; Andreasen, M.; Enghild, J. J.; Pedersen, J. S.; Dobson, C. M.; Knowles, T. P. J.; Otzen, D. E. The Role of Stable α-Synuclein Oligomers in the Molecular Events Underlying Amyloid Formation. *J. Am. Chem. Soc.* **2014**, *136* (10), 3859–3868.

(180) Cremades, N.; Cohen, S. I. A.; Deas, E.; Abramov, A. Y.; Chen, A. Y.; Orte, A.; Sandal, M.; Clarke, R. W.; Dunne, P.; Aprile, F. A.; Bertoncini, C. W.; Wood, N. W.; Knowles, T. P. J.; Dobson, C. M.; Klenerman, D. Direct Observation of the Interconversion of Normal and Toxic Forms of α-Synuclein. *Cell* **2012**, *149* (5), 1048–1059.

(181) Campioni, S.; Mannini, B.; Zampagni, M.; Pensalfini, A.; Parrini, C.; Evangelisti, E.; Relini, A.; Stefani, M.; Dobson, C. M.; Cecchi, C.; Chiti, F. A Causative Link between the Structure of Aberrant Protein Oligomers and Their Toxicity. *Nat. Chem. Biol.* **2010**, *6* (2), 140–147.

(182) Auer, S.; Meersman, F.; Dobson, C. M.; Vendruscolo, M. A Generic Mechanism of Emergence of Amyloid Protofilaments from Disordered Oligomeric Aggregates. *PLoS Comput. Biol.* **2008**, *4* (11), e1000222.

(183) Knowles, T. P. J.; Buehler, M. J. Nanomechanics of Functional and Pathological Amyloid Materials. *Nat. Nanotechnol.* **2011**, *6* (8), 469–479.

(184) Tanaka, M.; Collins, S. R.; Toyama, B. H.; Weissman, J. S. The Physical Basis of How Prion Conformations Determine Strain Phenotypes. *Nature* **2006**, *442* (7102), 585–

589.

(185) Nakatani-Webster, E.; Nath, A. Inferring Mechanistic Parameters from Amyloid Formation Kinetics by Approximate Bayesian Computation. *Biophys. J.* **2017**, *112* (5), 868–880.

(186) Knowles, T. P. J.; Waudby, C. a; Devlin, G. L.; Cohen, S. I. a; Aguzzi, A.; Vendruscolo, M.; Terentjev, E. M.; Welland, M. E.; Dobson, C. M. An Analytical Solution to the Kinetics of Breakable Filament Assembly. *Science* **2009**, *326* (5959), 1533–1537.

(187) Collins, S. R.; Douglass, A.; Vale, R. D.; Weissman, J. S. Mechanism of Prion Propagation: Amyloid Growth Occurs by Monomer Addition. *PLoS Biol.* **2004**, *2* (10), e321.

(188) Toyama, B. H.; Kelly, M. J. S.; Gross, J. D.; Weissman, J. S. The Structural Basis of Yeast Prion Strain Variants. *Nature* **2007**, *449* (7159), 233–237.

(189) Aguzzi, A. Understanding the Diversity of Prions. *Nat. Cell Biol.* **2004**, *6* (4), 290–292.

(190) Cohen, S. I. A.; Vendruscolo, M.; Dobson, C. M.; Knowles, T. P. J. From Macroscopic Measurements to Microscopic Mechanisms of Protein Aggregation. *J. Mol. Biol.* **2012**, *421* (2–3), 160–171.

(191) Iljina, M.; Garcia, G. A.; Horrocks, M. H.; Tosatto, L.; Choi, M. L.; Ganzinger, K. A.; Abramov, A. Y.; Gandhi, S.; Wood, N. W.; Cremades, N.; Dobson, C. M.; Knowles, T. P. J.; Klenerman, D. Kinetic Model of the Aggregation of Alpha-Synuclein Provides Insights into Prion-like Spreading. *Proc. Natl. Acad. Sci. U. S. A.* **2016**, *113* (9), E1206-15.

(192) Kundel, F.; Hong, L.; Falcon, B.; McEwan, W. A.; Michaels, T. C. T.; Meisl, G.; Esteras, N.; Abramov, A. Y.; Knowles, T. J. P.; Goedert, M.; Klenerman, D. Measurement of Tau Filament Fragmentation Provides Insights into Prion-like Spreading. *ACS Chem. Neurosci.* **2018**, *9* (6), 1276–1282.

(193) Meisl, G.; Kirkegaard, J. B.; Arosio, P.; Michaels, T. C. T.; Vendruscolo, M.; Dobson, C. M.; Linse, S.; Knowles, T. P. J. Molecular Mechanisms of Protein Aggregation from Global Fitting of Kinetic Models. *Nat. Protoc.* **2016**, *11* (2), 252–272.

(194) Cohen, S. I. a; Linse, S.; Luheshi, L. M.; Hellstrand, E.; White, D. a; Rajah, L.; Otzen, D. E.; Vendruscolo, M.; Dobson, C. M.; Knowles, T. P. J. Proliferation of Amyloid-B42 Aggregates Occurs through a Secondary Nucleation Mechanism. *Proc. Natl. Acad. Sci. U. S. A.* **2013**, *110* (24), 9758–9763.

(195) Shammas, S. L.; Garcia, G. A.; Kumar, S.; Kjaergaard, M.; Horrocks, M. H.; Shivji, N.; Mandelkow, E.; Knowles, T. P. J.; Mandelkow, E.; Klenerman, D. A Mechanistic Model of Tau Amyloid Aggregation Based on Direct Observation of Oligomers. *Nat. Commun.* **2015**, *6*, 7025.

(196) Bucciantini, M.; Giannoni, E.; Chiti, F.; Baroni, F.; Formigli, L.; Zurdo, J.; Taddei, N.; Ramponi, G.; Dobson, C. M.; Stefani, M. Inherent Toxicity of Aggregates Implies a Common Mechanism for Protein Misfolding Diseases. *Nature* **2002**, *416* (6880), 507–511.

(197) Stefani, M.; Dobson, C. M. Protein Aggregation and Aggregate Toxicity: New Insights into Protein Folding, Misfolding Diseases and Biological Evolution. *J. Mol. Med.* **2003**, *81* (11), 678–699.

(198) Baglioni, S.; Casamenti, F.; Bucciantini, M.; Luheshi, L. M.; Taddei, N.; Chiti, F.; Dobson, C. M.; Stefani, M. Prefibrillar Amyloid Aggregates Could Be Generic Toxins in Higher Organisms. *J. Neurosci.* **2006**, *26* (31), 8160–8167.

(199) Zhang, C.; Jackson, A. P.; Zhang, Z.-R.; Han, Y.; Yu, S.; He, R.-Q.; Perrett, S. Amyloid-like Aggregates of the Yeast Prion Protein Ure2 Enter Vertebrate Cells by Specific Endocytotic Pathways and Induce Apoptosis. *PLoS One* **2010**, *5* (9), 1–12.

(200) Simoneau, S.; Rezaei, H.; Salès, N.; Kaiser-Schulz, G.; Lefebvre-Roque, M.; Vidal, C.; Fournier, J.-G.; Comte, J.; Wopfner, F.; Grosclaude, J.; Schätzl, H.; Lasmézas, C. I. In Vitro and in Vivo Neurotoxicity of Prion Protein Oligomers. *PLoS Pathog.* **2007**, *3* (8), e125.

(201) Kazlauskaite, J.; Young, A.; Gardner, C. E.; Macpherson, J. V; Vénien-Bryan, C.; Pinheiro, T. J. T. An Unusual Soluble β-Turn-Rich Conformation of Prion Is Involved in Fibril Formation and Toxic to Neuronal Cells. *Biochem. Biophys. Res. Commun.* **2005**, *328* (1), 292–305.

(202) Novitskaya, V.; Bocharova, O. V.; Bronstein, I.; Baskakov, I. V. Amyloid Fibrils of Mammalian Prion Protein Are Highly Toxic to Cultured Cells and Primary Neurons. *J. Biol. Chem.* **2006**, *281* (19), 13828–13836.

(203) Huang, P.; Lian, F.; Wen, Y.; Guo, C.; Lin, D. Prion Protein Oligomer and Its Neurotoxicity. *Acta Biochim. Biophys. Sin.* **2013**, *45* (6), 442–451.

(204) Sanghera, N.; Wall, M.; Vénien-Bryan, C.; Pinheiro, T. J. T. Globular and Pre-Fibrillar Prion Aggregates Are Toxic to Neuronal Cells and Perturb Their Electrophysiology. *Biochim. Biophys. Acta* **2008**, *1784* (6), 873–881.

(205) Haass, C.; Selkoe, D. J. Soluble Protein Oligomers in Neurodegeneration: Lessons from the Alzheimer's Amyloid β-Peptide. *Nat. Rev. Mol. Cell Biol.* **2007**, *8* (2), 101–112.

(206) Walsh, D. M.; Klyubin, I.; Fadeeva, J. V.; Cullen, W. K.; Anwyl, R.; Wolfe, M. S.; Rowan, M. J.; Selkoe, D. J. Naturally Secreted Oligomers of Amyloid β Protein Potently Inhibit Hippocampal Long-Term Potentiation in Vivo. *Nature* **2002**, *416* (6880), 535–539.

(207) Lesné, S.; Koh, M. T.; Kotilinek, L.; Kayed, R.; Glabe, C. G.; Yang, A.; Gallagher, M.; Ashe, K. H. A Specific Amyloid-β Protein Assembly in the Brain Impairs Memory. *Nature* **2006**, *440* (7082), 352–357.

(208) Koffie, R. M.; Meyer-Luehmann, M.; Hashimoto, T.; Adams, K. W.; Mielke, M. L.; Garcia-Alloza, M.; Micheva, K. D.; Smith, S. J.; Kim, M. L.; Lee, V. M.; Hyman, B. T.; Spires-Jones, T. L. Oligomeric Amyloid β Associates with Postsynaptic Densities and Correlates with Excitatory Synapse Loss near Senile Plaques. *Proc. Natl. Acad. Sci. U. S. A.* **2009**, *106* (10), 4012–4017.

(209) Winner, B.; Jappelli, R.; Maji, S. K.; Desplats, P. A.; Boyer, L.; Aigner, S.; Hetzer, C.; Loher, T.; Vilar, M.; Campioni, S.; Tzitzilonis, C.; Soragni, A.; Jessberger, S.; Mira, H.; Consiglio, A.; Pham, E.; Masliah, E.; Gage, F. H.; Riek, R. In Vivo Demonstration That α-Synuclein Oligomers Are Toxic. *Proc. Natl. Acad. Sci. U. S. A.* **2011**, *108* (10), 4194–4199.

(210) Kristiansen, M.; Deriziotis, P.; Dimcheff, D. E.; Jackson, G. S.; Ovaa, H.; Naumann, H.; Clarke, A. R.; van Leeuwen, F. W. B.; Menéndez-Benito, V.; Dantuma, N. P.; Portis, J. L.; Collinge, J.; Tabrizi, S. J. Disease-Associated Prion Protein Oligomers Inhibit the 26S Proteasome. *Mol. Cell* **2007**, *26* (2), 175–188.

(211) Landreh, M.; Sawaya, M. R.; Hipp, M. S.; Eisenberg, D. S.; Wüthrich, K.; Hartl, F. U. The Formation, Function and Regulation of Amyloids: Insights from Structural Biology. *J. Intern. Med.* **2016**, *280* (2), 164–176.

(212) Marshall, K. E.; Marchante, R.; Xue, W.-F.; Serpell, L. C. The Relationship between Amyloid Structure and Cytotoxicity. *Prion* **2014**, *8* (2), 1–5.

(213) Treusch, S.; Cyr, D. M.; Lindquist, S. Amyloid Deposits: Protection against Toxic Protein Species? *Cell cycle* **2009**, *8* (11), 1668–1674.

(214) Douglas, P. M.; Treusch, S.; Ren, H.-Y.; Halfmann, R.; Duennwald, M. L.; Lindquist, S.; Cyr, D. M. Chaperone-Dependent Amyloid Assembly Protects Cells from Prion Toxicity. *Proc. Natl. Acad. Sci. U. S. A.* **2008**, *105* (20), 7206–7211.

(215) Saá, P.; Harris, D. A.; Cervenakova, L. Mechanisms of Prion-Induced Neurodegeneration. *Expert Rev. Mol. Med.* **2016**, *18*, e5.

(216) Zhou, M.; Ottenberg, G.; Sferrazza, G. F.; Lasmézas, C. I. Highly Neurotoxic Monomeric α-Helical Prion Protein. *Proc. Natl. Acad. Sci. U. S. A.* **2012**, *109* (8), 3113–3118.

(217) Esposito, Z.; Belli, L.; Toniolo, S.; Sancesario, G.; Bianconi, C.; Martorana, A. Amyloid β, Glutamate, Excitotoxicity in Alzheimer's Disease: Are We on the Right Track? *CNS Neurosci. Ther.* **2013**, *19* (8), 549–555.

(218) Biasini, E.; Unterberger, U.; Solomon, I. H.; Massignan, T.; Senatore, A.; Bian, H.; Voigtlaender, T.; Bowman, F. P.; Bonetto, V.; Chiesa, R.; Luebke, J.; Toselli, P.; Harris, D. A. A Mutant Prion Protein Sensitizes Neurons to Glutamate-Induced Excitotoxicity. *J. Neurosci.* **2013**, *33* (6), 2408–2418.

(219) Molinuevo, J. L.; Lladó, A.; Rami, L. Memantine: Targeting Glutamate Excitotoxicity in Alzheimer's Disease and Other Dementias. *Am. J. Alzheimers. Dis. Other Demen.* **2005**, *20* (2), 77–85.

(220) Scallet, A. C.; Ye, X. Excitotoxic Mechanisms of Neurodegeneration in Transmissible Spongiform Encephalopathies. *Ann. N. Y. Acad. Sci.* **1997**, *825* (2), 194–205.

(221) Mays, C. E.; Soto, C. The Stress of Prion Disease. *Brain Res.* **2016**, *1648*, 553–560.

(222) Torres, M.; Matamala, J. M.; Duran-Aniotz, C.; Cornejo, V. H.; Foley, A.; Hetz, C. ER Stress Signaling and Neurodegeneration: At the Intersection between Alzheimer's Disease and Prion-Related Disorders. *Virus Res.* **2015**, *207*, 69–75.

(223) Doyle, K. M.; Kennedy, D.; Gorman, A. M.; Gupta, S.; Healy, S. J. M.; Samali, A. Unfolded Proteins and Endoplasmic Reticulum Stress in Neurodegenerative Disorders. *J. Cell. Mol. Med.* **2011**, *15* (10), 2025–2039.

(224) Cai, Y.; Arikkath, J.; Yang, L.; Guo, M. L.; Periyasamy, P.; Buch, S. Interplay of Endoplasmic Reticulum Stress and Autophagy in Neurodegenerative Disorders. *Autophagy* **2016**, *12* (2), 225–244.

(225) Martini-Stoica, H.; Xu, Y.; Ballabio, A.; Zheng, H. The Autophagy-Lysosomal Pathway in Neurodegeneration: A TFEB Perspective. *Trends Neurosci.* **2016**, *39* (4), 221–234.

(226) Milisav, I.; Šuput, D.; Ribarič, S. Unfolded Protein Response and Macroautophagy in Alzheimer's, Parkinson's and Prion Diseases. *Molecules* **2015**, *20* (12), 22718–

22756.

(227) Yao, H.; Zhao, D.; Khan, S. H.; Yang, L. Role of Autophagy in Prion Protein-Induced Neurodegenerative Diseases. *Acta Biochim. Biophys. Sin.* **2013**, *45* (6), 494–502.

(228) Liberski, P. P.; Sikorska, B.; Gibson, P.; Brown, P. Autophagy Contributes to Widespread Neuronal Degeneration in Hamsters Infected with the Echigo-1 Strain of Creutzfeldt-Jakob Disease and Mice Infected with the Fujisaki Strain of Gerstmann-Sträussler-Scheinker (GSS) Syndrome. *Ultrastruct. Pathol.* **2011**, *35* (1), 31–36.

(229) Christensen, H. M.; Dikranian, K.; Li, A.; Baysac, K. C.; Walls, K. C.; Olney, J. W.; Roth, K. A.; Harris, D. A. A Highly Toxic Cellular Prion Protein Induces a Novel, Nonapoptotic Form of Neuronal Death. *Am. J. Pathol.* **2010**, *176* (6), 2695–2706.

(230) Bolognesi, B.; Kumita, J. R.; Barros, T. P.; Esbjorner, E. K.; Luheshi, L. M.; Crowther, D. C.; Wilson, M. R.; Dobson, C. M.; Favrin, G.; Yerbury, J. J. ANS Binding Reveals Common Features of Cytotoxic Amyloid Species. *ACS Chem. Biol.* **2010**, *5* (8), 735–740.

(231) Cheon, M.; Chang, I.; Mohanty, S.; Luheshi, L. M.; Dobson, C. M.; Vendruscolo, M.; Favrin, G. Structural Reorganisation and Potential Toxicity of Oligomeric Species Formed during the Assembly of Amyloid Fibrils. *PLoS Comput. Biol.* **2007**, *3* (9), 1727–1738.

(232) Narayan, P.; Ganzinger, K. A.; McColl, J.; Weimann, L.; Meehan, S.; Qamar, S.; Carver, J. A.; Wilson, M. R.; St George-Hyslop, P.; Dobson, C. M.; Klenerman, D. Single Molecule Characterization of the Interactions between Amyloid-β Peptides and the Membranes of Hippocampal Cells. *J. Am. Chem. Soc.* **2013**, *135* (4), 1491–1498.

(233) Serra-Batiste, M.; Ninot-Pedrosa, M.; Bayoumi, M.; Gairí, M.; Maglia, G.; Carulla, N. Aβ42 Assembles into Specific β-Barrel Pore-Forming Oligomers in Membrane-Mimicking Environments. *Proc. Natl. Acad. Sci. U. S. A.* **2016**, *113* (39), 10866–10871.

(234) Andreasen, M.; Lorenzen, N.; Otzen, D. Interactions between Misfolded Protein Oligomers and Membranes: A Central Topic in Neurodegenerative Diseases? *Biochim. Biophys. Acta* **2015**, *1848* (9), 1897–1907.

(235) Benilova, I.; Karran, E.; De Strooper, B. The Toxic Aβ Oligomer and Alzheimer's Disease: An Emperor in Need of Clothes. *Nat. Neurosci.* **2012**, *15* (3), 349–357.

(236) Soto, C. Unfolding the Role of Protein Misfolding in Neurodegenerative Diseases.

Nat. Rev. Neurosci. **2003**, *4* (1), 49–60.

(237) Quist, A.; Doudevski, I.; Lin, H.; Azimova, R.; Ng, D.; Frangione, B.; Kagan, B.; Ghiso, J.; Lal, R. Amyloid Ion Channels: A Common Structural Link for Protein-Misfolding Disease. *Proc. Natl. Acad. Sci. U. S. A.* **2005**, *102* (30), 10427–10432.

(238) Evangelisti, E.; Cascella, R.; Becatti, M.; Marrazza, G.; Dobson, C. M.; Chiti, F.; Stefani, M.; Cecchi, C. Binding Affinity of Amyloid Oligomers to Cellular Membranes Is a Generic Indicator of Cellular Dysfunction in Protein Misfolding Diseases. *Sci. Rep.* **2016**, *6* (3), 32721.

(239) Laferrière, F.; Tixador, P.; Moudjou, M.; Chapuis, J.; Sibille, P.; Herzog, L.; Reine, F.; Jaumain, E.; Laude, H.; Rezaei, H.; Béringue, V. Quaternary Structure of Pathological Prion Protein as a Determining Factor of Strain-Specific Prion Replication Dynamics. *PLoS Pathog.* **2013**, *9* (10), e1003702.

(240) Kim, C.; Haldiman, T.; Surewicz, K.; Cohen, Y.; Chen, W.; Blevins, J.; Sy, M.-S.; Cohen, M.; Kong, Q.; Telling, G. C.; Surewicz, W. K.; Safar, J. G. Small Protease Sensitive Oligomers of PrPSc in Distinct Human Prions Determine Conversion Rate of PrPC. *PLoS Pathog.* **2012**, *8* (8), e1002835.

(241) Tixador, P.; Herzog, L.; Reine, F.; Jaumain, E.; Chapuis, J.; Le Dur, A.; Laude, H.; Béringue, V. The Physical Relationship between Infectivity and Prion Protein Aggregates Is Strain-Dependent. *PLoS Pathog.* **2010**, *6* (4), e1000859.

(242) Silveira, J. R.; Raymond, G. J.; Hughson, A. G.; Race, R. E.; Sim, V. L.; Hayes, S. F.; Caughey, B. The Most Infectious Prion Protein Particles. *Nature* **2005**, *437* (7056), 257–261.

(243) Radford, H. E.; Mallucci, G. R. The Role of GPI-Anchored PrP C in Mediating the Neurotoxic Effect of Scrapie Prions in Neurons. *Curr. Issues Mol. Biol.* **2010**, *12* (2), 119–127.

(244) Sandberg, M. K.; Al-Doujaily, H.; Sharps, B.; De Oliveira, M. W.; Schmidt, C.; Richard-Londt, A.; Lyall, S.; Linehan, J. M.; Brandner, S.; Wadsworth, J. D. F.; Clarke, A. R.; Collinge, J. Prion Neuropathology Follows the Accumulation of Alternate Prion Protein Isoforms after Infective Titre Has Peaked. *Nat. Commun.* **2014**, *5* (May), 4347.

(245) Sandberg, M. K.; Al-Doujaily, H.; Sharps, B.; Clarke, A. R.; Collinge, J. Prion Propagation and Toxicity in Vivo Occur in Two Distinct Mechanistic Phases. *Nature* **2011**, *470* (7335), 540–542.

(246) Cronier, S.; Gros, N.; Tattum, M. H.; Jackson, G. S.; Clarke, A. R.; Collinge, J.; Wadsworth, J. D. F. Detection and Characterization of Proteinase K-Sensitive Disease-Related Prion Protein with Thermolysin. *Biochem. J.* **2008**, *416* (2), 297–305.

(247) Berardi, V. A.; Cardone, F.; Valanzano, A.; Lu, M.; Pocchiari, M. Preparation of Soluble Infectious Samples from Scrapie-Infected Brain: A New Tool to Study the Clearance of Transmissible Spongiform Encephalopathy Agents during Plasma Fractionation. *Transfusion* **2006**, *46* (4), 652–658.

(248) Safar, J. G.; Geschwind, M. D.; Deering, C.; Didorenko, S.; Sattavat, M.; Sanchez, H.; Serban, A.; Vey, M.; Baron, H.; Giles, K.; Miller, B. L.; Dearmond, S. J.; Prusiner, S. B. Diagnosis of Human Prion Disease. *Proc. Natl. Acad. Sci. U. S. A.* **2005**, *102* (9), 3501–3506.

(249) Fraser, P. E. Prions and Prion-like Proteins. *J. Biol. Chem.* **2014**, *289* (29), 19839–19840.

(250) Guo, J. L.; Lee, V. M. Y. Cell-to-Cell Transmission of Pathogenic Proteins in Neurodegenerative Diseases. *Nat. Med.* **2014**, *20* (2), 130–138.

(251) Soto, C. Transmissible Proteins: Expanding the Prion Heresy. *Cell* **2012**, *149* (5), 968–977.

(252) Chen, B.; Bruce, K. L.; Newnam, G. P.; Gyoneva, S.; Romanyuk, A. V.; Chernoff, Y. O. Genetic and Epigenetic Control of the Efficiency and Fidelity of Cross-Species Prion Transmission. *Mol. Microbiol.* **2010**, *76* (6), 1483–1499.

(253) Meyer-Luehmann, M.; Coomaraswamy, J.; Bolmont, T.; Kaeser, S.; Schaefer, C.; Kilger, E.; Neuenschwander, A.; Abramowski, D.; Frey, P.; Jaton, A. L.; Vigouret, J.-M.; Paganetti, P.; Walsh, D. M.; Mathews, P. M.; Ghiso, J.; Staufenbiel, M.; Walker, L. C.; Jucker, M. Exogenous Induction of Cerebral β-Amyloidogenesis Is Governed by Agent and Host. *Science* **2006**, *313* (5794), 1781–1784.

(254) Goedert, M.; Falcon, B.; Clavaguera, F.; Tolnay, M. Prion-like Mechanisms in the Pathogenesis of Tauopathies and Synucleinopathies. *Curr. Neurol. Neurosci. Rep.* **2014**, *14* (11), 495.

(255) Holmes, B. B.; Diamond, M. I. Prion-like Properties of Tau Protein: The Importance of Extracellular Tau as a Therapeutic Target. *J. Biol. Chem.* **2014**, *289* (29), 19855–19861.

(256) Chauhan, A.; Jeans, A. F. Is Parkinson's Disease Truly a Prion-like Disorder? An

Appraisal of Current Evidence. *Neurol. Res. Int.* **2015**, *2015*, 345285.

(257) Golde, T. E.; Borchelt, D. R.; Giasson, B. I.; Lewis, J. Thinking Laterally about Neurodegenerative Proteinopathies. *J. Clin. Invest.* **2013**, *123* (5), 1847–1855.

(258) Masuda-Suzukake, M.; Nonaka, T.; Hosokawa, M.; Oikawa, T.; Arai, T.; Akiyama, H.; Mann, D. M. A.; Hasegawa, M. Prion-like Spreading of Pathological α-Synuclein in Brain. *Brain* **2013**, *136* (4), 1128–1138.

(259) Luk, K. C.; Kehm, V. M.; Zhang, B.; O?Brien, P.; Trojanowski, J. Q.; Lee, V. M. Y. Intracerebral Inoculation of Pathological α-Synuclein Initiates a Rapidly Progressive Neurodegenerative α-Synucleinopathy in Mice. *J. Exp. Med.* **2012**, *209* (5), 975–986.

(260) Mendez, I.; Viñuela, A.; Astradsson, A.; Mukhida, K.; Hallett, P.; Robertson, H.; Tierney, T.; Holness, R.; Dagher, A.; Trojanowski, J. Q.; Isacson, O. Dopamine Neurons Implanted into People with Parkinson's Disease Survive without Pathology for 14 Years. *Nat. Med.* **2008**, *14* (5), 507–509.

(261) Brundin, P.; Li, J.-Y.; Holton, J. L.; Lindvall, O.; Revesz, T. Research in Motion: The Enigma of Parkinson's Disease Pathology Spread. *Nat. Rev. Neurosci.* **2008**, *9* (10), 741–745.

(262) Silva, J. L.; Cino, E. A.; Soares, I. N.; Ferreira, V. F.; A P de Oliveira, G. Targeting the Prion-like Aggregation of Mutant P53 to Combat Cancer. *Acc. Chem. Res.* **2018**, *51* (1), 181–190.

(263) Ghosh, S.; Salot, S.; Sengupta, S.; Navalkar, A.; Ghosh, D.; Jacob, R.; Das, S.; Kumar, R.; Jha, N. N.; Sahay, S.; Mehra, S.; Mohite, G. M.; Ghosh, S. K.; Kombrabail, M.; Krishnamoorthy, G.; Chaudhari, P.; Maji, S. K. P53 Amyloid Formation Leading to Its Loss of Function: Implications in Cancer Pathogenesis. *Cell Death Differ.* **2017**, *24* (10), 1784–1798.

(264) Ano Bom, A. P. D.; Rangel, L. P.; Costa, D. C. F.; de Oliveira, G. A. P.; Sanches, D.; Braga, C. A.; Gava, L. M.; Ramos, C. H. I.; Cepeda, A. O. T.; Stumbo, A. C.; De Moura Gallo, C. V.; Cordeiro, Y.; Silva, J. L. Mutant P53 Aggregates into Prion-like Amyloid Oligomers and Fibrils: Implications for Cancer. *J. Biol. Chem.* **2012**, *287* (33), 28152–28162.

(265) Dillingham, M. S.; Wallace, M. I. Protein Modification for Single Molecule Fluorescence Microscopy. *Org. Biomol. Chem.* **2008**, *6* (17), 3031–3037.

(266) Boyer, R. Spectroscopy for the Biological Sciences: Hammes, G. G. *Biochem. Mol. Biol. Educ.* **2006**, *34* (2), 161b–162.

(267) Stokes, G. G. On the Change of Refrangibility of Light. *Philos. Trans. R. Soc. London* **1852**, *142*, 463–562.

(268) Moerner, W. E.; Fromm, D. P. Methods of Single-Molecule Fluorescence Spectroscopy and Microscopy. *Rev. Sci. Instrum.* **2003**, *74* (8), 3597–3619.

(269) Axelrod, D. Total Internal Reflection Fluorescence Microscopy in Cell Biology. *Traffic* **2001**, *2* (11), 764–774.

(270) Bhasikuttan, A. C.; Pal, H.; Mohanty, J. Cucurbit[n]Uril Based Supramolecular Assemblies: Tunable Physico-Chemical Properties and Their Prospects. *Chem. Commun.* **2011**, *47* (36), 9959–9971.

(271) Sulatskaya, A. I.; Maskevich, A. A.; Kuznetsova, I. M.; Uversky, V. N.; Turoverov, K. K. Fluorescence Quantum Yield of Thioflavin T in Rigid Isotropic Solution and Incorporated into the Amyloid Fibrils. *PLoS One* **2010**, *5* (10), e15385.

(272) Biancalana, M.; Koide, S. Molecular Mechanism of Thioflavin-T Binding to Amyloid Fibrils. *Biochim. Biophys. Acta* **2010**, *1804* (7), 1405–1412.

(273) Groenning, M. Binding Mode of Thioflavin T and Other Molecular Probes in the Context of Amyloid Fibrils-Current Status. *J. Chem. Biol.* **2010**, *3* (1), 1–18.

(274) Groenning, M.; Olsen, L.; van de Weert, M.; Flink, J. M.; Frokjaer, S.; Jørgensen, F. S. Study on the Binding of Thioflavin T to β-Sheet-Rich and Non-β-Sheet Cavities. *J. Struct. Biol.* **2007**, *158* (3), 358–369.

(275) Khurana, R.; Coleman, C.; Ionescu-Zanetti, C.; Carter, S. a.; Krishna, V.; Grover, R. K.; Roy, R.; Singh, S. Mechanism of Thioflavin T Binding to Amyloid Fibrils. *J. Struct. Biol.* **2005**, *151* (3), 229–238.

(276) Horrocks, M. H.; Lee, S. F.; Gandhi, S.; Magdalinou, N. K.; Chen, S. W.; Devine, M. J.; Tosatto, L.; Kjaergaard, M.; Beckwith, J. S.; Zetterberg, H.; Iljina, M.; Cremades, N.; Dobson, C. M.; Wood, N. W.; Klenerman, D. Single-Molecule Imaging of Individual Amyloid Protein Aggregates in Human Biofluids. *ACS Chem. Neurosci.* **2016**, *7* (3), 399–406.

(277) Galbraith, C. G.; Galbraith, J. A. Super-Resolution Microscopy at a Glance. *J. Cell Sci.* **2011**, *124* (10), 1607–1611.

(278) Huang, B.; Wang, W.; Bates, M.; Zhuang, X. Three-Dimensional Super-Resolution Reconstruction Microscopy. *Science* **2008**, *319* (February), 810–813.

(279) Betzig, E.; Patterson, G. H.; Sougrat, R.; Lindwasser, O. W.; Olenych, S.; Bonifacino, J.

S.; Davidson, M. W.; Lippincott-Schwartz, J.; Hess, H. F. Imaging Intracellular Fluorescent Proteins at Nanometer Resolution. *Science* **2006**, *313* (5793), 1642–1645.

(280) Hell, S. W.; Wichmann, J. Breaking the Diffraction Resolution Limit by Stimulated Emission: Stimulated-Emission-Depletion Fluorescence Microscopy. *Opt. Lett.* **1994**, *19* (11), 780–782.

(281) Mlodzianoski, M. J.; Curthoys, N. M.; Gunewardene, M. S.; Carter, S.; Hess, S. T. Super-Resolution Imaging of Molecular Emission Spectra and Single Molecule Spectral Fluctuations. *PLoS One* **2016**, *11* (3), e0147506.

(282) Zhang, Z.; Kenny, S. J.; Hauser, M.; Li, W.; Xu, K. Ultrahigh-Throughput Single-Molecule Spectroscopy and Spectrally Resolved Super-Resolution Microscopy. *Nat. Methods* **2015**, *12* (10), 935–938.

(283) Broeken, J.; Rieger, B.; Stallinga, S. Simultaneous Measurement of Position and Color of Single Fluorescent Emitters Using Diffractive Optics. *Opt. Lett.* **2014**, *39* (11), 3352–3355.

(284) Bongiovanni, M. N.; Godet, J.; Horrocks, M. H.; Tosatto, L.; Carr, A. R.; Wirthensohn, D. C.; Ranasinghe, R. T.; Lee, J.-E.; Ponjavic, A.; Fritz, J. V.; Dobson, C. M.; Klenerman, D.; Lee, S. F. Multi-Dimensional Super-Resolution Imaging Enables Surface Hydrophobicity Mapping. *Nat. Commun.* **2016**, *7* (1), 13544.

(285) Hawe, A.; Sutter, M.; Jiskoot, W. Extrinsic Fluorescent Dyes as Tools for Protein Characterization. *Pharm. Res.* **2008**, *25* (7), 1487–1499.

(286) Sackett, D. L.; Knutson, J. R.; Wolff, J. Hydrophobic Surfaces of Tubulin Probed by Time-Resolved and Steady-State Fluorescence of Nile Red. *J. Biol. Chem.* **1990**, *265* (25), 14899–14906.

(287) Greenspan, P.; Fowler, S. D. Spectrofluorometric Studies of the Lipid Probe, Nile Red. *J. Lipid Res.* **1985**, *26* (7), 781–789.

(288) Sharonov, A.; Hochstrasser, R. M. Wide-Field Subdiffraction Imaging by Accumulated Binding of Diffusing Probes. *Proc. Natl. Acad. Sci. U. S. A.* **2006**, *103* (50), 18911–18916.

(289) Giannone, G.; Hosy, E.; Levet, F.; Constals, A.; Schulze, K.; Sobolevsky, A. I.; Rosconi, M. P.; Gouaux, E.; Tampé, R.; Choquet, D.; Cognet, L. Dynamic Superresolution Imaging of Endogenous Proteins on Living Cells at Ultra-High Density. *Biophys. J.* **2010**, *99* (4), 1303–1310.

(290) Jungmann, R.; Steinhauer, C.; Scheible, M.; Kuzyk, A.; Tinnefeld, P.; Simmel, F. C. Single-Molecule Kinetics and Super-Resolution Microscopy by Fluorescence Imaging of Transient Binding on DNA Origami. *Nano Lett.* **2010**, *10* (11), 4756–4761.

(291) Jungmann, R.; Avendaño, M. S.; Woehrstein, J. B.; Dai, M.; Shih, W. M.; Yin, P. Multiplexed 3D Cellular Super-Resolution Imaging with DNA-PAINT and Exchange-PAINT. *Nat. Methods* **2014**, *11* (3), 313–318.

(292) Dutta, A.; Chen, S.; Surewicz, W. K. The Effect of B2-A2 Loop Mutation on Amyloidogenic Properties of the Prion Protein. *FEBS Lett.* **2013**, *587* (18), 2918–2923.

(293) Looman, A. C.; Bodlaender, J.; Comstock, L. J.; Eaton, D.; Jhurani, P.; de Boer, H. A.; van Knippenberg, P. H. Influence of the Codon Following the AUG Initiation Codon on the Expression of a Modified LacZ Gene in Escherichia Coli. *EMBO J.* **1987**, *6* (8), 2489–2492.

(294) Wong, E.; Thackray, A. M.; Bujdoso, R. Copper Induces Increased β-Sheet Content in the Scrapie-Susceptible Ovine Prion Protein PrPVRQ Compared with the Resistant Allelic Variant PrPARR. *Biochem. J.* **2004**, *380* (1), 273–282.

(295) Trevitt, C. R.; Hosszu, L. L. P.; Batchelor, M.; Panico, S.; Terry, C.; Nicoll, A. J.; Risse, E.; Taylor, W. a; Sandberg, M. K.; Al-Doujaily, H.; Linehan, J. M.; Saibil, H. R.; Scott, D. J.; Collinge, J.; Waltho, J. P.; Clarke, A. R. N-Terminal Domain of Prion Protein Directs Its Oligomeric Association. *J. Biol. Chem.* **2014**, *289* (37), 25497–25508.

(296) Emmanouilidou, E.; Elenis, D.; Papasilekas, T.; Stranjalis, G.; Gerozissis, K.; Ioannou, P. C.; Vekrellis, K. Assessment of α-Synuclein Secretion in Mouse and Human Brain Parenchyma. *PLoS One* **2011**, *6* (7), e22225.

(297) Chen, R. H. C.; Wislet-Gendebien, S.; Samuel, F.; Visanji, N. P.; Zhang, G.; Marsilio, D.; Langman, T.; Fraser, P. E.; Tandon, A. α-Synuclein Membrane Association Is Regulated by the Rab3a Recycling Machinery and Presynaptic Activity. *J. Biol. Chem.* **2013**, *288* (11), 7438–7449.

(298) Godsave, S. F.; Wille, H.; Kujala, P.; Latawiec, D.; DeArmond, S. J.; Serban, A.; Prusiner, S. B.; Peters, P. J. Cryo-Immunogold Electron Microscopy for Prions: Toward Identification of a Conversion Site. *J. Neurosci.* **2008**, *28* (47), 12489–12499.

(299) Goold, R.; Rabbanian, S.; Sutton, L.; Andre, R.; Arora, P.; Moonga, J.; Clarke, A. R.; Schiavo, G.; Jat, P.; Collinge, J.; Tabrizi, S. J. Rapid Cell-Surface Prion Protein

Conversion Revealed Using a Novel Cell System. *Nat. Commun.* **2011**, *2*, 281.

(300) Godsave, S. F.; Wille, H.; Pierson, J.; Prusiner, S. B.; Peters, P. J. Plasma Membrane Invaginations Containing Clusters of Full-Length PrPSc Are an Early Form of Prion-Associated Neuropathology in Vivo. *Neurobiol. Aging* **2013**, *34* (6), 1621–1631.

(301) Saá, P.; Castilla, J.; Soto, C. Presymptomatic Detection of Prions in Blood. *Science* **2006**, *313* (5783), 92–94.

(302) Chen, B.; Morales, R.; Barria, M. a; Soto, C. Estimating Prion Concentration in Fluids and Tissues by Quantitative PMCA. *Nat. Methods* **2010**, *7* (7), 519–520.

(303) Urayama, A.; Concha-Marambio, L.; Khan, U.; Bravo-Alegria, J.; Kharat, V.; Soto, C. Prions Efficiently Cross the Intestinal Barrier after Oral Administration: Study of the Bioavailability, and Cellular and Tissue Distribution in Vivo. *Sci. Rep.* **2016**, *6* (1), 32338.

(304) Hwang, D.; Lee, I. Y.; Yoo, H.; Gehlenborg, N.; Cho, J.-H.; Petritis, B.; Baxter, D.; Pitstick, R.; Young, R.; Spicer, D.; Price, N. D.; Hohmann, J. G.; Dearmond, S. J.; Carlson, G. a; Hood, L. E. A Systems Approach to Prion Disease. *Mol. Syst. Biol.* **2009**, *5* (252), 252.

(305) Zampieri, M.; Legname, G.; Segrè, D.; Altafini, C. A System-Level Approach for Deciphering the Transcriptional Response to Prion Infection. *Bioinformatics* **2011**, *27* (24), 3407–3414.

(306) Mays, C. E.; Kim, C.; Haldiman, T.; van der Merwe, J.; Lau, A.; Yang, J.; Grams, J.; Di Bari, M. A.; Nonno, R.; Telling, G. C.; Kong, Q.; Langeveld, J.; McKenzie, D.; Westaway, D.; Safar, J. G. Prion Disease Tempo Determined by Host-Dependent Substrate Reduction. *J. Clin. Invest.* **2014**, *124* (2), 847–858.

(307) Sang, J. C.; Meisl, G.; Thackray, A. M.; Hong, L.; Ponjavic, A.; Knowles, T. P. J.; Bujdoso, R.; Klenerman, D. Direct Observation of Murine Prion Protein Replication in Vitro. *J. Am. Chem. Soc.* **2018**, *140* (44), 14789–14798.

(308) Flagmeier, P.; De, S.; Wirthensohn, D. C.; Lee, S. F.; Vincke, C.; Muyldermans, S.; Knowles, T. P. J.; Gandhi, S.; Dobson, C. M.; Klenerman, D. Ultrasensitive Measurement of Ca(2+) Influx into Lipid Vesicles Induced by Protein Aggregates. *Angew. Chem. Int. Ed. Engl.* **2017**, *56* (27), 7750–7754.

(309) Wang, X.; Huang, L. Identifying Dynamic Interactors of Protein Complexes by Quantitative Mass Spectrometry. *Mol. Cell. proteomics* **2008**, *7* (1), 46–57.

(310) Qi, X.; Moore, R. A.; Mcguirl, M. A. Dissociation of Recombinant Prion Protein Fibrils

into Short Protofilaments: Implications for the Endocytic Pathway and Involvement of the N-Terminal Domain. *Biochemistry* **2012**, *51* (22), 4600–4608.

(311) Aguzzi, A.; Weissmann, C. Prion Research: The next Frontiers. *Nature* **1997**, *389* (6653), 795–798.

(312) Aguzzi, A.; Rajendran, L. The Transcellular Spread of Cytosolic Amyloids, Prions, and Prionoids. *Neuron* **2009**, *64* (6), 783–790.

(313) Orte, A.; Birkett, N. R.; Clarke, R. W.; Devlin, G. L.; Dobson, C. M.; Klenerman, D. Direct Characterization of Amyloidogenic Oligomers by Single-Molecule Fluorescence. *Proc. Natl. Acad. Sci. U. S. A.* **2008**, *105* (38), 14424–14429.

(314) Ganzinger, K. A.; Narayan, P.; Qamar, S. S.; Weimann, L.; Ranasinghe, R. T.; Aguzzi, A.; Dobson, C. M.; McColl, J.; St George-Hyslop, P.; Klenerman, D. Single-Molecule Imaging Reveals That Small Amyloid-B1-42 Oligomers Interact with the Cellular Prion Protein (PrPC). *Chembiochem* **2014**, *15* (17), 2515–2521.

(315) Sun, Y.; Makarava, N.; Lee, C.-I.; Laksanalamai, P.; Robb, F. T.; Baskakov, I. V. Conformational Stability of PrP Amyloid Fibrils Controls Their Smallest Possible Fragment Size. *J. Mol. Biol.* **2008**, *376* (4), 1155–1167.

(316) Kang, H.-E.; Mo, Y.; Abd Rahim, R.; Lee, H.-M.; Ryou, C. Prion Diagnosis: Application of Real-Time Quaking-Induced Conversion. *Biomed Res. Int.* **2017**, *2017*, 5413936.

(317) Mironov, A.; Latawiec, D.; Wille, H.; Bouzamondo-Bernstein, E.; Legname, G.; Williamson, R. A.; Burton, D.; DeArmond, S. J.; Prusiner, S. B.; Peters, P. J. Cytosolic Prion Protein in Neurons. *J. Neurosci.* **2003**, *23* (18), 7183–7193.

(318) Ban, T.; Hamada, D.; Hasegawa, K.; Naiki, H.; Goto, Y. Direct Observation of Amyloid Fibril Growth Monitored by Thioflavin T Fluorescence. *J. Biol. Chem.* **2003**, *278* (19), 16462–16465.

(319) Ban, T.; Hoshino, M.; Takahashi, S.; Hamada, D.; Hasegawa, K.; Naiki, H.; Goto, Y. Direct Observation of Abeta Amyloid Fibril Growth and Inhibition. *J. Mol. Biol.* **2004**, *344* (3), 757–767.

(320) Taniguchi, A.; Shimizu, Y.; Oisaki, K.; Sohma, Y.; Kanai, M. Switchable Photooxygenation Catalysts That Sense Higher-Order Amyloid Structures. *Nat. Chem.* **2016**, *8* (10), 974–982.

(321) Breydo, L.; Bocharova, O. V.; Makarava, N.; Salnikov, V. V.; Anderson, M.; Baskakov, I. V. Methionine Oxidation Interferes with Conversion of the Prion Protein into the

Fibrillar Proteinase K-Resistant Conformation. *Biochemistry* **2005**, *44* (47), 15534–15543.

(322) Norris, B. J.; Meckstroth, M. L.; Heineman, W. R. Optically Transparent Thin Layer Electrode for Anaerobic Measurements on Redox Enzymes. *Anal. Chem.* **1976**, *48* (3), 630–632.

(323) Senftleber, F.; Bowling, D.; Stahr, M. S. Removal of Oxygen from Solvents for Liquid Chromatography with Electrochemical Detection. *Anal. Chem.* **1983**, *55* (4), 810–812.

(324) Rollie, M. E.; Patonay, G.; Warner, I. M. Deoxygenation of Solutions and Its Analytical Applications. *Ind. Eng. Chem. Res.* **1987**, *26* (1), 1–6.

(325) Aitken, C. E.; Marshall, R. A.; Puglisi, J. D. An Oxygen Scavenging System for Improvement of Dye Stability in Single-Molecule Fluorescence Experiments. *Biophys. J.* **2008**, *94* (5), 1826–1835.

(326) Swoboda, M.; Henig, J.; Cheng, H.-M.; Brugger, D.; Haltrich, D.; Plumeré, N.; Schlierf, M. Enzymatic Oxygen Scavenging for Photostability without PH Drop in Single-Molecule Experiments. *ACS Nano* **2012**, *6* (7), 6364–6369.

(327) Shi, X.; Lim, J.; Ha, T. Acidification of the Oxygen Scavenging System in Single-Molecule Fluorescence Studies: In Situ Sensing with a Ratiometric Dual-Emission Probe. *Anal. Chem.* **2010**, *82* (14), 6132–6138.

(328) Collinge, J. Mammalian Prions and Their Wider Relevance in Neurodegenerative Diseases. *Nature* **2016**, *539* (7628), 217–226.

(329) Colby, D. W.; Wain, R.; Baskakov, I. V.; Legname, G.; Palmer, C. G.; Nguyen, H.-O. B.; Lemus, A.; Cohen, F. E.; DeArmond, S. J.; Prusiner, S. B. Protease-Sensitive Synthetic Prions. *PLoS Pathog.* **2010**, *6* (1), e1000736.

(330) Tzaban, S.; Friedlander, G.; Schonberger, O.; Horonchik, L.; Yedidia, Y.; Shaked, G.; Gabizon, R.; Taraboulos, A. Protease-Sensitive Scrapie Prion Protein in Aggregates of Heterogeneous Sizes. *Biochemistry* **2002**, *41* (42), 12868–12875.

(331) Safar, J.; Wille, H.; Itri, V.; Groth, D.; Serban, H.; Torchia, M.; Cohen, F. E.; Prusiner, S. B. Eight Prion Strains Have PrP(Sc) Molecules with Different Conformations. *Nat. Med.* **1998**, *4* (10), 1157–1165.

(332) Bucciantini, M.; Calloni, G.; Chiti, F.; Formigli, L.; Nosi, D.; Dobson, C. M.; Stefani, M. Prefibrillar Amyloid Protein Aggregates Share Common Features of Cytotoxicity. *J.*

Biol. Chem. **2004**, *279* (30), 31374–31382.

(333) Nath, S.; Agholme, L.; Kurudenkandy, F. R.; Granseth, B.; Marcusson, J.; Hallbeck, M. Spreading of Neurodegenerative Pathology via Neuron-to-Neuron Transmission of β-Amyloid. *J. Neurosci.* **2012**, *32* (26), 8767–8777.

(334) Bemporad, F.; Chiti, F. Protein Misfolded Oligomers: Experimental Approaches, Mechanism of Formation, and Structure-Toxicity Relationships. *Chem. Biol.* **2012**, *19* (3), 315–327.

(335) Chen, S. W.; Drakulic, S.; Deas, E.; Ouberai, M.; Aprile, F. A.; Arranz, R.; Ness, S.; Roodveldt, C.; Guilliams, T.; De-Genst, E. J.; Klenerman, D.; Wood, N. W.; Knowles, T. P. J.; Alfonso, C.; Rivas, G.; Abramov, A. Y.; Valpuesta, J. M.; Dobson, C. M.; Cremades, N. Structural Characterization of Toxic Oligomers That Are Kinetically Trapped during α-Synuclein Fibril Formation. *Proc. Natl. Acad. Sci. U. S. A.* **2015**, *112* (16), E1994–E2003.

(336) Ruggeri, F. S.; Longo, G.; Faggiano, S.; Lipiec, E.; Pastore, A.; Dietler, G. Infrared Nanospectroscopy Characterization of Oligomeric and Fibrillar Aggregates during Amyloid Formation. *Nat. Commun.* **2015**, *6*, 7831.

(337) Tosatto, L.; Horrocks, M. H.; Dear, A. J.; Knowles, T. P. J.; Dalla Serra, M.; Cremades, N.; Dobson, C. M.; Klenerman, D. Single-Molecule FRET Studies on Alpha-Synuclein Oligomerization of Parkinson's Disease Genetically Related Mutants. *Sci. Rep.* **2015**, *5* (July), 16696.

(338) Horrocks, M. H.; Tosatto, L.; Dear, A. J.; Garcia, G. A.; Iljina, M.; Cremades, N.; Dalla Serra, M.; Knowles, T. P. J.; Dobson, C. M.; Klenerman, D. Fast Flow Microfluidics and Single-Molecule Fluorescence for the Rapid Characterization of α-Synuclein Oligomers. *Anal. Chem.* **2015**, *87* (17), 8818–8826.

(339) Spillantini, M. G.; Crowther, R. A.; Jakes, R.; Cairns, N. J.; Lantos, P. L.; Goedert, M. Filamentous α-Synuclein Inclusions Link Multiple System Atrophy with Parkinson's Disease and Dementia with Lewy Bodies. *Neurosci. Lett.* **1998**, *251* (3), 205–208.

(340) Braak, H.; Del Tredici, K.; Rüb, U.; de Vos, R. A. I.; Jansen Steur, E. N. H.; Braak, E. Staging of Brain Pathology Related to Sporadic Parkinson's Disease. *Neurobiol. Aging* **2003**, *24* (2), 197–211.

(341) Li, J.-Y.; Englund, E.; Holton, J. L.; Soulet, D.; Hagell, P.; Lees, A. J.; Lashley, T.; Quinn, N. P.; Rehncrona, S.; Björklund, A.; Widner, H.; Revesz, T.; Lindvall, O.; Brundin, P. Lewy Bodies in Grafted Neurons in Subjects with Parkinson's Disease Suggest Host-

to-Graft Disease Propagation. *Nat. Med.* **2008**, *14* (5), 501–503.

(342) Kordower, J. H.; Chu, Y.; Hauser, R. A.; Olanow, C. W.; Freeman, T. B. Transplanted Dopaminergic Neurons Develop PD Pathologic Changes: A Second Case Report. *Mov. Disord.* **2008**, *23* (16), 2303–2306.

(343) Kordower, J. H.; Chu, Y.; Hauser, R. A.; Freeman, T. B.; Olanow, C. W. Lewy Body-like Pathology in Long-Term Embryonic Nigral Transplants in Parkinson's Disease. *Nat. Med.* **2008**, *14* (5), 504–506.

(344) Luk, K. C.; Kehm, V.; Carroll, J.; Zhang, B.; O'Brien, P.; Trojanowski, J. Q.; Lee, V. M.-Y. Pathological α-Synuclein Transmission Initiates Parkinson-like Neurodegeneration in Nontransgenic Mice. *Science* **2012**, *338* (6109), 949–953.

(345) Mougenot, A.-L.; Nicot, S.; Bencsik, A.; Morignat, E.; Verchère, J.; Lakhdar, L.; Legastelois, S.; Baron, T. Prion-like Acceleration of a Synucleinopathy in a Transgenic Mouse Model. *Neurobiol. Aging* **2012**, *33* (9), 2225–2228.

(346) Watts, J. C.; Giles, K.; Oehler, A.; Middleton, L.; Dexter, D. T.; Gentleman, S. M.; DeArmond, S. J.; Prusiner, S. B. Transmission of Multiple System Atrophy Prions to Transgenic Mice. *Proc. Natl. Acad. Sci. U. S. A.* **2013**, *110* (48), 19555–19560.

(347) Angot, E.; Steiner, J. A.; Hansen, C.; Li, J.-Y.; Brundin, P. Are Synucleinopathies Prion-like Disorders? *Lancet Neurol.* **2010**, *9* (11), 1128–1138.

(348) Olanow, C. W.; Prusiner, S. B. Is Parkinson's Disease a Prion Disorder? *Proc. Natl. Acad. Sci. U. S. A.* **2009**, *106* (31), 12571–12572.

(349) Apetri, M. M.; Harkes, R.; Subramaniam, V.; Canters, G. W.; Schmidt, T.; Aartsma, T. J. Direct Observation of α-Synuclein Amyloid Aggregates in Endocytic Vesicles of Neuroblastoma Cells. *PLoS One* **2016**, *11* (4), e0153020.

(350) Westphal, C. H.; Chandra, S. S. Monomeric Synucleins Generate Membrane Curvature. *J. Biol. Chem.* **2013**, *288* (3), 1829–1840.

(351) Peelaerts, W.; Baekelandt, V. α-Synuclein Strains and the Variable Pathologies of Synucleinopathies. *J. Neurochem.* **2016**, *139 Suppl*, 256–274.

(352) Makky, A.; Bousset, L.; Polesel-Maris, J.; Melki, R. Nanomechanical Properties of Distinct Fibrillar Polymorphs of the Protein α-Synuclein. *Sci. Rep.* **2016**, *6*, 1–10.

(353) Peelaerts, W.; Bousset, L.; Van Der Perren, A.; Moskalyuk, A.; Pulizzi, R.; Giugliano, M.; Van Den Haute, C.; Melki, R.; Baekelandt, V. α-Synuclein Strains Cause Distinct Synucleinopathies after Local and Systemic Administration. *Nature* **2015**, *522*

(7556), 340–344.

(354) Conway, K. A.; Lee, S. J.; Rochet, J. C.; Ding, T. T.; Williamson, R. E.; Lansbury, P. T. Acceleration of Oligomerization, Not Fibrillization, Is a Shared Property of Both α-Synuclein Mutations Linked to Early-Onset Parkinson's Disease: Implications for Pathogenesis and Therapy. *Proc. Natl. Acad. Sci. U. S. A.* **2000**, *97* (2), 571–576.

(355) Lau, A.; So, R. W. L.; Sang, J. C.; Lau, H. H. C.; Ruiz-Riquelme, A.; Stuart, E.; Visanji, N. P.; Meisl, G.; Marano, M.; Wang, Z.; Fraser, P. E.; Tandon, A.; Ingelsson, M.; Klenerman, D.; Watts, J. C. α-Synuclein Strains Exhibit All the Hallmarks of Prion Strains. (Submitted).

(356) Webb, J. L.; Ravikumar, B.; Atkins, J.; Skepper, J. N.; Rubinsztein, D. C. α-Synuclein Is Degraded by Both Autophagy and the Proteasome. *J. Biol. Chem.* **2003**, *278* (27), 25009–25013.

(357) Wang, Y.; Mandelkow, E. Degradation of Tau Protein by Autophagy and Proteasomal Pathways. *Biochem. Soc. Trans.* **2012**, *40* (4), 644–652.

(358) Rubinsztein, D. C. The Roles of Intracellular Protein-Degradation Pathways in Neurodegeneration. *Nature* **2006**, *443* (7113), 780–786.

(359) Schmidt, M.; Finley, D. Regulation of Proteasome Activity in Health and Disease. *Biochim. Biophys. Acta* **2014**, *1843* (1), 13–25.

(360) Bhattacharyya, S.; Yu, H.; Mim, C.; Matouschek, A. Regulated Protein Turnover: Snapshots of the Proteasome in Action. *Nat. Rev. Mol. Cell Biol.* **2014**, *15* (2), 122–133.

(361) Lee, B.-H.; Lee, M. J.; Park, S.; Oh, D.-C.; Elsasser, S.; Chen, P.-C.; Gartner, C.; Dimova, N.; Hanna, J.; Gygi, S. P.; Wilson, S. M.; King, R. W.; Finley, D. Enhancement of Proteasome Activity by a Small-Molecule Inhibitor of USP14. *Nature* **2010**, *467* (7312), 179–184.

(362) Rott, R.; Szargel, R.; Haskin, J.; Bandopadhyay, R.; Lees, A. J.; Shani, V.; Engelender, S. α-Synuclein Fate Is Determined by USP9X-Regulated Monoubiquitination. *Proc. Natl. Acad. Sci. U. S. A.* **2011**, *108* (46), 18666–18671.

(363) Myeku, N.; Clelland, C. L.; Emrani, S.; Kukushkin, N. V.; Yu, W. H.; Goldberg, A. L.; Duff, K. E. Tau-Driven 26S Proteasome Impairment and Cognitive Dysfunction Can Be Prevented Early in Disease by Activating CAMP-PKA Signaling. *Nat. Med.* **2016**, *22* (1), 46–53.

(364) Tseng, B. P.; Green, K. N.; Chan, J. L.; Blurton-Jones, M.; LaFerla, F. M. Abeta Inhibits the Proteasome and Enhances Amyloid and Tau Accumulation. *Neurobiol. Aging* **2008**, *29* (11), 1607–1618.

(365) Lindersson, E.; Beedholm, R.; Højrup, P.; Moos, T.; Gai, W.; Hendil, K. B.; Jensen, P. H. Proteasomal Inhibition by α-Synuclein Filaments and Oligomers. *J. Biol. Chem.* **2004**, *279* (13), 12924–12934.

(366) Cliffe, R.; Sang, J. C.; Kundel, F.; Finley, D.; Klenerman, D.; Ye, Y. Filamentous Aggregates Are Fragmented by the Proteasome Holoenzyme.

(367) Brelstaff, J.; Ossola, B.; Neher, J. J.; Klingstedt, T.; Nilsson, K. P. R.; Goedert, M.; Spillantini, M. G.; Tolkovsky, A. M. The Fluorescent Pentameric Oligothiophene PFTAA Identifies Filamentous Tau in Live Neurons Cultured from Adult P301S Tau Mice. *Front. Neurosci.* **2015**, *9* (May), 184.

(368) Karpowicz, R. J.; Haney, C. M.; Mihaila, T. S.; Sandler, R. M.; Petersson, E. J.; Lee, V. M.-Y. M. Y. Selective Imaging of Internalized Proteopathic α-Synuclein Seeds in Primary Neurons Reveals Mechanistic Insight into Transmission of Synucleinopathies. *J. Biol. Chem.* **2017**, *292* (32), 13482–13497.

(369) Nanduri, P.; Hao, R.; Fitzpatrick, T.; Yao, T.-P. Chaperone-Mediated 26S Proteasome Remodeling Facilitates Free K63 Ubiquitin Chain Production and Aggresome Clearance. *J. Biol. Chem.* **2015**, *290* (15), 9455–9464.

(370) Hao, R.; Nanduri, P.; Rao, Y.; Panichelli, R. S.; Ito, A.; Yoshida, M.; Yao, T.-P. Proteasomes Activate Aggresome Disassembly and Clearance by Producing Unanchored Ubiquitin Chains. *Mol. Cell* **2013**, *51* (6), 819–828.

(371) Guo, Q.; Lehmer, C.; Martínez-Sánchez, A.; Rudack, T.; Beck, F.; Hartmann, H.; Pérez-Berlanga, M.; Frottin, F.; Hipp, M. S.; Hartl, F. U.; Edbauer, D.; Baumeister, W.; Fernández-Busnadiego, R. In Situ Structure of Neuronal C9orf72 Poly-GA Aggregates Reveals Proteasome Recruitment. *Cell* **2018**, *172* (4), 696–705.e12.

(372) Thibaudeau, T. A.; Anderson, R. T.; Smith, D. M. A Common Mechanism of Proteasome Impairment by Neurodegenerative Disease-Associated Oligomers. *Nat. Commun.* **2018**, *9* (1), 1097.

(373) Nonaka, T.; Watanabe, S. T.; Iwatsubo, T.; Hasegawa, M. Seeded Aggregation and Toxicity of α-Synuclein and Tau. *J. Biol. Chem.* **2010**, *285* (45), 34885–34898.

(374) Volpicelli-Daley, L. A.; Luk, K. C.; Patel, T. P.; Tanik, S. A.; Riddle, D. M.; Stieber, A.; Meaney, D. F.; Trojanowski, J. Q.; Lee, V. M.-Y. Exogenous α-Synuclein Fibrils Induce

Lewy Body Pathology Leading to Synaptic Dysfunction and Neuron Death. *Neuron* **2011**, *72* (1), 57–71.

(375) Guo, J. L.; Lee, V. M. Y. Neurofibrillary Tangle-like Tau Pathology Induced by Synthetic Tau Fibrils in Primary Neurons over-Expressing Mutant Tau. *FEBS Lett.* **2013**, *587* (6), 717–723.

(376) Münch, C.; O'Brien, J.; Bertolotti, A. Prion-like Propagation of Mutant Superoxide Dismutase-1 Misfolding in Neuronal Cells. *Proc. Natl. Acad. Sci. U. S. A.* **2011**, *108* (9), 3548–3553.

(377) Nonaka, T.; Masuda-Suzukake, M.; Arai, T.; Hasegawa, Y.; Akatsu, H.; Obi, T.; Yoshida, M.; Murayama, S.; Mann, D. M. A.; Akiyama, H.; Hasegawa, M. Prion-like Properties of Pathological TDP-43 Aggregates from Diseased Brains. *Cell Rep.* **2013**, *4* (1), 124–134.

(378) Brundin, P.; Melki, R.; Kopito, R. Prion-like Transmission of Protein Aggregates in Neurodegenerative Diseases. *Nat. Rev. Mol. Cell Biol.* **2010**, *11* (4), 301–307.

(379) Lee, S.-J.; Desplats, P.; Sigurdson, C.; Tsigelny, I.; Masliah, E. Cell-to-Cell Transmission of Non-Prion Protein Aggregates. *Nat. Rev. Neurol.* **2010**, *6* (12), 702–706.

(380) Yamaguchi, K.; Inoue, M.; Goshima, N. Efficient Protein Transduction Method Using Cationic Peptides and Lipids. *J. Biomed. Biotechnol.* **2011**, *2011*, 872065.

(381) Luk, K. C.; Song, C.; O'Brien, P.; Stieber, A.; Branch, J. R.; Brunden, K. R.; Trojanowski, J. Q.; Lee, V. M.-Y. Exogenous α-Synuclein Fibrils Seed the Formation of Lewy Body-like Intracellular Inclusions in Cultured Cells. *Proc. Natl. Acad. Sci. U. S. A.* **2009**, *106* (47), 20051–20056.

(382) Gabizon, R.; McKinley, M. P.; Prusiner, S. B. Purified Prion Proteins and Scrapie Infectivity Copartition into Liposomes. *Proc. Natl. Acad. Sci. U. S. A.* **1987**, *84* (12), 4017–4021.

(383) Aguzzi, A.; Heikenwalder, M.; Polymenidou, M. Insights into Prion Strains and Neurotoxicity. *Nat. Rev. Mol. Cell Biol.* **2007**, *8* (7), 552–561.

(384) Westaway, D.; Goodman, P. A.; Mirenda, C. A.; McKinley, M. P.; Carlson, G. A.; Prusiner, S. B. Distinct Prion Proteins in Short and Long Scrapie Incubation Period Mice. *Cell* **1987**, *51* (4), 651–662.

(385) Bruce, M. E. Scrapie Strain Variation and Mutation. *Br. Med. Bull.* **1993**, *49* (4), 822–838.

(386) Morales, R.; Abid, K.; Soto, C. The Prion Strain Phenomenon: Molecular Basis and Unprecedented Features. *Biochim. Biophys. Acta* **2007**, *1772* (6), 681–691.

(387) Kuczius, T.; Groschup, M. H. Differences in Proteinase K Resistance and Neuronal Deposition of Abnormal Prion Proteins Characterize Bovine Spongiform Encephalopathy (BSE) and Scrapie Strains. *Mol. Med.* **1999**, *5* (6), 406–418.

(388) Wadsworth, J. D. F.; Hill, A. F.; Joiner, S.; Jackson, G. S.; Clarke, A. R.; Collinge, J. Strain-Specific Prion-Protein Conformation Determined by Metal Ions. *Nat. Cell Biol.* **1999**, *1* (1), 55–59.

(389) Collinge, J.; Sidle, K. C. L.; Meads, J.; Ironside, J.; Hill, A. F. Molecular Analysis of Prion Strain Variation and the Aetiology of "new Variant" CJD. *Nature* **1996**, *383* (6602), 685–690.

(390) Telling, G. C.; Parchi, P.; DeArmond, S. J.; Cortelli, P.; Montagna, P.; Gabizon, R.; Mastrianni, J.; Lugaresi, E.; Gambetti, P.; Prusiner, S. B. Evidence for the Conformation of the Pathologic Isoform of the Prion Protein Enciphering and Propagating Prion Diversity. *Science* **1996**, *274* (5295), 2079–2082.

(391) Bessen, R. a; Marsh, R. F. Distinct PrP Properties Suggest the Molecular Basis of Strain Variation in Transmissible Mink Encephalopathy. *J. Virol.* **1994**, *68* (12), 7859–7868.

(392) Kang, L.; Wu, K.-P.; Vendruscolo, M.; Baum, J. The A53T Mutation Is Key in Defining the Differences in the Aggregation Kinetics of Human and Mouse α-Synuclein. *J. Am. Chem. Soc.* **2011**, *133* (34), 13465–13470.

(393) Brelstaff, J.; Tolkovsky, A. M.; Ghetti, B.; Goedert, M.; Spillantini, M. G. Living Neurons with Tau Filaments Aberrantly Expose Phosphatidylserine and Are Phagocytosed by Microglia. *Cell Rep.* **2018**, *24* (8), 1939–1948.e4.

(394) Bergh, J.; Zetterström, P.; Andersen, P. M.; Brännström, T.; Graffmo, K. S.; Jonsson, P. A.; Lang, L.; Danielsson, J.; Oliveberg, M.; Marklund, S. L. Structural and Kinetic Analysis of Protein-Aggregate Strains in Vivo Using Binary Epitope Mapping. *Proc. Natl. Acad. Sci. U. S. A.* **2015**, *112* (14), 4489–4494.

(395) Bocharova, O. V; Breydo, L.; Parfenov, A. S.; Salnikov, V. V; Baskakov, I. V. In Vitro Conversion of Full-Length Mammalian Prion Protein Produces Amyloid Form with Physical Properties of PrPSc. *J. Mol. Biol.* **2005**, *346* (2), 645–659.

(396) Legname, G.; Baskakov, I. V; Nguyen, H.-O. B.; Riesner, D.; Cohen, F. E.; DeArmond, S. J.; Prusiner, S. B. Synthetic Mammalian Prions. *Science* **2004**, *305* (5684), 673–676.

(397) Jackson, G. S.; Hosszu, L. L.; Power, A.; Hill, A. F.; Kenney, J.; Saibil, H.; Craven, C. J.; Waltho, J. P.; Clarke, A. R.; Collinge, J. Reversible Conversion of Monomeric Human Prion Protein between Native and Fibrilogenic Conformations. *Science* **1999**, *283* (5409), 1935–1937.

(398) Jackson, G. S.; Hill, A. F.; Joseph, C.; Hosszu, L.; Power, A.; Waltho, J. P.; Clarke, A. R.; Collinge, J. Multiple Folding Pathways for Heterologously Expressed Human Prion Protein. *Biochim. Biophys. Acta* **1999**, *1431* (1), 1–13.

(399) Makarava, N.; Ostapchenko, V. G.; Savtchenko, R.; Baskakov, I. V. Conformational Switching within Individual Amyloid Fibrils. *J. Biol. Chem.* **2009**, *284* (21), 14386–14395.

(400) Baskakov, I. V; Legname, G.; Baldwin, M. a; Prusiner, S. B.; Cohen, F. E. Pathway Complexity of Prion Protein Assembly into Amyloid. *J. Biol. Chem.* **2002**, *277* (24), 21140–21148.

(401) Riesner, D.; Kellings, K.; Post, K.; Wille, H.; Serban, H.; Groth, D.; Baldwin, M. A.; Prusiner, S. B. Disruption of Prion Rods Generates 10-Nm Spherical Particles Having High α-Helical Content and Lacking Scrapie Infectivity. *J. Virol.* **1996**, *70* (3), 1714–1722.

(402) Wu, J. W.; Herman, M.; Liu, L.; Simoes, S.; Acker, C. M.; Figueroa, H.; Steinberg, J. I.; Margittai, M.; Kayed, R.; Zurzolo, C.; Di Paolo, G.; Duff, K. E. Small Misfolded Tau Species Are Internalized via Bulk Endocytosis and Anterogradely and Retrogradely Transported in Neurons. *J. Biol. Chem.* **2013**, *288* (3), 1856–1870.

(403) Danzer, K. M.; Krebs, S. K.; Wolff, M.; Birk, G.; Hengerer, B. Seeding Induced by α-Synuclein Oligomers Provides Evidence for Spreading of α-Synuclein Pathology. *J. Neurochem.* **2009**, *111* (1), 192–203.

(404) Danzer, K. M.; Haasen, D.; Karow, A. R.; Moussaud, S.; Habeck, M.; Giese, A.; Kretzschmar, H.; Hengerer, B.; Kostka, M. Different Species of α-Synuclein Oligomers Induce Calcium Influx and Seeding. *J. Neurosci.* **2007**, *27* (34), 9220–9232.

(405) Desplats, P.; Lee, H.-J.; Bae, E.-J.; Patrick, C.; Rockenstein, E.; Crews, L.; Spencer, B.; Masliah, E.; Lee, S.-J. Inclusion Formation and Neuronal Cell Death through Neuron-to-Neuron Transmission of α-Synuclein. *Proc. Natl. Acad. Sci. U. S. A.* **2009**, *106* (31), 13010–13015.

(406) Schell, H.; Hasegawa, T.; Neumann, M.; Kahle, P. J. Nuclear and Neuritic Distribution

of Serine-129 Phosphorylated α-Synuclein in Transgenic Mice. *Neuroscience* **2009**, *160* (4), 796–804.

(407) Okochi, M.; Walter, J.; Koyama, A.; Nakajo, S.; Baba, M.; Iwatsubo, T.; Meijer, L.; Kahle, P. J.; Haass, C. Constitutive Phosphorylation of the Parkinson's Disease Associated α-Synuclein. *J. Biol. Chem.* **2000**, *275* (1), 390–397.

(408) Pronin, A. N.; Morris, A. J.; Surguchov, A.; Benovic, J. L. Synucleins Are a Novel Class of Substrates for G Protein-Coupled Receptor Kinases. *J. Biol. Chem.* **2000**, *275* (34), 26515–26522.

(409) Fujiwara, H.; Hasegawa, M.; Dohmae, N.; Kawashima, A.; Masliah, E.; Goldberg, M. S.; Shen, J.; Takio, K.; Iwatsubo, T. α-Synuclein Is Phosphorylated in Synucleinopathy Lesions. *Nat. Cell Biol.* **2002**, *4* (2), 160–164.

(410) Nixon, R. A.; Cataldo, A. M. The Endosomal-Lysosomal System of Neurons: New Roles. *Trends Neurosci.* **1995**, *18* (11), 489–496.

(411) McCann, H.; Stevens, C. H.; Cartwright, H.; Halliday, G. M. α-Synucleinopathy Phenotypes. *Parkinsonism Relat. Disord.* **2014**, *20 Suppl 1*, S62-7.

(412) Arosio, P.; Knowles, T. P. J.; Linse, S. On the Lag Phase in Amyloid Fibril Formation. *Phys. Chem. Chem. Phys.* **2015**, *17* (12), 7606–7618.